Alma Mater Studiorum – Università di Bologna

DOTTORATO DI RICERCA IN

GEOFISICA

Ciclo XXI

Settore Concorsuale: 04/A4

Settore Scientifico Disciplinare: GEO/10

Hydrological crustal deformation in the Eastern Southern Alps

Presentata da: Francesco Pintori

Coordinatore Dottorato

Prof.ssa Nadia Pinardi

Supervisore

Prof.ssa Maria Elina Belardinelli

Co-Supervisore

Dott. Enrico Serpelloni

Esame finale anno 2019

When nothing seems to help, I go and look at a stonecutter hammering away at his rock, perhaps a hundred times without as much as a crack showing in it. Yet at the hundred and first blow it will split in two, and I know it was not that last blow that did it, but all that had gone before.

Jacob A. Riis

Contents

Acknowledgments

I would like to thank my supervisor, prof. Belardinelli, for her support and her advices, which have been fundamental for the realization of this project.

I am grateful to dott. Serpelloni for having involved me without hesitation in a very interesting project and followed me step by step.

Thanks to dott. Laurent Longuevergne, who hosted me at University Rennes 1. The collaboration with him has been a great positive turning point of this thesis.

I have really appreciated the opportunity to work with Adriano Gualandi, Enrico Scoccimarro, Letizia Anderlini, Adriano Cavaliere, Micol Todesco and many others, who helped me with productive discussion and gave me fundamental suggestions about what is necessary to improve the quality of a scientific research.

I thank Lucio D'Alberto and prof. Dario Zampieri for their support on the hydrological and geological sections of this work.

I am grateful to Kristel Chanard and Jean-Paul Boy for having shared with me fundamental data.

I really appreciated the review on this thesis made by dott. Roberto Devoti and prof. Carla Braitenberg. Their contribution has been important to improve the quality of this work.

I would like to mention my PhD colleagues Emanuele, Glauco, Antonio, Liang and Camilla. Each of you gave me something that made this experience better.

I finally thank my family and Ilaria for always sustaining me, especially during the bad times.

Abstract

We applied a blind source separation algorithm to the ground displacements time-series obtained from the analysis of continuous GPS stations operating in the Eastern Southern Alps and northern Dinarides. This analysis highlighted both annual common mode component signals and a time-variable, non-cyclic signal characterized by a spatially variable response in the horizontal component, while in the vertical one its amplitude is below the noise level in most of the stations. The first signal is well described by loading effects caused by Earth surface water mass redistributions, while the latter one has a temporal evolution that well correlates with the history of cumulated precipitations at monthly time scales and has larger amplitudes in three karst areas of the study region. The GPS stations respond to this signal by moving in opposite direction, reversing the sense of movement in time, implying a succession of extensional/compressional strains, with variable amplitudes through time, oriented normal to rock fractures of the karst areas.

In this thesis we focus on the Val Belluna (i.e. Piave river basin) and the pedemountain front of the Venetian Southern Alps, and test the hypothesis that the succession of horizontal extensions and contractions recorded by the GPS stations are caused by the variation of the water level in hydrologically-connected fractures, whose temporal evolution is guided by water storage variation in the hydrological basin of this area. Water storage has been modeled by using rainfall-runoff hydrological models, which describe how the precipitation over a basin turns into river flow once given as input precipitation and potential evapotranspiration. Having found high correlations between the temporal evolution of water storage variations and the deformation signal, we built a bi-dimensional numerical model based on finite-element method, containing the geologic feature of the study area, with the goal of understanding how water storage variations generate the observed displacements. Then, we tested different sources of deformation in order to find the one that best reproduces the displacements obtained from the geodetic analysis, locating it in the shallow part of the backthrust of the Bassano-Valdobbiadene thrust fault. This backthrust fault is just north of the M.te Grappa-M.te Cesen mountain chain, which is karstified and corresponds to an anticline on top of the south-verging Bassano-Valdobbiadene thrust fault. Since the hinge of the anticline is characterized by sub-vertical fractures, we made the hypothesis that precipitation penetrates through the fractures and flow along the rock layers, converging to the sub-vertical structure corresponding to the backthrust of the Bassano-Valdobbiadene thrust fault. Here, the water accumulates because of the larger permeability of the fractured rock faults, varying its level up to tens of meter and then generating pressure changes that cause the observed displacements. Finally, we estimated the crustal stress perturbation generated by the source of deformation, showing that for depths higher than about 3 km it tends toward zero.

1 Introduction

The increased accuracy, density of the measurements and temporal sampling of modern space geodetic techniques, are revolutionizing our knowledge about the many processes that cause the Earth's crust to deform, opening new perspectives for understanding large spectra of active Earth's processes that drive natural hazards, weather, and climate. In particular, continuously operating Global Positioning System (GPS) networks, or more generally Global Navigation Satellite System (GNSS) networks, are now used worldwide to track, with mm accuracies, how points on the Earth's surface move. The primary application of GPS time series analysis is the study of tectonic forces that drive the earthquake cycle, which is characterized by long periods of steady motion (interseismic deformation) across tectonic plate boundaries, during which stress is accumulated and released suddenly during earthquakes (coseismic deformation), followed by a period of relaxation of the crust (postseismic deformation), and then a return to the steady interseismic state. This simple model is expected to be at best applicable over the long term, averaged over many earthquakes; while in order to study the ongoing deformation of a specific region, it is necessary identify several additional transitory and non-secular strain accumulation processes in the crust that cause temporary deviations from the linear interseismic trend. Such processes, commonly associated with natural and anthropogenic causes, are generally known as transient deformation signals. Among the tectonic transient signals, aseismic processes like afterslip, slow-slip earthquakes, and pre-seismic slip can be considered.

Afterslip is slip immediately following an earthquake on the same faulting surface. It is characterized by slip duration of a few days to a few months, with a rapid initial slip rate followed by logarithmic decay (Schwartz and Roskosky, 2007). This is different from viscoelastic postseismic processes, where the entire volume surrounding an earthquake, notably the lower crust and upper mantle, deforms in the months to years following an event. Another example of transient tectonic signal is the so-called slow-slip earthquake, which is an episodic movement across a fault that releases energy on timescales of hours to weeks rather than seconds to minutes as it commonly occurs during earthquakes. Since a slow slip event does not generate seismic waves, it is also known as "silent" earthquake, even though it has been observed that it can release the equivalent energy of a magnitude 6 earthquake. These events were first recognized by modeling anomalies in GPS time series as a slow thrust event in the Bungo Channel in Japan (Hirose *et al.*, 1999), and now there are evidences in other subduction areas of the Earth, like Mexico, Cascadia, Alaska, Costa Rica and New Zealand (Jiang *et al.*, 2012). Since slow slip events do not generate seismic waves, the only way to identify them is the detection of anomalies on Earth surface displacements, which are caused by slip on the fault at depth. This has been possible only since the advent of global positioning system (GPS) networks. It follows that the contribution of space geodesy in the study of these processes was, and still is, crucial. The last and most-debated class of tectonic transient deformation is preseismic slip. This phase (nucleation phase) has been hypothesized for geologic faults based on small variations with respect to a constant friction prior to a slip event that have been seen in laboratory rock experiments (Dieterich, 1979). Transient preslip deformation was reported at one station preceding an Mw 7.6 aftershock to the 2001 Mw 8.4 Peru earthquake (Melbourne *et al.*, 2002). A subsequent study reported ten credible accounts of preseismic geodetic transients and it also noted their absence for many more large earthquakes (Roeloffs, 2006).

Even though GPS data are primarily used for tectonic studies, or more in general for studies of the solid Earth, their application also involve other Earth science disciplines, like the study of atmosphere, hydrosphere and climate. Since the GPS signal is significantly delayed by the refraction in the troposphere, which is a function of atmospheric water vapor, pressure, and temperature; the estimation of this delay is used for short-term weather forecasting and long-term climate studies. Furthermore, Total Electron Content (TEC) variations in GPS signals can be exploited to detect perturbations in the ionosphere caused by a wide variety of sources. Internal sources include atmospheric perturbations from earthquakes, tsunamis, volcanic eruptions, or deep convective events (large hurricanes or tornadoes). External sources as such geomagnetic storms, aurora, and plasma instabilities, and man-made sources such as explosions and rocket ascents are also observable. Important indicators of climate changes are ice sheets melting and the sea level rise, which can be monitored by GPS data analysis. In fact, observations of contemporary vertical land motion (VLM) of coastal areas near traditional tide gauges and 3D GPS displacement on bedrock at the periphery of ice sheets, as well as other indirect measurements of glacial isostatic adjustment (GIA), can be used for quantifying absolute sea level rise. The correct quantification of

GIA is crucial, since it is one of the biggest sources of error in contemporary ice sheet mass balance calculations for the assessment of variations in mass loss and their impact on sea level rise due to climate change (Shepherd *et al.*, 2012). Finally, recent destructive natural events have motivated the proliferation of continuous GPS geodetic networks that sample at high rates and in real time, providing natural hazard mitigation systems for earthquakes, tsunamis, and volcanic eruptions.

In this thesis we will focus on both transient and seasonal non-tectonic signals present in GPS time series. Dong et al. (2002) investigated the possible sources of seasonal effects on global GPS displacement time series and sorted them into three categories. The first is related to the gravitational attraction of the Sun and Moon, including seasonal polar motion, Earth rotation variations and loading displacements due to solid Earth, ocean, atmospheric and pole tides. The second category is related to hydrodynamics and thermal effects, including atmospheric pressure loading, non-tidal sea surface fluctuations (Williams and Penna, 2011), anthropogenic groundwater and mineral extraction, snow accumulation, local thermal expansion, and seasonal changes in the reflecting surface (soil moisture and vegetation) that produce multipath errors. The third category includes effects specific to GPS analysis such as satellite orbital errors. On the other hand, non-tectonic transient deformation signals, especially of hydrological origin, are attracting more and more attention. The importance of the identification and characterization of these processes involve both the study of the earthquake cycle and the environment. In fact, improving the knowledge of transients helps monitoring possibly geographically shifting physical changes that may impact society such as scarce water resources, agricultural productivity to feed growing populations, increased flooding hazards, and more extreme weather. Furthermore, their relevance in the study of tectonic processes is twofold; first, thanks to a proper modeling of non-tectonic deformation it is possible to improve the accuracy of long-term tectonic rates, second because hydrological processes can perturb crustal stress at seismogenic depths, with effects on the background seismicity rate and on the seismic cycle. Recently, Johnson *et al.* (2017) showed that the vertical motions of GPS sites in California, caused by the changing water load, influence the state of stress on shallow faults. In particular, an analysis of fault failure conditions indicates that the rise and fall of the surface due to water loading and unloading creates a small amount of additional stress on the faults and can trigger small earthquakes. Similar processes have been recorded in the Himalayan region, where the water loading variations induced by the monsoon modulate the annual seismicity (Bettinelli *et al.* 2008, Fu *et al.* 2013, Hainzl *et al.* 2006).

One of the most useful tools to analyze large-scale hydrological processes is the NASA's Gravity Recovery and Climate Experiment (GRACE) experiment, which provides estimation of water mass changes on Earth by monitoring the variations of the gravity field of our planet. Even though both the temporal and the spatial resolution of these data are poor (monthly, on 200 $\times$ 200 km grids), this experiment provided crucial information on large-scale climate events, like the severe drought that California has experienced. When dealing with local scale processes, involving areas smaller than the thousands of km squares, especially if characterized by a daily signature, GRACE data are not useful. Nonetheless, recent studies highlighted the ability of the GPS technique in identifying hydrological-related deformation at different spatial scales. For example, the California drought has been observed and modeled by GPS data analysis (Amos *et al.*, 2014, Argus *et al.*, 2014) obtaining results that are in agreement with GRACE ones; furthermore more local scales studies (e.g., Devoti *et al.*, 2015; Moreau and Dauteuil, 2013) evidenced displacements related with the hydrological cycle, in particular to rainfall, that are undetectable by GRACE.

In this thesis we studied GPS position time series of stations located in the South-Eastern sector of the European Alps. This region accommodates large part of the Adria-Eurasia convergence, through large earthquakes in the past, and is now precisely monitored by a dense network of continuous GPS stations. Here, thanks to the ability of the GPS technique in detecting tectonic strains, it was possible to get partially reliable maps of interseismic coupling which show that for some segments of the Adria-Eurasia boundary aseismic deformation may occur. However, Devoti *et al.* (2015) found that a portion of the same area (Cansiglio Plateau) is affected by transient deformation processes associated with the hydrological cycle in karsts, in particular to rainfall; furthermore Silverii *et al.* (2016) discussed seasonal and multi-year deformation in GPS time series of a wider region, the southern Apennines of Italy, which have been associated with groundwater variations in karst aquifers. Most of the authors, when analyzing the link between hydrological processes and crustal deformation recorded by geodesy, focus on the study of temporal correlations by examining the temporal signature of precipitation events, river flows and/or spring discharges. This approach can be useful, since it can give first hints about connections between processes that

apparently belongs to different spheres, i.e. hydrology and mechanics. Nonetheless, this may be limitative if the link between these two study fields is missing, so that the way hydrology and other mechanics processes interact is not explained. In this thesis we tried not only to highlight existing correlations between these different processes, but we applied a physical approach with the goal of explaining and measure the processes that link hydrology to rock deformation, taking into consideration the geological features of the areas under analysis. We then implemented the results of a hydrological model in a mechanical one, with the goal of describing how the hydrological cycle, in particular the variations of water stored in the subsurface, affects crustal deformation and stress. Following this procedure, it would then become possible to study the effect of stress variations induced by non-tectonic processes, such as the ones here investigated, on tectonic structures such as faults. Even if it was not the goal of this thesis, it is worth noting that strain time series can also be used as a constraint for hydrological data in environmental monitoring. The technique used in this thesis for time series analysis is the Variational Bayesian Independent Component Analysis (vbICA) (Gualandi *et al.*, 2016), a multivariate statistical analysis based on the solution of blind source separation (BSS) problem. The goal of BSS consists in determining, once known the observed time series, the temporal signatures of the original different physical processes generating them, making the fewest (and the most reasonable) number of assumptions as possible. This approach has been successfully used, in recent times, to separate both continental-scale hydrological signals from tectonic transients in several tectonic settings (Gualandi, *et al.*, 2016; Gualandi, *et al.*, 2017).

This dissertation is organized as follows. In chapter 2 we describe geologically and tectonically the study region, providing also details on karst systems and on the models used to determine water storage variations. In chapter 3 we describe the GPS technique, how geodetic data are initially gathered, processed and then finally analyzed by using the vbICA technique. In chapter 4 we present the results of the vbICA applied to the investigated region, discussing the physical sources that originate seasonal signals and the model used to describe these processes. In chapter 5 we give an interpretation of a transient deformation signal, highlighting its connection with precipitation and water storage variations in karst systems; and finally, in chapter 6, we present two models that describe how water storage variations cause the detected transient displacements.

2 Description of the area under analysis and hydrological models

The area under investigation in this thesis is represented by the red rectangle of Figure 1, which mainly includes the South-Eastern Alps and the Northern Dinarides.

In section 2.1 and 2.2 we discuss the geologic and tectonic features of the Alps, focusing in particular on the study area. In section 2.3 we describe the features of karst aquifers, while in section 2.4 the hydrological models we used in the following chapters.

2.1 Geologic settings

Geographically, the Alps extend from the Gulf of Genoa to Vienna, through the French-Italian western Alpine arc and the east-west-trending central and eastern Alps (Figure 1). South of Genoa, the Alpine range disappears, because it collapsed and was fragmented during the Late Neogene opening of the Tyrrhenian basin (southern segments of the Alpine belt are preserved in Corsica and Calabria). To the east, the former connection between the Alpine and Carpathian belts is buried below the Neogene fill of the Vienna and Styria (Pannonian) basins.

The Alps can be subdivided into different main tectonic-stratigraphic facies zones: the South Alpine, the East and West Alpine (Austroalpine), the Penninic and the Helvetic zone. Synorogenic Flysch sediments are present within all the main zones and late- to post-orogenic Molasse foreland basins formed north and south of the Alps (Figure 1).

The Alpine orogenesis started in the Cretaceous by subduction of a Mesozoic ocean (Tethys) followed by collision between the Adriatic (Austroalpine-Southalpine) and Eurasian (Penninic-Helvetic) continental margins. The continent-continent collision started after the subduction and thrusting of the Penninic flysch units, during the Eocene ($\sim$50 Ma) (Decker and Peresson, 1996). This process had been an asymmetric orogene: The Helvetic, Penninic and East Alpine units were transported as large thrust sheets (nappes) in northern direction. The East Alpine nappes were thrust on top of the Penninic nappes and both were thrust on top of the Helvetic nappes. The nappes consist both of the sedimentary cover and the crystalline, pre-Alpine basement. During the last stage of orogenesis, folding and thrusting affected even the southern margin of the Molasse basin north of the Alps. Due to the northward movement of the nappes, most of the thrusts and folds are north-verging. In contrast to that, the South Alpine zone is characterized by south-verging structures.

The north-verging Eastern Austroalpine Alps and the south-verging Southern Alps are separated by a first order tectonic boundary, the Periadriatic (Insubric) line (Schmid *et al.*, 1989); nonetheless, close analogies in basement petrography and sedimentary sequence prove that the two zones originate from the southern margin of Tethys and form a unity in terms of paleogeography and stratigraphy (Laubscher, 1989). In fact, during the Triassic, the Tethys flooded the South and East Alpine and extensive carbonate platforms with reefs formed: up to 4000 m of sediments were deposited on the subsiding passive continental margins (Prey, 1978). Since the late Triassic and during the Jurassic, the South Penninic ocean had been opening, so that the carbonate platforms broke down and a mosaic of blocks was formed. Up to 4000 m thick sediments were deposited in the quickly subsiding grabens, while sedimentation stopped on the horsts. During the Upper Jurassic and Lower Cretaceous, the South Penninic ocean was further expanding and deep marine, pelagic sediments (e.g. radiolarites) were deposited. In the Lower Cretaceous, the relative movement between the African and European plate reversed and the oceanic basins came under compression. The differentiation between Southern and Eastern Alps happened between the Upper Cretaceous and the Eocene, when ocean basins were subsiding and filled with sediments of the "Gosau" facies. During the Gosau sedimentation, the East Alpine was uplifted and formed the front of the upper plate, while the South Alpine subsided and was partly covered with Flysch sediments. As a result, the Southern Alps are mainly composed by Mesozoic sedimentary rocks, most of them limestones.

The western Austroalpine consists of the Sesia-Lanzo zone and numerous more external thrust units traditionally grouped as Argands Dent Blanche nappe. These units override and are partly tectonically interleaved with the structurally composite ophiolitic Piedmont zone, the major remnant of the Mesozoic ocean.

The Penninic nappes form large parts of the Western Alps and outcrop in tectonic windows under the East Alpine nappes in the central Eastern Alps. The Penninic zone is highly heterogeneous: there are all kinds of continental, shallow- and deep- marine sediments, as well as remnants

of oceanic crust (ophiolites). Furthermore, large parts of the Penninic unit underwent a regional metamorphosis after subduction and carbonate platforms formed locally in its middle zone during the Jurassic.

The Helvetic nappes form the outer zone of the French and Swiss Alps, as well as parts of West Austria. Further to the east, a narrow and discontinuous strip of Helvetic rocks follows the northern margin of the Northern Limestone Alps (Schonenberg and Neugebauer, 1997). It consists of shallower basement slices and decolled cover units derived from the proximal part of the European margin, mainly imbricated from the Oligocene onwards. The vertical nappe sequence and their deformation age generally reflect the outward propagation of the orogenic front.

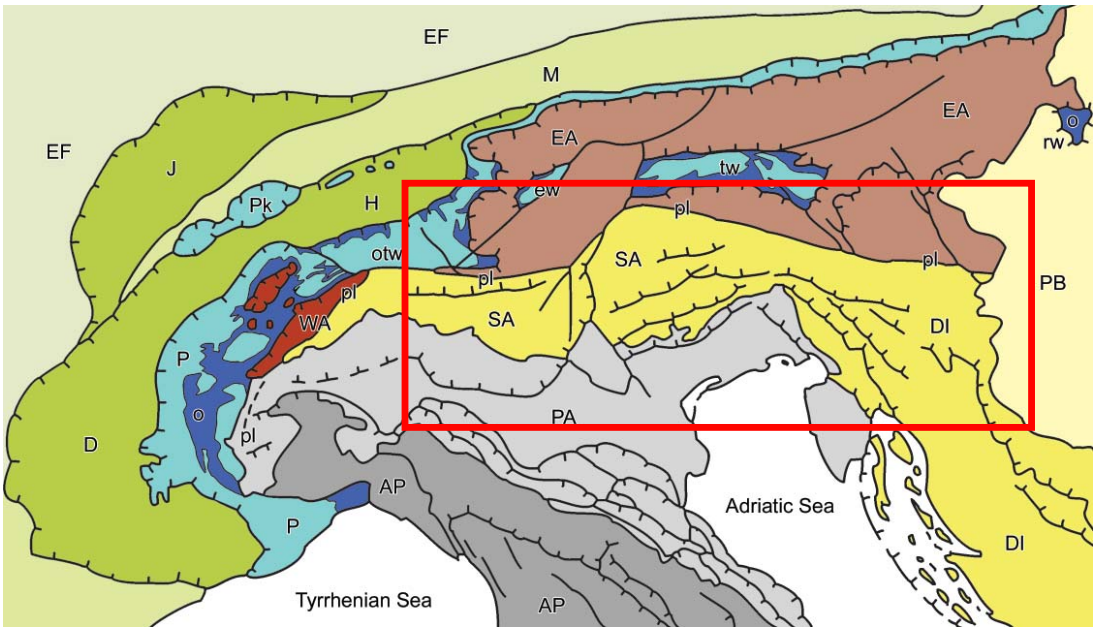

Figure 1: Geological map of the Alps, modified from Dal Piaz, 2003. Europe-vergent collisional belt: Western (WA) and Eastern (EA) Austroalpine; Penninic domain: continental and ophiolitic (o) nappes in western Alpine arc (P) and tectonic windows (otw: Ossola-Ticino, ew: Engadine, tw: Tauern, rw: Rechnitz); Prealpine klippen (Pk); Helvetic-Dauphinois (H-D) domain; Molasse foredeep (M); Jura belt (J). Southern Alps (SA), bounded to the north by the Periadriatic lineament (pl). Pannonian basin (PB), European (EF) and Po Valley-Adriatic (PA) forelands, Dinaric (DI) and Apenninic (AP) thrust-and-fold belts. The red rectangle represents the area under analysis

.

2.2 Tectonic settings

The boundary between Adriatic and Eurasian plates is marked by the Eastern Alps and northern Dinarides (see Figure 2) through a wide zone of deformation including a variety of tectonic styles within a complex network of crustal and lithospheric faults (see Serpelloni *et al.* (2016), for a recent synoptic view). The Dinarides are a Late Jurassic to recent, mainly SW vergent fold-and-thrust belt that extends from the Southern Alps in the NW to the Albanides/Hellenides to the SE. They are formed largely of Mesozoic and Cenozoic sedimentary rocks like dolomite, limestone, sandstone, and conglomerate.

The large part of the Adria-Eurasia convergence is now accommodated across the southernmost Eastern-Southern Alps (ESA) thrust front, where the Adriatic lithosphere underthrusts the Alpine mountain belt. The Adriatic plate rotates counterclockwise at $\sim 0.3°$/Myrs (Serpelloni *et al.*, 2016) around a pole of rotation located in the western Po Plain of Italy, implying rates of convergence between Adria and Eurasia between 1.5 and 2.0 mm/yr in the study region (Figure 2). The highest geodetic strain rates are observed in the ESA central segment (the Montello and Cansiglio thrusts; Danesi *et al.*, 2015; Serpelloni et al., 2016).

Cheloni *et al.* (2014) and Serpelloni *et al.* (2016) showed that the ESA thrust front presents variable interseismic coupling, but uncertainties on coupling values, in particular for its central (i.e., Venetian) sector, are large, due to uncertainties in long-term motion rates of GPS sites

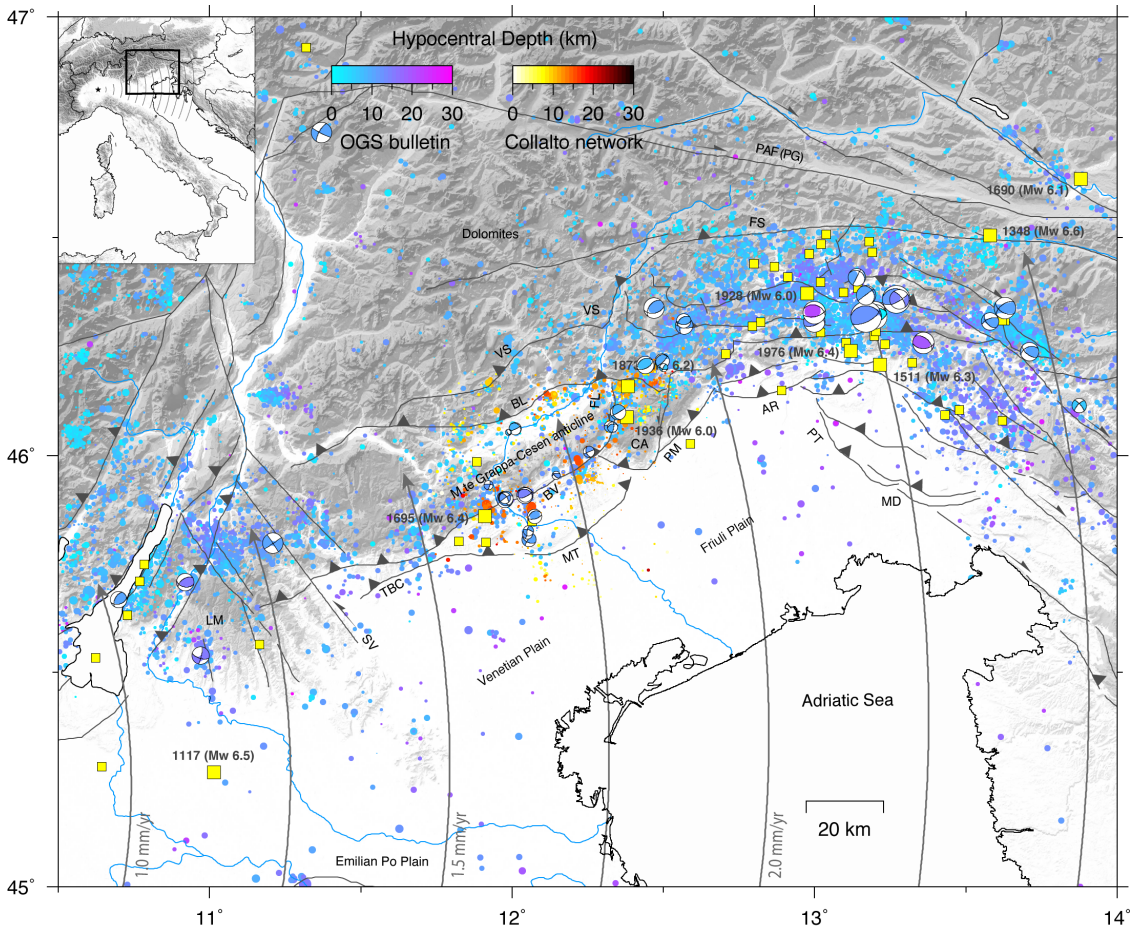

Figure 2: Seismotectonic map of the study area, with the major tectonic lineaments shown in black (from Serpelloni *et al.*, 2016). LM: Lessini Mountains; SV: Schio-Vicenza line; TBC: Thiene-Bassano-Cornuda thrust; MT: Montello thrust; BV: Bassano-Valdobbiadene thrust; BL: Belluno thrust; VS: Valsugana thrust; CA: Cansiglio plateau; PM: Polcenigo-Maniago thrust; AR: Araba-Ragona thrust; PT: Pozzuolo thrust; MD: Medea thrust, FS: Fella-Sava line; PAF (PG): Peri-adriatic fault - Pusteri-Gailtal line. Major historical events (Mw>6) are shown as yellow squares. The blue-purple symbols show instrumental seismicity for the 2000-2017 time-span extracted from the OGS bulletins (*http://www.crs.inogs.it/bollettino/RSFVG*). The yellow-red circles show instrumental seismicity for the 2012-2018 time-span recorded by the OGS Collalto seismic network (http://rete-collalto.crs.inogs.it). The focal mechanisms (from Anselmi *et al.*, 2011; Danesi *et al.*, 2015; Serpelloni *et al.*, 2016) are plotted with the same color palette of the OGS instrumental seismicity. The small circles around the geodetic pole of rotation showing the motion direction of Adria relative to Eurasia, from Serpelloni *et al.*, 2016, are shown in gray, with arrows indicating the motion of Adria.

located in the Cansiglio Plateau (CA in Figure 2). Moreover, Serpelloni *et al.* (2016) have shown that GPS velocity gradients along the Adria-Eurasia convergence direction across the Montello-Cansiglio thrusts are difficult to be explained with elastic coupling models. The main thrusts of the Venetian Alps are, from the internal parts to the foreland, the Valsugana thrust (VS in Figure 2), the Belluno thrust (BL in Figure 2) and the Bassano-Valdobbiadene thrust (BV in Figure 2), the latter being associated with a morphological relief of ∼1200 m above the plain, known as Pedemountain flexure. They are composed by carbonate rocks, where the principal formations are well-bedded limestones of Jurassic age (the Calcari Grigi and the Rosso Ammonitico) that are overlaid by cherty or marly, more densely fractured, Cretaceous limestones (Maiolica formation, a chalk, and the Scaglia Variegata Alpina).

In the westernmost sector, the ESA is crossed by the NW-SE trending Schio-Vicenza (SV in Figure 2) strike-slip fault system, a Late Miocene-Quaternary kinematic junction between the ESA and the Central-Western Southern Alps (Castellarin and Cantelli, 2000). The Schio-Vicenza line borders to the east the Giudicarie-Lessini region, a triangular-shaped block wedged with its apex into the Neogene Southern Alps fold-and-thrust belt. East of the Schio-Vicenza line, the southernmost front of the ESA in Veneto consists of (Figure 2) the Thiene-Bassano-Cornuda thrust and the Montello thrust (e.g. Benedetti *et al.*, 2000; Fantoni *et al.*, 2001; Galadini *et al.*, 2005; Burrato *et al.*, 2008; Danesi *et al.*, 2015). The Montello hill is generally interpreted as an actively growing ramp anticline on top of an active, north dipping, thrust that has migrated south of the mountain into the foreland (Benedetti et al., 2000). Benedetti *et al.* (2000) suggested that the Piave river changed its course because of the growth of the Montello hill, at a rate of 0.5 mm/yr to 1.0 mm/yr estimated from the ages of the river terraces. Modeling the deformation of the river terraces as a result of motion on the thrust ramp, Benedetti *et al.*, (2000) estimated a constant slip rate of 1.8-2.0 mm/yr.

In the Friuli ESA the most recent compressive front affects the base of the Venetian and Carnic Alps and corresponds to the WSW-ENE striking Polcenigo-Maniago and Arba-Ragogna thrusts (Poli *et al.*, 2002; Galadini *et al.*, 2005). In the eastern (i.e., Julian) sector of the ESA the front extends southward and in the Udine-Gorizia sector it corresponds to a set of S-verging, WNW-ESE trending low-angle thrusts geometrically influenced by the inherited structures of the NW-SE Dinaric Palaeogene front.

The eastward extent of the ESA thrust belt is controversial. Southern and southwestern Slovenia is extensively faulted by NW-SE-trending dextral faults, which form conspicuous topographic lineaments, particularly in karstic areas, such as the Idrja and Rasa faults (Figure 2). Since the faults are parallel to the strike of Dinaric folds and thrusts, they are classically called Dinaric faults although no structural connection with Dinaric thrusting is known. These faults cut and displace both Dinaric and South-Alpine fold-and-thrust structures. In the Julian Alps and western Slovenia, the South-Alpine front overthrusted and refolded Dinaric thrust structures (Doglioni, 1987; Placer and Car, 1998). The south Alpine thrusts of the Julian Alps in western Slovenia continue into the Valsugana thrust system in Italy of mid- to late Miocene age (e.g., Castellarin and Cantelli, 2000). Thrust sheets exposed in the Sava Folds region (Figure 2) are considered as south-Alpine, due to the paleogeographic affinities of the thrust units (e.g., Placer, 1999), but Oligocene sediments apparently cover the thrusts (Placer, 1999b), implying that thrusting in the Sava Folds region predates the Miocene South-Alpine episode. Also the Post-Oligocene thrusts of the Kamnik Alps are South-Alpine, however the entire unit was probably subsequently displaced eastward several tens of kilometers along the dextral Sava fault (see Figure 2). Therefore, the eastern boundary of ESA thrust front originally could have been at the present-day longitude of the Julian Alps in western Slovenia.

The PAF zone represents a major topographic and structural boundary in northern Slovenia. The E-W- to NW-SE-trending, gently curved dextral Sava fault south of the PAF has impressive topographic expression. Toward the west in Italy, where the Sava fault is known as the Fella Line, the slip sense gradually changes to reverse dextral, and the fault merges with the South-Alpine thrusts. Eastward, the Sava fault merges with the Sostanj fault and the Labot fault, together forming the continuation of the PAF zone toward the Drava graben.

The ESA mountain front and foreland is the locus of several Mw>6 earthquakes (yellow squares in Figure 2) in the last 2000 years (Serpelloni *et al.*, 2016), but most of the seismogenic sources associated with these large earthquakes are still debated (DISS working group), although there is a general consensus for some of these earthquakes that the fault sources belong to the ESA thrust fault system, emerging at the boundary between the Venetian plane and the mountain front

in northeastern Italy (Benedetti *et al.*, 2000; Burrato *et al.*, 2008; Galadini *et al.*, 2005; Cheloni *et al.*, 2012). Information from historical sources and modern earthquake catalogues show that there were at least 12 earthquakes with a magnitude of $\geqslant 6$ in the past thousand years in the Italian Southern Alps. The last one (Mw 6.4) took place in 1976 in Friuli. Although the extent of damage for historical events can sometimes be difficult to be estimated, it is likely that at least three of the quakes shown in Figure 2 caused >10000 deaths. The largest earthquake in the study area is the 1695 Asolo earthquake, which is estimated, from the interpretation of historical information, as a ∼Mw 6.4 event. However, the seimogenic source of this important earthquake is not well constrained. Uncertainties on the location, geometry and seismic potential of active faults in the Venetian Southern Alps persists due to: i) the complex structural framework of the region, inherited by the geodynamic evolution of this area and resulting in deformation distributed over a vast area, ii) the slow deformation rates at mainly blind faults, iii) the spatially sparse instrumental seismicity.

2.3 Karst aquifers

The rocks forming the Southern Alps are mainly carbonates (Figure 3), most of them are karstified, having the capability of naturally storing and transmitting high quantities of water. Rocks with these features are called *aquifers*, which are a very important source of drinking water for the population.

Karts massifs are present also in the area under analysis (see Figure 1), among which the most important ones are the Lessini Mountains, the Asiago Plateau and the Cansiglio Plateau along the Venetian Southern Alps front, and the Classical Karst, extending across the border between SW Slovenia and NE Italy.

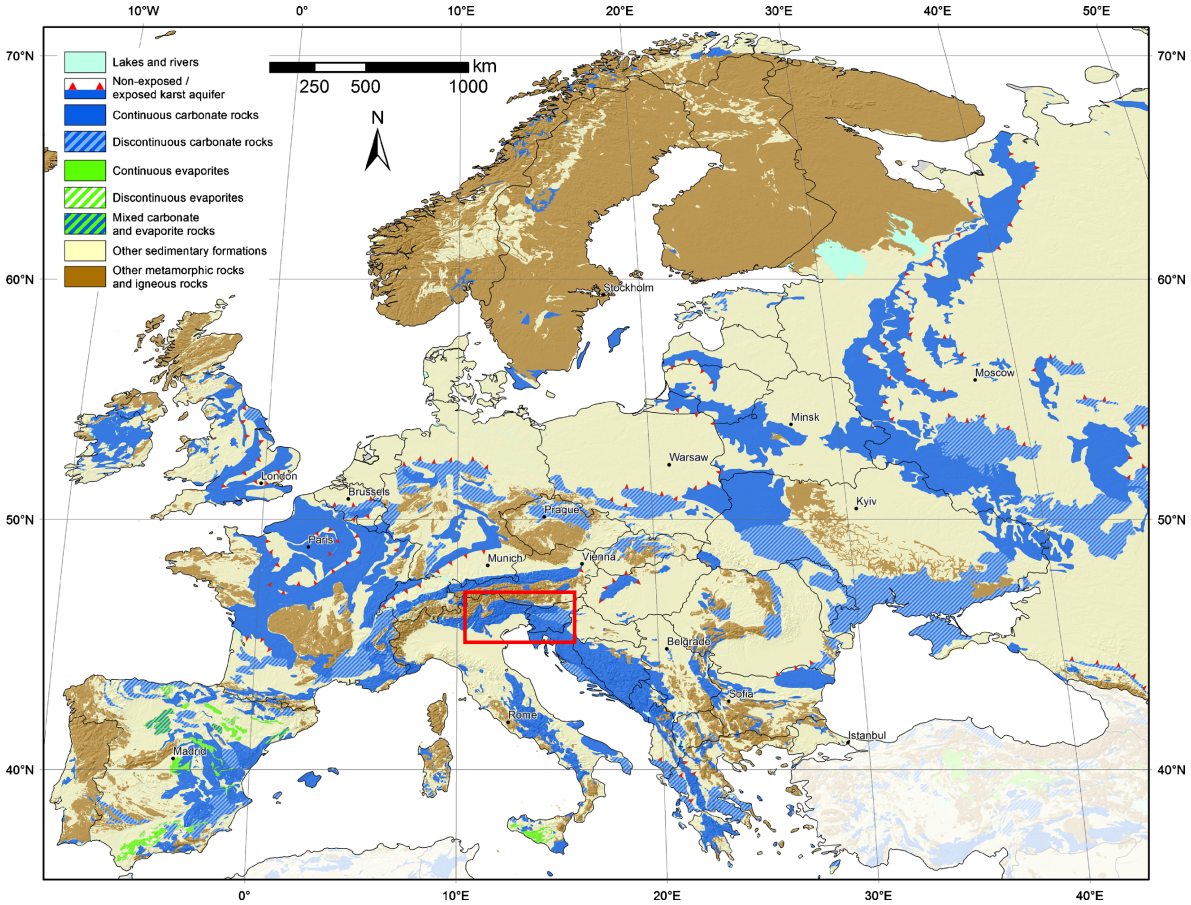

Figure 3: Karst aquifer map of Europe, modified from Chen *et al.*, 2017. The red rectangle represents the study area

.

2.3.1 Typology of aquifers

In general, aquifers can be divided in three categories: *confined*, *unconfined* and *perched*.

Confined aquifers are permeable rocks units which are contained between relatively impervious rocks that overlie and underlie it. Because of the presence of impermeable formation, the water that is present in an aquifer of this type is "isolated" and often under considerable pressure, which is usually originated by high elevation recharge or by the weight of the overlying rock and soil.

Unconfined aquifers holds water that is in direct contact with the atmosphere through the open pore spaces of the overlying soil or rock. In this case it is possible to define the *water table*, which is the top of the groundwater system.

Perched aquifers occur above discontinuous impermeable rock formations, at elevation higher than the regional water table. Compared to aquifers of the other two types, the dimensions of perched aquifers are generally lower and they are also more sensitive to climate conditions. It follows that they are highly variable in time.

One of the most important property characterizing the permeable rocks forming an aquifer is the porosity (η), which defines the quantity of water that can be stored. It is defined as the ratio, reported as percentage, between the volume of the void space of the rock (V_{voids}) where the water can be stored, and the total volume V_{total}:

$$\eta = \frac{V_{voids}}{V_{total}} \times 100 \tag{1}$$

In each rock formation the water can be stored in the voids among grains of the rocks, which formed during the deposition process that drove to rock generation. This is called primary porosity, but it is not the only possible type. When we considered rocks that undergo weathering, caused by physical or chemical processes, or strong tectonic effects, it is likely to observe voids generated by fracturing, folding and faulting processes, which take the name of secondary porosity. Finally, in karst aquifers it is possible to identify the so-called tertiary porosity, which consists in large conduits and caves where the groundwater is free to circulate.

Since in the Alps most of the aquifers originated from karst processes, in the next section we describe the features of karst systems.

2.3.2 Karst systems

Karsts are found in widely scattered sections of the Europe (Figure 3) and world (http://web.env.auckland.ac.nz/our_research/karst) and contain aquifers that are capable of providing large supplies of water, with more than 25% of the world's population either living on or obtaining its water from karst aquifers.

Karst systems are the result of selective dissolution of mineral grains and cements during and after consolidation of carbonate rocks, which formed from calcareous deposits of marine organisms. The dissolution process causes an increase of secondary and tertiary porosity features, which make karst aquifers unique: karst terrains are characterized by barren, rocky ground, caves, sinkholes, underground rivers, and the absence of surface streams and lakes, resulting from the excavating effects of underground water on the soluble rocks.

Conditions that promote karst development are well-jointed limestone near the surface, a moderate to heavy rainfall and good groundwater circulation. In fact, an important way that karst aquifers differ from other aquifers is that a groundwater basin boundary may have little relationship to surface watershed boundaries. Recharge water may originate from the karst area itself or from adjacent nonkarstic areas, with infiltration either occurring through the soil or being concentrated via shallow holes/sinks and fractures.

The properties of karst aquifers greatly vary in space and depend on the orientation of geologic fabric elements. Openings forming karst aquifers may be partly or completely water filled and the water tables can be highly irregular in elevation, because water-carrying conduits can develop at various elevations. Moreover, the water table in karst aquifers can sometimes fluctuate tens or even hundreds of meters even in relatively short periods of time (hours to days).

Karst systems are conceptually divided into three layers: *epikarst*, *infiltration zone*, and *saturated zone* (Mangin, 1975). The epikarst zone (green dashed box in Figure 5), including both soil and weathered rock, has 5-30 m depth. This zone has a high secondary porosity and is expected to be an important water reservoir (Williams, 1983, 2008). The high storage capacity, highly variable void distribution and spatially variable nature of water flow within the epikarst distinguishes it

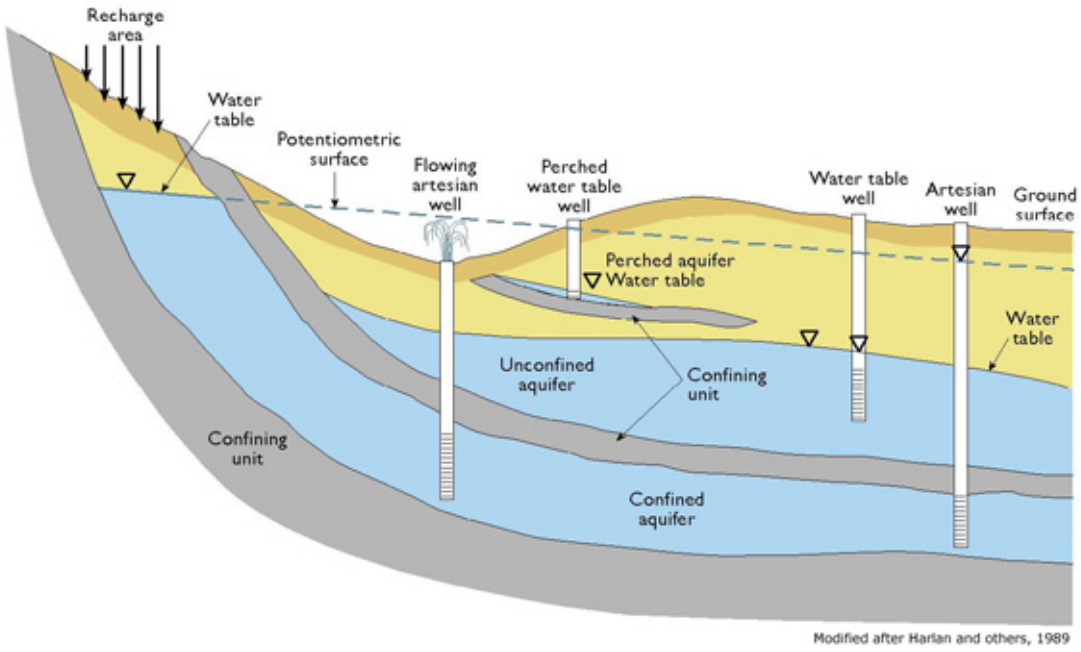

Figure 4: Schematic cross section of aquifer types, from Topper *et al.*, (2003). Water table elevation is indicated with black triangles, which correspond to water level of wells in perched and unconfined aquifers. In confined aquifers the water is often under pressure, then it is possible to define a potentiometric surface (dashed line), which is the hypothetical level to which groundwater would rise if not trapped. Wells in confined aquifers are called artesian and the water level in artesian well correspond to the potentiometric surface (top right black triangle). If an artesian well is drilled where the land surface is below the potentiometric surface, it is called flowing artesian well.

from the rest of the underlying infiltration zone (upper part of the red dashed box in Figure 5), which functions mainly as a transmission zone (Bakalowicz, 1995) with minimal storage. The flow in karst systems can be slow when happening through the rock matrix or in small karst fissures, but also fast and turbolent in swallow holes in the epikarst or in larger fractures and conduits. Generally, the epikarst drains water faster than the underlying transmission zone, then it is possible that the water accumulates at the base of a well developed epikarst area. The reason of this mechanism is that the network of fissures through which percolation water passes is widened by dissolution near the surface, but the extent and frequency of widening diminishes gradually with depth. It follows that permeability also diminishes with depth and a strong contrast in hydraulic conductivity develops between the near surface and the subsurface. Whereas relatively unweathered crystalline limestone typically has a porosity of $< 2\%$, that in the epikarst typically exceeds 20%. Nevertheless, large fractures and conduits are present also in the transmission zone, even if they are rarer than in the epikarst. They become the main drainage routes for the water path to the saturation zone (lower part of the red dashed box in Figure 5), acting as the foci for centripetal flow paths that under-drain the fissured epikarst. The saturated or phreatic zone is formed by large conduits and it is characterized by a mostly horizontal water flow to the outlet. Dyke (1995) showed that natural fracture can be highly conductive, with openings of several mm even at considerable depths. In fact, as pointed out by Gentier (1986) and Sausse (2002), the area of contact between two natural fractures can be less than 40-60% for normal stresses up to 35 MPa, which correspond to a depth of 1500 m. This means that the saturated zone top may reach depths of 1-2 km.

The response of karst systems to rainfall happen at different timescales. During storm (or snowmelt) events the volume of water within the epikarst aquifer rises, causing an increase of the hydraulic head and producing a pressure pulse (pulse-through) that stimulates a transfer of water. This piston effect process is distinct from the transit of individual molecules (flow-through) of water through the system (Bakalowicz, 1995). These effects lead to different pulse-through and flow-through times following a recharge event, the latter being significantly longer. The pressure pulse effect stimulated by rising head can cause percolation drips at stalactites in caves of the

epikarst to respond to rain within an hour or so, whereas the associated flow-through time can be weeks to months.

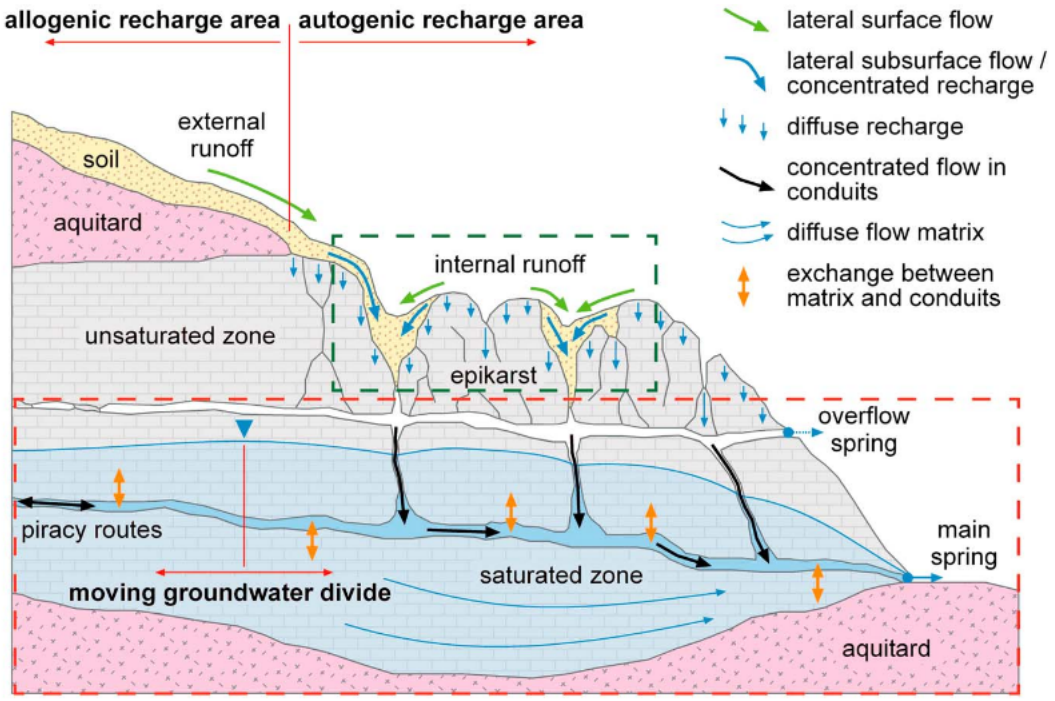

Figure 5: Schematic representation of a karst system, from Hartmann *et al.* 2014.

According to Maillet (1905), the emptying of a reservoir through a porous outlet is described by

$$Q_t = Q_0 e^{-\alpha t} \tag{2}$$

where Q_t is the discharge at time t, Q_0 is the discharge at the start of the recession, and α (in days^{-1}) is a recession coefficient that depends upon the geological and morphological structure of the catchment. This equation has been widely used to describe the discharge hydrographs of karst aquifers to constrain their transportation and storage characteristics. Recession coefficients evaluated for karst springs systems in France and Jordan Valley are in the range of 0.004-0.006 days^{-1} (e.g., Fleury *et al.*, 2007; Forkasiewicz and Paloc, 1967; Milanovic, 1981; Sauter, 1992; Schmidt *et al.*, 2014).

2.4 Hydrological modeling approaches

In order to describe the behavior of a karst system, in particular to determine the variation of stored water inside it, in chapter 5 we will use rainfall-runoff hydrological models. Then, in this section we generally describe what is an hydrological model and why it is very useful for our purposes.

Hydrological models have been developed by hydrologist to describe how rainfall turns into runoff at watershed scale, which is one of the most important problems researchers have to deal with in the study of surface hydrology. These kind of models are called rainfall-runoff models, which are defined as a set of equations that helps in the estimation of runoff as a function of various parameters used for describing watershed characteristics (Gayathri K. Devi *et al.* (2015). The parameters are calibrated by using flow data of the river that drains the basin as output, while the main inputs are precipitation and drainage area. Hydrological models can be divided in three main classes: *physically-based* models, *conceptual* models and *empirical* models.

Physically-based models are mathematically idealized representations of real phenomena, characterized by finite differences equations that precisely describe the flow of water through a medium. Then, precise informations about the watershed features are necessary, like soil moisture content, initial water depth, topography, dimensions of river network etc. The advantage of this kind of

model is that the catchment behavior is very well described in all its part, and what is modeled is as close as possible to reality. Furthermore, the parameters used always have a physical interpretation. Anyway, it is necessary to get a large amount of physical data, which is not always easy to do. In addition, the more precise a physically-based model is, the longer the computation time is. An example of physically-based model is SHE (Abbott *et al.*, 1986).

Conceptual models require a smaller number of physical data than the physically-based, since a precise description of the hydrological cycle is out of the scope of these kind of models. They still model all the components of hydrological processes through interconnected reservoirs, which represents the physical elements in a catchment. Each reservoir is described by submodels representing physical elements of the basin through semi empirical equations and model parameters, which are assessed not only from field data but also through calibration. The submodels represent input flows (rainfall, infiltration and percolation) and the output flows (evaporation, runoff, drainage) that characterize each element of the basin. Finally, all the physical elements are put together to mimic the organization of actual flowpaths. The Stanford model (James, 1972) is an example of this kind of models.

Empirical models are the furthest from physical knowledge, since they are the result of an empirical combination of mathematical operators yielding the observed output once given input data. Modeling the physical processes of a catchment basin is not the goal of this kind of models, then initially they are developed trying to represent the observed output flows in the simplest way, including complexities only when they are really necessary to improve the modeling. The great advantage of this class of models is that it is not necessary to know any intrinsic feature of the basin described, the only data needed are the inputs (usually precipitation and potential evapotranspiration) and output (river flow that drains the basin). Their limitation is that it is not possible to give precise physical interpretation to the parameters that characterized the model except for the variation of the water stored in the basin. An example of empirical model is GR3J (Edijatno *et al.*, 1999).

It is worth noting that each class of hydrological model allows to compute the variations of the water stored in a basin, which is what we are really interested in.

In order to describe the behavior of the basin we considered three different models: the GR4J, GR5J and TOPMO.

2.4.1 GR4J and GR5J

The GR4J and GR5J rainfall-runoff models belong to the class of empirical models. They are *lumped-parameters* models: the spatial variability of a basin is not taken into account, then they are considered as a whole. Lumped-parameters models are characterized by internal flows to different stores where the water remains for a certain time, defined by equations and model parameters, and then it flows to other stores or to the final outlet. The equations that describe the internal flows do not change with time.

GR4J and GR5J are characterized by the same parameters and equations, except for the modeling of the water exchange with the environment outside the basin. These exchanges are modeled by just one parameter in GR4J and by two parameters in GR5J, then the total number of parameters that characterize the two models are 4 for GR4J and 5 for GR5J. GR4J is schematized in Figure 6.

GR4J and GR5J are characterized by two stores: the *Production store*, which collects a part of the water after a precipitation event, and the *Routing store*, which holds a portion of the internal water and transmit it to the outlet. These two stores are very important for the computation of the water storage variation, since it is represented by the time evolution of the sum of the water level in the two stores.

The inputs of the models are the catchment precipitation P and the potential evapotranspiration E. All water quantities (input, output, internal variables) are expressed in mm, by dividing water volumes by catchment area, when necessary.

In the following paragraphs we describe how these models describe the water fluxes from precipitation to river flow.

Determination of net precipitation and evapotranspiration The first operation made by the models is the subtraction of E from P to determine either a net rainfall P_n or a net evapotranspiration capacity E_n. P_n and E_n are computed with the following equations:

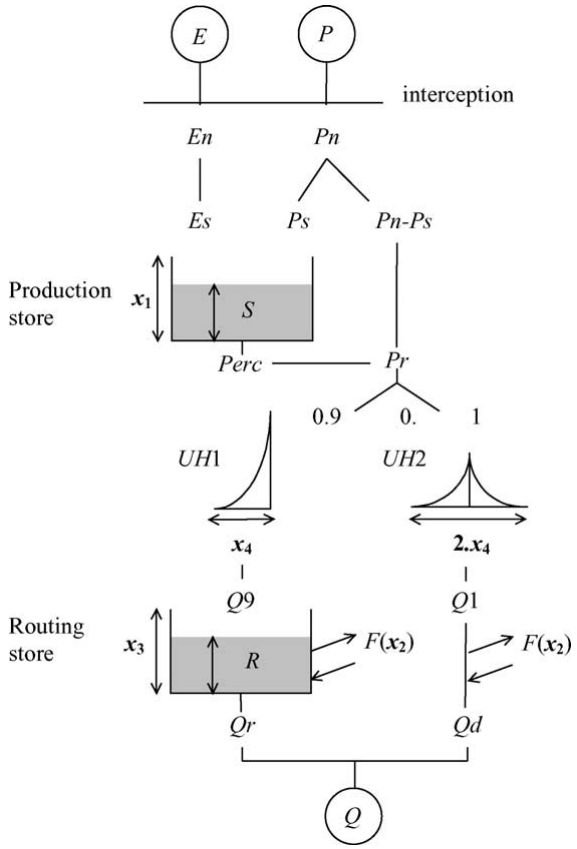

Figure 6: Diagram of the GR4J rainfall-runoff model, from Perrin *et al.* (2003).

$$\text{If } P > E; \text{ then } P_n = P - E \text{ and } E_n = 0; \tag{3}$$

$$\text{Otherwise } P_n = 0 \text{ and } E_n = E - P; \tag{4}$$

Production store In case P_n is not zero, a part P_s of P_n fills the Production store. It is determined as a function of the level S by:

$$\frac{dS}{dt} = \frac{x_1 \left(1 - \left(\frac{S}{x_1}\right)^2\right) \tanh\left(\frac{P_n}{x_1}\right)}{1 + \frac{S}{x_1} \tanh\left(\frac{P_n}{x_1}\right)} \tag{5}$$

where x_1 (mm) is the maximum capacity of the Production store. In the case when E_n is not zero, an actual evaporation rate is determined as a function of the level in the Production store to calculate the quantity E_s of water that will evaporate from the store. It is obtained by:

$$E_s = \frac{S \left(2 - \frac{S}{x_1}\right) \tanh\left(\frac{E_n}{x_1}\right)}{1 + \left(1 - \frac{S}{x_1}\right) \tanh\left(\frac{E_n}{x_1}\right)} \tag{6}$$

The water content in the Production store is then updated with:

$$S = S - E_s + P_s \tag{7}$$

Note that S can never exceed the maximum capacity of the Production store, as demonstrated in section 5.4.3. A percolation leakage $Perc$ from the production store is then calculated as a power function of the reservoir content:

$$Perc = S \left\{ 1 - \left[1 + \left(\frac{4}{9} \frac{S}{x_1} \right)^4 \right]^{-1/4} \right\} \tag{8}$$

$Perc$ is always lower than S. The reservoir content becomes:

$$S = S - Perc \tag{9}$$

Linear routing with unit hydrographs The total quantity P_r of water that reaches the routing functions is given by:

$$P_r = Perc + (P_n - P_s) \tag{10}$$

P_r is divided into two flow components according to a fixed split: 90% of P_r is routed by a unit hydrograph UH1 and then a non-linear routing store, and the remaining 10% of P_r are routed by a single unit hydrograph UH2. Both unit hydrographs depend on the same time parameter x_4 expressed in days. However, UH1 has a time base of x_4 days whereas UH2 has a time base of $2x_4$ days. x_4 can take real values and is greater than 0.5 days. The ordinates of both unit hydrographs are derived from the corresponding S-curves (cumulative proportion of the input with time) denoted by SH1 and SH2, respectively.

SH1 is defined along time t by:

$$\text{For } t \leq 0,\ SH1(t) = 0 \tag{11}$$

$$\text{For } 0 < t < x_4,\ SH1(t) = \left(\frac{t}{x_4} \right)^{5/2} \tag{12}$$

$$\text{For } t \geq x_4,\ SH1(t) = 1 \tag{13}$$

SH2 is similarly defined by:

$$\text{For } t \leq 0,\ SH2(t) = 0 \tag{14}$$

$$\text{For } x_4 < t < 2x_4,\ SH2(t) = \frac{1}{2} \left(\frac{t}{x_4} \right)^{5/2} \tag{15}$$

$$\text{For } x_4 < t < 2x_4,\ SH2(t) = 1 - \frac{1}{2} \left(2 - \frac{t}{x_4} \right)^{5/2} \tag{16}$$

$$\text{For } t \geq 2x_4,\ SH2(t) = 1 \tag{17}$$

Catchment water exchange In GR4J, a groundwater exchange term F that acts on both flow components, is calculated as:

$$F = x_2 \left(\frac{R}{x_3} \right)^{7/2} \tag{18}$$

where R is the level in the Routing store, x_3 its "reference" capacity and x_2 the water exchange coefficient. x_2 can be either positive in case of water imports, negative for water exports or zero when there is no water exchange. The higher the level in the Routing store, the larger the exchange. In absolute value, F cannot be greater than x_2: x_2 represents the maximum quantity of water that can be added (or released) to (from) each model flow component when the Routing store level equals x_3.

In the case of the seven-parameter GR5J the groundwater exchange term is calculated as:

$$F = x_2 \left(\frac{R}{x_3} - x_5 \right) \tag{19}$$

This is the only difference between the GR4J and the GR5J models.

Non-linear Routing store The level in the Routing store is updated by adding the output Q9 of UH1 and F as follows:

$$R = max(0; R + Q9 + F) \tag{20}$$

The outflow Q_r of the reservoir is then calculated as:

$$Q_r = R \left\{ 1 - \left[1 + \left(\frac{R}{x_3} \right)^4 \right]^{-1/4} \right\} \tag{21}$$

Q_r is always lower than R. The level in the reservoir becomes:

$$R = R - Q_r \tag{22}$$

Once R and S are computed, it is possible to calculate the total water storage as the sum R+S; then water storage variations are represented by the time evolution of R+S.

Total streamflow Like the content of the Routing store, the output Q_1 of UH2 is subject to the same water exchange F to give the flow component Q_d as follows:

$$Q_d = max(0; Q_1 + F) \tag{23}$$

Total streamflow Q is finally obtained by:

$$Q = Q_r + Q_d \tag{24}$$

Snow inclusion When we take into account the snow and ice, P_n must be recomputed. We follow the method described in the HBV (Hydrologiska Byrns Vattenbalansavdelning) model (*Lindstrom et al.*, 1997). It states that in any given day where precipitation occurs, if the temperature is below a specified threshold x_6, all rainfall is considered to fall as snow that does not directly infliltrates in the soil; while if the temperature is above the threshold, all precipitation is assumed to be rain.

Melt is assumed to occur when the daily temperature T is higher than the specified melt temperature threshold x_7; if T is smaller than x_7, no melt occurs. It is then defined as following:

$$\text{Melt} = \begin{cases} x_8 \left(T - x_7 \right), \ T > x_7 \\ 0, \ T \leq x_7 \end{cases} \tag{25}$$

x_8 is called *melting factor*.

What we called *net rainfall* P_n is now P_{SNOWn}. This quantity takes into account the fact that when the weather is too cold the water remains above the Earth surface ($P_{SNOWn} = 0$); while as the temperature increases, snow melting is taken into account, so it may happen that $P_{SNOWn} > 0$ even if there is no precipitation.

The inclusion of the snow needs three more parameters: x_6, x_7, x_8. Then, the total number of parameters of the two models becomes 7 for GR4J and 8 for GR5J.

2.4.2 TOPMO

The TOPMO is a lumped daily eight-parameter topography-based conceptual model developed by Beven and Kirkby (1979).

The inputs of this model are the total precipitation P and the potential evapotranspiration PE, as for the GR4J. It is characterized by eight parameters and three different compartments (stores), called *Interception store*, *Soil Moisture Accounting store (SMA)* and *Routing store*.

The interception store has a capacity $X3$ and a water content T. When a precipitation event occurs, the water content become:

$$T = T + P \tag{26}$$

Once calculated T, the evapotranspiration Et from the interception store can be computed as

$$Et = min(T, PE) \tag{27}$$

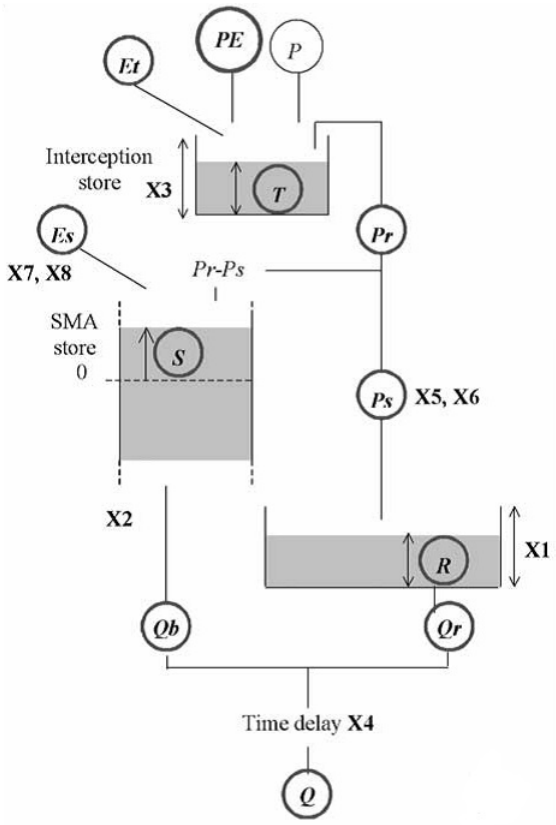

Figure 7: Diagram of the TOPMO model, from Oudin *et al.* (2004).

The water content is then updated with:

$$T = T - Et \tag{28}$$

The output of the Interception store is the effective rainfall after interception Pr, defined as:

$$Pr = max(0; T - X3) \tag{29}$$

A portion Ps of Pr fills the Routing reservoir. This quantity can be computed as follows:

$$Ps = \frac{Pr}{1 + e^{\left(X5 - \frac{T}{X6}\right)}} \tag{30}$$

Where $X5$ and $X6$ are two parameters defining the distribution curve of the topographic index. Considering this inflow, the water level R of the Routing reservoir is:

$$R = R + Ps \tag{31}$$

The outflow from the Routing reservoir is given by:

$$Q_r = \frac{R^2}{R + X1} \tag{32}$$

Where $X1$ is the capacity of the Routing reservoir. The water level in the Routing reservoir then become

$$R = R - Q_r \tag{33}$$

The amount of water $Ps - Pr$ that does not go into the Routing reservoir, reaches the *Soil Moisture Accounting* (SMA) store. The water content S of the SMA store is then:

$$S = S + Ps - Pr \tag{34}$$

It is possible to calculate the evaporation from the SMA reservoir Es by using the following formula:

$$Es = \frac{PE - Et}{1 + e^{\left(X7 - \frac{T}{X8}\right)}} \tag{35}$$

Where $X7$ and $X8$ are the actual evaporation computation coefficients. The percolation flow from this reservoir is:

$$Q_b = X2 \; e^{\frac{S}{X2}} \tag{36}$$

Where $X2$ is outflow parameter of the moisture accounting store. The water level of the SMA then becomes:

$$S = S - Q_b \tag{37}$$

Finally, the total streamflow that exit from the basin described by the model is:

$$Q = Q_r - Q_b \tag{38}$$

The lag between the precipitation and Q is expressed by the parameter $X4$.

3 Data and technique

In this chapter we describe the functioning of the GPS technique (section 3.1), how GPS time series we use are obtained and which are their features (section 3.2). Finally, in section 3.3 we present the blind source separation algorithm used to identify the different signals contained in GPS data.

3.1 GPS technique

3.1.1 Introduction

The Global Positioning System (GPS) is a satellite-based navigation system that provides precise 3-D position and time information anywhere on Earth in all meteorologic conditions. The GPS project started in 1973 for military application, but its data are available also for civilian users; in particular its contribution for the solution of geodetic problems has been included since 1980s.

This system is composed by about 30 satellites, placed in orbits of approximately 20.2×10^3 km altitude above Earth's surface, which continuously transmit a radio signal in the microwave frequency.

The GPS is based on the principle of trilateration, which consists in determining the position of a point P once computed the ranges between it and at least three other points of known coordinates. In the GPS case, the points of known coordinates are the satellites, while P is the GPS receiver. In theory, it is then necessary to know the ranges of at least 3 satellites from the receiver simultaneously to establish its position. In practice, the ranges are computed by comparing the transmission time of the satellite with the clock on the receiver. The difference Δt between the two clocks is the time the signal takes to travel from the satellite to the receiver, then the satellite-receiver range is Δt multiplied by the signal travel velocity, i.e. the speed of light. Anyway, the receiver and satellite clocks have not the same quality (the satellite clocks are much more precise), then they are not perfectly synchronized and what it is measured is a biased range, called *pseudorange*. The bias at any given time is the same for each satellite, it follows that the parameters that must be defined to retrieve the position of a receiver are 4: longitude, latitude, altitude, time bias. As a consequence, it is necessary to compute at least 4 pseudoranges at the same time instead of 3 as required by a standard trilateration. For this reason the orbits of the satellites has been defined so that at least 4 satellites are simultaneously visible above the horizon anytime and anywhere on Earth.

3.1.2 GPS composition

The GPS is composed by 3 main segments: the *Space Segment*, the *Control Segment* and the *User and Ground Segment*.

Space Segment This segment is composed by the satellite constellation. Each satellite transmits data by using two ultra-high frequency carrier signals: L_1 (1.575 GHz) and L_2 (1.228 GHz). The data transmitted can be divided into:

- navigation signals (*codes*);
- navigation and system data (*message*).

The *codes* transmitted are the precise P-code and the less precise C/A code (Clear Access), which consist in a sequence of +1 or -1 that modify the carriers. In particular, the P-code has a frequency of 10.23 MHz and its sequence is very long: it only repeats after 266 days. This code is divided among the different satellites in seven days long portions, so that, even if they transmit on the same frequency, each satellite can be identified by its one-week segment. While the P-code is placed on both L_1 and L_2, the C/A code is present in L_1 only, it has a length of only one millisecond and its frequency is 1.023 MHz.

The *message* contains information that can be read by the user's receiver. It includes all the necessary parameters for the computation of the satellite coordinates as Cartesian coordinates in a geocentric system and for the ionospheric corrections. Furthermore, it transmits orbit parameters (*ephemeris*), information on satellite health status and clock. It is modulated on both L_1 and L_2 frequencies and transmits with a rate of 50 bits per second, repeating every 30 seconds.

Control Segment The Control Segment continuously monitors and control the Space Segment and updates periodically the navigation message for each particular satellite. It determines the GPS system time, predicting also the satellite ephemerides. It is composed by the Master Control Station (MCS), located near Colorado Springs (USA), six monitor stations located around the world and four ground antennas for uploading data into the satellites.

User and Ground Segment It is composed by all GPS receivers and data-processing softwares. In a receiver, the signal is initially identified by an antenna, which detects the electromagnetic waves arriving from the satellite. The frequency of the waves is then down-converted in the Radio Frequency (RF) section from the original microwave to a lower radio frequency. Finally, the signal is analyzed by a microprocessor, which controls the receiver operation like the acquiring of signals, the signal processing and the decoding of the broadcast message.

3.1.3 Observation Principle

Recalling the concepts introduced in the previous section, it is possible to give more details on how a pseudorange PR is computed and which are the error sources that cause a decrease of the GPS measurements quality. The travel time of the signal is computed by comparing the phase shift between the carrier signal sent by the satellite and the copy of it produced by the receiver. Then, the distance PR between satellite and receiver can be computed as:

$$PR = (\Delta\Phi + N)\,\frac{c}{f} + cdt_s + cdt_u + cdt_a + \epsilon_R; \tag{39}$$

where $\Delta\Phi$ is the phase shift, N the number of cycles made by the carrier signal (*ambiguity term*), c the speed of light and f the frequency of the carrier signal. The additional terms are the sources of error of the pseudorange measure.

The accuracy of this measurement is about 3×10^{-3} of a cycle, that when multiplied with the speed of light results to be about 0.5 mm. Anyway, in order to achieve such a precision, it is necessary to well estimate the last four terms of equation 39. In particular, cdt_s is the satellite clock error, cdt_u the clock synchronization error, cdt_a the atmospheric propagation delay, that can be distinguished in its ionospheric cdt_{ion} and tropospheric cdt_{trop} parts, and finally ϵ_R is the observation noise.

In order to eliminate or reduce the errors that are present in the original observations, it is useful to consider different pseudorange measurements at the same time and a linear combination of them. For example, single differences can be formed between two receivers, two satellites, or between two epochs.

The satellite clock error dt_s is eliminated through the computation of differences between two receivers, which consist in making pseudoranges measurements at one station and subtract them from simultaneous pseudoranges measurements of the same satellite at a second station.

The receiver clock term dt_u can be canceled differencing observations of two satellites that are transmitting data to the same receiver simultaneously. This is why 4 satellites are necessary for the trilateraion instead of 3: the additional one is necessary to determine the clock synchronization error. dt_a depends on the conditions of the atmosphere at a certain time, and can not be removed by using linear combination of the measurements. The ionospheric delay can be estimated starting from the computation the phase differences between L_1 and L_2. In fact, the electrons density of the ionosphere affects the velocity of the signals differently, depending on the frequency of the signal. Then, it is possible to retrieve the original travel velocity of two signals, with known frequency, from the phase difference results.

The tropospheric delay is caused by the fact that the troposphere is a refractive medium, and the velocity of a signal through it is influenced by two main factors: air pressure and water vapor content. As a consequence, it is necessary to estimate both quantities in order to quantify dt_{trop}. It worth noting that air pressure slowly varies with time, while the dynamic of the water vapor content is much faster and a bad estimation of it can cause large positioning errors.

The observation noise ϵ_R gathers different error sources that, unlike dt_{trop}, can not be quantified. For example, they are distortions of the signals caused by electrical interferences, GPS receiver malfunctioning and multipath effects, which happen when the signal from the satellite reach the receiver after a bounce off a reflective surface so that the antenna detects a double signal at different epochs.

It is also important to point out that the receiver can discern only the phase of the carrier signals, but not the number N of cycles it made. It follows that the ambiguity term can not be directly defined, so it is estimated by combining all the available phase and code observations to get a set of equations from which a least-square algorithm can be applied to estimate both the distance and the ambiguity value.

There are softwares with tools that helps in maximizing GPS data precision and reducing the GPS sources of noise. They include algorithms for the computation of N, and models of the solid Earth, atmosphere, and satellite dynamics.

3.2 Measurements and Networks

3.2.1 Stations and Networks

In the area we analyzed there are hundreds of GPS permanent stations, which are managed by different scientific and commercial institutions. A permanent station, often called cGPS station, is characterized by a receiver in a monumented point (as in Figure 8) which continuously acquires data, with variable sample rates. The most used antenna for permanent stations is the *choke-ring* type (Figure 9), which consists of strips of conductor concentric with the vertical axis of the antenna and connected to a ground plane, fulfilling the requirement of the circular polarization. In fact, the GPS signal is weak and needs very sensitive antennas, which also has to allow signal reception from all elevations and azimuths of the visible hemisphere.

Figure 8: Station MGRD, belonging to the Rete Integrata Nazionale GPS (RING) network, monumented with a tripod on a rock outcrop. Others monumentation types are used for permanent stations, i.e. concrete or metallic pillar and steel mast. It is also very common to find GPS stations directly installed on buildings.

Taking into account only the sites that lie inside the area under analysis, we observed that the GPS stations belong to 13 different networks, each one managed by a different institution (Table

Figure 9: Example of a choke-type GPS antenna (from Mekik *et al.*, 2010).

1). A GPS network includes stations having similar receivers quality and precision, constantly connected to a web infrastructure which allow the data management in real time.

These networks are very heterogeneous, both in terms of number of stations managed and instruments used for the monitoring. The widest network we (partially) used for our analysis is EUREF, covering the entire Europe; while STPOS and TPOS are very local and dense networks, each one managing only about 10 stations.

It is worth noting that some GPS stations are not specifically devoted to geophysical monitoring, since they are installed for other purposes, like the cadastrial and topographic ones, and may potentially be of lower quality in terms of monumentation and data flow. Nonetheless, their integration has a large potential to improve the resolution of the kinematic patterns of the area.

3.2.2 Position time series

In geophysics, GPS measurements are used to retrieve direct and precise estimations of the deformation velocity of a geographic area with respect to certain regions on the Earth, called *reference frames*. Anyway, to be able to monitor deformation continuously, or in near real-time, continuous GPS observations are needed. In this thesis we analyzed the day-by-day evolution of the GPS stations positions, which we call GPS time series.

The GPS technique is able to detect movements having different causes (Figure 10). The most evident feature of a GPS time series is the presence of a linear trend, resulting from the tectonic movement (Figure 10 and 11). This linear trend can be largely affected by sudden events like earthquakes or volcanic activities. Since they directly impact on ground displacements, they can be clearly recognized when looking at GPS data. In particular, when considering earthquakes, the GPS stations near the epicenter are characterized by an offset in the time series. Following a seismic event a transient postseismic signal can be also present, even if with a smaller final amplitude than the coseismic offset (Figure 10).

Another interesting features of GPS data is the presence of periodic (often called *seasonal*) variations, mainly with annual period, that are present in global and regional time series for sites on all continents. The causes of these signals can be different and grouped into three categories, as discussed by Dong *et al.* (2002). The first category include the displacements caused by gravitational excitation, mostly from the Sun and Moon. The effect of this force are loading-induced displacements due to tides originated by solid Earth, ocean, atmosphere and pole motion. The second category of seasonal variations is of thermal origin coupled with hydrodynamics. Temperature can directly affect GPS measurements if it produces thermal expansion of the bedrock beneath the GPS benchmark. Other seasonal deformations associated with this category are caused by variations of atmospheric pressure, nontidal sea surface and groundwater (both liquid and solid). The third category takes into account various errors, which also may generate apparent seasonal variations. The seasonal errors from satellite orbital models, atmospheric models, water vapor distribution models, phase center variation models, thermal noise of the antenna, local multipath,

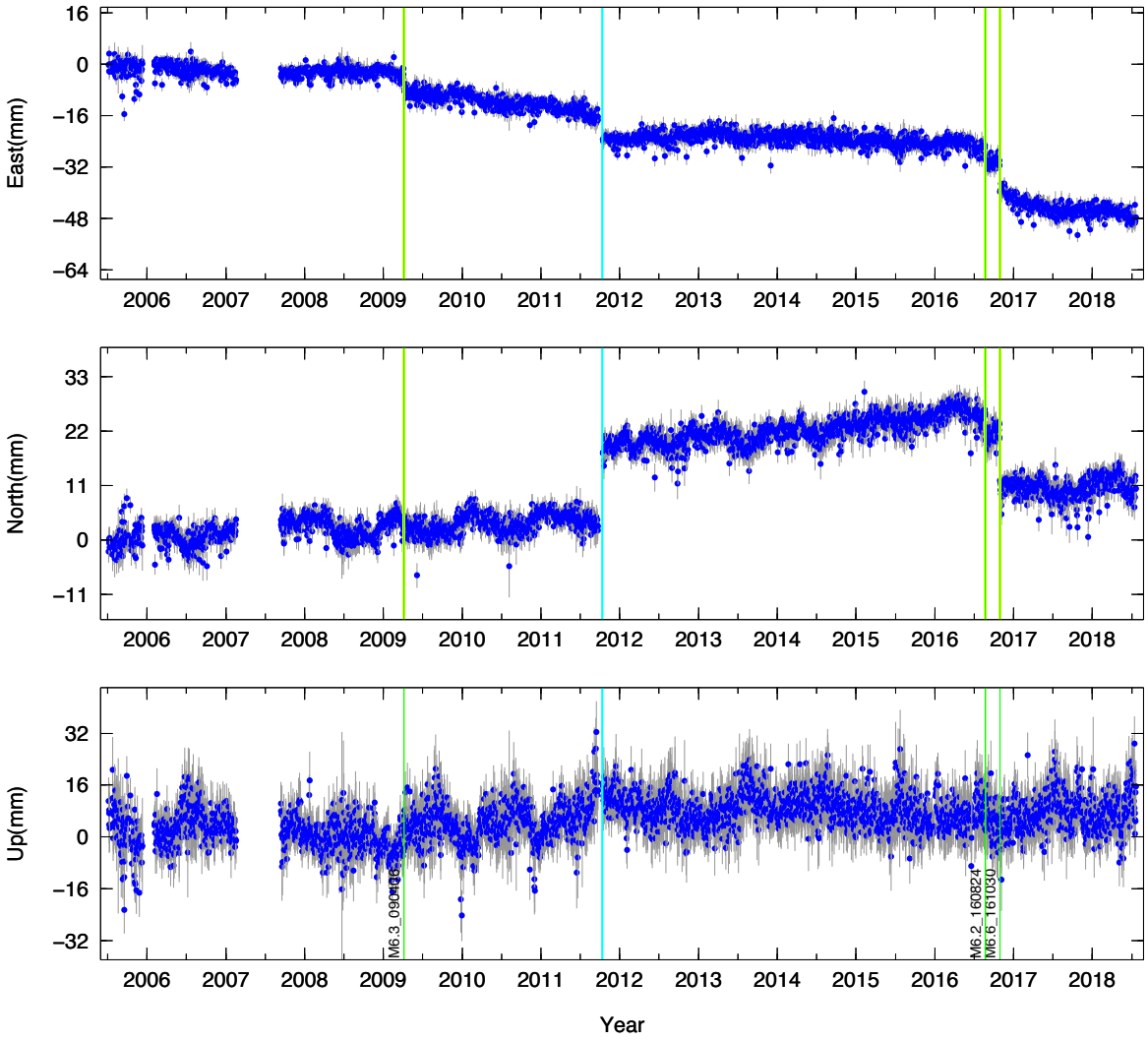

Figure 10: The blue dots represent the temporal evolution of the GPS station RIET (central Italy) in the Eurasia-fixed reference frame, which was affected by both Mw 6.3 L'Aquila earthquake (2009) and the two earthquakes in Central Italy during summer 2016 (Mw 6.2 and 6.6). The earthquake events are highlighted by green bars. Coseismic offset caused by the seismic events are evident especially in the north and east component. We can also observe a post-seismic signal in the east component, following the second earthquake of 2016. The cyan line represent a change in the GPS station equipment, this cause an offset that during the data processing has to be removed. Finally, a linear trend is evident mainly in the north component during the period 2012-2016.

Network	Location	Official-Owner	Provider
ItalPOS	Italy	Leica Geosystems	http://it.web.nrtk.eu/SpiderWeb/frmIndex.aspx
GeoDAF	Italy	ASI/CGS	http://geodaf.mt.asi.it/
EUREF	Europe	EUREF Consortium	http://www.epncb.oma.be/
RING	Italy	INGV	http://ring.gm.ingv.it/
SPIN GNSS	Northern-Italy	Regione Piemonte/Lombardia	https://www.spingnss.it/spiderweb/frmIndex.aspx
OLGGPS	Austria	Austrian Academy of Sciences, Space Research Institute	http://www.bev.gv.at
FVG	Northern-Italy	Regione Friuli-Venezia-Giulia	http://gnss.regione.fvg.it/dati-GPS
NETGEO	Italy	Topcon Positioning Italy	http://www.netgeo.it
EPOSA	Austria	EPOSA	http://www.eposa.at/
ASSOGEO	Italy	Assogeo S.p.a.	http://www.assogeo.it/
STPOS	Northern-Italy	Provincia autonoma di Bolzano	http://www.stpos.it/Spiderweb/
TPOS	Northern-Italy	Provincia autonoma di Trento	http://www.catasto.provincia.tn.it/TPOS
SIGNAL	Slovenia	Republic of Slovenia	http://www.gu-signal.si/onas
VENETO	Northern-Italy	Regione Veneto	http://http://retegnssveneto.cisas.unipd.it/

Table 1: List of the networks used for the acquisition of GPS time series.

and snow cover on the antenna all cause apparent variations in estimated site positions.

3.2.3 Data processing

The daily position time series of all cGPS networks operating in the study region were obtained following the three-step procedure described in Serpelloni *et al.* (2006, 2013) that includes: 1) acquisition of raw data, 2) combination of loosely constrained network solutions and reference frame definition and 3) time-series analysis, including velocity estimates and spatial filtering of common mode errors. Each step will be described in the following.

The raw GPS observables have been analyzed using the 10.6 version of the GAMIT/GLOBK package (Herring *et al.*, 2015) adopting standards defined in the framework of the IGS *Repro2 campaign* (http://acc.igs.org/reprocess2.html). The GAMIT software is used to estimate station positions, atmospheric delays, satellite orbits, and the Earth orientation parameters from ionosphere-free linear combination GPS phase observables using double differencing techniques to eliminate phase biases caused by drifts in the satellite and receiver clock oscillators. GPS pseudo-range observables are used to constrain clock timing offsets and to improve automated editing of the phase data, assisting in the resolution of integer phase ambiguities. GPS phase data are weighted according to an elevation-angle-dependent error model (Herring *et al.*, 2015) using an iterative analysis procedure whereby the elevation dependence is determined from the observed scatter of phase residuals.

In this analysis the satellites orbit parameters are fixed to the IGS final products. We use the IGS absolute antenna phase center model for both satellite and ground-based antennas, which improves the accuracy of estimates for the vertical components of site position by mitigating reference frame scale and atmospheric mapping function errors (e.g., Schmid *et al.*, 2005, 2007). While the first-order ionospheric delay is eliminated by the ionosphere-free linear combination, the second-order ionospheric corrections are applied based on the formulation of Petrie *et al.* (2010), using IONEX files from the Center for Orbit Determination in Europe (CODE). The tropospheric delay is modeled as piecewise linear model and estimated using the Vienna Mapping Function 1 (VMF1; Boehm *et al.*, 2006) with a 10° cutoff. We use the Global Pressure and Temperature 2 (GPT2; Lagler *et al.*, 2013) model to provide a priori hydrostatic delays. The pole tide was also corrected in GAMIT by IERS standards. The Earth Orientation Parameters (EOP) are tightly constrained to priori values obtained from IERS Bulletin B. Non-tidal atmospheric loading and

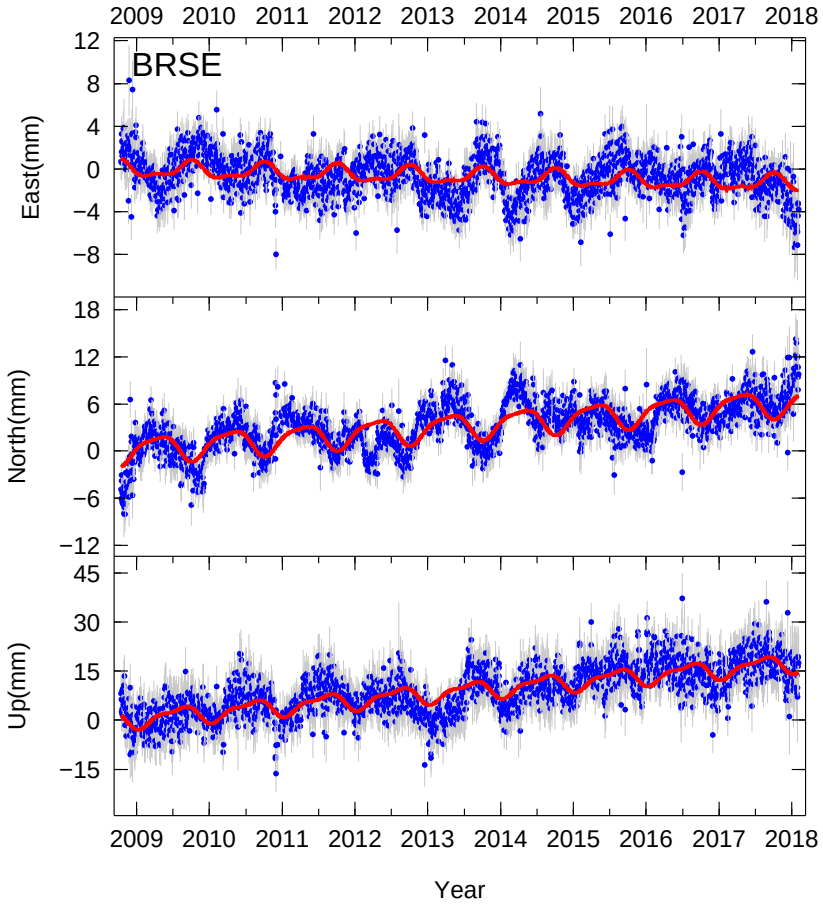

Figure 11: *Blue dots*: time evolution of the position of the GPS station BRSE in the Eurasia-fixed reference frame. Trend and annual signal are evident in all the components of the displacements. *Red line*: attempt to model the displacements with a linear plus annual plus semi-annual signal.

ocean tidal loading are corrected using MIT filtered atmospheric displacements files (available at ftp://everest.mit.edu/pub/GRIDS) and the FES2004 (Lyard *et al.*, 2006) model, respectively. The International Earth Rotation Service (IERS) 2003 model for diurnal and semi-diurnal solid Earth tides was set.

In the second step we use the ST_FILTER program of the QOCA software (http://qoca.jpl.nasa.gov), which adopts a Kalman filter estimation algorithm (Dong *et al.*, 1998, 2002), to combine all the daily loosely constrained solutions with the global solution of the IGS network made available by MIT (http://sopac.ucsd.edu), and simultaneously realize a global reference frame by applying generalized constraints (Dong *et al.*, 1998). Specifically, we define the reference frame by minimizing the velocities of the IGS core stations (http://igscb.jpl.nasa.gov), while estimating a seven-parameter transformation with respect to the GPS realization of the ITRF2008 frame (Altamimi *et al.*, 2011), i.e., the IGb08 reference frame.

In the third step we analyze the position time series in order to estimate and correct offsets due to stations equipment changes, while simultaneously estimating annual and semi-annual periodic signals and a linear velocity term. In this analysis we retain only data from GPS stations with an observation period longer than 2.5 years, as shorter intervals may result in biased estimates of linear velocities (Blewitt and Lavallee, 2002). The model derived from the combination of these signals is then subtracted from the position time series in order to get the residual positions.

Residual time series contain various systematic errors and random errors, as well as unmodeled signals. In regional network analysis, the so-called common mode error (CME) is one of the major spatially correlated error sources in GPS solutions, which is mitigated through a technique commonly referred to as regional filtering. This was first introduced by Wdowinski *et al.* (1997) by removing a common mode bias from each coordinate components computed by stacking the position residuals of the stations and estimating and removing the mean value. This approach assumes that the CME is spatially uniform. Dong *et al.* (2006) adopted a PCA technique (section 3.3, in particular 3.3.1 for details), which decomposes the network time series into a set of temporally varying modes, each of which consists of a common temporal function and related different spatial response, providing a mathematical framework to perform spatiotemporal filtering, removing the assumption of spatially uniform distribution, and letting data themselves reveal the spatial distribution of CME (Serpelloni *et al.* (2013)). The PCA is performed at a continental-scale, over the same area used by Serpelloni *et al.* (2013), and the first two PCs are here considered as CME. This prevents the removal of the eventual more localized signals of geophysical interests recorded by the GPS stations in the study region, since the PCA detects the signals common to a much larger region. As a result, after removing the CME, the typical repeatability in our analysis is $\sim$1 mm for the horizontal components, and $\sim$3 mm for the vertical component, with a 30% gain in the daily repeatability and a significant improvement of the signal to noise ratio. After the spatial filtering, the estimated seasonal motions are added back to the filtered time-series, obtaining position time series with a reduced scatter around the adopted model.

3.3 Independent Component Analysis (ICA) technique

The use of GPS stations to monitor and measure Earth surface movements has given the opportunity to the scientific community to collect high precision data with a good spatial and temporal resolution. This large amount of data poses the following challenges: 1) How can we extract the relevant information out of the whole volume of data at our disposal? 2) Once the relevant information is extracted, is there a way to assign a physical meaning to it?

To answer the first question, we will introduce the principles behind the Principal Component Analysis (PCA), which has the goal to reduce the number of features in a given dataset, focusing only on those explaining most of the variance associated with the observations. This technique is usually not enough to answer the second question gaining physical insights about the various competing sources at play though. In the specific case here under study, what a group of GPS stations measures is not caused by a single physical process, but it is the result of different sources of deformation acting at the same time. Examples of deformation sources are both tectonic (inter-, co-, and post-seismic activity, Slow Slip Events) and non-tectonic (hydrological load, thermal strain, anthropic activity). To identify and separate the different deformation processes, the Independent Component Analysis (ICA) is a more suitable technique than the PCA. The second order statistic (variance) of the data considered by PCA is applicable to data with a Gaussian distribution. GPS time series contain geophysical signals that commonly have non-gaussian distribution (Ming *et al.*,

2017), then in this case the variance may not be the quantity of interest.

ICA is a blind source separation method that can separate statistically independent signals from mixed signals, using their higher order statistical characteristics. Moreover, ICA can be seen as an extension of PCA (Comon, 1994), which will be discussed in the next sub-section. There are several ways to implement statistical independence of the sources (e.g., Hyvarinen and Oja, 1997; Cardoso, 1999). In the remaining part of this section, we will introduce the variational Bayesian ICA (vbICA), the application of which to real data is shown in subsequent chapters.

3.3.1 Theoretical basis (the PCA)

Let us consider M sensors collecting data for a number T of epochs. The data can be collected in $\mathbf{X}$: a M x T matrix, where the i-th row represents the measurements of the i-th sensor. Each row (i.e., each time series) can be seen as the sample realization of a random variable x_i. Following a matrix notation, we can write $\mathbf{X}$ as a collection of M random variables (rvs):

$$\mathbf{X} = \begin{pmatrix} \mathbf{x_1} \\ \vdots \\ \mathbf{x_M} \end{pmatrix}$$

It is possible that most of these random variables are redundant. In other words, we are looking for a new set of random variables such that most of the variance of X is explained by them. We thus compute the covariance matrix $\mathbf{C_x}$, which has dimensions M x M. A generic element C^{ij} of $\mathbf{C_x}$ is defined as:

$$C^{ij} = \frac{1}{T} \sum_{t=1}^{T} (x_{it} - \mu_i)(x_{jt} - \mu_j) \tag{40}$$

where x_{it} represent the measurement of the i-th sensor at the epoch t, while μ_i is the expected value for the i-th row. In matrix notation:

$$\mathbf{C_x} = \frac{1}{T} (\mathbf{X} - \boldsymbol{\mu})(\mathbf{X} - \boldsymbol{\mu})^T \tag{41}$$

The covariance matrix is square, positive-semidefinite and symmetric. Then, it is possible to calculate $\mathbf{C_x}$ eigenvectors, which have unit norm, and eigenvalues. If we assume the data already centered, so that $\boldsymbol{\mu} = 0$:

$$\frac{1}{T}\mathbf{X}\mathbf{X}^T = \mathbf{C_x} = \mathbf{U}\mathbf{D}\mathbf{U}^T \tag{42}$$

where $\mathbf{D}$ is the diagonal matrix containing the $\mathbf{C_x}$ eigenvalues and $\mathbf{U}$ is the orthogonal eigenvectors matrix. The eigenvectors that form the $\mathbf{U}$ matrix are ordered according to the related eigenvalue, from the highest to lowest one.

It is then possible to get a new data matrix $\mathbf{Y}$ in the reference system defined by the orthogonal basis $\mathbf{U}$:

$$\mathbf{Y} = \mathbf{U^T}\mathbf{X} \tag{43}$$

Because of the orthogonality of $\mathbf{U}$, we also have that:

$$\mathbf{X} = \mathbf{U}\mathbf{Y} \tag{44}$$

The rows y_j, with $j = 1, .., M$ of $\mathbf{Y}$ are the Principal Components (PCs) of the original data matrix $\mathbf{X}$. PCs are directly related to the eigenvectors of the matrix $\mathbf{U}$, which are ordered according the related eigenvalue, then the order of the PCs follows the significance in describing the data.

As a consequence, it is possible to ignore the last rows of $\mathbf{Y}$, i.e. the PCs of lesser significance, without losing the ability to explain most of the original signal variance. Then, the dimension of the data matrix can be reduced from an original dimension M to a smaller one.

3.3.2 Basic principles of ICA

Two main properties should belong to the separation method used to distinguish the processes ongoing on the Earth. One is that the signals resulting from a separation algorithm, when summed up, give as result the original observation. This means that the effects of different physical processes acting at the same time is equivalent to the linear sum of the effect of each process individually considered. The second one is that each signal can be studied separately: there is no mutual interaction between them, then they can be considered reciprocally independent and useful to identify and separate the different processes under study.

Let us clarify that with an example. If the motion of a network of GPS stations is caused only by thermoelastic displacements and plate motions, each station records the combined effect of them. When we make a separation analysis, we will find a signal representing the thermoelastic effect and another one describing the plate motion. According to the properties just introduced, the thermoelastic effect does not affect the plate motion at all: they are completely independent. Furthermore, when we sum the displacements caused by each process, the result obtained approximates what originally was recorded at the GPS station.

At this point, it is necessary to give more details about the meaning of *independence*: here we make the assumption that the independence of geophysical processes effects is accomplished if the correspondent sources are statistically independent. On a statistical point of view, if we consider two random variables s_1 and s_2, with probability density functions $p_1(s_1)$ and $p_2(s_2)$, they are independent if and only if the joint probability density function (pdf) of s_1 and s_2 is:

$$p(s_1, s_2) = p_1(s_1)p_2(s_2) \tag{45}$$

Extending this definition to a number n of variables, the necessary and sufficient condition for their independence is that:

$$p(s_1, .., s_L) = \prod_{i=1}^{L} p_i(s_i) \tag{46}$$

It is worth noting that statistically independence is not satisfied by the PCA, since in general two uncorrelated variables are not guaranteed to be independent. The more stringent Independent Component Analysis (ICA) allows us to extract components (ICs) mutually independent one from the other. Since the goal of the ICA is to maximize the independence of the different s_i, this has to be done by minimizing the differences between the two sides of equation 46 assuming trial probability density functions for each ICs. One of the most used method to measure the difference between two probability density functions is to compute the *Kullback-Leibler (KL)-divergence* (Kullback and Leibler, 1951). In the particular case of the pdfs in equation (46), this quantity is also known as *mutual information (MI)*, a positive quantity that depends on $p(s_1, .., s_n)$ (equation 2.6 in Gualandi, 2015). Specifically, to get independent sources *MI* must be minimized. Anyway, since the value of $p(s_1, .., s_n)$ is unknown, this method can not be directly used. Alternatively, Hyvarinen and Oja (2000) demonstrated that the maximization of the non-gaussianity of the p_i corresponds to the minimization of the *MI*.

In the case of GPS data, we make the hypothesis that data can be explained by $L \leq M$ source signals. According to the first property reported at the beginning of this section, the data matrix $\mathbf{X}$ can be written in a way similar to equation 44 as:

$$\mathbf{X}_{M\times T} = \mathbf{A}_{M\times L}\mathbf{S}_{L\times T} + \mathbf{N}_{M\times T} \tag{47}$$

where both $\mathbf{A}$, $\mathbf{S}$ and $\mathbf{N}$ are unknown and the goal of ICA is to determine them: $\mathbf{A}$ is called mixing matrix, $\mathbf{S}$ is the source signal matrix and $\mathbf{N}$ is the noise. In particular to satisfy the second property discussed at the beginning of this section, ICA determines $\mathbf{S}$ by maximizing the independence of its rows, while the orthogonality condition is relaxed, unlike equation 44.

3.3.3 Variational Bayesian ICA (vbICA)

In order to look for the independent components, it is possible to find a linear function Υ that relates the data space $\mathbb{R}^M$ to an independent source space $\mathbb{R}^L$ (a), or vice-versa (b). The case a is called *mapping approach* and it is used in the PCA case (for $L = M$) , where Υ is the rotation matrix U^T. On the contrary, in the *generative model approach* a linear function that relates the independent source space $\mathbb{R}^L$ to the data space $\mathbb{R}^M$ is looked for. This second approach is the one

used in this thesis, adopting a variational Bayesian algorithm (vbICA), developed by Choudrey and Roberts (2003) and implemented in the ICAIM code (Independent Component Analysis-based Inversion Method)(Gualandi, 2015; Gualandi *et al.*, 2016), where trial values of ICs are generated and tested against data values. This approach has been demonstrated to be superior to more common ICA techniques based on the mapping approach (Choudrey, 2002).

A generative model is composed by observed variables, i.e. the data $\mathbf{X}$, hidden variables (random variables for which we do not know the distribution, i.e. $\mathbf{A}$, $\mathbf{S}$ and $\mathbf{N}$) and hidden parameters. The latter are the ones used in the distribution of hidden variables and data, and make the particular model under consideration work. We indicate hidden variables and parameters as weights ($\mathbf{W}$). A model is defined once the relation among all data and weights is specified. The goal of a generative model is to find the best weights in order to explain the observations and match the a priori knowledge.

Considering the Bayesian approach used by Gualandi and Choudrey, the best weights are found by maximizing their posterior probability given the data:

$$p(\mathbf{W}|\mathbf{X}) = \frac{p(\mathbf{X}|\mathbf{W})p(\mathbf{W})}{p(\mathbf{X})} \tag{48}$$

Where $p(\mathbf{W})$ is the prior probability, $p(\mathbf{X}|\mathbf{W})$ the probability of the data given the weights, while $p(\mathbf{X})$ is called evidence and defined as:

$$p(\mathbf{X}) = \int p(\mathbf{X}|\mathbf{W})p(\mathbf{W})d\mathbf{W} \tag{49}$$

Unluckily the valuation of this integral is impossible in most of the cases because $p(\mathbf{W})$ is unknown, then an approximation is necessary. Actually, in order to determine $\mathbf{W}$, the posterior density $p(\mathbf{W}|\mathbf{X})$ is approximated with a density function $p'(\mathbf{W})$. The approximating posterior $p'(\mathbf{W})$ is chosen as the best approximation of $p(\mathbf{W}|\mathbf{X})$ by maximizing a quantity called Negative Free Energy (NFE) defined as:

$$NFE(\mathbf{X}) \equiv \int p'(\mathbf{W}) ln(p(\mathbf{X}, \mathbf{W})/p'(\mathbf{W}))d\mathbf{W} \tag{50}$$

In fact it is possible to demonstrate that the *KLdivergence* between $p(\mathbf{W}|\mathbf{X})$ and $p'(\mathbf{W})$ is minimized if NFE is maximized with respect of the $p'(\mathbf{W})$ choice.

The process of NFE maximization is then performed by using an Expectation-Maximization iterative algorithm (learning process) using at each iteration trial values of $\mathbf{W}$, whose equations are described in detail in Gualandi *et al.* (2015), Sect. S1 of the Supplementary Material.

Tractability is achieved assuming that $p'(\mathbf{W})$ factorizes into $\prod_{i=1}^{N} p'(w_i)$ for some partition $\{W_1, ..., W_N\}$ of $\mathbf{W}$ as it is in the case of independent variables. The NFE is then maximized for each factorizing $p'(W_i)$ iteratively. The vbICA approach makes use of the following partition: $\mathbf{W} = \{\mathbf{A}, \mathbf{S}, \mathbf{\Lambda}, \mathbf{q}, \boldsymbol{\theta}\}$, where $\mathbf{A}$ are the random variables (rvs) describing the mixing matrix, $\mathbf{\Lambda}$ the rvs describing the precision (i.e., the inverse of the variance) associated with the noise, $\mathbf{S}$ the rvs describing the sources, while $\mathbf{q}$ and $\boldsymbol{\theta}$ are parameters. The elements of the mixing matrix $\mathbf{A}$ are assumed to have Gaussian distribution. The noise is Gaussian with zero mean. Each source $i = 1, .., L$ is modeled by a mixture of m_i Gaussians, which are governed by three parameters: μ_{i,q_i}, the mean; β_{i,q_i}, the precision and π_{i,q_i}, which represents the probability that a Gaussian is actually used to explain the source, with $q_i = 1, .., m_i$.

3.3.4 vbICA application on data

The first step of the vbICA is, starting from the data matrix, to initialize the trial values of the mixing matrix $\mathbf{A}$ and of the sources $\mathbf{S}$. This can be done either through a random process (random initialization) or by using the result of a PCA. Since it is always possible to decompose a matrix in the product of a unit column norm matrix and a diagonal matrix, then we may re-write equation 47 as it follows:

$$\mathbf{X} = \mathbf{AS} = \mathbf{U}\mathbf{\Sigma}_A\mathbf{\Sigma}_S\mathbf{V}^T = \mathbf{U}\mathbf{\Sigma}\mathbf{V}^T \tag{51}$$

where $\mathbf{U}$ and $\mathbf{V}$ have unit norm non-dimensional columns and $\mathbf{\Sigma}$ is a diagonal matrix. Noting that $\mathbf{S}$ is equal to $\mathbf{\Sigma}_S\mathbf{V}^T$ we can say that the columns V^i of $\mathbf{V}$ represent the temporal evolution of the

i-th source, while $\mathbf{U}$ contain its spatial information. The diagonal matrix $\mathbf{\Sigma}$ contains the weights (mm) associated with each source contributing to $\mathbf{X}$.

We consider two PCA algorithms to take into account missing data. One is a weighted low-rank approximation, developed by Srebro and Jaakkola (2003), which gives weight zero to the missing data. The other was developed by Bailey (2012) and consists in an Expectation-Maximization routine (EMPCA). The main difference between the two methods is that the first does not impose orthogonality to the eigenvectors, then the centering and decomposition are made iteratively until convergence is found. In EMPCA, on the other hand, there is the orthogonality constraint for the eigenvectors and the centering is not performed iteratively, so that this algorithm results to be much faster.

The number of components (L) used to decompose the original signal needs to be defined a-priori. In the PCA case the matrix $\mathbf{D}$ (equation 42) contains the variances of the dataset in decreasing order, then once established the threshold of variance that must be represented, the number of components needed can be directly determined. Since this threshold is arbitrary; it is useful to identify alternative criteria to discern how many components should be employed; in the case of ICA these criteria are even more useful since the components are not weighted according to the explained variance.

Two widely used statistical tests that can be performed are the reduced χ^2 (χ^2_{red}) test and the F-Test.

χ^2_{red} is defined as:

$$\chi^2_{red} = \frac{1}{d - L\,(N + M + 1)} \sum_{i=1}^{M} \sum_{j=1}^{N} \frac{\left(X(i,j) - X_L(i,j)\right)^2}{\sigma(i,j)^2} \tag{52}$$

where d is the number of data, N the total number of epochs, M the total number of sensors, L the number of components, $X(i,j)$ the real data, $X_L(i,j)$ the modeled results. When $\chi^2_{red} < 1$ the real data, that in our case are GPS measurements, are satisfactorily represented by the model, i.e. ICA reconstruction using L components.

Let us assume that we have selected L components for our ICA analysis. How can we discern if it is necessary to use $L + 1$ instead? This answer is given by the F-Test, which tells us if the fit gain due to the addition of parameters is significant given the number of added parameters. The computed F value is given by Kositsky and Avouac (2010):

$$F = \frac{\chi^2_n - \chi^2_{n+1}}{\chi^2_{n+1}} \frac{\nu_{n+1}}{\nu_{n+1} - \nu_n} \tag{53}$$

where ν_n is the number of degree of freedom of the L-th component.

Specifically for the vbICA, another method used to set the number of components is the Automatic Relevance Determination (ARD), described in MacKay (1995). This criterion considers the so-called "variance" associated with each column of the mixing matrix, which measures how much the elements of each column vary from the a-priori value. Since a null a priori is supposed for the mixing matrix, if the variance of a column is low, then the associated component is not particularly useful in explaining the data, because it remains similar to the a-priori value. In fact, this results in heavy suppression of the correspondent source signal. On the contrary, if the variance is large, we can say data played a more important role than priors in guiding the learning process. According to the ARD criterion, when the difference between the variances of two components becomes larger than one order of magnitude, the one associated with the smaller should be discarded.

Finally, we propose an example of vbICA decomposition described in Gualandi *et al.* (2016) by using synthetic data. They simulated a GPS network affected by a seasonal signal, co- ad post-seismic signals, and a Mogi source signal (red lines in Figure 12). After the co-seismic offset correction, the result of a vbICA on this group of stations is the definition of 3 ICs (black dots in Figure 12), each one reproducing the correspondent synthetic signal.

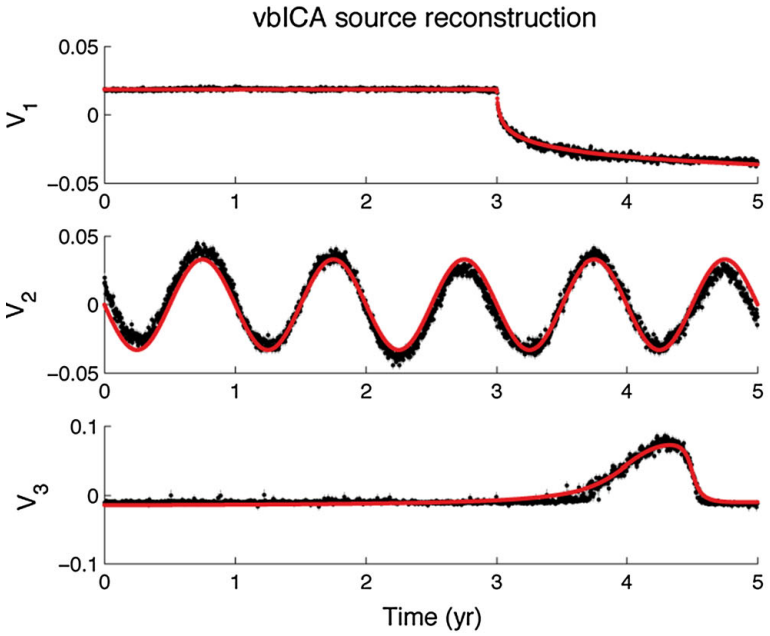

Figure 12: Figure from Gualandi *et al.* (2016). Red lines represent the effects of the actual synthetic sources of deformation, black dots ICA reconstruction. V_1 reproduce the post-seismic signal, V_2 the seasonal and $V3$ the effect of a Mogi source.

4 vbICA results

4.1 ICs temporal and spatial features

The goal of the vbICA analysis is to separate the different sources of deformation that generate the observed displacement. In fact, the output of this analysis is the definition of a limited number of ICs, each one reproducing the displacement caused by a different source of deformation.

We recall that an IC is characterized by a specific spatial distribution (U) and follows a specific temporal evolution (V). Both the spatial and temporal responses associated with every IC have unit norm, so that a weight coefficient S (in mm) is necessary to rescale their contribution in explaining the original data. The displacement time series at a given station can be reconstructed by linearly summing up the contributions from all the ICs, each of which is obtained by multiplying the specific spatial distribution by the associated weight times the temporal evolution.

Gualandi *et al.* (2016) pointed out that the ability of the vbICA algorithm to correctly separate the sources improves when the correlation of the dataset is reduced, and this can be achieved by using de-trended time series. For this reason we removed the linear trend from our data, which has been estimated from the absolute (i.e., IGb08) time series, corrected for known offsets due to changes in stations equipment.

In order to limit missing data, we removed from the analysis stations presenting large data gaps and stations having < 3.5 years of data, so that the mean missing data percentage of our time-series is 35%.

The analysis on the study region (black polygon of Figure 13) yields that five ICs are required to properly reconstruct the time series, where this number is based on the automatic relevance determination (ARD) criterion and the estimation of the negative free energy associated with the generative model, as described in section 3.3.2.

The temporal evolution (V) and the power spectral density of the five ICs are shown in Figure 14.

Map views of the spatial response (U) corresponding to each IC and the associated weight (S in mm) are shown in Figure 15, where the color of circles and the length of the green arrows indicate the direction and the amplitude of U at each station in the vertical and horizontal components, respectively.

In order to better interpret the displacement time series reconstructed by each IC from V (Figure 14) and U (Figure 15), it is worth noting that positive values of U in the vertical component of the displacement (red dots) imply an upward movement of a GPS station when the V is increasing, while when the correspondent V is decreasing red dots represent a downward movement. Stations having negative values of U in the vertical component (blue dots) move downward when red dots are moving upward and vice-versa. Similarly, the direction pointed by the green arrows represent the direction of the horizontal displacement of a station when the V is increasing, while when V is decreasing the direction of the displacement is reversed.

For each station and each IC, we computed the signal to noise ratio (SNR) value as the ratio of the squared difference between the maximum and minimum displacements associated with the IC and the mean uncertainty (one standard deviation) of the GPS measurements. Figure 16 shows maps of the spatial response for the ICs, except IC2 that will be discussed later, for the stations with SNR > 1 at least in one of the horizontal components or in the vertical one. For each IC the number of stations with SNR > 1 provides an indication on how important is the single IC in describing the measured displacements time series.

The frequency analysis (Figure 14B) shows that the temporal evolution of the first and third ICs (V1 and V3) has peaks corresponding to annual signals. The two ICs have a phase lag of 96 $\pm$ 2 days, where the uncertainties calculations are reported in Appendix B, with V3 anticipating V1.

V2 and V4 have more power at low frequencies, with V4 representing a multiyear signal. V2, in particular, combines different long-period signals with smaller power at annual and semiannual periods, displaying a noncyclic signal that varies in amplitude during the investigated time span. The time spans presenting larger variations of V2 are shown in gray in Figure 14A and correspond to the two time intervals considered section 4.3 for a more in-depth study. During periods of rapid increase (light gray areas in Figure 14) the signal seems to have a linear trend, whereas during periods of decrease (dark gray areas in Figure 14), the decay rate does not seem as constant. V5 power spectrum does not exhibit dominant peaks, suggesting that this component represents mainly noise in the GPS time series.

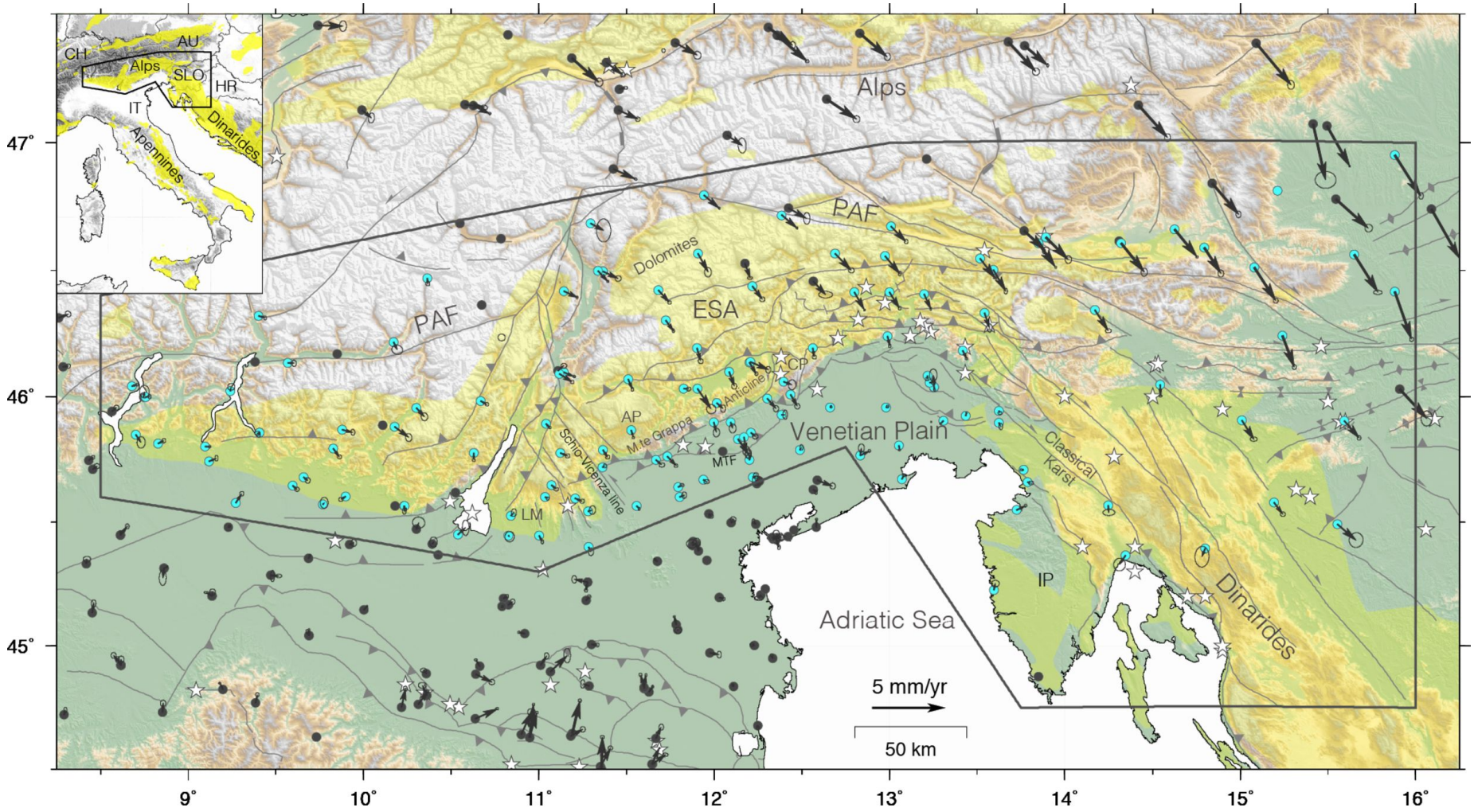

Figure 13: Map of the study region. The cyan circles indicate the Global Positioning System stations located within the black polygon and included in the time series analysis. In yellow areas where carbonate rocks outcrop (http://web.env.auckland.ac.nz/our_research/karst). The gray lines are faults from Serpelloni *et al.* (2016). The black arrows show horizontal Global Positioning System velocities (with 95% error ellipses) in an Adria-fixed frame (from Serpelloni *et al.*, 2016). The dark gray circles indicate stations outside the polygon or excluded from the analysis because of short time series or large data gaps. The white stars indicate locations of M > 5.5 earthquakes from http://emidius.mi.ingv.it/CPTI15-DBMI15. ESA = Eastern Southern Alps; LM = Lessini Mountains; PAF = Periadriatic Fault; ; MTF = Montello thrust fault; AP = Asiago Plateau; CP = Cansiglio Plateau; IP = Istria peninsula.

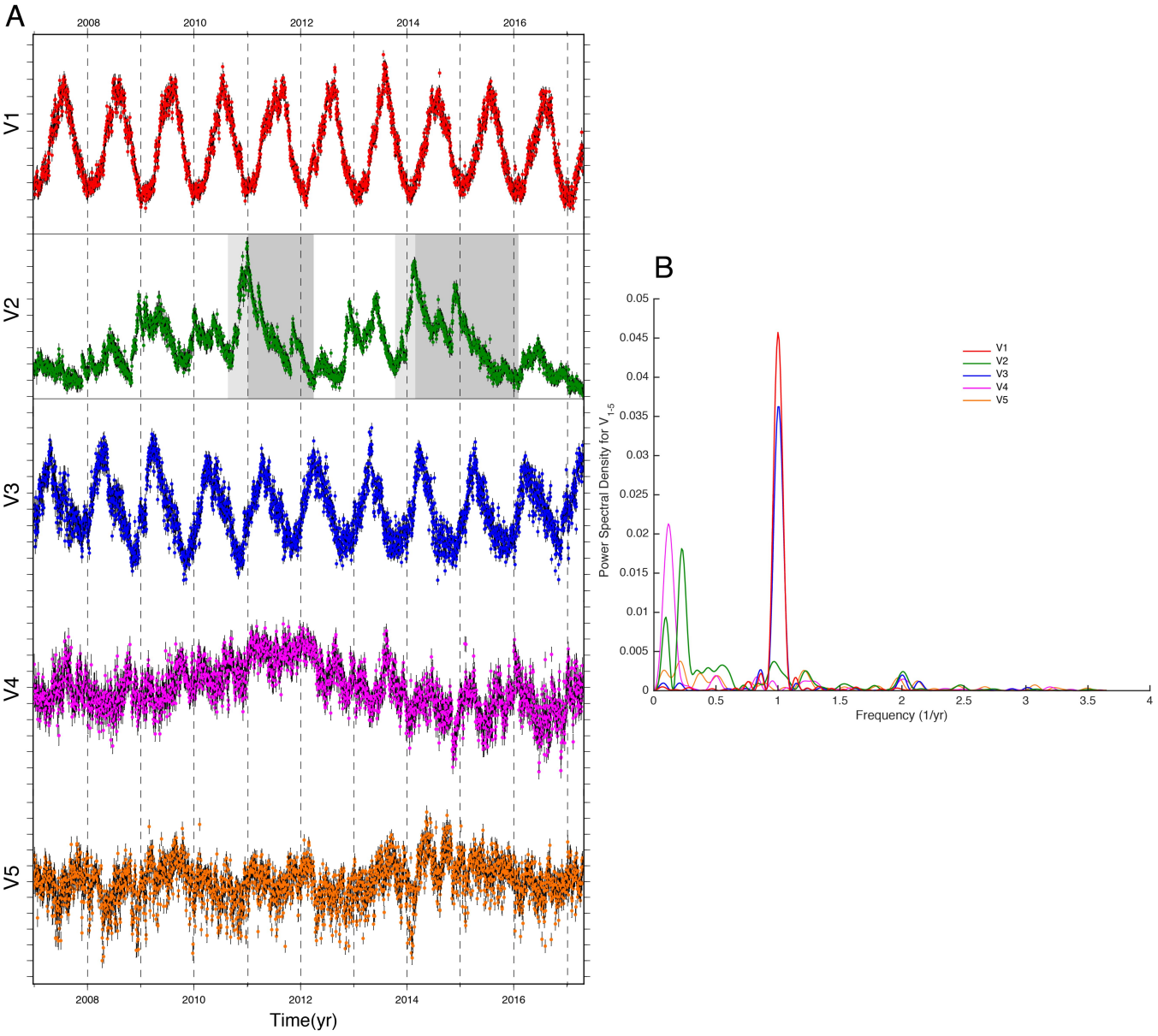

Figure 14: (A) Temporal evolution (V) of the five independent components determined from the variational Bayesian independent component analysis and (B) corresponding power spectral density plots, where the red, green, blue, purple, and orange symbols and lines refer to IC1, IC2, IC3, IC4, and IC5. Gray bars are one standard deviation errors.

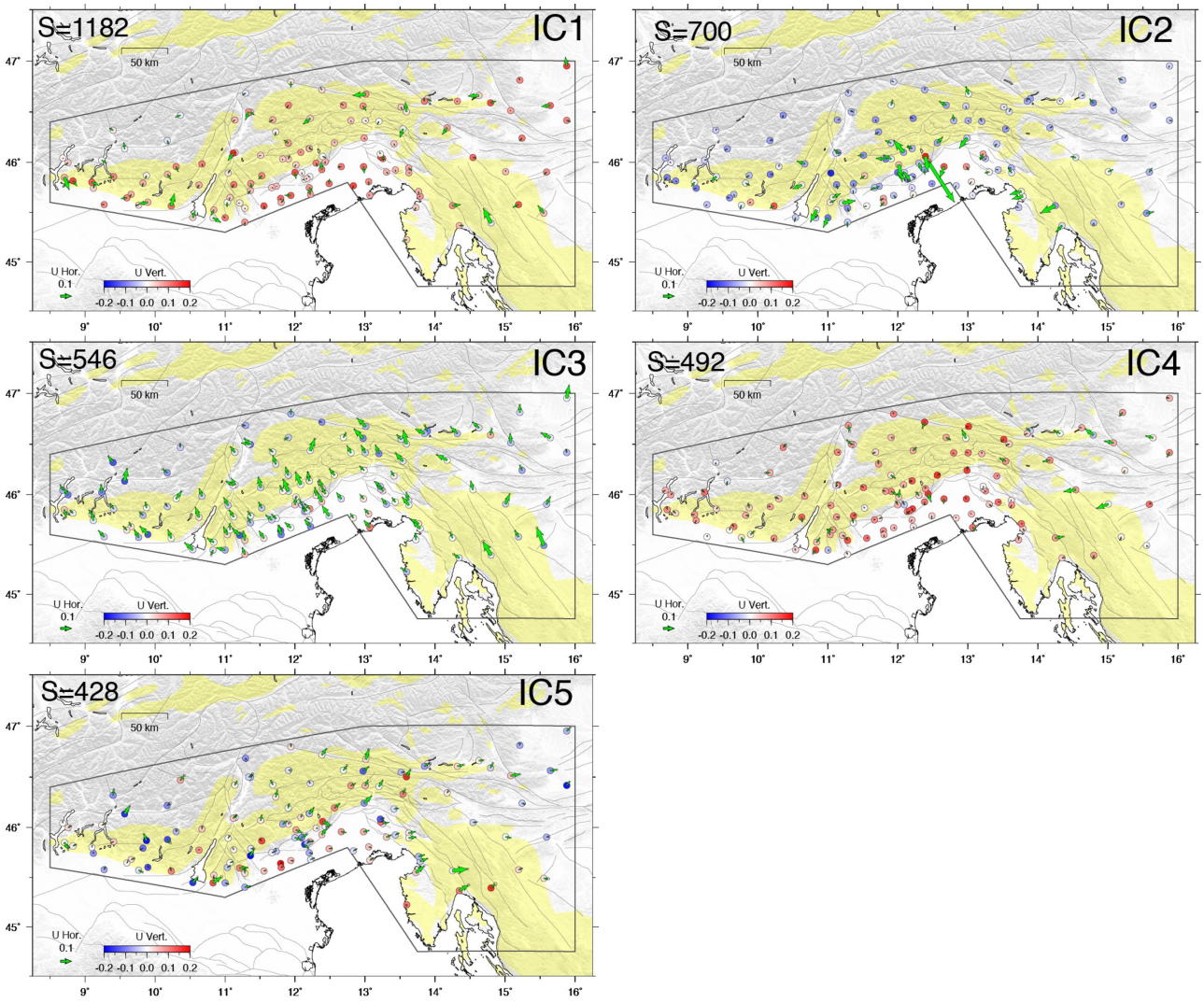

Figure 15: Map views of the spatial response, U, for the five independent components, where the green arrows show the horizontal response and the color scale refers to the vertical response. The weight S (in mm) for each independent component is shown in the upper left corner. The spatial response describes the directions along which the Global Positioning System station moves and the arrow length, or color, is proportional to the importance of this specific component at each single station.

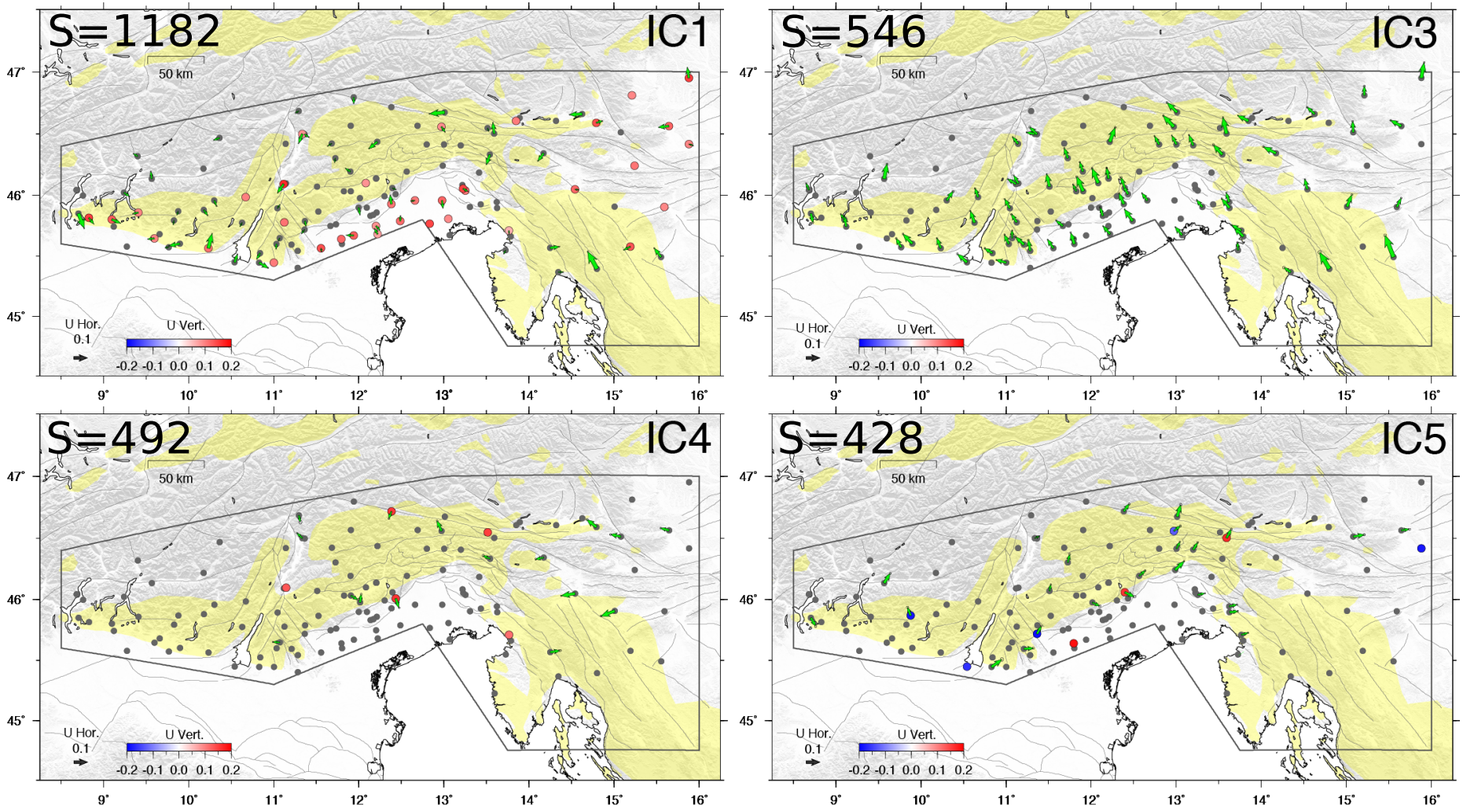

Figure 16: Map views of the spatial response, U, for IC1, IC3, IC4 and IC5, where the green arrows show the horizontal response and the color scale refers to the vertical response, respectively, only for stations that have a Signal-to-Noise-Ratio (SNR)>1 in at least one component. See Figure 17 for IC2.

In terms of spatial response (shown in Figure 15), IC1 and IC3 look like common mode signals, with stations moving at annual periods coherently in the same direction; for IC1 mostly up and down and for IC3 mostly NW-SE, since no stations have SNR > 1 in the vertical components for IC3, while for IC1 at sites with SNR > 1 the horizontal direction is variable (see Figure 16). IC2, on the contrary, shows a more heterogeneous spatial response in the horizontal component, with high SNR at stations located in the Southern Alps and northern Dinarides (see Figure 17). On the other hand, only very few sites have SNR > 1 in the vertical component for IC2. For IC4 and IC5 only 1-10% of sites have SNR > 1 and marginally contribute in describing the measured displacements at very few stations.

Figure 18 shows the observed (in blue) and reconstructed (in red) time series for four stations, as obtained by combining the five ICs with their weights and the site-specific spatial response, and the time series of the displacements associated with each IC for all GPS stations. The dark gray lines in Figure 18 show the annual + semiannual model, commonly used in GPS time series modeling (Dong *et al.*, 2002), which in this case reproduces the observables much worse than the ICA reconstruction.

The temporal evolution of IC2 is indeed similar to the displacement time series measured at the CANV station, where the high peak-to-peak displacements observed (e.g., between 2011 and 2012) have been associated with rainfall-induced southward slope movements of the Alpago-Cansiglio karst plateau (CA in Figure 13) by Devoti *et al.* (2015). The presence of a similar signal over a much wider region points toward a common physical source, suggesting that rather than being a local feature, ground deformation induced by precipitation is active at a much larger scale. In order to strengthen this hypothesis, we run the ICA analysis excluding CANV. Figure 19 shows the temporal evolution and spatial response associated with IC2 as obtained not including CANV. We found no differences both in terms of temporal evolution and spatial response of the ICs, with the same order of ICs in terms of weight as in the analysis including CANV. For this reason, in the following we use the results obtained including CANV in the vbICA analysis.

4.2 Seasonal common mode signals

4.2.1 Large scale hydrologic models

When we analyze long displacements time series in regions like the Alps, taking into account the presence of the water stored in the continental interiors is as important as considering the water of the oceans (Boy *et al.*, 2009). In fact, most of seasonal motions can be attributed to loading effects caused by Earth surface and subsurface mass redistributions (e.g., Amos *et al.*, 2014; Argus *et al.*, 2014; Borsa *et al.*, 2014; Tregoning and van Dam, 2005; van Dam *et al.*, 1994). Furthermore, it has been demonstrated (Herring *et al.*, 2016) that the seasonal water storage variations, linked to the water cycle, causes displacements of several millimeters that can be clearly observed by GPS. The displacements associated with water storage variations are not constant on the Earth, but depend on climate and local geology. For this reason different research groups developed models to quantify water storage variations and reproduce the displacement caused by them.

Generally, surface displacements are computed using Greens function formalism (Farrell, 1972) based on the preliminary reference Earth model assuming a spherically symmetric, non-rotating, elastic and isotropic Earth (Dziewonski and Anderson, 1981), where the load Love numbers (LLNs) only depend on the spherical harmonic degree. It is also assumed that the loading processes happen in a superficial layer of the Earth having about the same thickness of the atmosphere, i.e. 10-15 km, which is very small compared to the mean Earth radius. These assumptions allows a unique inversion of geopotential and Earth shape changes into mass redistributions (Kusche and Schrama, 2005).

A water storage variation causes a surface density anomaly $\Delta\sigma(\lambda, \theta)$, depending on the longitude λ and co-latitude θ, which is interpreted as a departure from a multi-annual mean. Assuming a density of water ρ_w, the load thickness $T = \frac{\Delta\sigma}{\rho_w}$ is expressed as an equivalent water column.

The spherical harmonic (SH) expansion for the surface density anomaly is:

$$\Delta\sigma(\lambda,\theta) = a\rho_w \sum_{l,m} \left(\Delta C^{\sigma}_{l,m} cos\,(m\lambda) + \Delta S^{\sigma}_{l,m} sin\,(m\lambda)\right) \overline{P_{l,m}}\,(cos\,(\theta)) \tag{54}$$

where a is the Earth's mean radius; l and m the degree and the order, respectively, of the spherical harmonics; $\Delta C^{\sigma}_{l,m}$ and $\Delta S^{\sigma}_{l,m}$ the variations of the spherical harmonic hydrological load coefficients (Stokes coefficients); $\overline{P_{l,m}}$ the fully normalized Legendre polynomials.

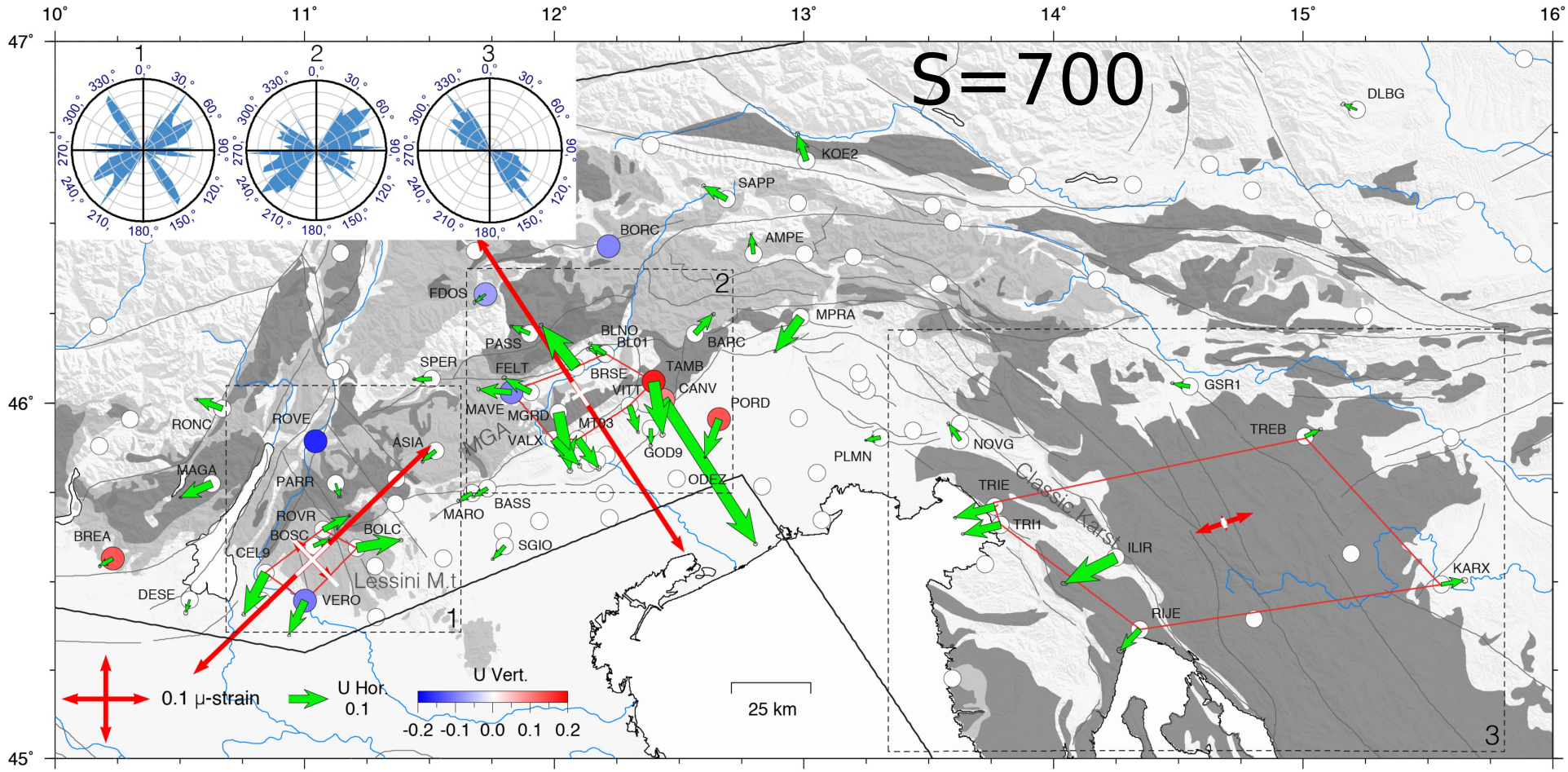

Figure 17: Spatial response (U) of IC2 for the vertical (colored circles) and the horizontal (green arrows) components, respectively, as in Figure 15. Here only stations having a SNR > 1 in one of the horizontal component or in the vertical are plotted. The position of other sites (with SNR < 1 for IC2 in all the three components) is plotted as white circles. The top left inset displays the rose diagrams showing the angular distribution of lineament orientations for the areas delimited by the dashed black boxes (1, 2, and 3), which include sites displaying the largest horizontal spatial response for IC2. The red arrows show the principal horizontal strain axes when the highest value of dilatation strain is attained during T1, see Figure 24. Strains are computed using Global Positioning System stations within the associated red polygons. The blue lines show major rivers. The dark and light gray areas represent highly productive fissured karst aquifers and low and moderately productive fissured karst aquifers from the International Hydrogeological Map of Europe 1:1,500,000 (*http://www.bgr.bund.de/ihme1500*). MGA = Monte Grappa- Monte Cesen anticline.

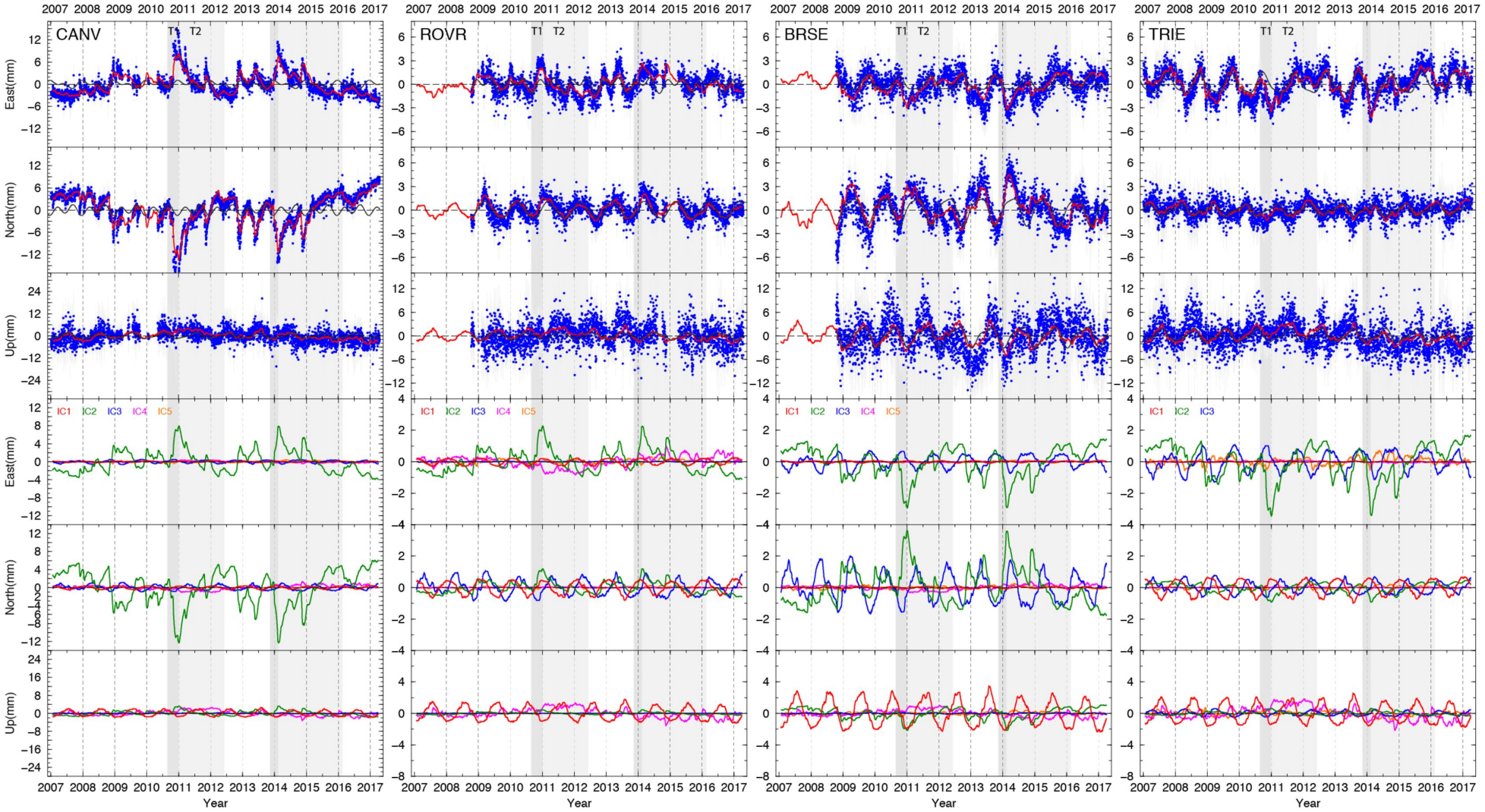

Figure 18: Results if the ICA analysis, performed with five ICs, at four GPS stations located in the three areas shown in Figure 17. Upper three lines of panel: detrended observed (blue dots) and reconstructed (red line) displacement time series. The dark gray lines show fit to the observations with an annual + semiannual model obtained by least squares fit of the Global Positioning System observations using the QOCA *analyze_tseri* package (*https* : *//qoca.jpl.nasa.gov*). The displacement time series associated with each of the five ICs are reported in the bottom panels with different colors. The gray areas indicate time intervals during which the cumulative displacements associated with the second IC are larger than average.

.

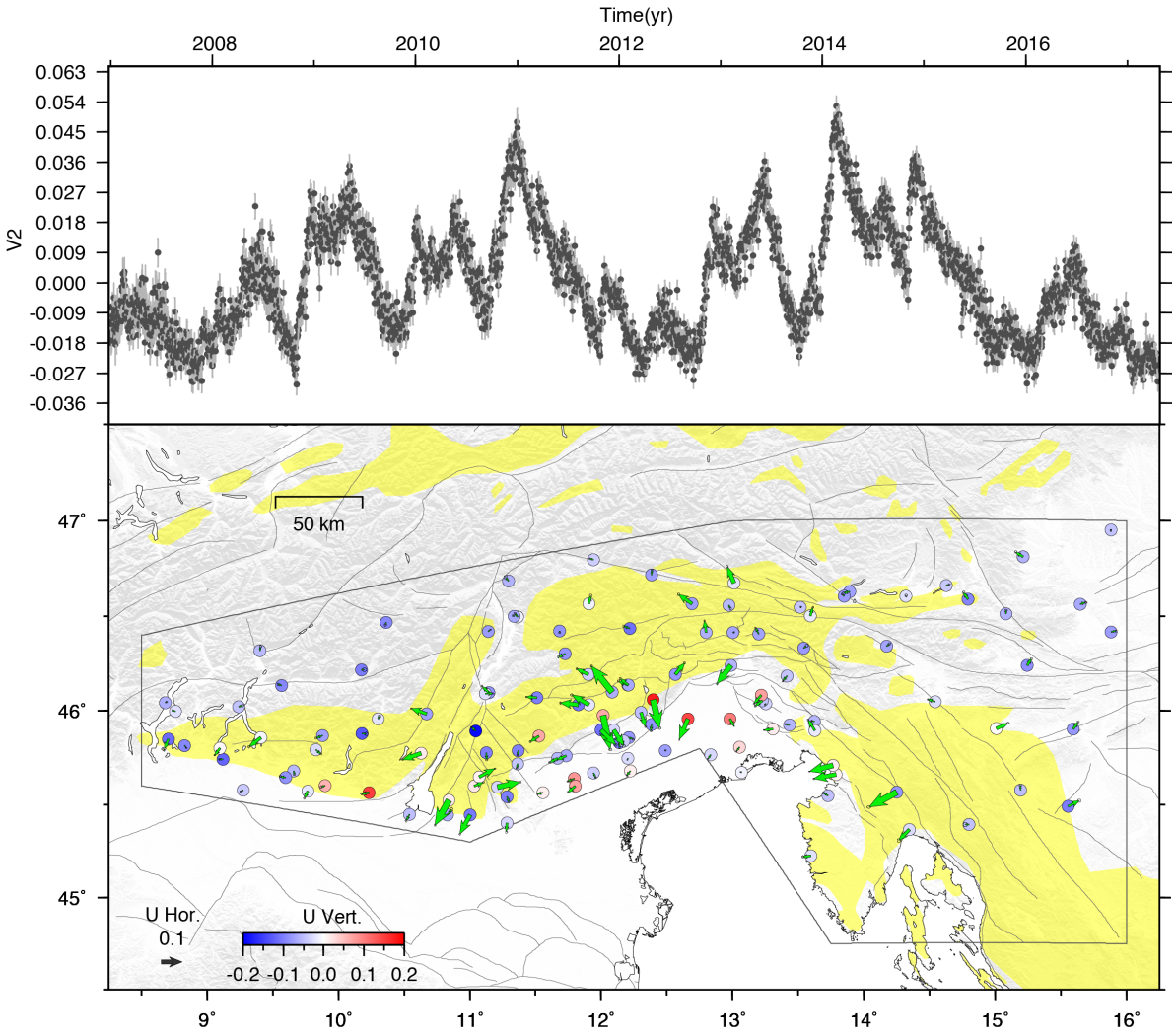

Figure 19: Temporal evolution (V2) and spatial response (as in Figure 16) for IC2, obtained excluding the station CANV from the vbICA analysis. S=635 mm.

According to Farrel theory (1972) it is possible to compute the coefficients of the spherical harmonics of the geoid change caused by the hydrological load, and of the horizontal and vertical displacements, starting from the Stokes coefficients.

The relation between the spherical harmonics of the geoid $C^g_{l,m}$ and of the load is:

$$\Delta C^g_{l,m} = 3\frac{\rho_w}{\rho_e}\frac{1+k'_l}{2l+1}\Delta C^\sigma_{l,m} \tag{55}$$

while when considering the spherical harmonics for vertical ($C^h_{l,m}$) and horizontal ($C^\psi_{l,m}$) displacement, the relations are:

$$\Delta C^h_{l,m} = 3\frac{\rho_w}{\rho_e}\frac{h'_l}{2l+1}\Delta C^\sigma_{l,m}; \tag{56}$$

$$\Delta C^\psi_{l,m} = 3\frac{\rho_w}{\rho_e}\frac{l'_l}{2l+1}\Delta C^\sigma_{l,m}; \tag{57}$$

where ρ_e is the mean Earth density, while k'_l, h'_l, l'_l are the load Love numbers.

Starting from spherical harmonics coefficients it is possible to compute the three component of the displacement (vertical Δh, east Δe and north Δn) by using the following formulas:

$$\Delta h = a\sum_{l,m}\left(\Delta C^h_{l,m} cos\left(m\lambda\right) + \Delta S^h_{l,m} sin\left(m\lambda\right)\right)\overline{P_{l,m}}\left(cos\left(\theta\right)\right) \tag{58}$$

$$\Delta e = \frac{a}{sin(\theta)}\sum_{l,m} m\left(-\Delta C^\psi_{l,m} sin\left(m\lambda\right) + \Delta S^\psi_{l,m} cos\left(m\lambda\right)\right)\overline{P_{l,m}}\left(cos\left(\theta\right)\right) \tag{59}$$

$$\Delta n = -a\sum_{l,m}\left(\Delta C^\psi_{l,m} cos\left(m\lambda\right) + \Delta S^\psi_{l,m} sin\left(m\lambda\right)\right)\frac{\partial}{\partial\theta}\overline{P_{l,m}}\left(cos\left(\theta\right)\right) \tag{60}$$

Once defined how it is possible to compute displacements from water storage variations, let us take a look to some products that allow the computation of the water mass changes in land area of Earth, which provide the coefficients of equation 54 and then determining the ones in (55).

GRACE The Gravity Recovery and Climate Experiment (GRACE) is a gravity satellite mission launched in 2002 which monitors the temporal variations of Earth's gravity field. GRACE consists of two identical spacecraft that fly about 220 km apart in a polar orbit 500 km above Earth, which map Earth's gravity field by making accurate measurements of their relative distance, using GPS and a microwave ranging system.

This experiment allows a monthly computation of the Stokes coefficient up to a degree of about 100, where the maximum spatial resolution depends on different processing and post-processing strategies. It is worth noting that the first two degree coefficients cannot be measured accurately by GRACE (Chen *et al.*, 2005): degree 1 coefficient, describing the relative motion between the Earth center of mass and a crust-fixed terrestrial reference frame; and degree 2 coefficients, linked to the Earth oblateness, must be evaluated independently from the results of GRACE mission.

The resolution of GRACE measurements implies a maximum obtainable spatial resolution of about 300 km. As shown before, it is possible to compute displacements caused by water mass changes through the analysis of the variation of Stokes coefficients; anyway the temporal (monthly) and spatial resolution of these data is too coarse for our purposes, in particular when compared to other products that allow us to compute displacements caused by hydrological loading variations.

GLDAS The Global Land Data Assimilation System (GLDAS) is a product of the collaboration between the National Aeronautics and Space Administration (NASA) Goddard Space Flight Center (GSFC) and the National Oceanic and Atmospheric Administration National Centers for Environmental Prediction (NOAA NCEP). GLDAS oversees different Land Surface Models (LSM): NOAH (Noah) 1.0, MOS (Mosaic) 1.0, and VIC (Variable Infiltration Capacity) 1.0. They have been developed pursuing the goal of simulating the transfer of mass, energy and momentum between the soil and vegetation surfaces and the atmosphere (Rodell, 2004).

The inputs of LSMs are forcing parameters estimated by considering both direct measurements and modeled data. They include precipitation, surface pressure, air temperature, specific humidity,

Model Name	Number of soils layers	Depths of Layers (m)
GLDAS MOS (Mosaic)	3	1) 0-0.02 2) 0.02-1.5 3) 1.5-3.5
GLDAS NOAH	4	1) 0-0.1 2) 0.1-0.4 3) 0.4-1.0 4) 1.0-2.0
GLDAS VIC (Variable Infiltration Capacity)	3	1) 0-0.1 2) 0.1-1.6 3) 1.6-1.9
ERA-Interim	4	1) 0-0.07 2) 0.07-0.28 3) 0.28-1.0 4) 1.0-2.89

Table 2: Soil composition according to different models.

Required forcing parameter	**Output**
Precipitation	Soil moisture in each layer
Downward shortwave radiation	Snow depth, fractional coverage, and water equivalent
Downward longwave radiation	Plant canopy surface water storage
Near-surface air temperature	Soil temperature in each layer
Near-surface specific humidity	Average surface temperature
Near-surface wind (North direction)	Surface and subsurface runoff
Near-surface wind (East direction)	Bare soil, snow, and surface water evaporation
Surface pressure	Canopy transpiration
	Latent, sensible, and ground heat flux
	Snowmelt
	Snowfall and rainfall
	Net surface shortwave and longwave radiation
	Aerodynamic conductance
	Canopy conductance
	Surface albedo

Table 3: GLDAS input parameters and output data (from Rondell, 2004).

long- and shortwave radiation, and wind (Rodell, 2004) having a spatial resolution ranging from 0.25° to 2.5°. The outputs of these models (Table 3) allow us to compute the hydrologic surface loads considering the water stored as soil moisture, snow and in vegetation. River flow variations are not taken into account. Then, starting from the reconstruction of water storage variations, LSMs compute 3-D elastic displacements at daily timescales over the entire planet on a global grid. The main difference among the LSMs is how the soil layers are modeled, in particular which is the number of layers considered and their thickness (Fang *et al.*, 2009 Mitchell *et al.*, 2004) (Table 2). It is worth noting that the GLDAS models only account for surface loading, so when there are significant changes in water storage at depths, the model does not reflect these.

In the following sections we consider data generated by the GLDAS Noah models, which are developed by the Global and Energy Water Cycle Experiment Continental-Scale International Project using a layered soil model and including a vegetation parameter for each grid square of resolution $0.25° \times 0.25°$ (Chen *et al.*, 1996 Koren *et al.*, 1999).

ERA-Interim The ERA-Interim is a project conducted by the European Centre for Medium-Range Weather Forecasts (ECMWF). It has been developed with the goal to produce a reanalysis of the parameters that characterize atmosphere, oceans, solid Earth surface and the relations among these "worlds" which are very strictly connected. For our goals, we consider only the products that describe the land surface and its water content variation.

The water storage is modeled by using the TESSEL (Tiled ECMWF Scheme for Surface Ex-

changes over Land) scheme, which diversifies the soil in four layers (Table 2). Soil moisture and snow are the two components of water storage that ERA-Interim takes into account. Soil moisture is computed considering observations of air temperature and humidity at 2 meters over the ground, while snow estimations are based on both in situ and satellite observations.

The original spatial resolution is T255, about 80km, then rescaled in a grid of size $0.5° \times 0.5°$; while the final temporal resolution is daily.

4.2.2 The interpretation of IC1 and IC3

In the study region IC1 and IC3 represent common mode annual signals, displaying rather uniform spatial responses (i.e., with sites moving coherently along the same direction) in the vertical and in the horizontal components, respectively (Figure 15). IC1 describes seasonal displacements that are larger in the vertical component (see Figure 21), with average (median) amplitude of ∼3.5 mm and maximum values up to ∼10 mm at sites located in the pedemountain area. In the horizontal components, IC1 describes much smaller seasonal displacements, with an average (median) amplitude of 1.20 and 1.41 mm in the east and north components, respectively. In the vertical component, positive peaks, describing uplift of the study region, are in June, and negative peaks, describing subsidence of the area, are in January, being in phase with temperature seasonal variations (see Figure 20). IC3, which is not in phase with temperature, shows positive peaks in spring and negative peaks in autumn, describing annual displacements mainly in the NW-SE directions (see Figure 16), with an average (median) amplitude of ∼0.8 (east) and 1.5 mm (north).

We compared the displacements associated with IC1 and IC3 with displacements due to the redistribution of fluids at the Earth's surface estimated using the global reanalysis models ERA-interim (European Centre for Medium-Range Weather Forecasts, ECMWF reanalysis) (Berrisford *et al.*, 2009; Dee *et al.*, 2011) and Global Land Data Assimilation System (GLDAS)/Noah (Rodell *et al.*, 2004), both described in section 4.2.1. These data have been provided by *http://loading.u-strasbg.fr* (Gegout *et al.*, 2010), which shares global gridded 3-D displacements for atmospheric, hydrological, and non tidal ocean loading obtained from different global models.

In order to evaluate the agreement between model and geodetic (in terms of ICs) displacements, we use the Lin correlation coefficient (Lin, 1989, 2000), which takes into account similarities on both the amplitudes and the shapes of two time series. If we consider two time series x and y, having means μ_x and μ_y and variances σ_x and σ_y respectively, the Lin correlation coefficient ρ_c is defined as:

$$\rho_c = \frac{2\rho\sigma_x\sigma_y}{\sigma_x^2 + \sigma_y^2 + (\mu_x - \mu_y)^2}; \tag{61}$$

where ρ is the Pearson correlation coefficient.

Figures 22 and 23 show maps of the Lin correlation coefficient values calculated comparing the displacements associated with IC1 and IC3 in the east, north, and vertical components, with hydrological loading displacement values estimated from the ERA-interim and GLDAS models, respectively. The Lin concordance correlation coefficient varies between -1 and 1, with values of 1 denoting perfect concordance and -1 discordance, while a value of 0 denotes complete absence of correlation. The vertical seasonal displacements associated with IC1 are in good agreement with GLDAS and ERA-interim models, both in terms of phase and amplitude, whereas the agreement in the horizontal components is poorer. Figure 20 shows the vertical hydrological loading displacements calculated from the ERA-interim model and the vertical displacements associated with IC1 for a few sites of the study region that are also influenced by the IC2 hydrological signal (see Figure 15).

As regards IC3, both ERA-interim and GLDAS modeled displacements show a better agreement in the north component than the east one (Figures 22 and 23). The displacements obtained by summing IC1 and IC3 show a slight improvement of the agreement with the modeled displacements (see Figures 22 and 23), suggesting that also horizontal seasonal displacements are associated with surface hydrological loading.

4.3 Time-variable ground deformation associated with IC2

Figure 17 shows the spatial response of IC2 only at sites having a SNR >1. Comparing Figure 17 and Figure 15, it is clear that vertical components associated with IC2 are above the noise level

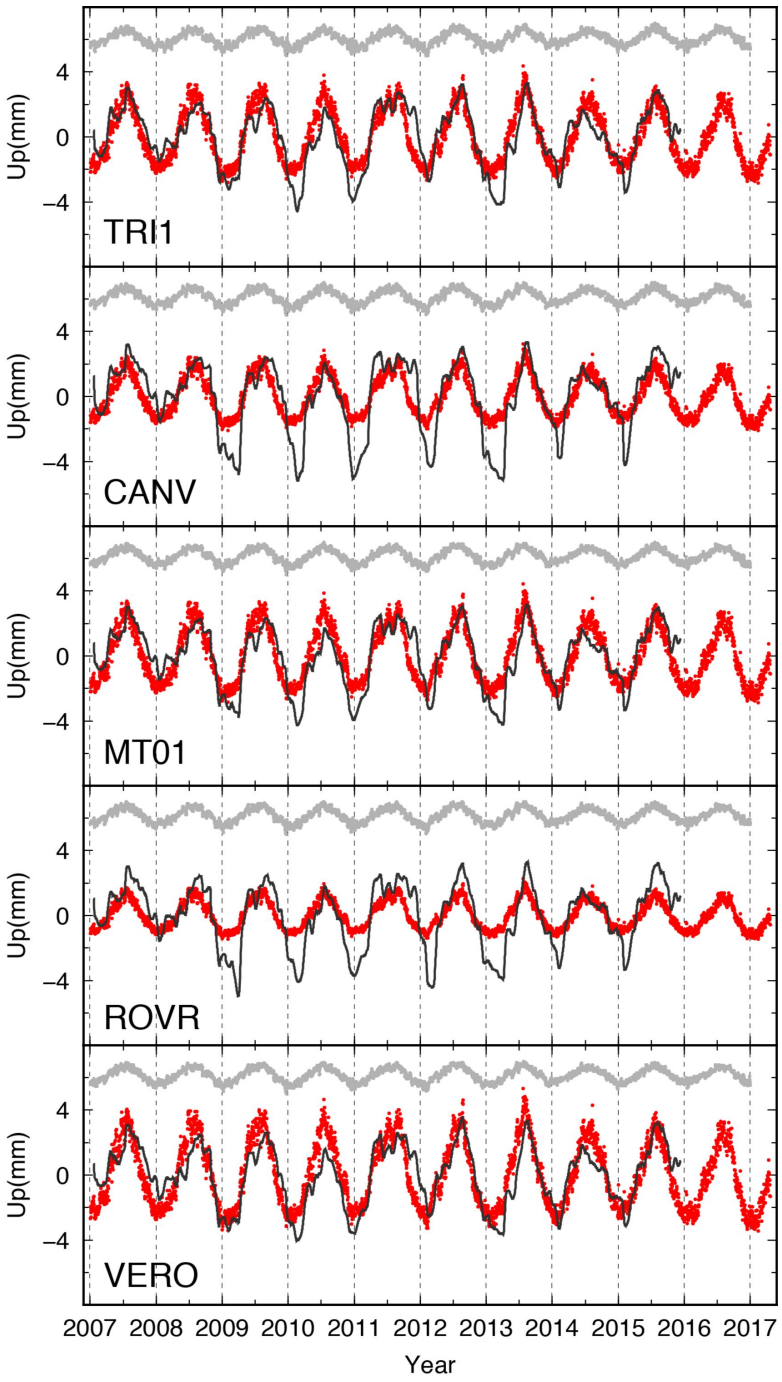

Figure 20: Vertical displacements associated with IC1 (in red) and corresponding surface hydrological loading displacements (black lines) estimated from the ERA-interim (European Centre for Medium-Range Weather Forecasts, ECMWF reanalysis) model for a few stations in the study region. In gray the normalized temperature variations at each station from the E-OBS (Haylock *et al.*, 2008) daily gridded observational data set.

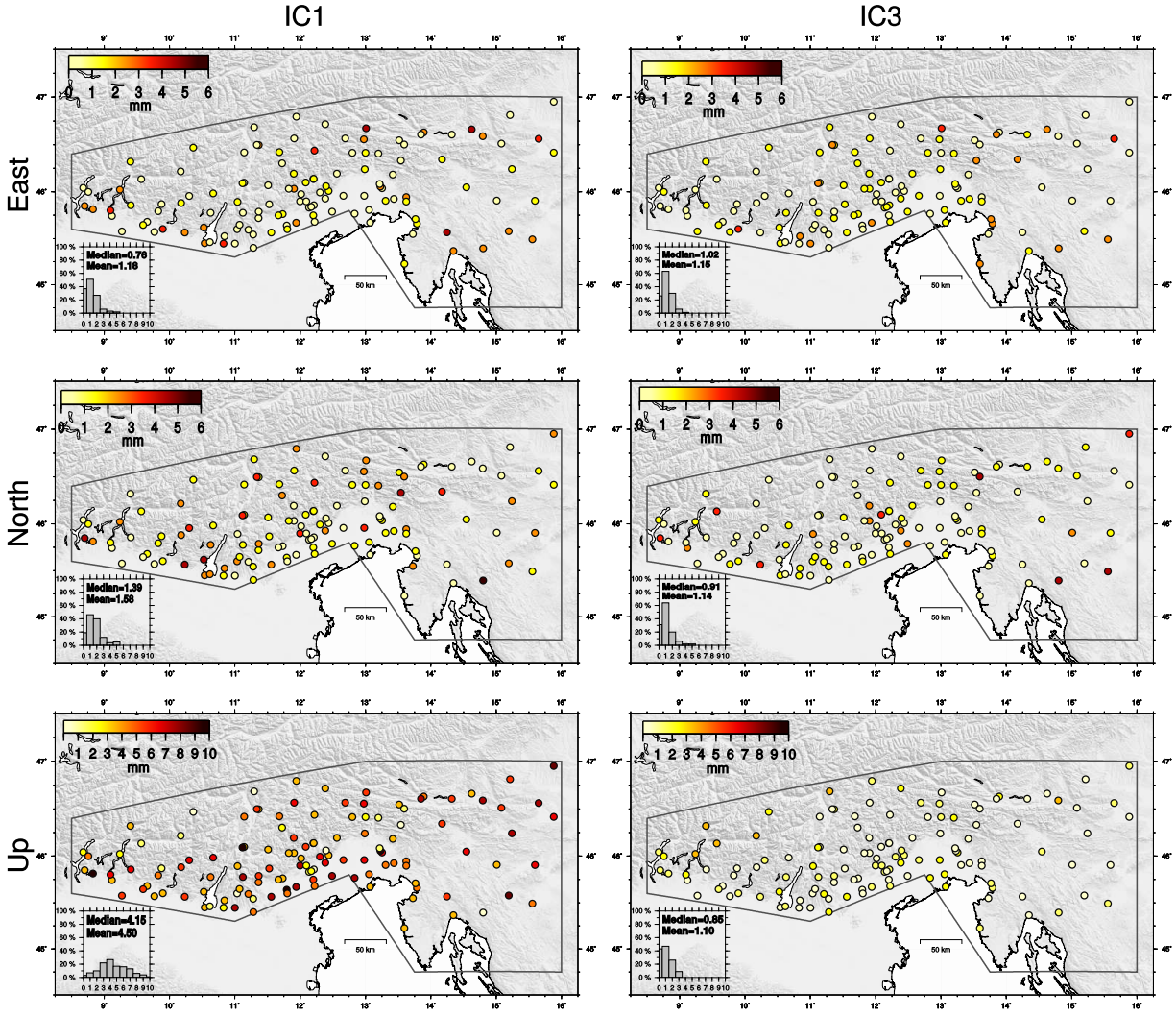

Figure 21: Map views of the amplitudes (color circles) of seasonal signals (IC1 and IC3) in the east, north and vertical components. The histograms show the frequency distribution of the values, with mean and median values in mm.

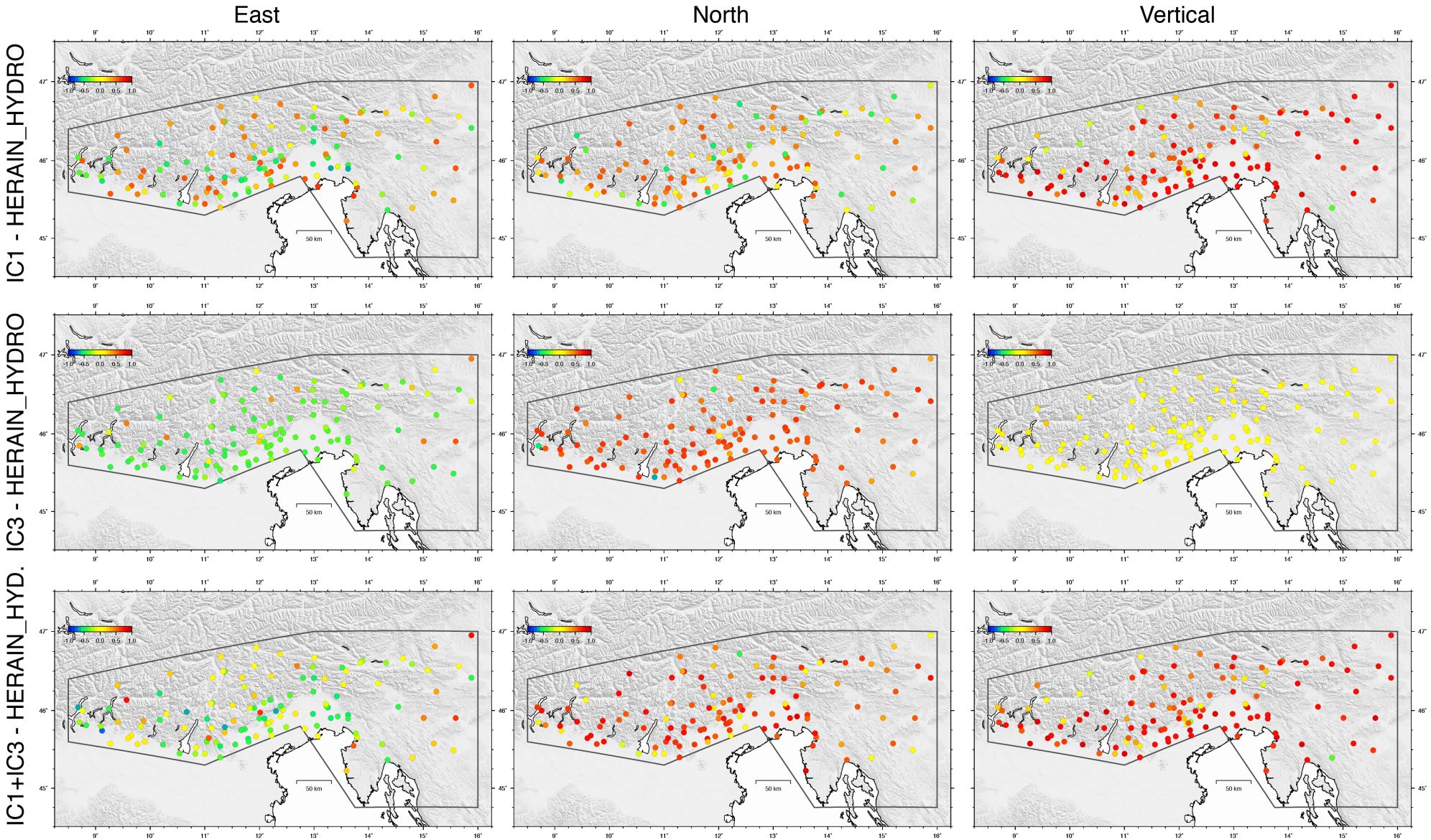

Figure 22: Map views of the Lin concordance correlation coefficient (colored circles), with values between -1 (blue) and +1 (red), obtained comparing the displacements associated with IC1, IC3 and IC1+IC3, for the east, north and vertical components, with displacements due to the redistribution of fluids at the Earth's surface estimated using the ERA-interim global reanalysis model provided by http://loading.u-strasbg.fr.

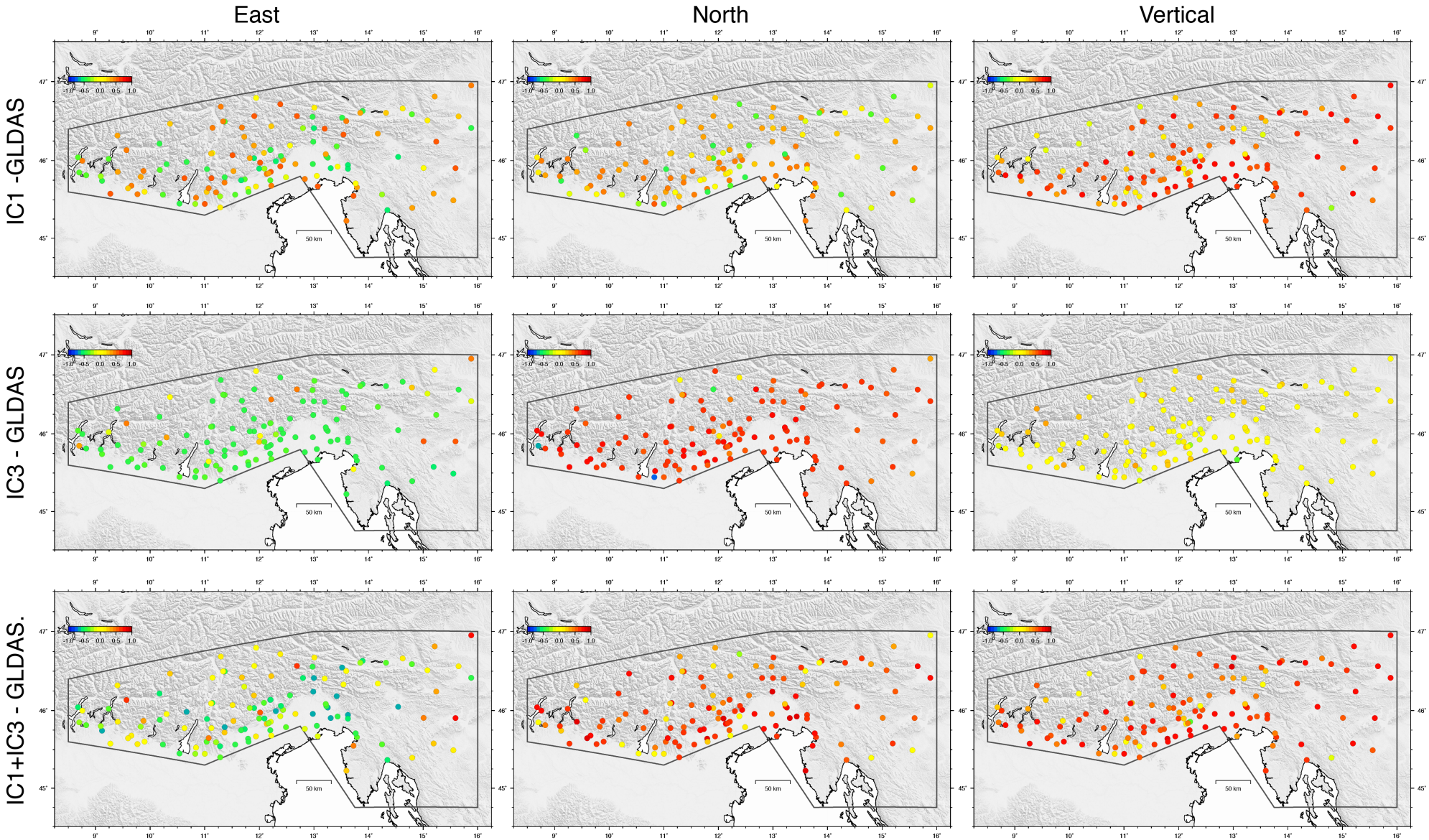

Figure 23: Map views of the Lin concordance correlation coefficient (colored circles), with values between -1 (blue) and +1 (red), obtained comparing the displacements associated with IC1, IC3 and IC1+IC3, for the east, north and vertical components, with displacements due to the redistribution of fluids at the Earth's surface estimated using the GLDAS global reanalysis model provided by http://loading.u-strasbg.fr

only at a few sites, and for this reason here we focus on the horizontal deformation signal. For IC2 the largest horizontal spatial responses are found at GPS sites located in three sectors of the study region: the Lessini Mountains (area 1 in Figure 17), the Venetian sector of the ESA fold-and-thrust belt, across the Monte Grappa Anticline, (area 2 of Figure 17) and the northern Dinarides (area 3 of Figure 17), across part of the Classical Karst. It is worth recalling that, being U and S time independent, if V increases (or decreases) between two epochs, the total displacement at a given GPS station between these two epochs will be in the same (or opposite) direction with respect to the green arrows (U vectors) in Figure 17. For example, focusing on the area 2, if we consider the two time intervals where V2 shows large variations, from mid-September to end of December 2010 and from January 2011 to end of April 2012 (T1 and T2 shown in gray tones in Figure 14), in Figure 17 the stations pointing toward SE (e.g., stations CANV, TAMB, VITT, MGRD, VALX, and MT03) move southeastward during T1 and then, on average during T2, toward NW (e.g., stations MAVE, FELT, BRSE, BL01, and BLNO), whereas the stations pointing toward NW move northwestward during T1 and then, on average during T2, toward SE. For the T1, T3, T2 and T4 time intervals the cumulative horizontal displacements of GPS sites in area 2 are shown in Figures 24A and 24B, respectively. Excluding CANV, the largest displacements are of the order of $\sim$8 mm. The uncertainties on the cumulative displacement are calculated as the square root of the squared sum of the uncertainties at the two epochs T1 and T2 (see Appendix A), consistent with the idea that the uncertainties at two different epochs are independent and thus uncorrelated.

A similar behavior, with sites moving alternatively in the opposite directions, is found in the Lessini Mountains (area 1) and in the northern Dinarides (area 3), resulting in a sequence of contractional and extensional deformation associated with the IC2 signal in the three areas. We estimated the temporal evolution of the horizontal strain associated with IC2 using the *analyze_strain* program of the QOCA software (http://qoca.jpl.nasa.gov) applied to the displacement time series associated with IC2 (green lines in Figure 18) for three polygonal areas shown with red lines in Figure 17. The red arrows in Figure 17 show the principal strain directions computed in the three areas with arrows length referring to 2011.0, when strain values are the largest. It is worth considering that the strain axes associated with this signal are oriented consistently with strain rate axes estimated from GPS velocities for long-term tectonic deformation (Figure 5 of Serpelloni *et al.*, 2016). We analyzed the 90-m resolution Shuttle Radar Topography Mission (*http://www2.jpl.nasa.gov/srtm*) digital elevation model to characterize the length and orientation of lineaments from topography using the TECLINES software (Rahnama and Gloaguen, 2014a, 2014b). The rose diagrams in Figure 17 show the preferred orientations of these lineaments in the three areas where the spatial response of IC2 is high (dashed boxes in Figure 17). In area 3 lineaments are oriented parallel to the main Dinaric faults, a major active right-lateral strike-slip fault system (Serpelloni *et al.*, 2016). In area 2 lineaments are mainly oriented parallel to the mountain front, where a SW-NE striking active fold-and-thrust-belt is present (Serpelloni *et al.*, 2016). In area 1 there are two different groups of lineaments: one, NW-SE oriented, parallel to Schio-Vicenza fault (see Figure 13) and the other one, NE-SW oriented, parallel to the ESA front (as in area 2). The principal strain axes associated with IC2 (red arrows in Figure 17) are normal to the preferred orientations of the lineaments from topography in the three areas. In the area 1 the displacements associated with IC2 at the five stations considered describe two directions of deformation acting about normal to the two main lineament orientations, but the NW-SE oriented strain is smaller and with larger uncertainties.

Focusing on area 2, where the density of GPS sites is higher, the time series of the dilatational strain (Figure 24C) displays a sequence of extensional (positive slopes) and contractional (negative slopes) phases occurring across the Monte Grappa-Cesen Anticline (Figure 17). In the computation of the strain time series for area 2 we have excluded CANV, considering that its larger IC2 spatial response and associated displacements are likely amplified by local topographic/geomorphological effects (Devoti *et al.*, 2016). For areas 1 and 3 the time evolution of dilatational strains is the same, but acting along different directions, as shown in Figure 17. Figure 24C shows that there are two peaks of positive dilatational strain values (with values > 0.15 microstrain in area 2), at the end of December 2010 and February 2014, reached through rapid, with an average constant positive rate, increase of dilatational strains, followed by a slower decreasing phase, whose average rate magnitude is decaying with time. The minima (around 0.08 microstrain) occur in autumn 2017, spring/summer 2012 and autumn 2015. It is worth considering that the positive dilatation rate calculated during T1, shown in Figure 24C, is 0.69 microstrain/year, which is an order of magnitude greater than the rates of tectonic deformation from GPS velocities in this area (in the

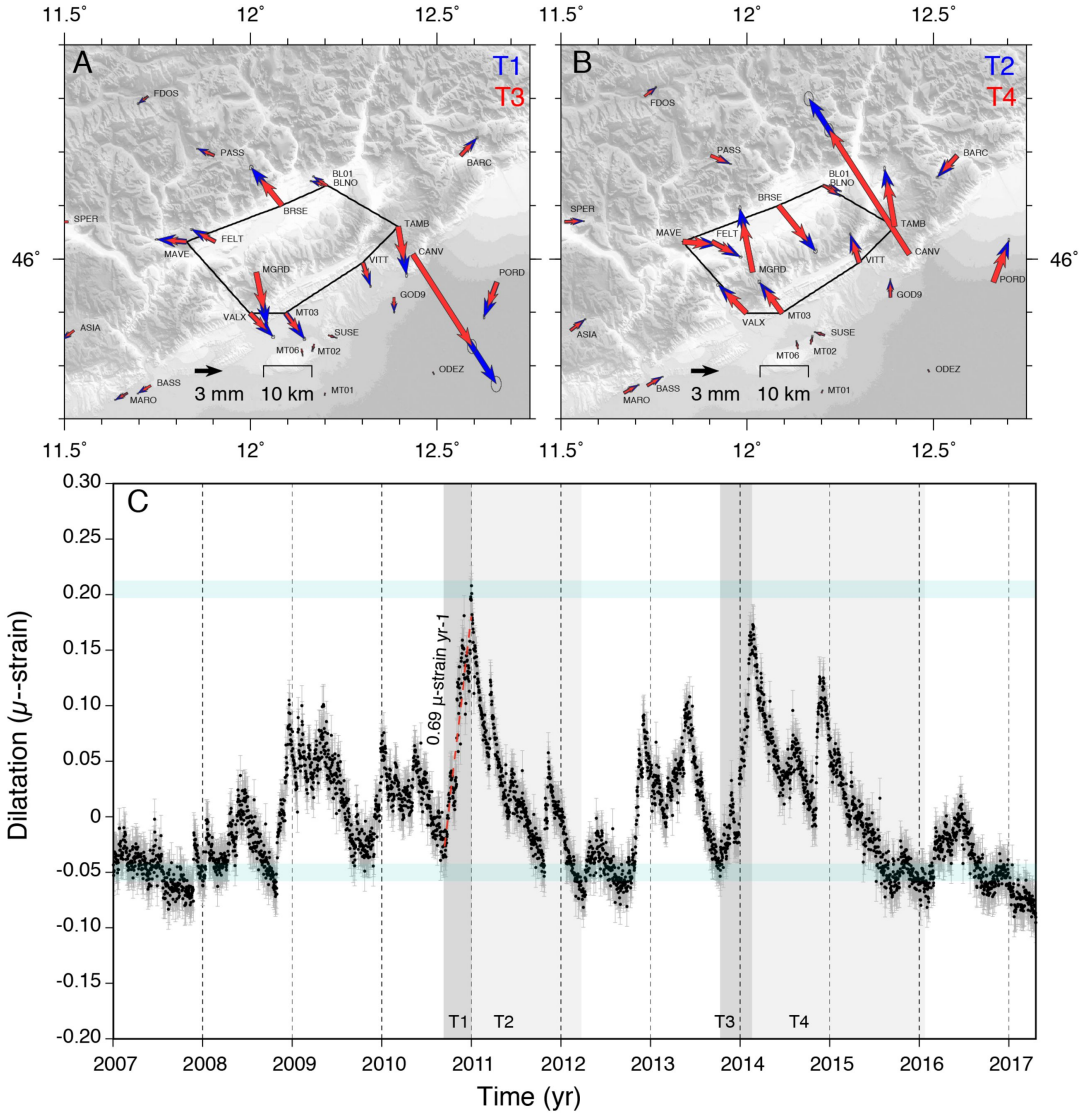

Figure 24: (A, B) Horizontal displacements associated with the IC2 signal in the T1 and T2 (blue arrows) and T3 and T4 (red arrows) time intervals, corresponding to the two periods where larger variations of V2 are present. (C) Time series of the dilatational strain (with 1 uncertainty error bars) obtained from the displacements time series associated with IC2 of stations included in the black polygon shown in (A) and (B). The gray areas indicate the two time intervals (T1 and T2) considered in (A) and (B). The dashed red lines and numbers show the linear fit of the dilatation time series and dilatation rates estimated in T1.

.

range of 0.01-0.06 microstrain/year; Danesi *et al.*, 2015).

Appendix A Error associated with the displacement reconstructed by the ICs

The uncertainties on the three components of the displacement reconstructed by the ICs are calculated following Gualandi, *et al.* (2016). We have shown in chapter 3 that the observed data X are reconstructed through equation 51, where the element x_{ij} of the matrix X can be written as:

$$x_{jt}^{ICA} = \sum_{i=1}^{L} x_{jt}^{IC_i} = \sum_{i=1}^{L} x_{jti} = \sum_{i=1}^{L} u_{ji} s_{ii} v_{it} \tag{A.1}$$

where $j = 1, ..., M$ is the number of time series, $t = 1, ..., T$ the number of epochs, and L the number of independent components used to approximate the original data.

To compute the uncertainties, it is assumed that the data are not correlated both spatially and temporally. In general, this is not true, since colored noise is present in daily position GPS time series (e.g. Mao *et al.*, 1999; Williams, 2003), and correlations exist between the position along the three directions at a specified site. Anyway, this remain a good first approximation, even if it may lead to an underestimation of the uncertainties.

It follows that the position calculated at a certain epoch and a given site does not depend on the uncertainties calculated at a different time and the same site or at a different site and the same time. Furthermore, possible correlations between the position at a given site along different directions (East, North, and Vertical) are neglected. Then, the elements of the vector representing a given IC spatial distribution (u_{ij}) and temporal evolution (v_{it}) are normally distributed around their best value and independent to the other elements of the same IC. Consequently, the variance of x_{jt}^{ICA} is given by:

$$var\left(x_{jt}^{ICA}\right) = var\left(\sum_{i=1}^{L} u_{ji} s_{ii} v_{it}\right) = \sum_{i=1}^{L} var\left(u_{ji} s_{ii} v_{it}\right) \tag{A.2}$$

As a result, assuming that the elements s_{ii} of the weighting diagonal matrix are composed just by scalar error-less quantities, the variance of the contribution of each independent component can be computed following Taylor (1982). For the i-th IC, it is:

$$var\left(x_{jti}\right) = var\left(u_{ji} s_{ii} v_{it}\right) = s_{ii}^2 \left[var(u_{ji})var(v_{it}) + var(u_{ji}E[v_{jt}]^2 + E[u_{ji}]^2 var(v_{jt})\right] \tag{A.3}$$

The expected value and the variance for each component are a direct result of the vbICA analysis, which is obtained from the dispersion of the actual data. Thus, the variance of the reconstructed displacement can be calculated, and the corresponding uncertainty will be the square root of the variance, i.e. the standard deviation.

In the computation of the uncertainties, only the actual data are taken into account and the differences between the uncertainties on two different points belonging to the dataset are not considered. This means that to the missing data is associated with a weight 0, while the others are weighted equally.

Appendix B Computation of the time lag between IC1 and IC3, and its uncertainty

The time lag between IC1 and IC3 and its uncertainty has been computed by performing the bootstrap statistical method proposed by Moore *et al.* (2003). According to this technique, we selected a random distribution of the two input vectors (V1 and V3), the same for both, and computed the cross correlation between the two time series by using the following formula:

$$c = \frac{1}{N-k-1} \frac{\sum_{i=1}^{N-k} \left(x_i - \bar{x}\right)\left(y_{i+k} - \bar{y}\right)}{\sqrt{\sigma_x \sigma_y}} \tag{B.1}$$

where c is the cross-correlation, k is the time lag, x_n and y_n are the n-th elements, N the total number of elements, $\bar{x}, \bar{y}$ the mean and σ_x, σ_y the standard deviations of the two time series.

By using equation B.1 for different values of k, it is possible to estimate the time lag that maximizes the correlation, that we interpret as the time lag between the two time series.

This process has been done 100 times, i.e. we computed the time-lag choosing 100 different random re-samplings of the input vectors. It is then constructed a distribution in time lag, where the mean represents the *best value*, i.e. the chosen time lag value between IC1 and IC3. The uncertainty of the time lag is finally estimated as the standard deviation of the distribution.

5 Interpretation of the temporal dependence of IC2

5.1 Precipitation data and IC2

In this section we compare the time evolution of the deformation signal associated with IC2 (i.e., V2) with precipitation. We made use of gridded precipitation data, in the form of daily mean values (in mm) for $0.25° \times 0.25°$ resolution cells, obtained from the National Aeronautics and Space Administration precipitation measurement missions (https://pmm.nasa.gov), consisting on satellites carrying advanced radar/radiometer systems to measure global precipitation from space. In particular, we used data from the Tropical Rainfall Measuring Mission (TRMM), integrated for 2017 by data from the Global Precipitation Measurements (GPM) satellite mission (Goddard Earth Sciences Data and Information Services Center (2016)).

We focus the analysis on the three areas where the spatial response of IC2 is larger (see previous chapter), using the grid cells shown in Figure 25A. We perform this analysis using both the original precipitation values (P) and the precipitation corrected for the evapotranspiration (ET) component, P-ET. It is important to emphasize that real ET is difficult to measure or estimate (Villagra *et al.*, 1995), since it depends on different controlling factors, among which the most important ones are temperature and humidity of the air, water condition of the soil, land use and pedological characteristic of the catchment. Moreover, it is worth considering that the high permeability of rocks outcropping in karst regions favors a rapid infiltration; thus, models of ET applied in these areas may be inaccurate. To evaluate the influence of ET, we used daily ET values calculated from the ECMWF meteorological model (Dee *et al.*, 2011), which are provided with the same temporal and spatial resolution of the gridded precipitation data.

We found no correlation between V2 and the daily precipitation. The correlation between V2 and the cumulative (for the 2007-2017 time span considered) and de-trended precipitation curve for the three areas is also low (see Figure 26 and CUM_DET in Table 4). Computing the cross correlation, we found a slight improvement of the correlation (CUM_DET_CC in Table 5), with the precipitation curve anticipating V2 of 9 to 30 days (TL in Table 5). Considering P-ET slightly improves both the correlation and cross-correlation values with V2, with correlation coefficients between 0.3 and 0.5 (PET_CUM_DET in Table 4). We then compared V2 with curves of cumulated precipitation over different time windows. In particular, for each area and for each day we computed cumulated precipitation curves by summing the precipitation occurred during a certain number of days before. The correlation coefficient between V2 and the curve of cumulative precipitation depends on the number of days of cumulated precipitation (solid lines in Figure 25B), with the highest correlation ($\sim$0.7) found using 250, 300, and 240 days for areas 1, 2, and 3, respectively. Panels (C)-(E) in Figure 25 compare the corresponding cumulative precipitation curves (solid lines) with V2. Using P-ET provides an improvement of the correlation coefficient, which is maximized using 150, 200, and 220 days of cumulated P-ET values (see last column of Table 4).

5.1.1 Comparison between local pluviometer and gridded data

The study region is covered by three different gridded datasets of meteo-climatic data (including air temperature, pressure and precipitation):
1) the E-OBS gridded values from ECA&D data (Haylock *et al.*, 2008);
2) the Alpine Precipitation Grid Dataset from the Federal Office of Meteorology and Climatology MeteoSwiss (*http://www.euro4m.eu/datasets.html*);
3) the Tropical Rainfall Measuring Mission (TRMM) from NASA (*https://trmm.gsfc.nasa.gov*).

While the TRMM dataset is based on satellite data, providing intensive and globally distributed observations, the first two gridded datasets are based on ground pluviometric stations, with the second one based on a much larger and denser network of stations. However, the Alpine Precipitation Grid Dataset currently covers the 1971-2008, so it is only very partially covering the time-period studied in this work.

We have first compared the precipitation values in the three gridded datasets for an area between longitude 10.5-16°E and latitude 45-47°N. Figure 27 highlights the agreement between the three gridded datasets, showing that the correlation between the curves of cumulated precipitation obtained from the three gridded datasets remain high (>0.8), independently from the number of days used to calculate the cumulative precipitation. Figure 28 displays the curves of cumulative precipitation obtained considering 240 days (the number of days that gives the highest correlation values in Figure 27) and the same area as in Figure 27 using the three gridded datasets, showing

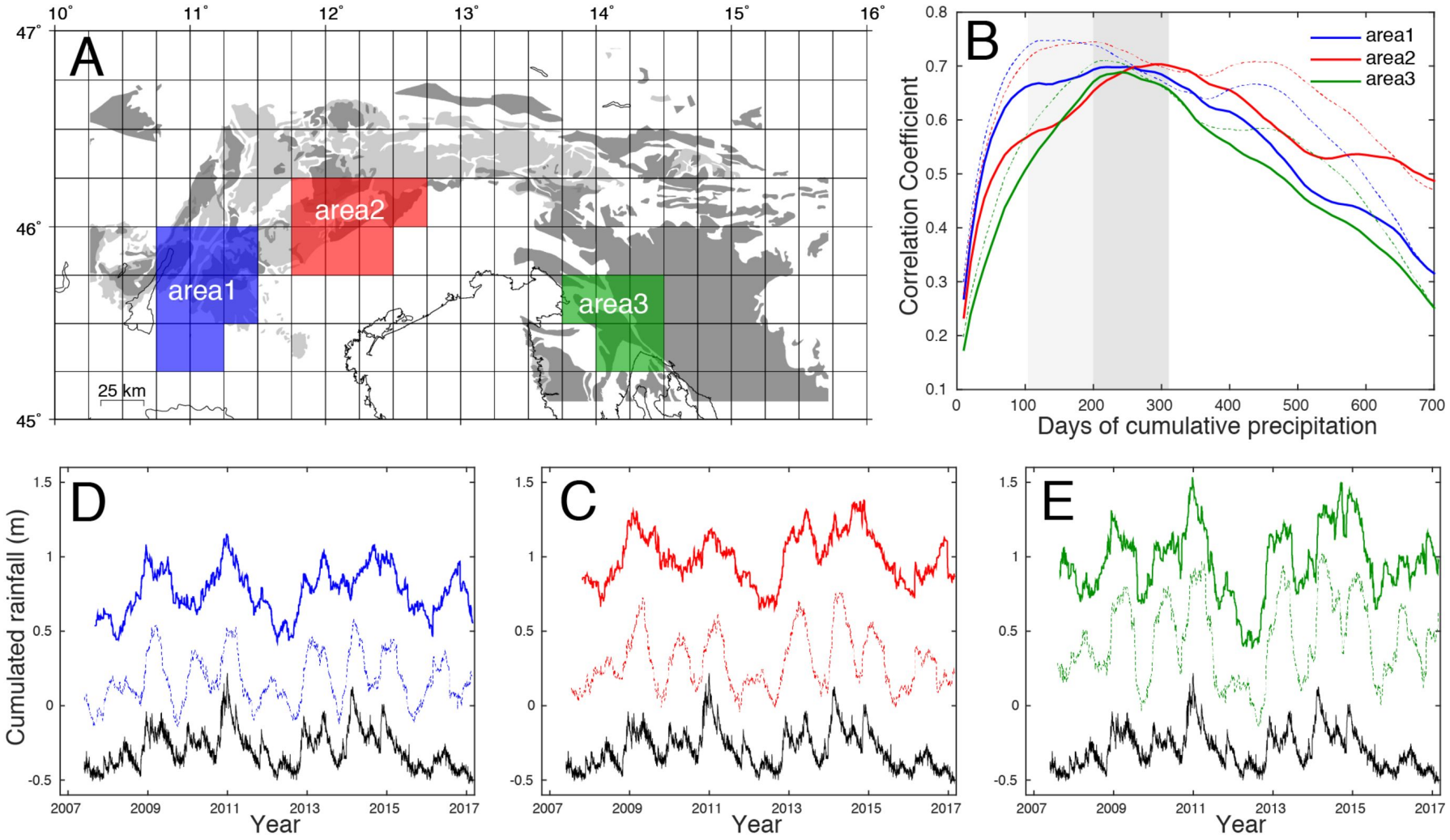

Figure 25: (A) The $0.25° \times 0.25°$ grid of the Tropical Rainfall Measuring Mission-Global Precipitation Measurements precipitation data, where the blue, red, and green regions are the sectors used to compute the curves of cumulative precipitation for the three areas in (B). (B) Correlation coefficient between V2 and the curves of cumulated precipitation as a function of the number of days used to calculate cumulative precipitation values for the three areas shown in (A). Solid and dashed lines refer to curves obtained using precipitation, P, and P minus evapotranspiration (ET), respectively. (C-E) V2 (in black) and the curves of cumulative precipitation obtained using the number of days providing the maximum value of the correlation coefficient (B) for the three areas in (A) using precipitation, P (solid lines), and P-ET (dashed lines).

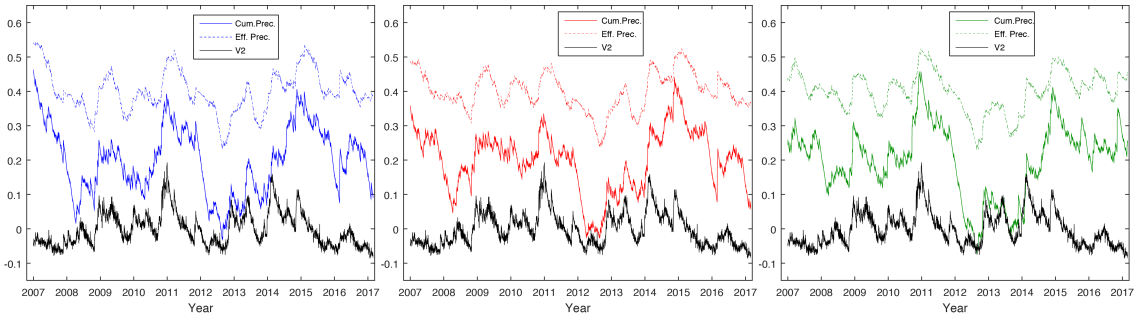

Figure 26: Comparison between V2 (in black) and curves of cumulative and de-trended precipitation accounting (dashed lines) or not (solid lines) for the evapotranspiration (ET) component.

a substantial agreement between the datasets.

We have then compared E-OBS precipitation data with data from pluviometric stations in the Southern Alps. Figure 29 displays the correlation coefficient calculated comparing the cumulated precipitation curves obtained from the measurements at three pluviometric stations located near the GPS stations of CANV, BOSC and TAMB in area 2 (see Figure 17), and the precipitation values in the corresponding cells from the E-OBS dataset, showing that the correlation is overall high independently from the number of days used to calculate the cumulative precipitation.

As its can be seen from Figure 30, considering a number of 240 days of cumulated precipitation, the correlation between V2 and the precipitation data measured at pluviometric stations near the three GPS stations is overall high.

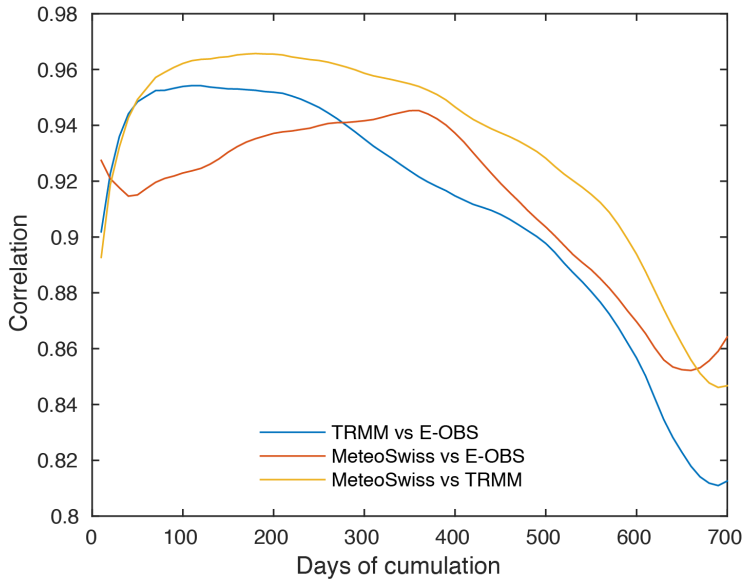

Figure 27: Correlation between the curves of cumulated precipitation as a function of the number of days used to calculate the cumulative precipitation value, obtained using the three different gridded datasets for the area between longitude 10.5-16°E and latitude 45-47°N.

5.2 From precipitation analysis to hydrological modeling

In section 5.1 we highlighted the correlation between an hydrological (precipitation-evaporation) signal with a deformation signal. Analyzing precipitation data does not require long computation times or any complicate modeling, then, since global gridded datasets of precipitation and evapotranspiration are available, comparisons with GPS signals can be replicated in every region of the world where geodetic data are present.

If the deformation signal is caused by water level variations in karst conduits or in the saturated zone (section 2.3.2), as assumed by other studies in similar environments (Devoti *et al.*, 2015, Silverii

Area	CUM_DET	PET_CUM_DET	CUM_VW	N.Days	PET_CUM_VW	N.days
1	0.2677	0.3732	0.6985	250	0.8493	150
2	0.4143	0.5023	0.7034	300	0.746	200
3	0.2592	0.3252	0.6888	240	0.7111	220

Table 4: Results of the correlation analyses between V2 and precipitation. Legend. CUM_DET: correlation coefficient between V2 and de-trended cumulative precipitation (estimated over the entire 2007-2017 time span); PET_CUM_DET:correlation coefficient between V2 and de-trended cumulative P-ET (estimated over the entire time span); CUM_VW: correlation coefficient between V2 and the cumulated precipitation curve obtained by using the number of days (N.Days) that maximize the correlation; PET_CUM_VW: same as CUM_VW except that P-ET is used.

Area	CUM_DET_CC	TL (days)	PET_CUM_DET_CC	TL_E (days)
1	0.2924	31	0.4051	25
2	0.416	9	0.5134	14
3	0.2631	9	0.3338	11

Table 5: Results of the cross-correlation analyses between V2 and precipitation.
Legend. CUM_DET_CC: cross correlation between V2 and de-trended cumulative P-ET: TL: time lag between V2 and de-trended cumulative P-ET curve (where CUM_DET_CC anticipate V2); TL_E: time lag between V2 and de-trended cumulative P-ET curve (where PET_CUM_DET_CC anticipate V2).

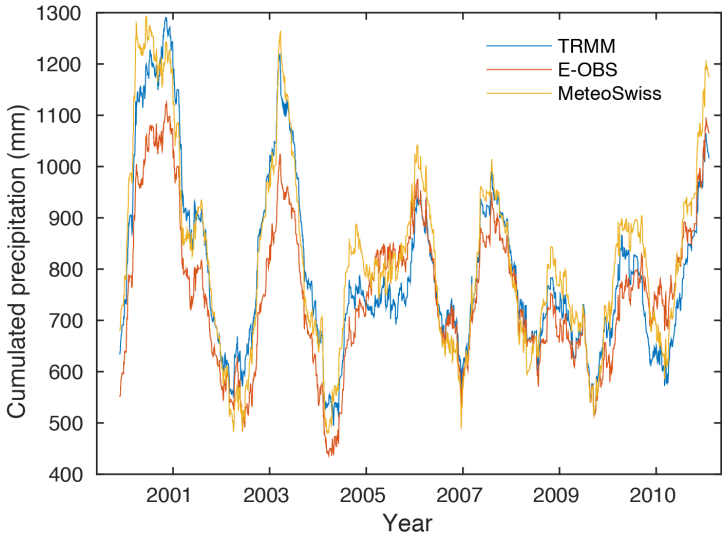

Figure 28: Curves of cumulated precipitation obtained considering 240 days of cumulative precipitation for the three different gridded datasets available in the area between longitude 10.5-16°E and latitude 45-47°N (same as Figure 27)

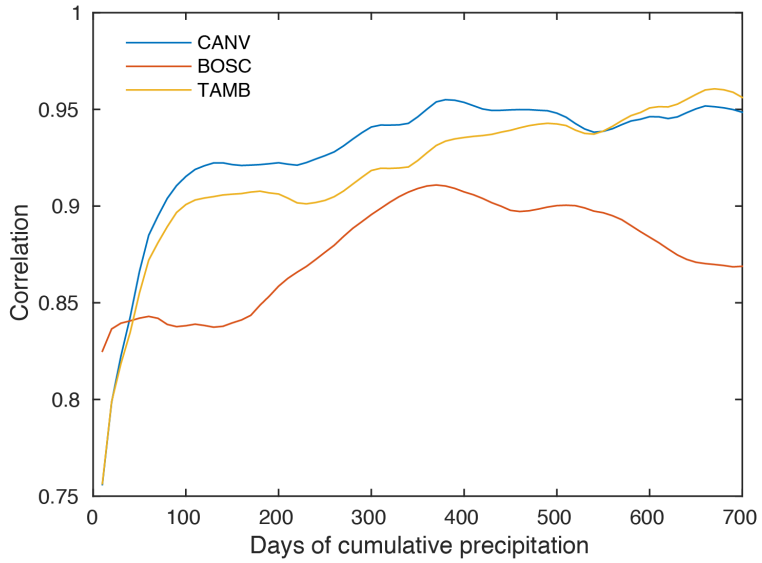

Figure 29: Correlation between the curves of cumulative precipitation as a function of the number of days considered to calculate the cumulative precipitation value obtained from data recorded at the single pluviometric stations located near three GPS stations used in this work (CANV in blue, BOSC in red and TAMB in yellow) and from the corresponding E-OBS grid cells where the pluviometers are located.

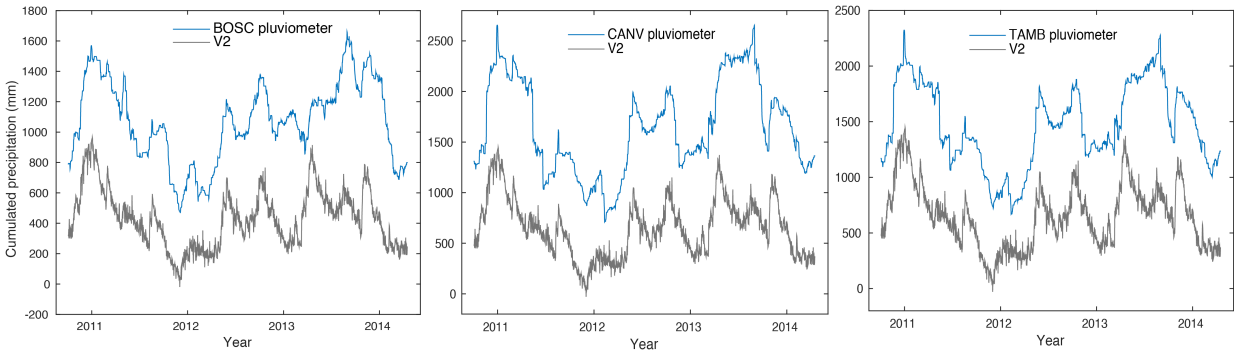

Figure 30: Comparison between V2 (in gray) and the curve of cumulated precipitation obtained considering 240 days of cumulative data for the pluviometers located near the GPS stations BOSC (left), CANV (center) and TAMB (right), in blue.

et al., 2016, Jacob *et al.*, 2010, Gilli *et al.*, 2010), it becomes crucial to quantify the water variations in karst systems. This quantity can be computed by analyzing the water storage variations of hydrological basins and looking only to precipitation, even if corrected by evapotranspiration, is limitative. In fact, water storage variations in time of an hydrological basin can be computed as:

$$\frac{dS}{dt} = P - E - Q; \tag{63}$$

where S, P, E and Q respectively stand for water storage, precipitation, actual evapotranspiration and river runoff. On a hydrological point of view, river runoff defines the response of the catchment to boundary conditions (P, E) and represents by essence the behavior of the main storage compartments (surface, unsaturated zone, shallow and deep saturated zones in section 2.3.2), at the same spatial scales that geodetic data allow investigating.

Even if the equation for water storage variations is very simple, using it directly can lead to misinterpretations. In fact, real evapotranspiration data are almost impossible to compute, especially in regions where the altitude and vegetation cover is variable. Furthermore, this equation assumes that the precipitation water falling in a catchment basin defined by the topography is drained by a river, neglecting possible exchanges with other basins. This last assumption for karst areas can be an oversimplification, because of the presence of subsurface flows that are completely independent from the topography. Finally, long river flow time series are often hard to be got, so that the storage could be computed only for few years. For these reasons we prefer to use empirical hydrological models (see section 2.4) in order to evaluate the water storage variations of a basin containing karst systems.

5.3 Calibration of rainfall-runoff models

In order to obtain the best possible modeling of a hydrological basin, and then the most reliable estimates of water storage variations, it is necessary to minimize the discrepancies between the modeled and the observed river flows. This is performed by accurately selecting the values of the internal parameters of the model, through a process called calibration. This consists in arbitrarily defining their values and then letting them vary in a defined interval. The best set of parameters values is then set by using the MATLAB function *lsqcurvefit*, which performs a non-linear least squares regression. It is worth noting that it is possible to calibrate the parameters of the model by considering the logarithm (base 10) or the square root of the discharge data, instead of the data themselves. The discharge variations are over two orders of magnitude, giving to high flows a predominant role. Since in this study we are interested in defining the mass balance in all conditions, we considered the logarithm of the data.

For the models calibration in the area of our interest, which is the south region of area 2 of Figure 17, we defined three hydrological basins by using the drainage direction maps available on *www.hydrosheds.org/page/availability* and the flow rates of the Piave river at Belluno and Segusino and the flow of the Cordevole river at Ponte Mas (Figure 31). These data are available since 01/01/2010 for the Piave and since 30/10/2010 for the Cordevole.

Hydrological basins are defined considering only the topography of the area, which may seem to be incorrect considering that in karst systems subsurface flows can be independent from the topography. Anyway, we will show that the models used takes into account the possibility of water exchanges among different basins, i.e. the basin is not defined as a close system.

5.3.1 Input data for the models

Initially, the input data of precipitation were computed by using the daily TRMM dataset (see section 5.1), whose spatial resolution is 0.25° x 0.25°. Since the basins we identified are relatively small compared with this spatial resolution, we made an interpolation to obtain 0.125° x 0.125°.

Temperature data used are from the E-Obs gridded dataset (same dataset used in 5.1.1 for precipitation), which has the same spatial and temporal resolution of TRMM, then also in this case we used an interpolation to improve the spatial resolution to 0.125° x 0.125°.

By using cells of this size, we observe that the number of the cells centers inside the basins is 6 for the Cordevole, 14 for Piave at Belluno and 24 for Piave at Segusino, which is the largest and includes the other two basins. Since the models we consider do not take into account the spatial variability of a basin, we always consider the spatial mean of these quantities.

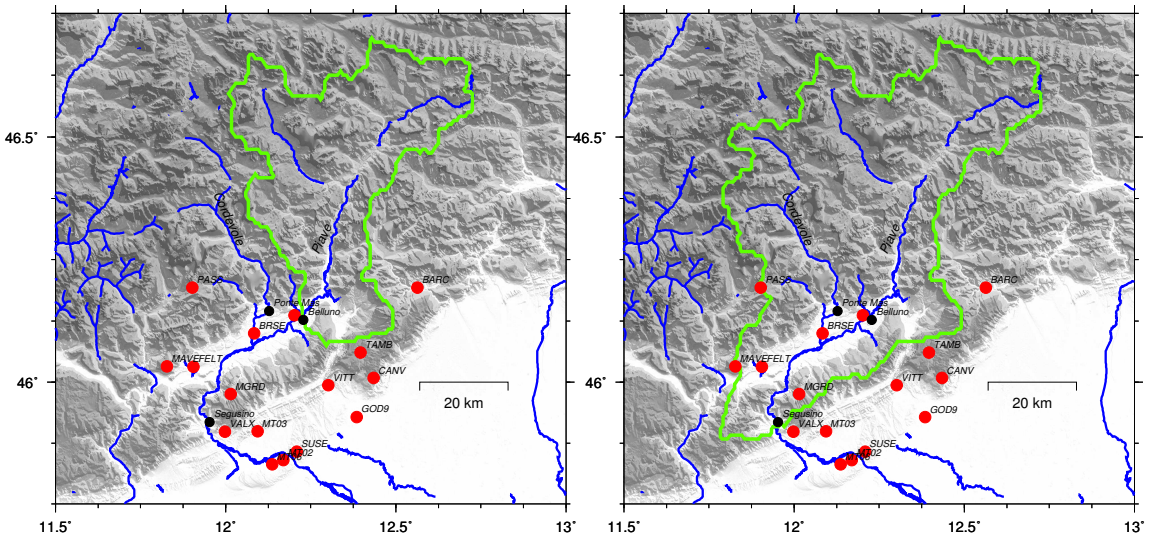

(a) Piave at Belluno basin.

(b) Piave at Segusino basin.

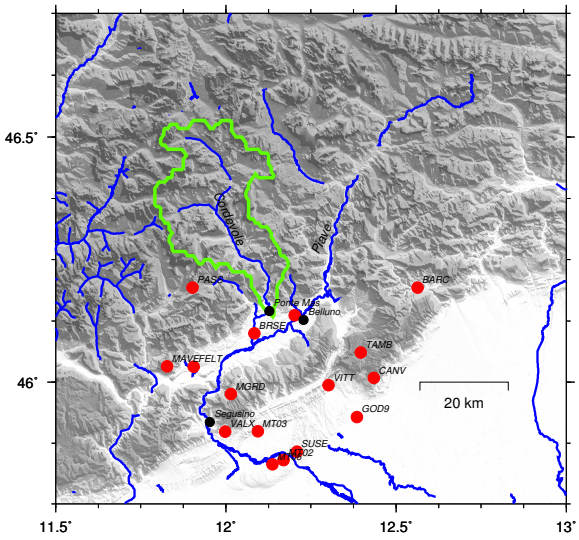

(c) Cordevole at Ponte Mas basin.

Figure 31: The catchment basins (green lines) where we applied the hydrological models. The red dots represent the position of GPS stations, while the black dots the position of river flow measurements.

The spatial resolution of temperature and precipitation gridded datasets is not very good, considering the dimension of the basins, then we decided to compute mean precipitation and temperature using also data from in-situ measurements. The pluviometers that are inside or very close to the edges of the Piave at Segusino basin are 54, while the temperature measurement stations are 55. Data are available from 2010 to present.

Daily mean precipitation and temperature from in-situ measurements We had to face the problem of how to compute the mean daily temperature and precipitation considering in-situ measurements, which are not uniformly distributed, and then it is necessary to pay attention not to introduce any bias.

In areas where more than one measuring station is present, the methods generally employed to compute the mean of a meteorologic variable are: *arithmetic average* method, *weighing mean* (or *Thiessen polygon*) method and *isohyetal* method.

In the following we discuss in detail the first two methods for the case of the precipitation, keeping in mind that for the temperature computation the process is exactly the same.

The **Arithmetic average method** is the simplest method for computing the average precipitation over a basin. As the name suggests, the result is obtained simply computing the mean of the precipitations recorded at different pluviometric stations of the basin. As a consequence, each station has the same weight in describing the data. This method gives good results only when the rain gauges are uniformly distributed over the area and the precipitation varies in a very regular manner. In our cases the pluviometers network is very dense but the station distribution not exactly uniform, moreover the variation of the precipitations is not regular; then we will compute the mean precipitation following another method.

The **Weighing mean method or Thiessen polygon method** allows us to take into account the fact that the precipitation is never uniform over the entire area of the basin, but varies in intensity and duration from place to place. Thus the precipitation recorded by each pluviometric station should be weighted according to the extension of the area it represents: the larger the area is, the more weight the pluviometer has.

This method consists in dividing the entire basin in Thiessen polygons, which are generated from a set of sample points, in our case the pluviometers. Each polygon has the property that any location inside it is closer to a specific pluviometer than any of the other sample points.

Assuming that inside (or very close to) the basin we are considering there are n pluviometers, the weighted mean precipitation (P_m) at certain time is computed as follows:

$$P_m = \frac{\sum_{i=1}^{n} p_i A_i}{\sum_{i=1}^{n} A_i} \tag{64}$$

Where p_i is the precipitation recorded by the i-th pluviometer and A_i the area of the polygon it represents. The time resolution of the data we are using is daily, then P_n is daily too.

This computation process can be complicated by the presence of missing data and by the fact that the calculus of polygon areas is not that easy.

As the reader may imagine, the shape of a river basin is very complicated and so the Thiessen polygons. Then, to compute the areas of Thiessen polygons, we build a grid with squared cells over the basin with a resolution of 2 km both in the N-S and E-W direction, and count how many grid cells points (at the corners of each cell) lie inside each polygon: the larger the polygon is the more points are inside it. In this way A_i in (64) becomes the number of points that are inside the i-th polygon (see for example Figure 32).

Finally, we observed that in the time series of the pluviometers there are some missing data. To avoid the problems that they may generate, at each time t we excluded the pluviometers with missing data and compute the weighted mean: then, at each time t, we also have to recompute the Thiessen polygons because they depend on the number and position of the active pluviometers. This process is very time consuming, but it is necessary to get the best possible quality for the data.

The **Isohyetal method** is the most complicated method that defines areas with the same mean precipitation amount by drawing isohyetal lines.

Because of the large number of both pluviometric and temperature stations, we decided to use the Thiessen polygon method to compute the daily mean precipitation and temperature of a basin, assuming that each station is really representative of the area defined by the corresponding polygon.

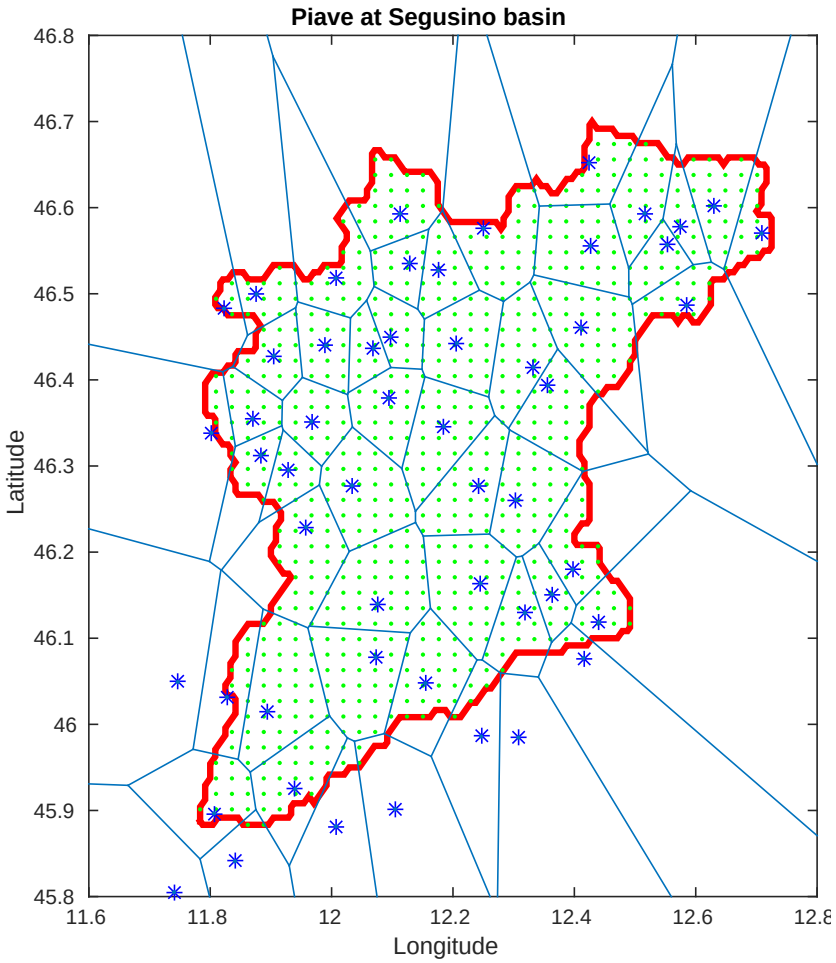

Figure 32: Piave at Segusino basin (red line). The blue stars represent the pluviometers that generate the Thiessen polygons (blue lines). The small green dots inside the basin are the grid points we used to compute A_i.

Potential evapotranspiration The Pennman-Moneith equation is widely considered a good way to compute potential evapotranspiration, anyway it needs a lot of input data that are hard to obtain. Then, we initially used a gridded monthly dataset provided by the University of East Anglia Climatic Research Unit (CRU, Jones and Harris, 2012) which computes the potential evapotranspiraion following the Pennman-Moneith method in a grid with resolution 0.5°x 0.5°, that we interpolated to get a resolution of 0.125°x 0.125°. The big disadvantage of this dataset is that it is monthly, so we had to do a temporal interpolation to get daily data. Furthermore, its spatial resolution is poor compared to the size of the basins.

In order to improve the quality of PET data, we looked to how other authors computed potential evapotranspiration as input for hydrological models. Oudin *et al.* (2005) discussed this problem in detail: they used 27 different PET formulas as input for hydrological models describing 308 catchments located in Australia, France and United States. The models used were GR4J, HBV0, IHAC, TOPMO. They evaluated the Nash-Sutcliffe efficiency (E) for each case, which is defined as:

$$E = 1 - \frac{\sum_{t=1}^{T} \left(Q_m^t - Q_0^t\right)^2}{\sum_{t=1}^{T} \left(Q_0^t - \bar{Q_0}\right)^2} \tag{65}$$

where $\bar{Q_0}$ is the mean of observed discharge; Q_m^t and Q_0^t are the modeled and observed discharge at time t.

Nash-Sutcliffe efficiency can range from -∞ to 1: the larger E is, the better the agreement between observed and modeled discharges becomes. The perfect match of modeled discharge to the observed data causes the numerator of the second part of (65) to be 0, then $E = 1$.

The authors created a ranking of the PET formulas that give the highest values of E and they focus on two formulas: Jensen-Haise (Jensen *et al.*, 1990) and McGuinness (McGuinness and Bordne, 1972) which are ranked 3rd and 1st, respectively. These PET models have the great advantage that they depend only on mean daily air temperature and extra-terrestrial radiation. They take the following generalized form:

$$\begin{cases} PE = \dfrac{R_e \left(T_a + K_2\right)}{\lambda \rho K_1} & \text{if } T_a + K_2 > 0 \quad (66a) \\ PE = 0 & \text{otherwise} \quad (66b) \end{cases}$$

where PE is the rate of potential evapotranspiration ($\frac{m}{day}$), R_e is extraterrestrial radiation ($\frac{MJ}{m^2 day}$), depending only on latitude and Julian day, λ is the latent heat flux (taken equal to 2.45 $\frac{MJ}{kg}$), ρ is the density of water ($\frac{kg}{m^3}$) and T_a is the mean daily air temperature ($°C$). K_1 ($°C$) and K_2 ($°C$) are constants to adjust over the catchment sample for each rainfall-runoff model. K_1 is the scaling factor and K_2 is the factor making it possible to vary the threshold for air temperature, i.e. the minimum value of air temperature for which PE is not zero. In order to adjust the two constants, the authors tested several values of K_1 and K_2 for each rainfall-runoff model and kept the association (K_1, K_2) that gives the best streamflow simulations over the catchment sample. In the Jensen-Haise and McGuinness models (K_1, K_2) are equal to (40, 0) and (68, 5), respectively. Finally, Oudin *et al.* (2005) proposed a model where K_1 and K_2 are independent to the structure of rainfall-runoff models, with a possible decrease less than 0.5% from the maximum value of the Nash criterion computed by using the Jensen-Haise or McGuinness models obtaining:

$$\begin{cases} PE = \dfrac{R_e \left(T_a + 5\right)}{100 \lambda \rho} & \text{if } T_a + 5 > 0 \quad (67a) \\ PE = 0 & \text{otherwise} \quad (67b) \end{cases}$$

We tested equations 67a and 67b as input for our hydrological models. We considered both gridded and in-situ data for mean daily temperature, which is T_a in (67a); while R_e data have been downloaded from the website $www.soda-pro.com$. We assumed $\lambda = 2.45 \frac{MJ}{kg}$ as in Oudin *et al.* (2005) and $\rho = 1000 \frac{Kg}{m^3}$.

Basin	Mean precipitation TRMM-GPM (mm)	Weighted mean pluviometers (mm)	RMSE (mm)
Cordevole at Ponte Mas	3.0797	3.8679	7.3881
Piave at Belluno	3.3246	3.8819	6.7615
Piave at Segusino	3.2334	4.1068	7.1601

Table 6: Mean daily precipitation on the three basins, computed by using both satellite and in-situ data. In the last column the root mean square error (RMSE) between the two datasets.

Basin	Mean temperature E-Obs (°C)	Weighted mean in-situ stations (°C)	RMSE (°C)
Cordevole at Ponte Mas	4.2304	7.0507	3.1711
Piave at Belluno	5.3401	7.3853	2.4388
Piave at Segusino	5.7249	8.0054	2.6237

Table 7: Mean temperature of the three basins, computed by using both gridded and in-situ data. In the last column the root mean square error (RMSE) between the two datasets.

5.3.2 Comparison between in-situ and gridded data of precipitation and temperature

Precipitation In this section we discuss the agreement of the mean precipitation over the three basins, computed using the weighted mean of in-situ data and the TRMM-GPM dataset. For this purpose, we estimated the Root Mean Square Error ($RMSE$), defined as:

$$RMSE = \sqrt{\frac{\sum_{t=1}^{T}\left(y_{situ}^{t} - y_{grid}^{t}\right)^{2}}{T}} \tag{68}$$

Where y_{situ}^{t} is the value of the first variable, at time t: in this case it is the mean precipitation computed by using in-situ data. y_{grid}^{t} is the other variable, in this case mean precipitation computed by using gridded data; while T is the length of the datasets. We considered the time interval 01/01/2010-27/02/2017.

We observe (Figure 33; Table 6) that the pluviometers record more precipitation than satellite data. When we look at the de-trended curves of precipitation, which highlight the deviation from the mean value, we observe very similar patterns, with the difference that the deviation from the mean value is a little bit larger for pluviometric data.

Temperature We computed the mean temperature of the three basins, using the weighted mean and the E-Obs gridded dataset. We considered the time interval 01/01/2010-31/12/2016. $RMSE$ is computed in this case too.

We observe (Figure 34; Table 7) that the in-situ temperatures are generally larger than gridded data.

5.3.3 Comparison of water storage variations with IC2

We considered different inputs for the hydrological models of the three basins, looking for the inputs that best reproduce the measured river flows. The models we tested are GR4J, GR5J (both with and without considering the snow) and TOPMO. We used the Nash - Sutcliffe efficiency method to select the best model. We found that, considering the time interval 30/10/2010-31/12/2016, the GR5J with the inclusion of the snow is the best model to reproduce the river flow in each basin. In Table 8 we reported the value of E, defined in (65), computed by using different combination of inputs. We observe that the river flow is best reproduced when using in-situ data rather than gridded ones: increasing the spatial quality of input data causes an improvement of the hydrological model. Figure 35 shows how GR5J with the inclusion of the snow models the river flow in the three basins considered.

We finally computed the correlation coefficient between V2 and total storage variations, defined as the sum of water levels of Production store and Routing store, considering the time interval 30/10/2010-31/12/2016 (last column of Table 8). The correlation coefficients we obtained are really high, especially for the two large basins defined by the Piave river. The correlation between V2

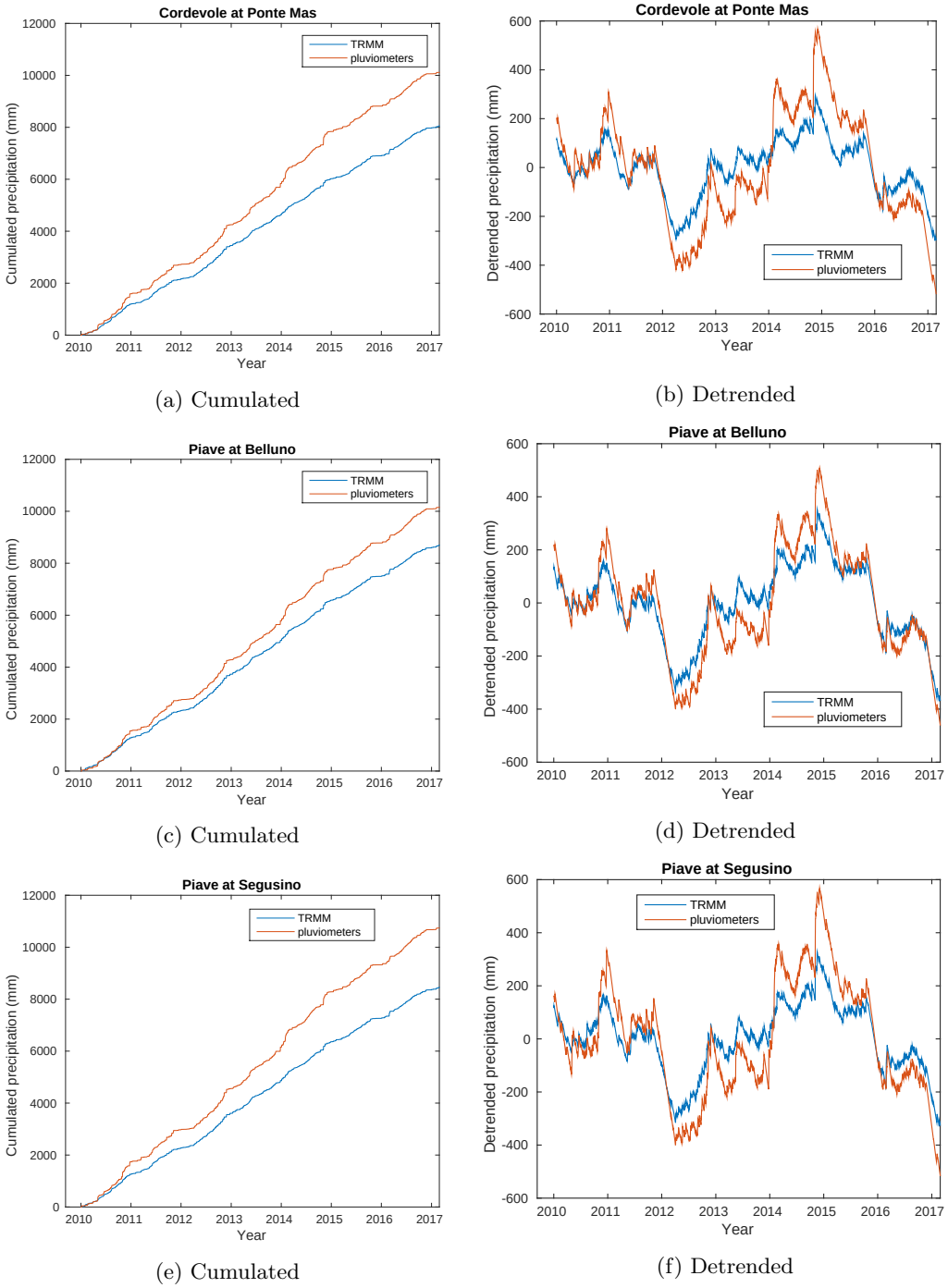

(a) Cumulated

(b) Detrended

(c) Cumulated

(d) Detrended

(e) Cumulated

(f) Detrended

Figure 33: Comparison of the mean precipitation over the Cordevole at Ponte Mas (a,b), Piave at Belluno (c,d) and Piave at Segusino (e,f) basins, considering the TRMM-GPM dataset (blue) and pluviometers weighted mean (red). In the figures on the left we considered the time evolution of the total cumulated precipitation since 2010, which obviously increases with time. In the figures on the right the total cumulated precipitation since 2010 after removing the linear trend.

.

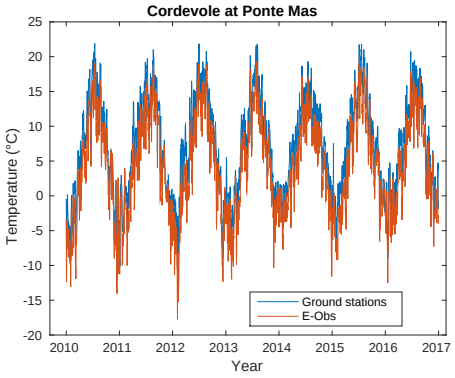

(a) Cordevole at Ponte Mas

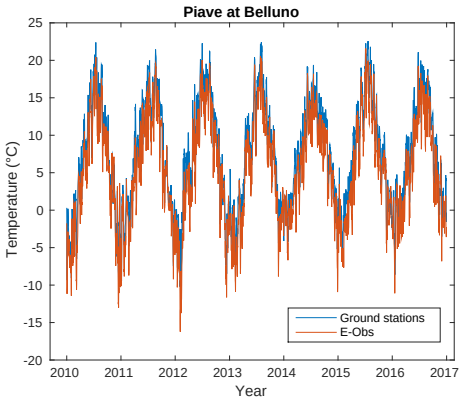

(b) Piave at Belluno

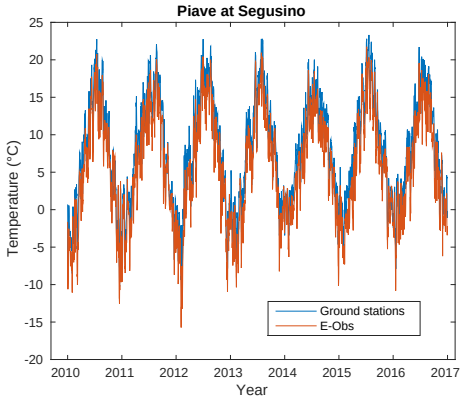

(c) Piave at Segusino

Figure 34: Comparison of daily temperatures considering the E-Obs dataset (red) and in-situ data weighted mean (blue).

.

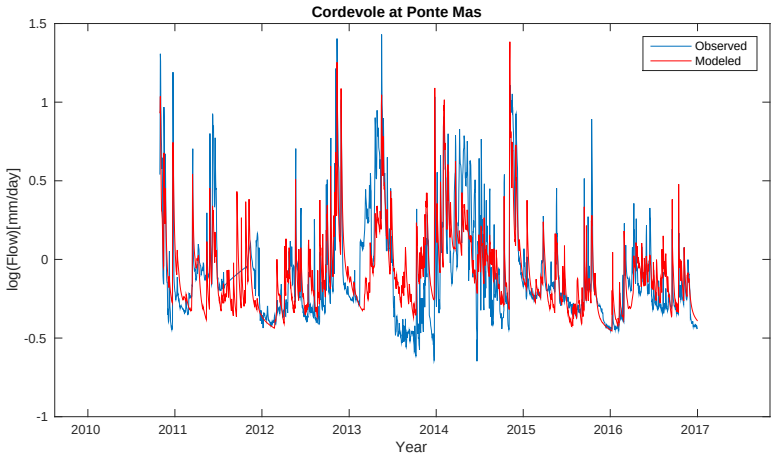

(a) Cordevole at Ponte Mas

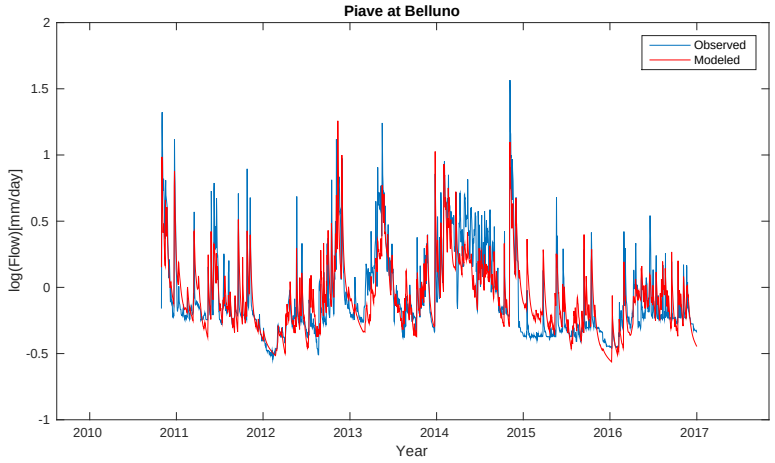

(b) Piave at Belluno

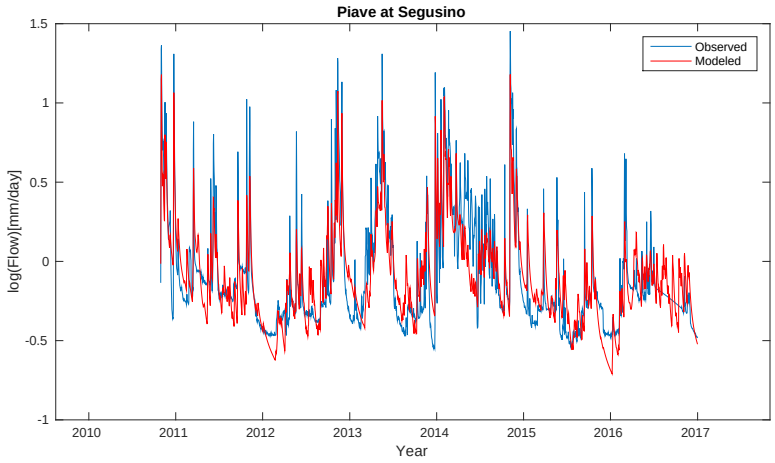

(c) Piave at Segusino

Figure 35: Comparison between logarithm of observed flows (blue) and modeled flows (red) for the three basins considered.

.

Basin	Precipitation data	PET data	Temperature data	E	Correlation
Piave at Belluno	TRMM-GPM	CRU (monthly)	E-Obs	0.58961	0.7928
Piave at Belluno	TRMM-GPM	Oudin gridded	E-Obs	0.56772	0.8300
Piave at Belluno	pluviometers	CRU (monthly)	in-situ	0.71259	0.8274
Piave at Belluno	pluviometers	Oudin in-situ	in-situ	0.73577	0.8900
Piave at Segusino	TRMM-GPM	CRU (monthly)	E-Obs	0.62181	0.7490
Piave at Segusino	TRMM-GPM	Oudin gridded	E-Obs	0.61744	0.7760
Piave at Segusino	pluviometers	CRU (monthly)	in-situ	0.73089	0.8752
Piave at Segusino	pluviometers	Oudin in-situ	in-situ	0.75948	0.9147
Cordevole at Ponte Mas	TRMM-GPM	CRU (monthly)	E-Obs	0.43048	0.6559
Cordevole at Ponte Mas	TRMM-GPM	Oudin gridded	E-Obs	0.50638	0.5977
Cordevole at Ponte Mas	pluviometers	CRU (monthly)	in-situ	0.55545	0.7606
Cordevole at Ponte Mas	pluviometers	Oudin in-situ	in-situ	0.61271	0.7804

Table 8: Combinations of datasets used as input for the hydrological models. In the last two columns we reported the value of E and the correlation between V2 and total storage variations. We consider the time interval 30/10/2010-31/12/2016.

and water storage variations is significantly larger than the correlation between V2 and cumulated precipitation (Figure 36 to be compared with Figure 25), suggesting that hydrological models describe the effects of the source of deformation more completely than considering cumulated precipitation only.

5.4 Response time modeled by GR5J

In this section we studied the response of a basin described by the GR5J model when abrupt changes of precipitation regimes happens. As shown in Figure 37, we consider the precipitation as constant for the first 2000 days. Then, we assume zero precipitation during days 2001-5000, and after that we assume the precipitation as constant, with the same intensity of the first 2000 days.

In order to estimate characteristic times of the hydrological model GR5J, we studied how fast the water storage, discharge and percolation go to zero when we pass from a constant precipitation rate (in this case about 4.1 mm/day) to zero precipitation. We also considered the case when the precipitation has been null for several years and we compute how long water storage, discharge and percolation take to reach constant values once precipitation restart. The potential evapotranspiration has always been considered constant (1.5 mm/day). Both precipitation and potential evapotranspiration mean values have been chosen according to the mean values computed in the basin defined by the Piave at Segusino by using in-situ data, considering the time span 2010-2016.

The set of parameters par $= [x_1,\ x_2,\ x_3,\ x_4,\ x_5,\ x_6,\ x_7]$ of GR5J was initially considered as equal to par_0, a reference parameter set, where each parameter is the same used to describe the Piave basin at Segusino except for the second parameter (x_2), the groundwater exchange coefficient, which is assumed as zero, so that:

$\text{par}_0 = [1566.5025,\ 0,\ 159.83709,\ 0.40,\ 0.26,\ 0.66359615,\ 0.48485537]$.

In Figure 38 we plot the time evolution of the discharge (Q), percolation *(Perc)*, production (PS) and routing store (RS) level of the basin described by the set of parameters par_0, compared with the input described above. We normalized the plots, so that the maximum value reached by these quantities is 1.

Precipitation as a square wave We then decided to use a different input, considering the precipitation as a square wave with a period of 5000 days, with a maximum value of 4.1 mm/day and minimum value of 0 (Figure 39). The potential evapotranspiration has always been considered constant, with the value assumed in the previous discussion (1.5 mm/day).

We studied if percolation, production and routing store were affected by several changes of precipitation regime. Anyway, we observed that the behavior of the discharge and recharge phase is the same for every cycle (see for example Figure 40).

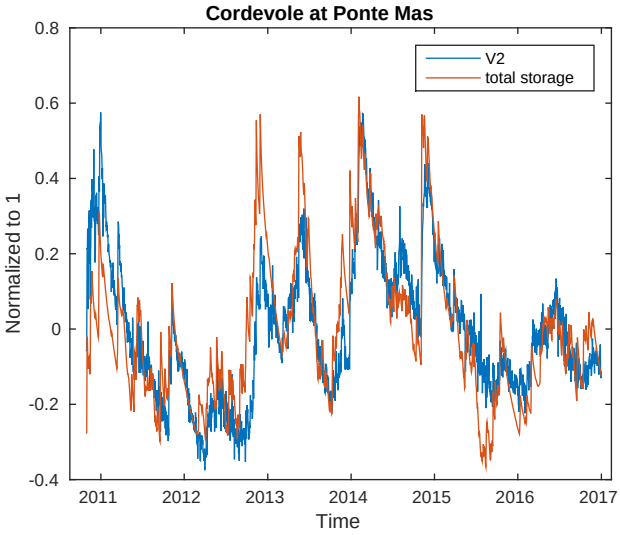

(a) Cordevole at Ponte Mas

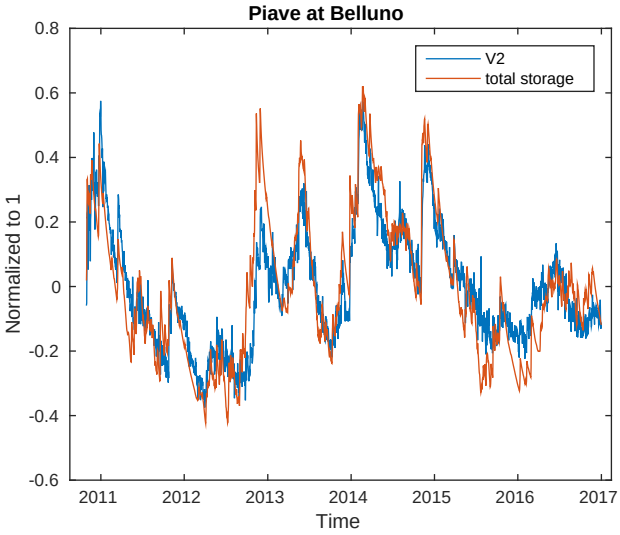

(b) Piave at Belluno

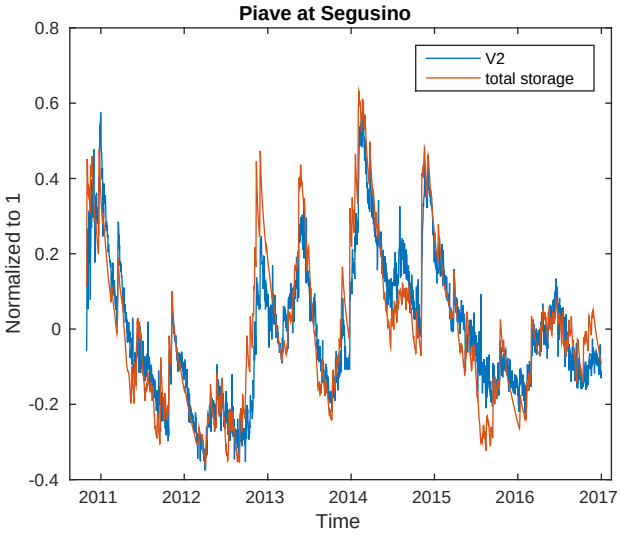

(c) Piave at Segusino

Figure 36: Comparison between total storage variations (red) and V2 (blue).

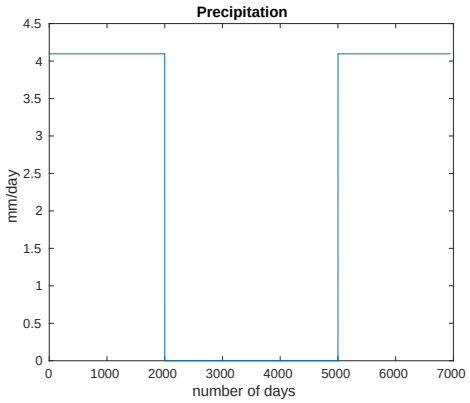

Figure 37: Time evolution of the precipitation.

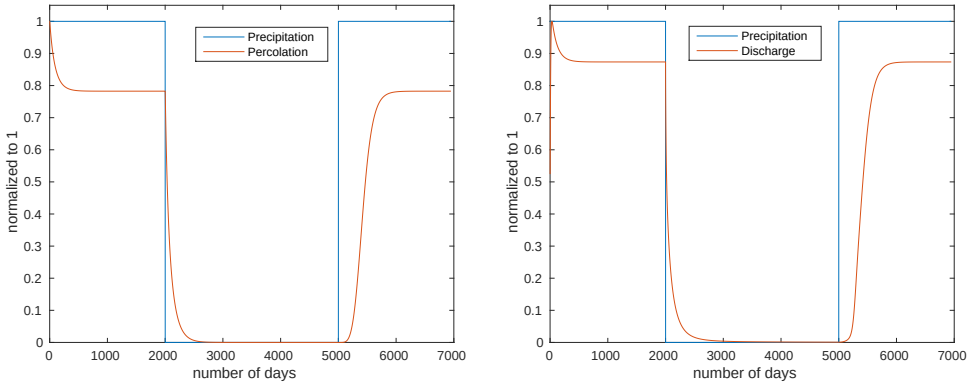

(a) Percolation

(b) Discharge

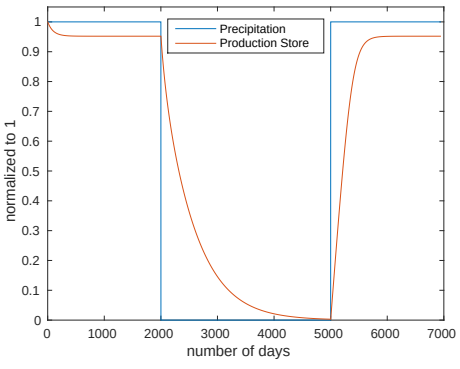

(c) Production store

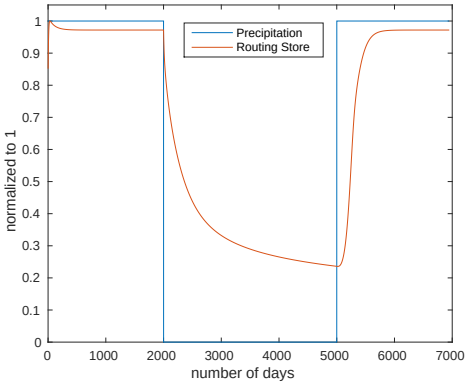

(d) Routing store

Figure 38: Time evolution of Perc (a), Q (b), PS (c), PR (d).

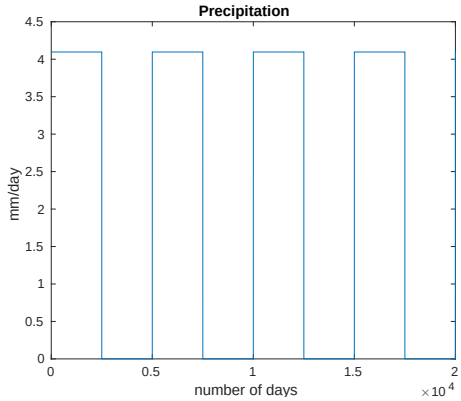

Figure 39: Time evolution of the precipitation.

x_1 (mm)	τ_Q (days)	τ_{Perc} (days)	τ_{PS} (days)
1000	66.0	62.0	352.2
1567	94.0	90.7	533.9
2000	114.7	111.6	655.3

Table 9: τ variations considering different values of x_1.

Then, in the next sections, we will discuss the discharge and recharge phase of PS, as well as the behavior of $Perc$ and Q, considering the simple precipitation regime of Figure 37 and constant potential evapotranspiration (E=1.5 mm/day).

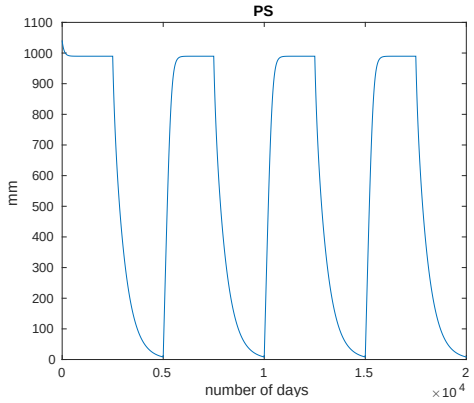

Figure 40: Time evolution of the production store, considering the precipitation as Figure 39.

5.4.1 Discharge time

We tried to model the characteristic time of the discharge stage during the period 2000-5000 days (Figure 38) using the formula $ae^{-t/\tau}$ and to evaluate the dependence of τ on some of the parameters par_0. Table 9 shows the values of τ considering different values of the first parameter (x_1, maximum capacity of the production store). We also tried to calculate the variation of the discharge Q by varying the third and fourth parameter of the GR5J model (x_3, x_4), which are the maximum capacity of the routing store and the time base of unit hydrograph. With respect to par_0, we let x_3 and x_4 vary only one at the time: we never let x_3 and x_4 be different from their value in par_0 at the same time. As you can see in Table 10, we observed that Q is slightly affected by the variation of x_3 and x_4. The parameter that has the largest influence on the discharge is x_1 and from Table 9 we see that τ increases with x_1. It's worth noting that the only parameter that affect the percolation and the production store level variations is x_1.

x_3 (mm)	τ_Q(days)		x_4(mm)	τ_Q(days)
50	90.8		0.2	94.0
100	91.7		0.4	94.0
159.8	94.0		1	93.8
200	95.8		2	92.1

Table 10: Characteristic time obtained for the evolution of Q considering different values of x_3, x_4

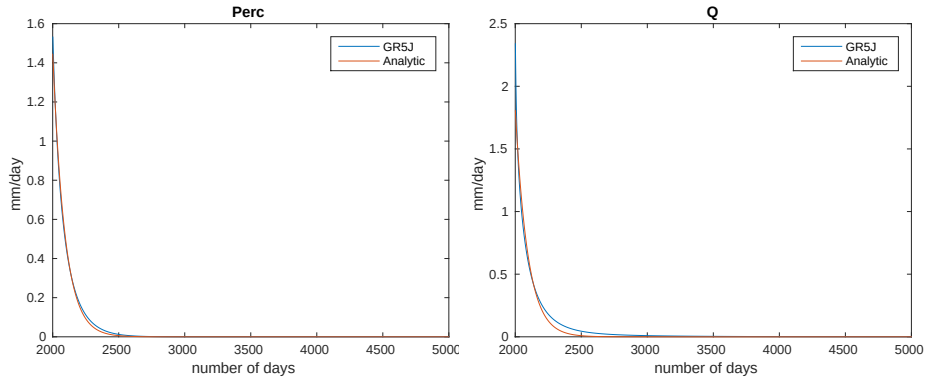

(a) Percolation

(b) Discharge

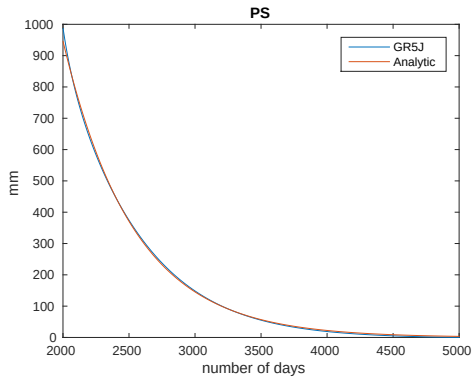

(c) Production store

Figure 41: Time evolution of $Perc$ (a), Q (b), PS (c), computed by GR5J using the set of parameters par_0 (blue) and modeled by using the formula $ae^{-t/\tau}$ (red).

x_1 (mm)	τ_Q (days)	τ_{Perc} (days)	τ_{PS} (days)
1000	78.8	79.5	172.3
1567	136.0	140.2	253.2
2000	195.8	206.9	313.6

Table 11: The final part of the recharge stage is represented by $a(1-e^{-t/\tau})$ (limited to the period 5401 days $\leq t \leq$ 6900 days in Figure 38 for Q and $Perc$). τ variations considering different values of x_1.

5.4.2 Recharge time

Considering the period $t >$ 5000 days in Figure 38 when the precipitation is re-applied after the long drought, we observe that the evolution of Q, $Perc$, and the RS level is characterized by an inflection point (Figure 38a, 38b, 38d), which is not present in the production store level evolution (Figure 38c). We compute how long Q, $Perc$, and the RS level take to reach the inflection point after the recharge begins. Using the set of parameters par_0, we found that $Perc$ reaches the inflection points 592 days after the precipitation restart, while RS and Q take 249 and 307 days. The routing store reaches its absolute minimum at the epoch 5017 days, i.e 17 days after the precipitation restart.

We tried to model the evolution of Q, $Perc$, and the RS level during the recharge stage. Initially, we focus on reproducing the evolution at the final epochs when these quantities finish to raise and reach a constant value. In order to model this behavior, we used the formula $a(1-e^{-t/\tau})$ (limited to the period 5400 days $\leq t \leq$ 6900 days for Q and $Perc$ in Figure 38). Results are shown in Figure 42. As done before, we let x_1, x_3, x_4 vary one at a time with respect to the values in par_0 and computed how τ varies. We present the results in Tables 11 and 12. We notice that also in this case the Q characteristic time is mainly affected by the maximum capacity of x_1.

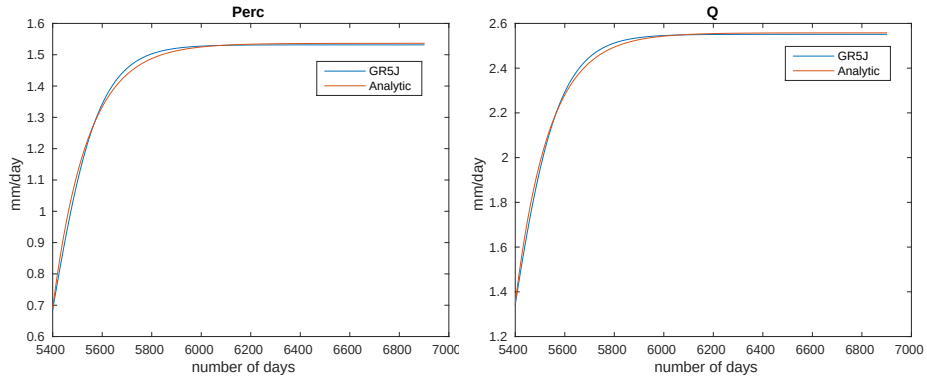

(a) Percolation (b) Discharge

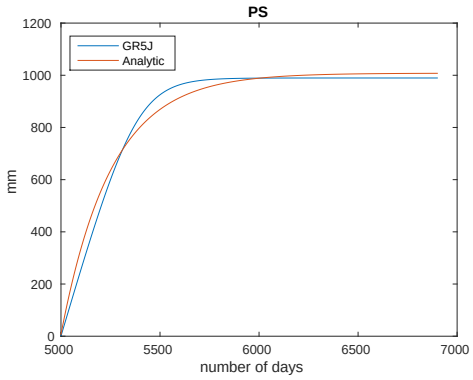

(c) Production store

Figure 42: Time evolution of $Perc$ (a), Q (b), PS (c), computed by GR5J using the set of parameters par_0 (blue) and modeled by using the formula $a(1-e^{-t/\tau})$ (red).

$x_3(mm)$	τ_Q (days)		x_4 (mm)	τ_Q (days)
50	136.2		0.2	136.0
100	136.1		0.4	136.0
159.8	136.0		1	136.0
200	135.5		2	136.2

Table 12: The final part of the recharge stage is represented by $a(1 - e^{-t/\tau})$ in the period 5400 days $\leq t \leq$ 6900 days. τ variations considering different values of x_3, x_4

x_1 (mm)	τ_Q (days)	τ_{Perc} (days)
1000	32.9	68.7
1567	45.9	56.4
2000	49.6	54.3

Table 13: The initial recharge is represented by $ae^{t/\tau}$.τ variations considering different values of x_1

Let's now take into consideration the initial raise of the recharge stage (period 5001 days $\leq t \leq$ 5300 days) of $Perc$ and Q. We tried to model the behavior of the basin described by the set of parameters par_0 by using the analytical expression $ae^{t/\tau}$ (Figure 43). The value of τ that fits the GR5J model at best is 56.4 for $Perc$ and 45.9 for Q. As done before, we let x_1, x_3, x_4 vary one at a time and computed how τ varies. We present the results in Tables 13 and 14.

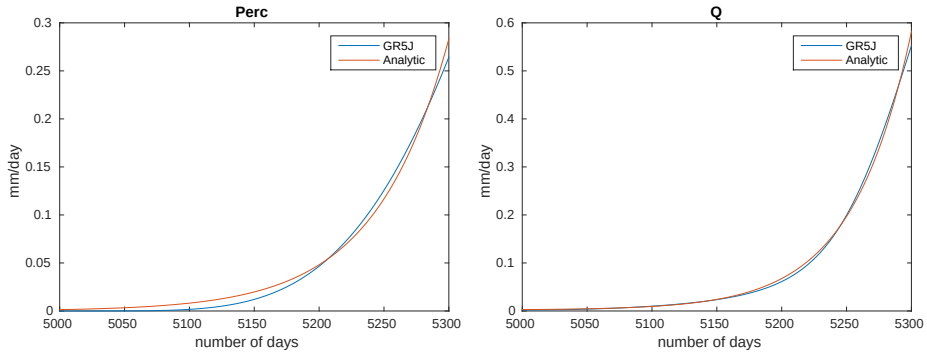

(a) Percolation (b) Discharge

Figure 43: Time evolution of $Perc$ (a) and Q (b), computed by GR5J using the set of parameters par_0 (blue) and modeled by using the formula $a(e^{t/\tau})$ *in the period* 5001 days $\leq t \leq$ 5400 days (red).

5.4.3 Analytic description of production store level variations

According to Perrin (2003) the level variation of the production store between two time steps is:

$$\frac{dS}{dt} = \frac{x_1\left(1-\left(\frac{S}{x_1}\right)^2\right)\tanh\left(\frac{P_n}{x_1}\right)}{1+\frac{S}{x_1}\tanh\left(\frac{P_n}{x_1}\right)} - \frac{S\left(2-\frac{S}{x_1}\right)\tanh\left(\frac{E_n}{x_1}\right)}{1+\left(1-\frac{S}{x_1}\right)\tanh\left(\frac{E_n}{x_1}\right)} - \\ - S\left\{1-\left[1+\left(\frac{4}{9}\frac{S}{x_1}\right)^4\right]^{-1/4}\right\} \tag{69}$$

We remind that, according to the GR5J model:

- if precipitation is larger than evapotranspiration, then

$$P_n = P - E;\ E_n = 0,\ \text{if}\ P > E \tag{70}$$

$x_3(mm)$	τ_Q (days)		x_4 (mm)	τ_Q (days)
50	31.23		0.2	45.9
100	41.0		0.4	45.9
159.8	45.9		1	45.8
200	45.8		2	45.6

Table 14: The initial recharge is represented by $ae^{t/\tau}$.τ variations considering different values of x_3, x_4

-otherwise,

$$E_n = E - P;\ P_n = 0,\ \text{if } P < E \tag{71}$$

Let us introduce the quantities $\alpha = \tanh\left(\frac{|P-E|}{x_1}\right)$ and $y = \frac{S}{x_1}$, then (69) can be re-expressed as:

$$\frac{dy}{dt} = \frac{(1-y^2)\alpha}{1+y\alpha} - y\left\{1 - \left[1 + \left(\tfrac{4}{9}y\right)^4\right]^{-1/4}\right\},\ P > E \tag{72}$$

$$\frac{dy}{dt} = -\frac{y(2-y)\alpha}{1-(y-1)\alpha} - y\left\{1 - \left[1 + \left(\tfrac{4}{9}y\right)^4\right]^{-1/4}\right\},\ P < E \tag{73}$$

In Figure 44 we represent the values that y reaches in steady conditions and how it is influenced by α.

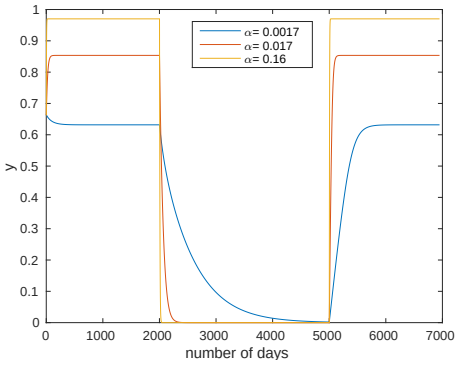

Figure 44: Time evolution of y for different values of α

We observe that as α increases, the production store takes less time to empty and to fill (Figure 44). In addition, y reaches higher values in steady condition as α increases.

Let us consider the two cases when precipitation is larger or smaller than evapotranspiration. To this aim we define

$$f(y) \equiv \frac{(1-y^2)\alpha}{1+y\alpha} \tag{74}$$

$$g(y) \equiv -\frac{y(2-y)\alpha}{1-(y-1)\alpha} \tag{75}$$

$$h(y) \equiv y\left\{1 - \left[1 + \left(\tfrac{4}{9}y\right)^4\right]^{-1/4}\right\} \tag{76}$$

Case 1: $P > E$ Equation (72) can be rewritten as

$$\frac{dy}{dt} = f(y) - h(y) \tag{77}$$

If we use the Taylor series and we stop at the first order in y, in $f(y)$ we can rewrite the factor $(1+y\alpha)^{-1}$=$1 - y\alpha$ so that the equation can be rewritten as

$$\frac{dy}{dt} = \left(1-y^2\right)\alpha(1-y\alpha) - y\left\{1-\left[1+\left(\frac{4}{9}y\right)^4\right]^{-1/4}\right\} \tag{78}$$

If we neglect the terms y^2 and powers of higher grades, which are smaller than one, we have that

$$\frac{dy}{dt} = \alpha(1-\alpha y)$$

where $h(y)$ is also neglected. Then $\frac{dy}{1-\alpha y} = \alpha dt$; $\ln(1-\alpha y) = -\alpha^2 t + C$; $y = \frac{1-Ce^{-\alpha^2 t}}{\alpha}$.

if $t = 0$, then $y(0) = \frac{1-C}{\alpha}$ and $C = 1-\alpha y(0)$

Finally, the time evolution of y is

$$y(t) = \frac{1-(1-\alpha y(0))\,e^{-\alpha^2 t}}{\alpha} \tag{79}$$

Figure 45 highlights that the agreement between (79) and the GR5J output is good only when y is low basically because we neglected the term $h(y)$ as we will see later.

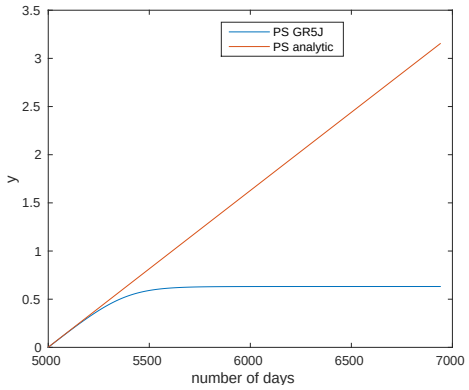

Figure 45: Comparison of the ratio $y = \frac{S}{x_1}$ computed by GR5J (blue) and the analytical solution (79) (red).

Case 2: $P < E$ Equation (73) can be rewritten as

$$\frac{dy}{dt} = g(y) - h(y) \tag{80}$$

Making some algebra, using again the Taylor series and neglecting the terms y^2, it is possible to write (73) as

$$\frac{dy}{y} = -\frac{2\alpha}{1+\alpha}dt \tag{81}$$

where in particular $h(y)$ is neglected.

Algebra details driving to equation 81 From Equation (73) we can write

$$\frac{dy}{y} = \frac{-(2-y)\alpha}{1+\alpha-y\alpha}dt = \frac{-(2-y)\alpha}{(1+\alpha)}\frac{1}{\left(1-\frac{\alpha}{1+\alpha}y\right)}dt \tag{82}$$

Using Taylor series

$$\frac{-(2-y)\alpha}{(1+\alpha)}\frac{1}{\left(1-\frac{\alpha}{1+\alpha}y\right)}dt = \frac{-(2-y)\alpha}{(1+\alpha)}\left(1+\frac{\alpha}{1+\alpha}y\right)dt \tag{83}$$

Neglecting the y^2 and α^2 terms, we obtain

$$\frac{dy}{y} = -\frac{2\alpha}{1+\alpha}dt \tag{84}$$

The final expression of y is then

$$y(t) = y(0)e^{-\frac{2\alpha}{1+\alpha}t} \tag{85}$$

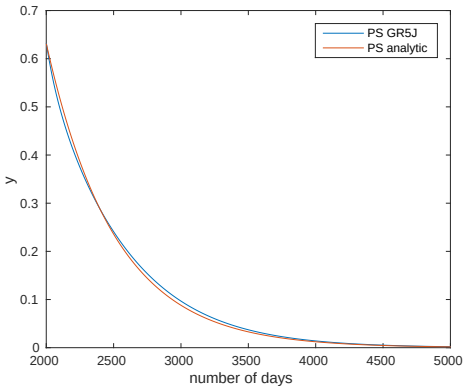

Figure 46: Comparison of the ratio $y = \frac{S}{x_1}$ computed by GR5J (blue) and the analytical solution (85) (red).

Figure 46 shows that there is a good agreement between the analytical solution and the GR5J output.

Validity of the approximations In both **Case 1** and **Case 2** we neglected the term $h(y)$ that represents the percolation, focusing only on the term $f(y)$ (portion of the precipitation that fills the production store) when $P > E$ and on $g(y)$ when $P < E$.

For the case $P > E$ we said that this approximation is good when $y \ll 1$, but let's study the trends of $f(y)$ and $h(y)$ considering increasing values of y. Figure 47a shows that $h(y)$ can be neglected only when y has values smaller than about 0.4, while when $y > 0.6$ $h(y)$ is even larger than $f(y)$. Then, the approximations we made in the previous sections are good only for $y < 0.4$, in accordance with Figure 45. We remind that we have considered $x_1 = 1566$ mm and $P_E = 1.6$ $\frac{mm}{day}$, then $\alpha = \tanh\left(\frac{P-E}{x_1}\right) = 0.0017$.

We studied also the cases when α is larger, by considering smaller values of x_1. In this case, it is possible to neglect $h(y)$ up to $y < 0.6$ (Figure 47b) and $y < 0.8$ (Figure 47c). Let us call $\hat{y}$ the value of y where $h(\hat{y}) = f(\hat{y})$. Figure 48 highlights that as α increases, $\hat{y}$ increases. It's worth remarking the importance of $\hat{y}$: during recharge, y increases until it reaches the value $\hat{y}$. After that, the input of the production store becomes smaller than its output, so that $\hat{y}x_1$ is the maximum level that the production store can attain.

Figure 49a, 49b and 49c are representative for the case $P < E$, when the production store level decreases with time. Then, at the beginning y assumes its largest value, that will reduce with time. As a consequence, at the beginning the values of $h(y)$ are not neglegible with respect to $|g(y)|$; nonetheless, as the time goes on, y becomes smaller and then the contribution of $h(y)$ to the leaking becomes negligible. Accordingly during discharge neglecting h is more justified than during the recharge phase as suggested by the good agreement between (85) and numerical results (Figure 46) Furthermore, by defining $\tilde{y}$ as the value of y where $|g(\tilde{y})| = h(\tilde{y})$ below which neglecting percolation is justified, we observe that as α increases, $\tilde{y}$ increases so that the validity of the approximation of neglecting percolation also increases.

For the case of the discharge, the values of y are always smaller than 0.6, while our approximate solution (85) holds only if $|g(y)|$ is more important than $h(y)$ that is for $y < 0.4$ (Figure 49a).

In the case of the recharge, $h(y)$ starts to play an important role for $y > 0.4$, causing the reduction of the rate of increase of PS and its stabilization to a constant value (see for example Figure 45). For this reason, the analytical solutions we obtained describe the discharge much better than the recharge.

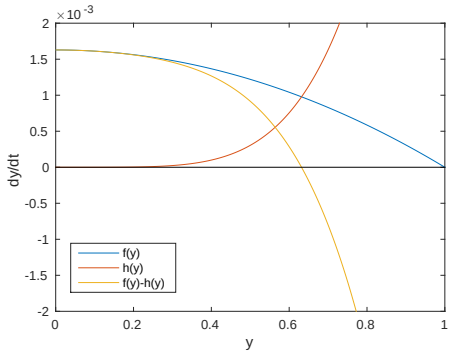

(a) $x_1 = 1566$, i.e. $\alpha = 0.0017$.

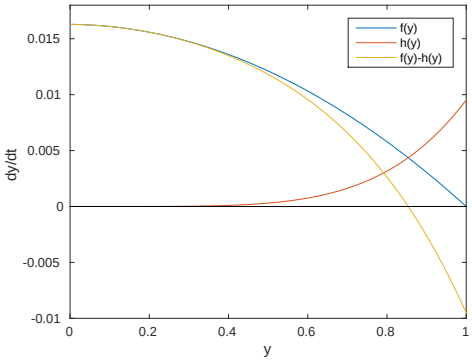

(b) $x_1 = 151.6$, i.e. $\alpha = 0.017$.

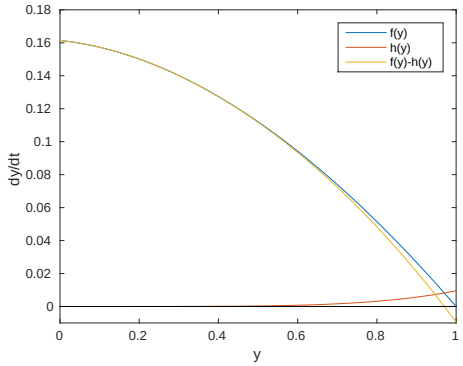

(c) $x_1 = 15.66$, i.e. $\alpha = 0.16$.

Figure 47: Comparison of the trends of $f(y)$, $h(y)$, and the difference $f(y) - h(y)$ assuming different valus of α.

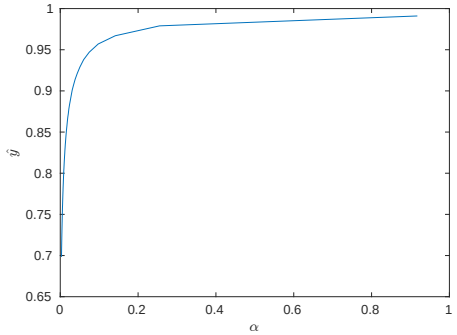

Figure 48: $\hat{y}$ dependence from α.

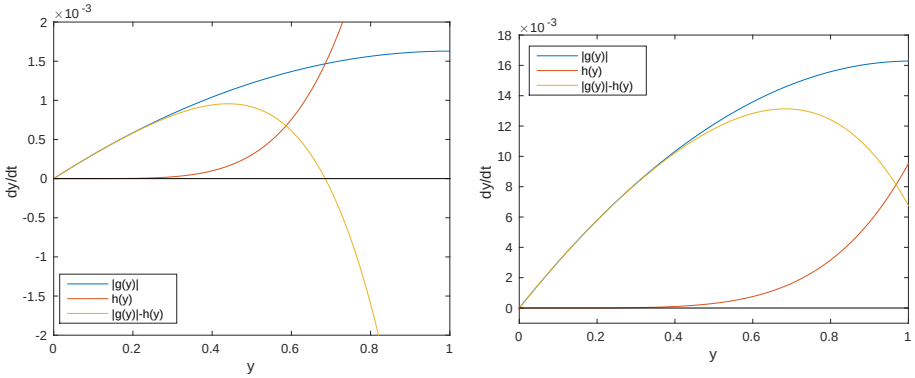

(a) $x_1 = 1566$, i.e. $\alpha = 0.0017$.

(b) $x_1 = 156.6$, i.e. $\alpha = 0.017$.

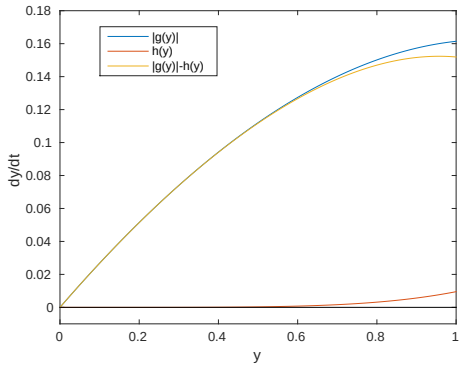

(c) $x_1 = 15.66$, i.e. $\alpha = 0.16$.

Figure 49: Comparison of the trends of $|g(y)|$, $h(y)$, and the difference $|g(y)| - h(y)$ assuming different values of α.

5.4.4 Residence Time and cumulated precipitation

According to the book *Physical Hydrology* by Dingman, the residence time (also called transit time or turnover time) of water in reservoir is the average length of time a "parcel" of water spends in the reservoir. Aquifer residence time also characterizes the timing of aquifer responses to changes in recharge, then the residence time is strictly related to α of equation 79.

For a reservoir in steady state, as it can be considered the sum of production and routing store just before the precipitation stops in Figure 37, the residence time T_r of the reservoir is defined as:

$$T_r = \frac{Reservoir\ average\ storage}{Average\ rate\ of\ input/output} \tag{86}$$

Since just before the precipitation stops the evapotranspiration, discharge, production and routing store levels are constant, we computed T_r as

$$T_r(days) = \frac{S(mm) + R(mm)}{P_n(\frac{mm}{days})} = 263.9\ days \tag{87}$$

Where S and R are the production and routing store levels and P_n is the precipitation.

In (87) we considered as denominator of (86) the input. We decided to compute T_r by using the rate of output to verify that T_r doesn't change:

$$T_r(days) = \frac{S(mm) + R(mm)}{Q(\frac{mm}{days}) + Etr(\frac{mm}{days})} = 263.9\ days \tag{88}$$

Q is the discharge and Etr the evapotranspiration. Equations (87) and (88) give rise to the same result, which is also consistent with the number of days of cumulative precipitation that maximize the correlation with the temporal evolution of IC2.

5.4.5 Link between storage variations and cumulative precipitation

If we compare the response time τ for $x_1 = 1566$ of Perc, Q and PS in dynamic conditions (Tables 9, 11 and 13), with the value of T_r in static conditions we obtain different values but generally the same order of magnitude.

τ computed through analytic calculation and approximations is, for the case of recharge (section 5.4.3), according to (79):

$$\tau = \frac{1}{\alpha^2} = 3.8 \times 10^5\ days \tag{89}$$

This value is much larger than τ of Table 11, i.e. 253.2.

If we consider discharge (section 5.4.3), according to (85):

$$\tau = \frac{1-\alpha}{2\alpha} = 306.5\ days \tag{90}$$

The response time of a system is the time during which the system keeps memory of the previous input conditions after a change of them. Equation 90 for small α and Figure 44 suggest that the production store response time increases with α^{-1} and then, for a given precipitation history, with the x_1 parameter as confirmed by Tables 9, 11, 13. On the basis of the results of the initial sections, this can be extended to each compartment of the GR5J model (Tables 9, 11, 13). For the case here analysed, the value of x_1 is chosen by calibrating the GR5J model to reproduce Q time series in the investigated region. This value provides response times which are in the same order of magnitude of the time scale required to make the cumulated precipitation correlating with IC2. This sounds reasonable because on one hand S in Equation (69) correlates with IC2, as shown in this chapter, on the other hand the net precipitation acts on the GRJ5 model variables through its integral over time, as it can be seen *e.g.* for S from (69) which can be rewritten as

$$\frac{dS}{dt} = P_s - E_s - Perc \tag{91}$$

where

$$P_s \equiv \frac{x_1\left(1 - \left(\frac{S}{x_1}\right)^2\right)\tanh\left(\frac{P_n}{x_1}\right)}{1 + \frac{S}{x_1}\tanh\left(\frac{P_n}{x_1}\right)}$$

is the part of precipitation that fills the production store,

$$E_s \equiv \frac{S\left(2-\frac{S}{x_1}\right)\tanh\left(\frac{E_n}{x_1}\right)}{1+\left(1-\frac{S}{x_1}\right)\tanh\left(\frac{E_n}{x_1}\right)}$$

is the part of water that evaporates from the production store and

$$Perc \equiv S\left\{1-\left[1+\left(\frac{4}{9}\frac{S}{x_1}\right)^4\right]^{-1/4}\right\}$$

is the percolation. For the definition of response time, τ, and $t > t_0 + \tau$ we can obtain from (91)

$$S(t) = S(t_0) + \int_{t_0}^{t}[P_s(t') - E_s(t') - Perc(t')]dt' \simeq \int_{t-\tau}^{t}[P_s(t') - E_s(t') - Perc(t')]dt'$$

which suggests that, neglecting $Perc$, $S(t)$ correlates with the cumulative effective precipitation in the previous τ days. Then, for the result of Section 5.3.3, also the IC2 correlates with the same quantity.

Here we demonstrated that the response time of the production store in the hydrological model scales with x_1, but it is not possible to link it to any specific parameter of the subsurface rocks. However, we saw in Section 5.4.4 that also residence time is comparable to the cumulation time of precipitation. Assuming the system is linear, from the residence time (estimated through the cumulation time) we can estimate the diffusivity below the surface.

6 Interpretation of spatial pattern of IC2 in Monte Cesen-Col Visentin (MCCV) Anticline

In chapter 5, we discussed the correlation between water storage changes and the temporal evolution (V2) of a transient geodetic signal. Here, we present two different models that describe how storage variations can generate the displacement patterns reconstructed by IC2. We decided to apply these models to the central sector of the Venetian Southern alps (area 2, see Figure 50 and 17), because of its great geologic relevance (discussed in chapter 2) and data availability.

6.1 Geologic and Hydrological Framework

Structurally, area 2 is characterized by the SW-NE elongated Monte Cesen-Col Visentin (MCCV) Anticline - Belluno Syncline pair, oriented along the NE-SW direction and confined between the Bassano-Valdobbiadene thrust and the Valsugana thrust (see Figure 50).

The MCCV anticline give rise to a mountain relief which in its western portion (Monte Cesen - Col de Moi) presents a length of about 12 km, where the north face is the widest one. The ridge is characterized by grazing lands having a smooth morphology, with heights in between 1400 m and 1500 m and maximum elevation slightly lower than 1600 m.

This asymmetric morphology is determined by the anticline, which produces wide Maiolica outcrops in its higher portion and Scaglia Rossa-Flysch on its slopes (Figure 51). In the internal part of the south face, which is steeper than the northern one, there are dolomites and limestones outcrops, mainly belonging to the Calcare del Vajont, which in this area is about 600 m thick. This formation presents wide fronts of secondary dolomitization, probably associated with faults, which generate a porosity of about 10-20% (Zempolich 1997). Locally, north of Valmareno (Follina) and along the Piave valley (Vas), the marly limestone with argillitic intercalations of the Formazione di Igne outcrops, constitues the aquiclude of this sector. In the upper part of the stratigraphic series there are heterotopic variations toward east, which consist in the substitution of the Rosso Ammonitico Veronese with the Fonzaso Formation and the emergence of bioclastic limestone layers within Maiolica. The hydrography on surface is present mainly in the north face within the deep transverse valleys, but the main springs, among the sixty that have been located, can be found in the western and southern slopes (Boscolo *et al.*, 2007).

In the western part of the massif, next to Vas, an important spring is present: Fium. During the period that goes from winter 2005 to summer 2006, the flows ranged from 0.8 m^3/s to 2.6 m^3/s, even if Pizzaia (2006) estimated a maximum flow of 14 m^3/s . The water comes out from a karst cavity and from a detritic coverage, that probably hides other cavities. The lithology is the upper part of the Calcare del Vajont, lying toward south, locally affected by a couple of slope variations (kink-bands). The recharge basin proposed by Fileccia (2006) includes the northeast area of the spring, a little bit beyond the Mount Zogo and Mount Cesen. The general runoff of the area is characterized by a main drainage within the Calcare del Vajont, whose basal contact with impermeable layers is not very deep, as confirmed by outcrops in several points. The drainage reaches the surface laterally along the Piave Valley (Val Belluna) and frontally near Follina, where the impermeable layer may be located at the Bassano-Valdobbiadene thrust.

The lateral extension of the eastern part (Col Visentin) of the mountain range decreases up to 4 km, while the maximum heights are in between 1600 m and 1700 m. The hydrography on the surface is characterized by a couple of deep valleys in the northern side, while the largest springs are in the southern side. Lithologically, the wide Maiolica outcrops are richer of bioclastic levels, so that they are defined as Calcare di Soccher formation whose upper part is similar to formations found in the Friulian Plain (Di Napoli Alliata *et al.*, 1970). Above this level there are more impermeable tertiary formations: Scaglia Rossa, Scaglia Cinerea, Flysh; which constitute the core of the shelf south of Limana.

Structurally, the anticline changes direction from south-east/north-west to south-north and in the north side a north-vergent thrust fault rises and isolates the core of the fold (Costa *et al.*, 1992). In the area of the axial rotation there are transversal faults that cross the main structure. There are about 30 springs in this sector, a third of them are located in the north face next to the faults.

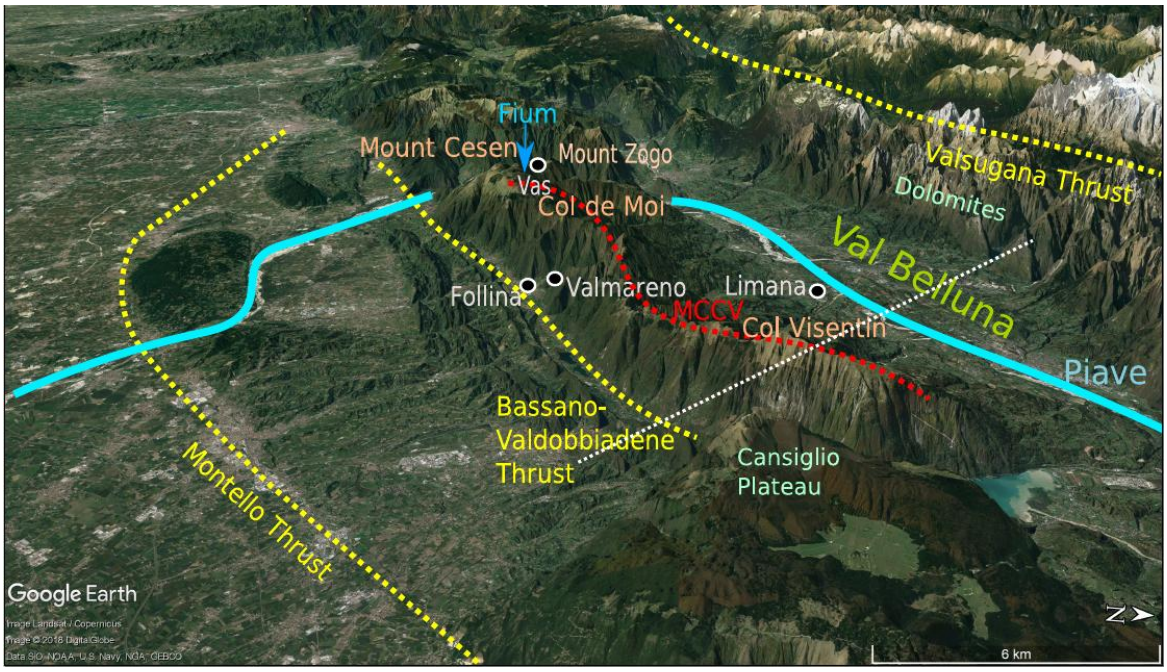

Figure 50: 3-D view from east of area 2. Yellow dashed lines: thrust faults. White dashed line: geological profile represented in Figure 51. Brown triangles: mounts that characterize the Mount Cesen - Col Visentin (MCCV) anticline (dashed red line). Light blue line: Piave river. White circles: cities. Blue arrow indicates Fium spring position.

6.2 Tensile fracture model

In the study area, the sources of deformation form a geodetic signal whose wavelength is longer than the one of signals recorded at a local scale using tiltmeters installed in natural caves (e.g., Grillo *et al.*, 2011). In fact, tiltmeters time series can be affected by hydrological processes involving both the more-local fast infiltration phase and the slower one, which affects also GPS measurements (Grillo *et al.*, 2018). We focus on area 2 (Figure 17), where the GPS network is denser than areas 1 and 3, thanks to past geodetic experiments (Danesi *et al.*, 2015) and used only horizontal displacements. We have excluded the site CANV, since the larger displacements observed at this site may also result from topographic amplification of the rainfall-induced deformation signal (Guglielmi *et al.*, 2005), being this station located at the edge of the steep slope of the Cansiglio plateau (see also Devoti *et al.*, 2016). In area 2 the horizontal principal strain axes associated with IC2 are normal to the seismically active pedemountain front and parallel to the direction of the long-term tectonic and geological deformation (see Figure 5 in Serpelloni *et al.*, 2016). For this reason, the deformation associated with this hydrological signal could be potentially misinterpreted with a transient of tectonic origin, for example, if analyzed only across limited time intervals. Moreover, some of the stations largely affected by the hydrological deformation, coincide with stations that poorly fit elastic interseismic models (see Figure 10 of Serpelloni *et al.*, 2016), posing the problem of how these stations can be used for tectonic studies.

6.2.1 Dislocation and crack models

In order to compute the displacement and stress field generated by a tensile fracture, it is possible to use two models built on different approaches: *dislocation models* and *crack models*.

The dislocation model is based on the assumption that the opening (or closing) of a fracture, i.e. the Burger vector, is known. Starting from this information, as shown by Okada (1992), it is possible to analytically compute displacement and stress field in a half-space.

On the other hand, in crack models the Burger vector is initially unknown, while the stress on fracture walls is given (Zeller and Pollard, 1992). For instance in the case of a tensile crack the overpressure is known and from this information both the fracture opening and then the displacement and stresses originated from it can be computed. It is worth noting that when considering crack models the opening of the fracture is not constant along its walls, but it is

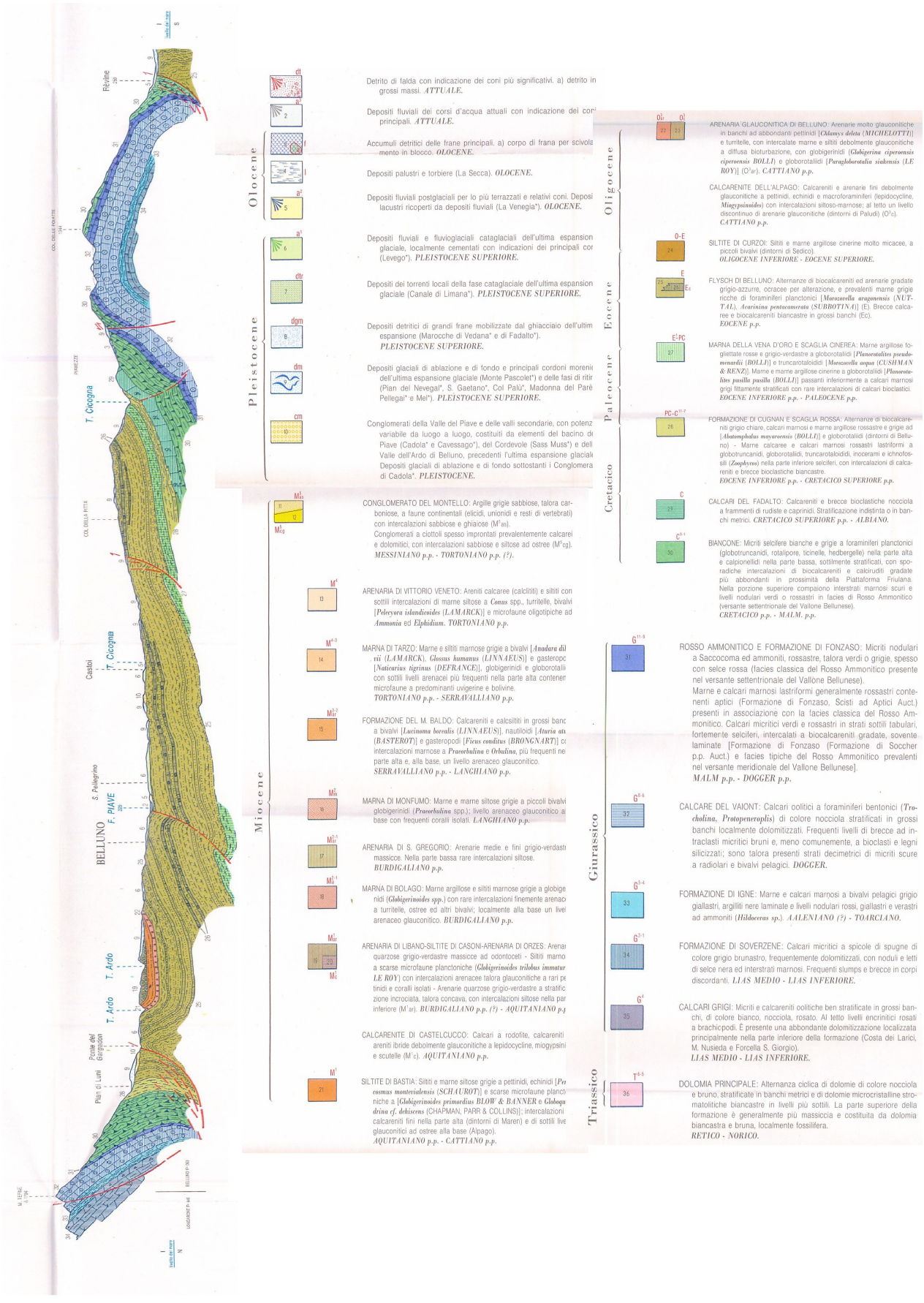

Figure 51: Geologic profile (and its complete legend) of the MCCV anticline and Val Belluna, from Carta Geologica d'Itaila, foglio Belluno. Profile position is represented in Figure 50 (dashed white line).

maximum in the center of the fracture and decreases towards fracture edges (Figure 54). Similarly, in dislocation models the pressure applied on fracture walls is not uniform.

6.2.2 Results in the case of a vertical tensile fracture in an homogeneous halfspace

Considering the two time intervals T1 (mid-September to December 2010) and T2 (January 2011 to April 2012), corresponding to extensional and compressional phases (Figure 24C), we can describe the displacements associated with IC2 (black arrows in Figures 24A and 24B) as due to a variable opening of a tensile dislocation (i.e., the equivalent tensile fracture).

We considered a rectangular, vertical tensile dislocation surface in an elastic half-space (Poisson's ratio of 0.25). To determine the geometry of this source of deformation we assumed a uniform opening. By fixing the dip angle at 90°, the mid-point along strike (Lon. = 12.25°E, Lat. = 46.07°N) and the top depth at 0 km (free surface), while allowing the other parameters (strike, length and width) to vary within larger bounds, we used a simulated annealing approach (Cervelli *et al.*, 2001) to estimate the optimal parameters. The bounds for the length, strike and width are 40-80 km, $50-80°$ N and 0.1-1.5 km, respectively. In order to define error bounds on the length, strike and width, we run the inversion 2000 times and analyze the parameter distributions. Figure 52 shows the frequency histograms of the modeled parameters, where the best values are defined as the median value of each distribution (red bars). These values are later used to estimate the opening distribution, interpreting the equivalent tensile fracture by means of a crack model (Zeller and Pollard, 1992), and the pressure changes that best fit the measured displacements with a boundary element approach, which is a numerical technique for solving integral equations that mathematically describe a physical problem (Aliabadi and Wrobel, 2002). The associated uncertainties, at the 68% confidence level, are determined from 16^{th} and 84^{th} percentile bounds (green bars). While length and strike are rather well constrained, the depth (1.1 km) is affected by a greater uncertainty (Figure 52), indicating anyhow that the deformation wavelength of the signal is likely associated with a structure as deep as 1 km. This is in agreement with the presence of a deep-rooted karst system in this area (Mietto and Sauro, 2000).

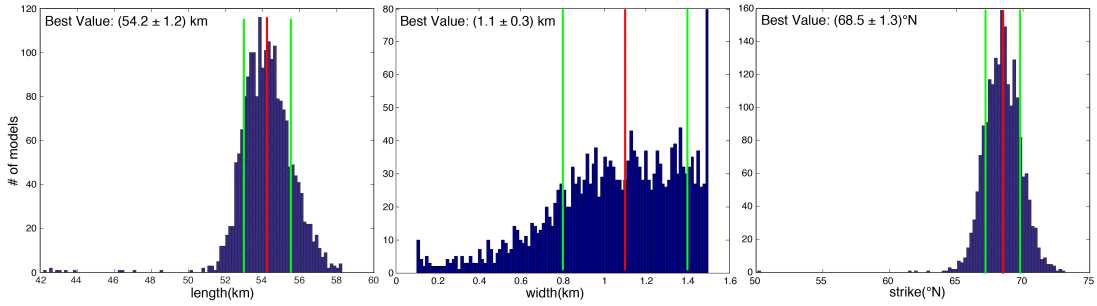

Figure 52: Frequency distribution of length, width and strike values of the tensile dislocation obtained from 2000 simulated annealing runs. The red and green lines show the median value and the 16^{th} and 84^{th} percentile confidence levels

The idealized equivalent tensile fracture has an orientation consistent with the one of the lineaments from topography (Figure 17). It might correspond with subvertical synfolding fractures originated in the hinge zone of the Mount Cesen-Col Visentin (MCCV) Anticline, where a highly productive karst aquifer (following the notation of the International Hydrogeological Map of Europe) is present along the anticline structure (Figure 53).

We can speculate that this system of fold-related subvertical fractures represents relatively narrow structural features that may drain water from large areas and react to the related pressure changes, causing the observed anisotropic displacements at the GPS stations. Assuming a rigidity modulus of 30×10^9Pa and a uniform pressure change along the tensile fracture surface, with a geometry defined by the mean parameter values (red dashed line in Figure 53), the horizontal displacements can be modeled through a boundary elements approach (Ferrari *et al.*, 2016).

A boundary element crack model is made by a number of interacting dislocation elements (NDP), opening within an elastic medium, under assigned stress condition, prescribed at the centre of each dislocation element. The dislocation elements used in our model, resulting from choosing NDP=526, are squares with area of about 10 m^2. The NDP value has been chosen as a compromise between computational efficiency and accuracy of the dislocation representation.

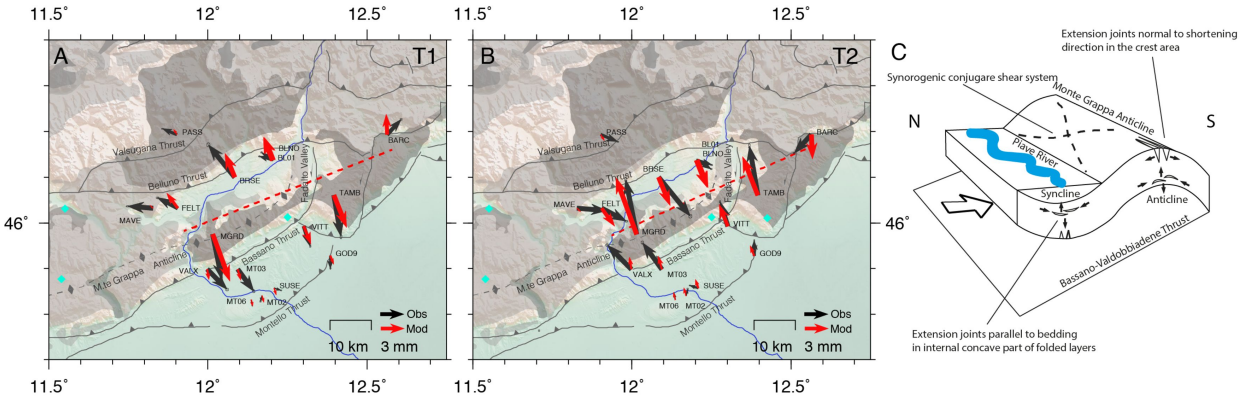

Figure 53: (A and B) Observed (black) and modeled (red) horizontal displacements during the T1 and T2 time intervals (see also Figure 24), respectively, using an effective vertical tensile dislocation (dashed red line). The blue line is the Piave River and the cyan diamonds show locations of major karst springs (Cavallo *et al.*, 2003). The dark and light gray areas represent highly productive fissured karst aquifers and low and moderately productive fissured karst aquifer from the International Hydrogeological Map of Europe 1:1,500,000 (*http://www.bgr.bund.de/ihme1500*). (C) Simplified sketch of the geological structure of the Belluno syncline and the Monte Grappa-Monte Cesen Anticline, with fold terminology from Ramsay and Huber (1983)

For the T1 and T2 intervals, a pressure increment of 790 kPa in ∼110 days and drop of 950 kPa in ∼450 days, respectively, minimizes the misfit between modeled (red arrows in Figure 53) and measured horizontal displacements. Similar root-mean-square misfit values of 2.1 and 2.6 mm are obtained by uniform opening of 4.3 cm and closing of 5.2 cm in the tensile dislocation model as well, capturing the first-order features of the original displacements. The pressure changes associated with opening and closing of the vertical tensile dislocation in area 2 correspond to a water level increase of ∼80 m during the opening phase (T1) and a water level drop of ∼97 m during the closure phase (T2). Groundwater fluctuations of the same order of magnitude (tens to hundreds of meters) over time spans like T1 and T2 (months) are common in high-developed karsts (Milanovic, 2005, 2014). Similar values of positive pressure changes (i.e., water level rise) can be expected for a second period of larger positive variations of V2, which is between November 2013 and February 2014 (T3 in Figure 24), after which there is a general negative trend of the dilatational strain lasting to 2017, with two smaller phases of positive trends in the winter 2015 and summer 2016. We can speculate that the same mechanism is active in the Lessini Mountains (area 1 of Figure 17) and the Classical Karst (area 3 of Figure 17), where subvertical strike-slip faults, oriented normal to the observed hydrogeodetic strain axes, are well developed and deep-rooted karst aquifers are present. In these two areas, however, additional cGPS sites would be necessary to better characterize the kinematic pattern of this deformation signal. Similarly, additional cGPS stations would be necessary to better describe the spatial extent of the hydrogeodetic signal around the Cansiglio Plateau, which would also help discriminating eventual different sources of deformation associated with the MCCV Anticline and the Cansiglio Plateau regions.

6.3 The FEM Model

The previous model does not take into consideration the topography and the different rock layers mechanical properties of area 2. For this reason we used the software COMSOL, based on finite-element method (FEM), to model the displacements reconstructed by IC2 taking into consideration the geological features of area 2.

The FEM methods are used to find approximate solutions to the partial differential equations (PDEs) that arise in geodynamic modeling (Islail-Zadeh and Tackley, 2010). It is performed by dividing the model domain into a number of sub-domains, called *finite elements*, and solving the PDEs for each of them. The solution for the entire domain is obtained through a recombination of the solutions obtained for each finite element.

We will discuss different possible sources of deformation that are compatible with the geologic features of the area in order to find the one that best reproduces the displacements reconstructed by IC2 and in particular, during the opening phase, the horizontal IC2 components, paying attention

not to generate vertical displacements that are large compared with the horizontal ones. In fact, if that happens, the hypothesis that the amplitude of the vertical displacements reconstructed by IC2 are, for most of the GPS stations, below the noise level, defined as the mean uncertainty (one standard deviation) of the GPS measurements, can not be true anymore.

6.3.1 Analytical test of Comsol

We decided to test the accuracy of the FEM implemented in COMSOL in reproducing the displacement field caused by a fracture in an homogeneous, isotropic, elastic space. In this particular setting, it's possible to analitically compute the displacement field caused by a pressurized crack for the constant-pressure case as done by Westergaard (1939), Sneddon and Elliot (1946), and Sneddon (1946).

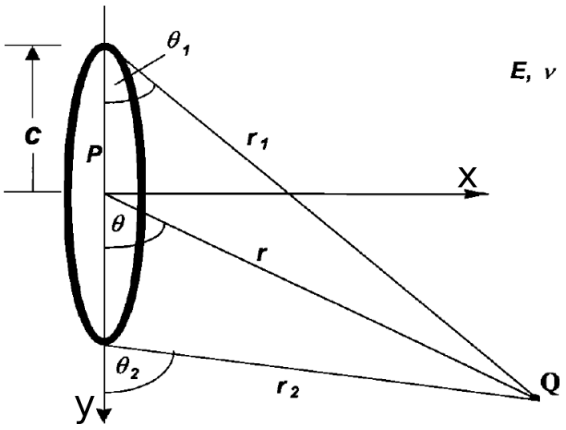

Figure 54: Geometry of the 2-D crack.

The geometry for this crack, shown in Figure 54, is rotated from Sneddon (1946) so that the crack height is $2c$, and all locations are measured by the three distance parameters r, r_1, and r_2, and the three angles θ, θ_1, and θ_2. The crack is uniformly pressurized at a level P in a material having a Young's modulus E and a Poisson's ratio ν.

The basic solution is from Westergaard (1939) in terms of a stress function, Z, given as

$$Z = P\left[\frac{z}{\sqrt{z^2 - c^2}} - 1\right] \tag{92}$$

where z is the complex variable, $z = y + ix$ and P is the pressurization of the crack. Furthermore

$$r_2 cos(\theta_2) = y - c \tag{93}$$

$$r_2 sin(\theta_2) = x \tag{94}$$

$$r_1 cos(\theta_1) = y + c \tag{95}$$

$$r_1 sin(\theta_1) = x \tag{96}$$

The displacements in the x and y direction, respectively u_x and u_y, are given by

$$\frac{E}{(1+\nu)} u_x = 2(1-\nu)\, Im\left[\bar{Z}\right] - x Re\left[Z\right] \tag{97}$$

$$\frac{E}{(1+\nu)} u_y = (1-2\nu)\, Re\left[\bar{Z}\right] - x Im\left[Z\right] \tag{98}$$

where the overbar represents the integral of the stress function Z with respect to z:

$$\bar{Z} = \sqrt{z^2 - c^2} - z \tag{99}$$

Noting that

$$z = re^{i\theta}, \qquad z^2 - c^2 = r_1 e^{i\theta_1} r_2 e^{i\theta_2} \tag{100}$$

we can write

$$Re[Z] = \frac{r}{\sqrt{r_1 r_2}} cos\left(\theta - \frac{1}{2}\theta_1 - \frac{1}{2}\theta_2\right) - 1 \tag{101}$$

$$Im[Z] = \frac{r}{\sqrt{r_1 r_2}} sin\left(\theta - \frac{1}{2}\theta_1 - \frac{1}{2}\theta_2\right) \tag{102}$$

$$Re[\bar{Z}] = \sqrt{r_1 r_2} cos\left(\frac{1}{2}\theta_1 + \frac{1}{2}\theta_2\right) - r\ cos(\theta) \tag{103}$$

$$Im[\bar{Z}] = \sqrt{r_1 r_2} sin\left(\frac{1}{2}\theta_1 + \frac{1}{2}\theta_2\right) - r\ sin(\theta) \tag{104}$$

Then, we can rewrite (97) and (98) as

$$u_x = \frac{P}{2\mu}\left[2(1-\nu)\left(\sqrt{r_1 r_2} sin\left(\frac{1}{2}\theta_1 + \frac{1}{2}\theta_2\right) - r\ sin(\theta)\right) - x\left(\frac{r}{\sqrt{r_1 r_2}} cos\left(\theta - \frac{1}{2}\theta_1 - \frac{1}{2}\theta_2\right) - 1\right)\right] \tag{105}$$

$$u_y = \frac{P}{2\mu}\left[(1-2\nu)\left(\sqrt{r_1 r_2} cos\left(\frac{1}{2}\theta_1 + \frac{1}{2}\theta_2\right) - r\ cos(\theta)\right) - x\left(\frac{r}{\sqrt{r_1 r_2}} sin\left(\theta - \frac{1}{2}\theta_1 - \frac{1}{2}\theta_2\right)\right)\right] \tag{106}$$

Once obtained the analytic results, we compare them with COMSOL results. We built a 1000 km long and 600 km large rectangle of homogeneus material. In the middle of it, we created a rectangle fracture 1 km long and 1 cm wide. Since the fracture is hundreds of km far from the boundaries, their effects are minimized. The boundary conditions applied are fixed constraints to all the sides of the rectangle and to the top and bottom of the fracture. In the vertical sides of the fracture, uniform pressure is applied. The mesh used is user-controlled, calibrated for general physics. The element size parameters are:

- Maximum element size: 10 km
- Minimum element size: 1 cm
- Maximum element growth rate: 1.1
- Curvature factor: 0.2
- Resolution of narrow regions: 1

In Figure 55 and 56 we plot the displacements computed through analytical formulas and modeled by COMSOL, using $E = 60$ GPa, $\nu = 0.25$, $P = 20$ MPa . We observe that COMSOL results are generally in good agreement with the analytical ones, even if COMSOL seems to underestimate analytical results. We also found (not shown in any figures) that if we keep the top and bottom bases as free, they extend and cause horizontal displacements larger than the analyical ones. Anyway, since we do not want the fracture dimensions to change, we keep the boundary condition that states that the top and bottom bases do not vary.

We tried to reduce the discrepancies by using finer meshes, but we observed that the results did not change, implying that the mesh used was already good enough. In order to reduce the ratio between initial opening and width, improving the representation of a crack, we considered a fracture that is 10 km long along the dip instead of 1 km. Nonetheless, the results obtained were basically the same obtained in the initial case.

6.3.2 How we model 3D displacements in 2D

In order to characterize the transient hydrological signal (IC2) in the portion of area 2 we described at the beginning of this chapter, we tried to model the displacements reconstructed by IC2 in 9 GPS stations (Figure 57). Having such a relative small number of data, the creation of a 3-D model seems to be an over-complication. Then, making the approximation that the features of the MCCV anticline and Val Belluna are constant along the SW-NE direction, we decided

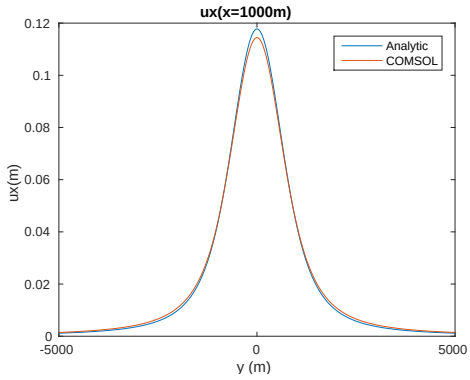

(a) u_x, Q=(1 km; -5 km : 5 km)

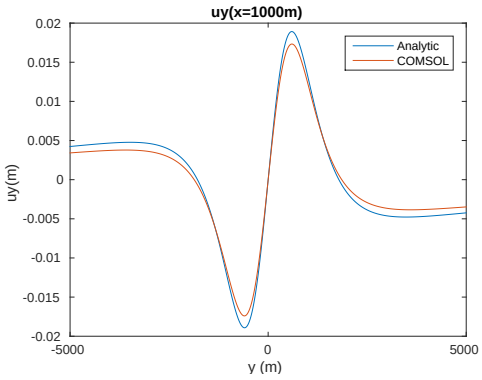

(b) u_y, Q=(1 km; -5 km : 5 km)

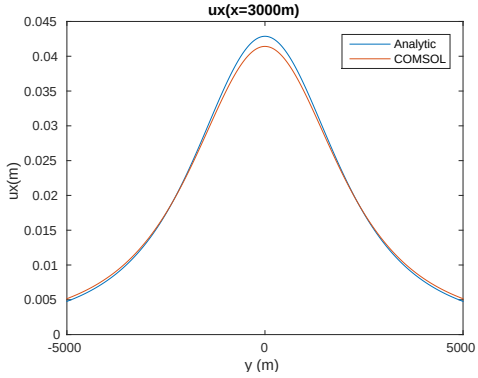

(c) u_x, Q=(3 km; -5 km : 5 km)

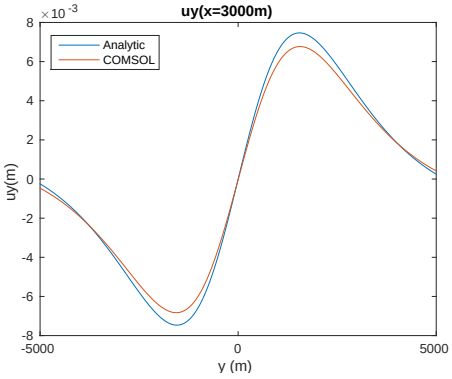

(d) u_y, Q=(3 km; -5 km : 5 km)

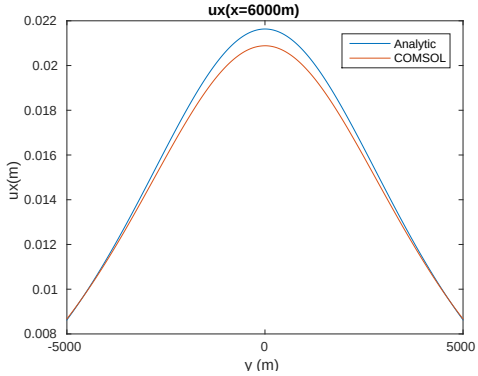

(e) u_x, Q=(6 km; -5 km : 5 km)

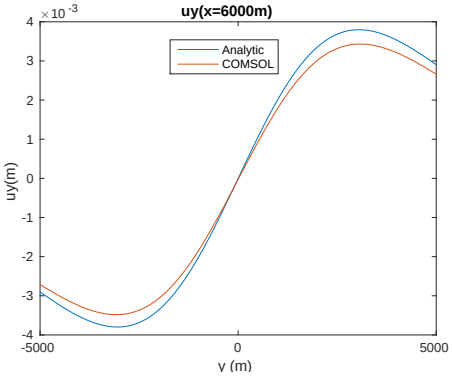

(f) u_y, Q=(6 km; -5 km : 5 km)

Figure 55: Displacements in Q caused by a vertical crack as in Figure 54 (blue) and computed by COMSOL (red). Focus on the variations along y axis.

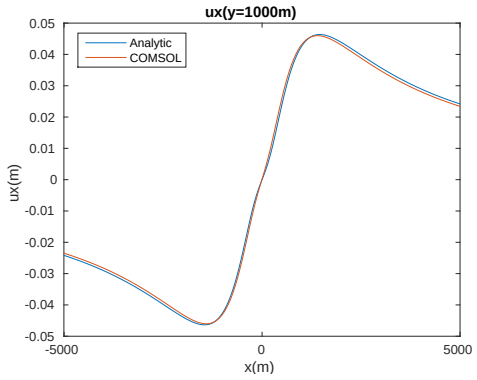

(a) u_x, Q=(-5 km : 5 km; 1 km)

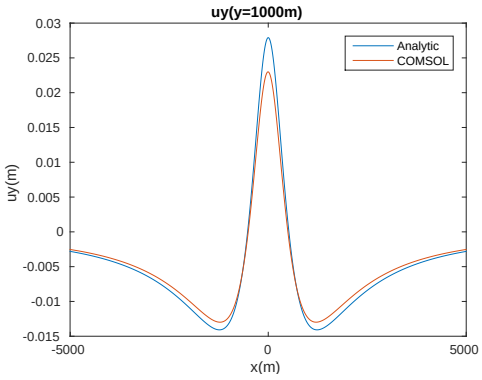

(b) u_y, Q=(-5 km : 5 km; 1 km)

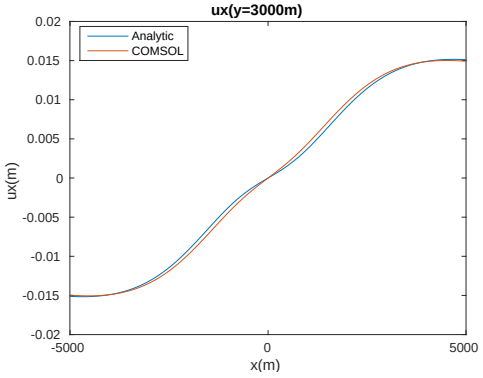

(c) u_x, Q=(-5 km : 5 km; 3 km)

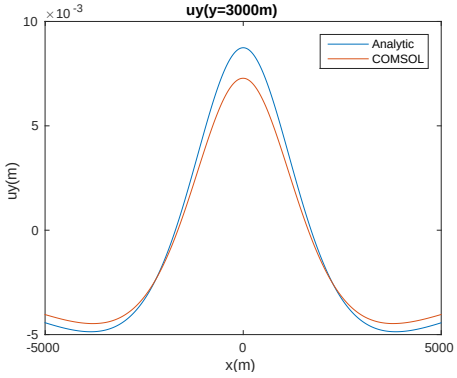

(d) u_y, Q=(-5 km : 5 km; 3 km)

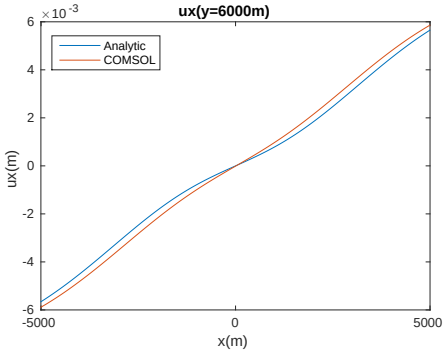

(e) u_x, Q=(-5 km : 5 km; 6 km)

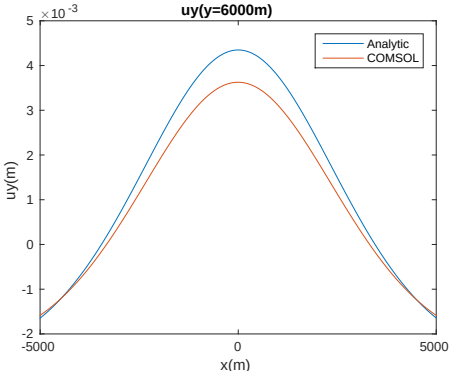

(f) u_y, Q=(-5 km : 5 km; 6 km)

Figure 56: Displacements in Q caused by a vertical crack as in Figure 54 (blue) and computed by COMSOL (red). Focus on the variations along x axis.

to develop 2-D FEM models with COMSOL. Then, we reconstructed displacements that have only one horizontal component and a vertical component. Since the results obtained by the ICA analysis are 3-D, we have to find an effective way to project the east and north component of the displacement into a single horizontal coordinate. The other problems we have to face are how to compute the distance between the GPS stations and the source of deformation and evaluating the relative distance between the stations. We decided to use Google Earth to plot the distance between each station and the south-eastern edge of the MCCV anticline, which corresponds to the Bassano-Valdobbiadene thrust (Figure 57). Then, we projected the horizontal displacements reconstructed by IC2 along the direction perpendicular to the Bassano-Valdobbiadene thrust. We assumed, when computing the projections of the displacements (d_{proj}) reconstructed by IC2, that the Bassano-Valdobbiadene thrust is always oriented in the direction 68.5° N. Then:

$$d_{proj} = u_{east} \times cos(68.5°) - u_{north} \times sin(68.5°) \tag{107}$$

Where u_{east} and u_{north} are the east and north components of the displacement reconstructed by IC2; in addition, d_{proj} is positive when directed toward south-east.

The orientation chosen for the Bassano-Valdobbiadene thrust is the same of the fracture we modeled by using LibHalfspace in Serpelloni *et al.* (2018).

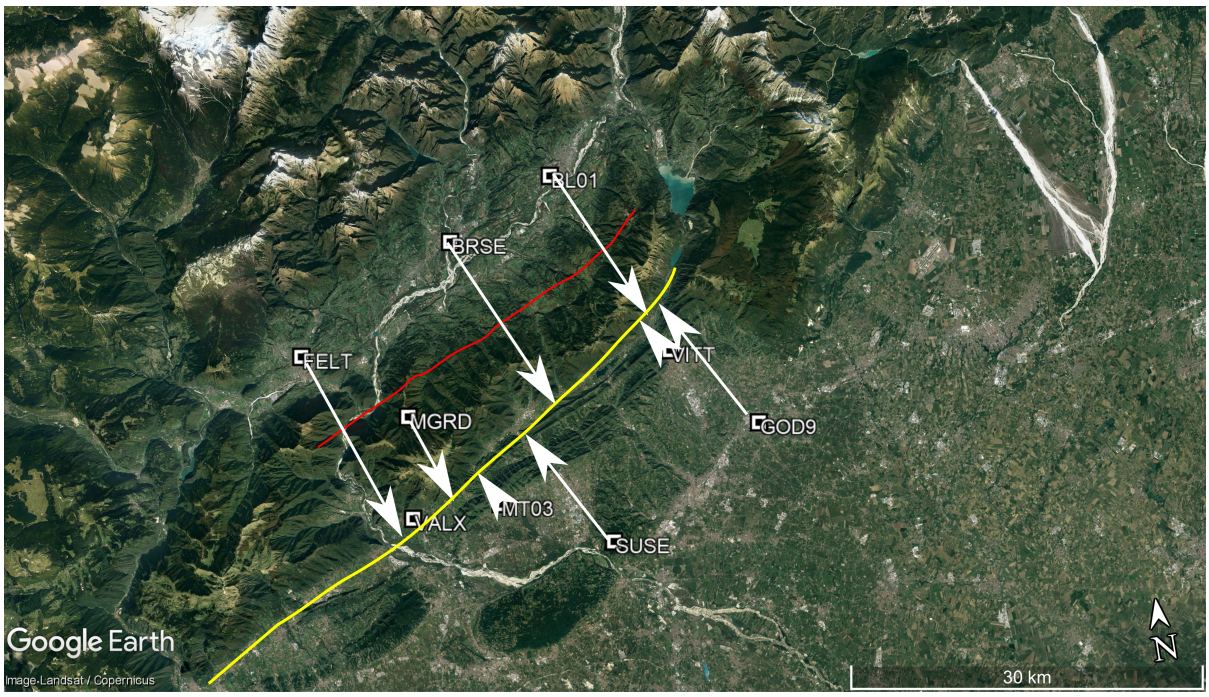

Figure 57: Yellow line: Bassano-Valdobbiadene thrust fault (from Carta Geologica d'Italia, foglio Belluno), white arrows: distances between the GPS stations (white squares) and the Bassano-Valdobbiadene thrust fault. Red: Backthrust of the Bassano-Valdobbiadene thrust (from Carta Geologica d'Italia, foglio Belluno), chosen as reference source of deformation.

6.3.3 The reference source of deformation

We tested several sources of deformation (Appendix C) that could generate the displacements reconstructed by IC2 during the opening phase T1, each one having a link with the topographic and geologic features of the investigated area. As a result, we select as a reference source of deformation a fracture that reaches the surface, is 0.1 m large and whose dip angle is 69° (Figure 66). The width of the fracture is 1 km according to the one described in Serpelloni *et al.* (2018). The position and the inclination of the fracture are selected in agreement with the features of the backthrust of the Bassano-Valdobbiadene thrust fault that is present in Val Belluna (57). In fact, as shown by Faulkner *et al.* (2010), the permeability and the fracturation of a medium increases next to a fault, so that the presence of permeable fractures in these sectors is more likely. The high level of fracturation, as long as the karstic features of the area, can make the fractures connected

for several meters, generating the source of deformation schematically represented in this section. Even if our fracture is constrained from a geological point of view, we will consider the effects of different dip angles and bottom depths with respect to the reference model (section 6.4.5).

Since it is relevant for comparing different sources of deformation here we also define the noise of data as it follows. The noise in the vertical component of the displacement has been computed as the mean value of the uncertainty (1 standard deviation) considering all the time steps. The noise in the horizontal component has been computed by summing the mean uncertainty in the east and north component, projected in the direction perpendicular to the Bassano-Valdobbiadene thrust: $noise_{horizontal} = abs(noise_{east} \times cos(68.5°)) + abs(noise_{north} \times sin(68.5°))$.

6.4 Homogeneous domain with a flat free surface

We start considering the simple case of the displacements generated by the reference fracture, when applying a uniform pressure of 1 MPa on its walls (Longuevergne *et al.*, 2009). We considered an homogeneous elastic domain: a 10^6 m long and $5{\times}10^5$ m wide box having the physical properties of Maiolica (Young's modulus 59 GPa, Poisson's ratio 0.26, Barla *et al.*, 2007).

6.4.1 Sensitivity to the initial opening of the fracture

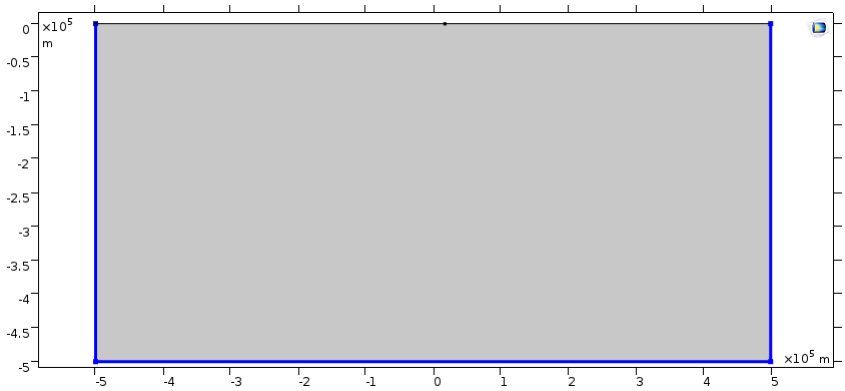

(a) Fixed constrain

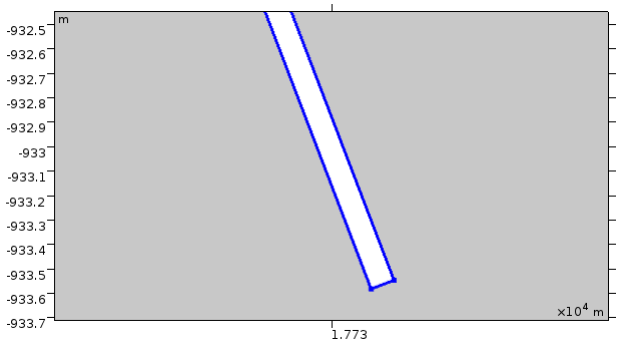

(b) Boundary load: pressure

Figure 58: Boundary conditions, highlighted in blue, applied to the case of a fracture in a homogeneous domain with a flat free surface. (a) Fixed constraints; (b) Boundary loaded by pressure.

In section 6.3.1 we arbitrarily selected $d = 0.1$ m as the initial opening of the fracture. In this subsection, we analyze displacement patterns considering different values of d; in particular we made test for $d = 1$ m, 0.1 m, 0.01 m, 0.001 m.

The boundary condition applied to the walls and to the bottom of the fracture is the same: boundary load of pressure type. We applied to each part of the fracture the same amount of pressure. The other boundary conditions applied to the domain are fixed constraints to the rectangle sides that embed the fracture, except for the top basis that represents the surface, which is free to move (Figure 58).

Mesh type	Maximum element size (m)	Minimum element size (m)	Max element growth rate	Curvature factor	Resolution of narrow regions	Domain elements	Boundary elements
Extremely fine	10000	20	1.1	0.2	1	30637	765
Extra fine	20000	75	1.2	0.25	1	7019	339
Finer	37000	125	1.25	0.25	1	3299	225
Fine	53000	300	1.3	0.3	1	1674	146
Normal	67000	300	1.3	0.3	1	1557	137
Coarse	100000	2000	1.4	0.4	1	572	74
Coarser	130000	6000	1.5	0.6	1	398	62
Extra coarse	200000	16000	1.8	0.8	1	234	44
Extremely coarse	330000	50000	2	1	0.9	347	65

Table 15: Parameters of the *physics − controlled* mesh, based on general physics.

We observe (Figure 59) that the horizontal displacements obtained are basically the same. Furthermore, the horizontal components are about one order of magnitude larger than the vertical ones.

The choice of $d = 0.1$ m seems reasonable: the horizontal displacement pattern is the same obtained for other values of d; considering that a choice of a larger initial opening, from a physical point of view (Lancia *et al.*, 2018), is unlikely.

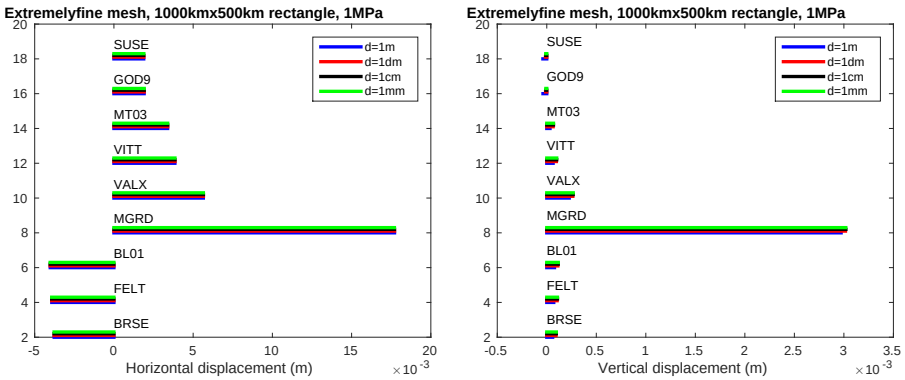

(a) Horizontal (b) Vertical

Figure 59: Pattern of displacement considering different values of the initial opening d of the fracture represented in Figure 58, assuming an overpressure of 1 MPa. Maiolica is the material used for the homogeneous halfspace. Horizontal displacement is positive when it is toward S-E; vertical displacement is positive when upward.

6.4.2 Influence of the mesh

In this subsection we discuss the effect of considering different kinds of mesh. We tested each of the nine meshes of the type *physically based* proposed by COMSOL, from extremely fine to extremely coarse. We observe that the choice of the mesh does not drive to very different results in terms of patterns, but the finer is the mesh, the larger the absolute displacements are (Figure 60b). The details of the meshes used are listed in Table 15.

6.4.3 Influence of the boundaries

In this subsection we discuss the influence of the boundaries on the displacement field generated by the opening of the fracture. We considered the fracture embeded in rectangles of different size, with the base always two times larger than the height, and studied the displacement patterns. We considered an *extremely fine* mesh.

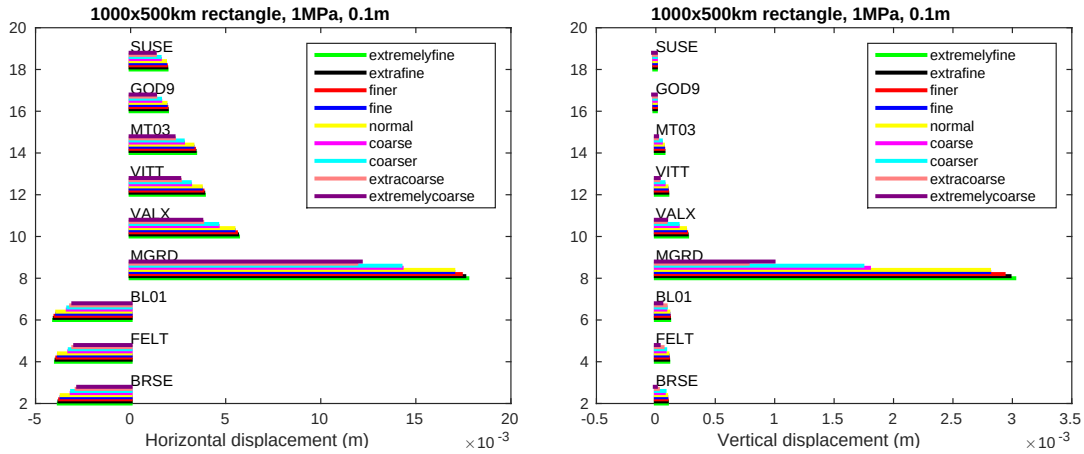

(a) Horizontal (b) Vertical

Figure 60: Same as Figure 59, considering different kind of mesh. The initial opening is 0.1 m.

When we consider horizontal displacements (Figure 61a), we observe that using a 100×50 km rectangle the results obtained are a little bit smaller than the ones from base lengths larger than 200 km. In fact, the other cases considered give rise to very similar results. On the other hand, considering vertical displacements (Figure 61b), the results obtained are equivalent only considering the three largest rectangles.

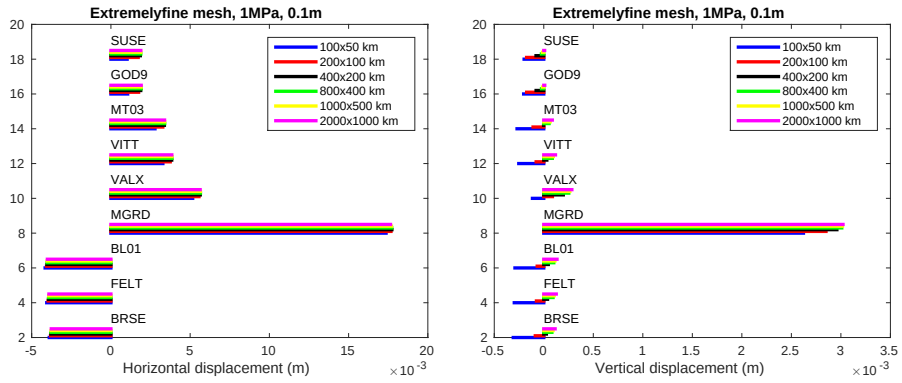

(a) Horizontal (b) Vertical

Figure 61: Same as Figure 59, considering different sizes for the rectangle where the fracture is placed. We used an extremely fine mesh.

6.4.4 Comparison with LibHalfSpace

We decided to make another test to compare the COMSOL and LibHalfSpace results at the GPS stations for the case of a vertical fracture reaching the free surface. We built in LibHalfSpace, which assumes 3-D sources, a 300 km long, assuming that it could be considered as infinite, and 10 km wide fracture, using 500 as value for the discretization parameter (NDP). Similarly to what done in section 6.3.1, we considered the displacements in the plane z=0 ortogonal to the fracture. The width of the fracture is unlikely for this case study, but here we focus only on the comparison between COMSOL and LibHalfSpace, and such a long fracture is necessary to get a good discretization in LibHalfSpace. The displacements resulting by applying an overpressure of 2 MPa on fracture walls, computed by COMSOL and LibHalfSpace at the GPS stations (Figure 62) are in a very good agreement both for the vertical and the horizontal component of the displacement. It is worth noting that in COMSOL we used an extremely fine mesh, a 1000 km × 500 km domain and an initial opening of 1 dm, in agreement with the results of sections 6.4.1, 6.4.2 and 6.4.3.

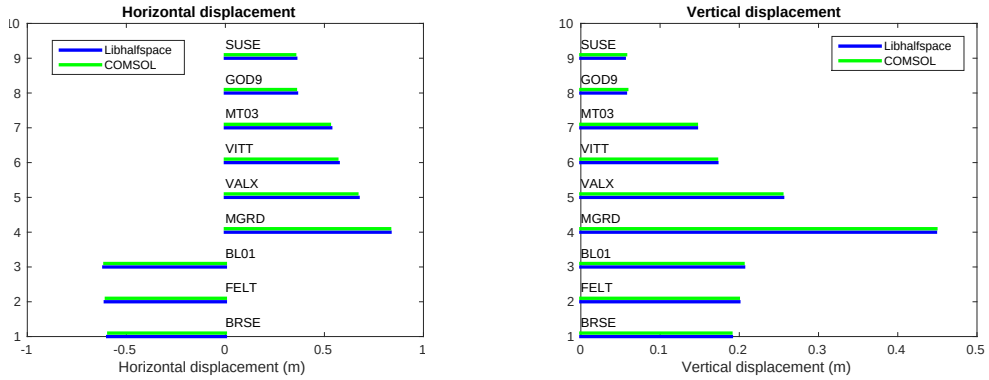

(a) (b)

Figure 62: Absolute horizontal (a) and vertical (b) displacements generated by a vertical fracture extending from the surface to -10km in a homogeneous domain with flat surface. Results from LibHalfspace (blue lines) and from COMSOL (green lines) are shown.

6.4.5 Results

Here we evaluate the displacement reconstructed by ICA during T1 and modeled by COMSOL, each one normalized by its standard deviation (Figure 63). In this way we mainly evaluate the displacement pattern generated by each model, but we will also provide information about the modeled absolute displacement. For horizontal displacements, the standard deviation is 6.8 mm for the COMSOL model and 4.1 mm for ICA; while for the vertical displacements it is 1.0 mm for COMSOL and 2.3 mm for ICA.

We also show the noise affecting the IC2 component of the reconstructed time series (green arrows in Figure 63b,c). We observe that in the vertical component, all the displacements reconstructed by IC2 are smaller than the noise level. In the horizontal SUSE is smaller than the noise, while GOD9 and BL01 are close but smaller than the noise. Focusing on horizontal displacements we will also compute the root-mean-square ($RMSE$, defined in equation 108) between the normalized horizontal displacement reconstructed by ICA and modeled by COMSOL, to quantitatively compare the capability of different sources of deformation to reproduce ICA results.

$$RMSE = \sqrt{\frac{\sum_{i=1}^{N} \left(\frac{u_i}{std(u)} - \frac{U_i}{std(U)} \right)^2}{N}} \tag{108}$$

where N is the number of GPS stations (9 in our case), u_i is the horizontal displacement modeled by COMSOL at the i-th station, U_i the one reconstructed by ICA. $std(u)$ and $std(U)$ are the standard deviations of the COMSOL and ICA horizontal displacements, respectively.

The vertical displacements modeled in COMSOL, whose absolute values are generally two orders of magnitude smaller than the horizontal ones, fail to reproduce the pattern of the ICA displacements (Figure 63c). On the contrary this source of deformation seems to be good in describing the horizontal displacements reconstructed by IC2, in comparison with the other sources considered in the appendix. In particular it provides a RMSE=0.4907.

Moreover we made some tests varying the dip angle and the bottom depth of the reference fracture: we consider a fracture having a variable dip but always the same width, i.e. 1000 m (Figure 64); and a fracture having a dip of 69° but reaching variable depths, from -300m to -1000m (Figure 65). Both in Figure 64 and 65 the fracture always reaches the free surface in the same point. We observe that the displacement patterns, when normalized by standard deviation, are not very sensitive to the variation of the bottom depth or dip. When looking at absolute values of displacement, great differences emerge in the case of variable bottom depth. This is because the wider a fracture is, reaching greater depths, the larger the displacements caused by it are. As for the comparison with LibHalfSpace, we used an extremely fine mesh, a 1000 km × 500 km domain and an initial opening of 1 dm, in agreement with the results of sections 6.4.1, 6.4.2 and 6.4.3.

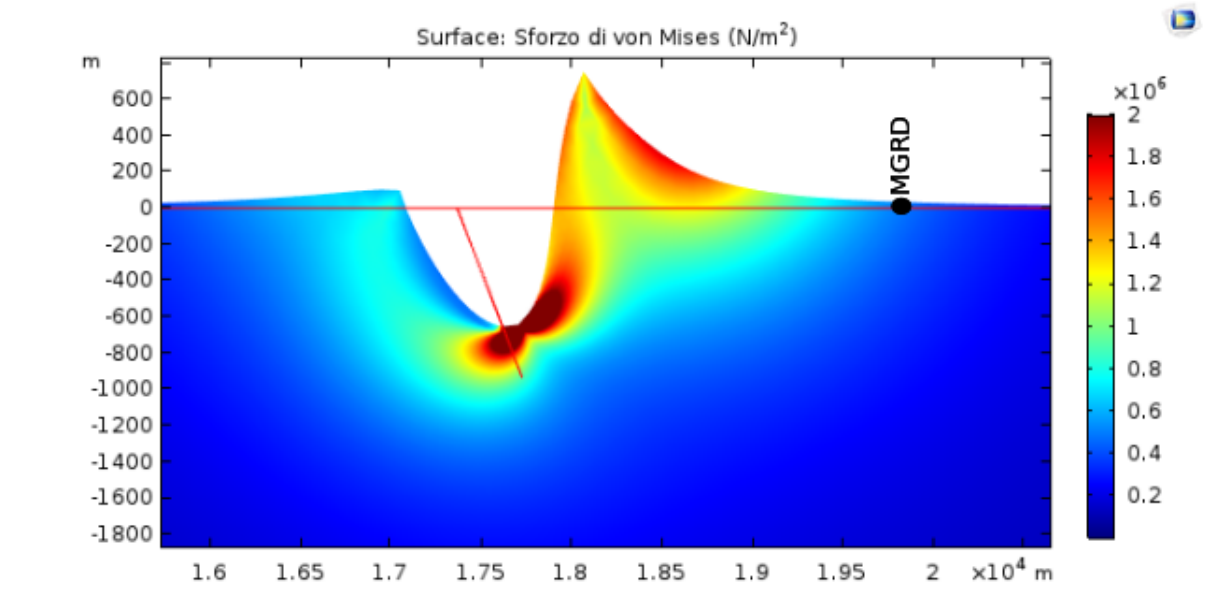

(a)

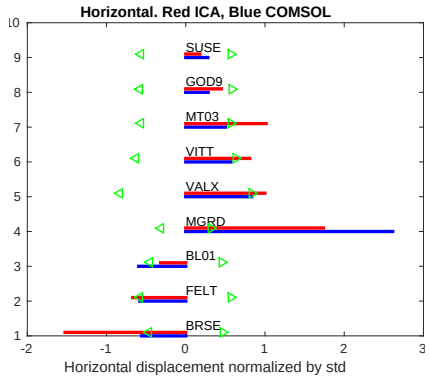

(b)

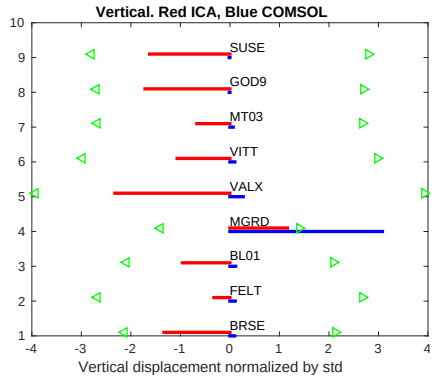

(c)

Figure 63: (a) Displacement pattern and Von Mises stress (Pa) generated by the fracture opening. The amplitude of the displacements are multiplied by a scale factor of 10^4 for a better visualization. The red lines represent the undeformed configuration. (b) and (c) horizontal and vertical displacements reconstructed by IC2 (red) and computed by COMSOL (blue), using the source of deformation shown in Figure 63a. Horizontal displacement is positive when it is toward S-E; vertical displacement is positive when upward. Displacements are normalized by their standard deviatons. The green arrows indicate the noise level, normalized dividing by the standard deviation of the displacements reconstructed by IC2. The standard deviation of horizontal displacements is 6.8 mm for the COMSOL model and 4.1 mm for ICA; while for the vertical displacements it is 1.0 mm for COMSOL and 2.3 mm for ICA.

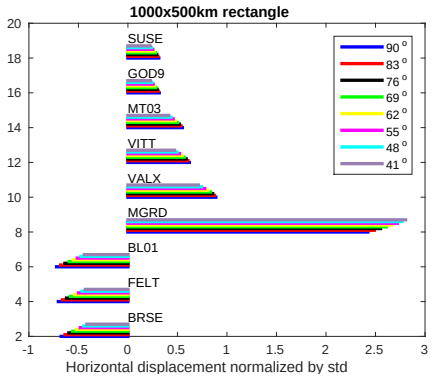

(a) Horizontal displacement normalized by std

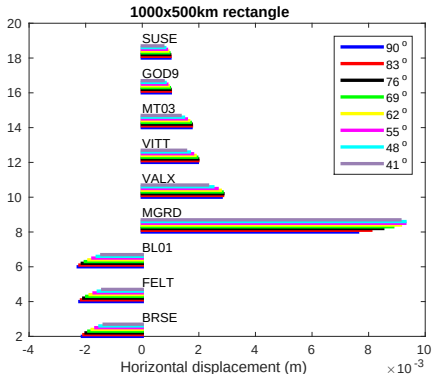

(b) Horizontal displacement (m)

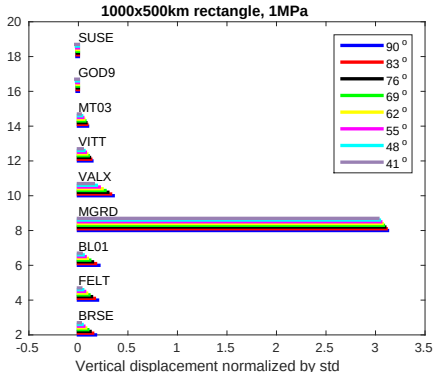

(c) Vertical displacement normalized by std

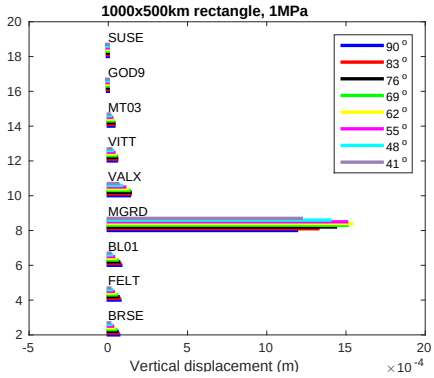

(d) Vertical displacement (m)

Figure 64: Horizontal (a,b), vertical (c,d) displacements generated by fractures with different dip angles, indicated in the legend of the panels, reaching the same depth(-300 m). We consider an homogeneous domain with a flat free surface.

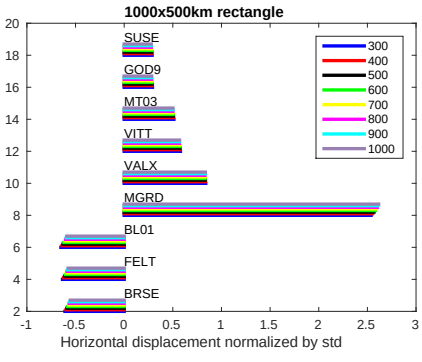

(a) Horizontal displacement normalized by std

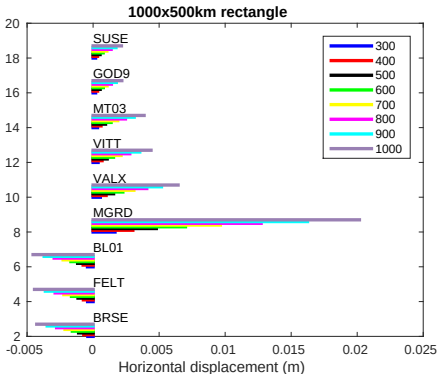

(b) Horizontal displacement (m)

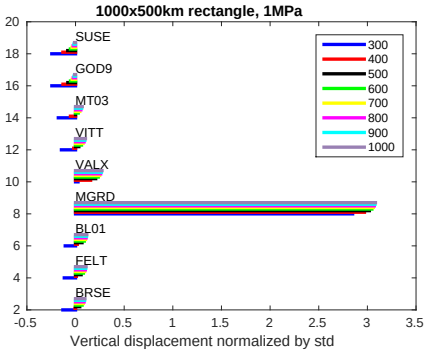

(c) Vertical displacement normalized by std

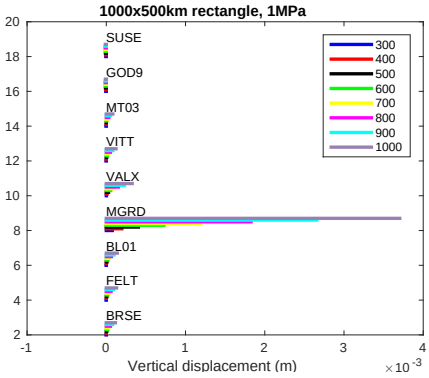

(d) Vertical displacement (m)

Figure 65: Horizontal (a,b) and vertical (c,d) displacements generated by fractures with the same dip angle (69°) reaching different depths, indicated in the legend of the panels (in meters). We consider an homogeneous domain with a flat free surface.

6.4.6 Von Mises Stress

In some figures of this chapter, like Figure 63a, we plot both a portion of the domain deformed by the source of deformation, and the Von Mises stress σ_v generated from it. σ_v, defined in equation 109, is a scalar measure of the deviatoric stress and helps to predict when a material start to yield: it happens when the yield's strenght value of a material is reached by the Von Mises stress. It is worth noting (Figure 63a) that the reference fracture tends to concentrate σ_v at the surface and closely below its bottom tip.

$$\sigma_v = \sqrt{\frac{1}{2}\left[(\sigma_{xx} - \sigma_{yy})^2 + (\sigma_{yy} - \sigma_{zz})^2 + (\sigma_{zz} - \sigma_{xx})^2\right] + 3\left(\sigma_{xy}^2 + \sigma_{yz}^2 + \sigma_{zx}^2\right)} \tag{109}$$

6.5 Including domain complexities: topography and layering

In section 6.4, the only information we used to link the source of deformation with the geological features of the area is the dip of the fracture, which follows the orientation of a backthrust fault of the Val Belluna. Here, we discuss how the inclusion of the topography and the stratification of the geological profile of the area (Figure 66 and Table 16) and layering may cause variations in the displacement patterns previously obtained, maintaining a 1000 km $\times$ 500 km domain, an initial opening of the reference fracture of 1 dm and a uniform overpressure on the fracture walls of 1 MPa (Longuevergne *et al.*, 2009).

6.5.1 The effect of topography in a homogeneous domain

The inclusion of a topography that is representative of the area is not straightforward: we have to deal with the problem that the altimetry profile that crosses each GPS station, parallel to the direction along which d_{proj} is computed, is variable. Then, we defined a simple "mean" altimetry profile that is representative of all the stations considered (Figure 66). As in the previous section we assume the same elastic properties of Maiolica (Table 16).

The results obtained (Figure 67) do not change much with respect the case of flat surface. We just observe that the vertical displacement of VALX has the same sign of ICA unlike the flat case. Furthermore, when we look at the ratio between horizontal and vertical displacements, we found that the horizontal ones are still one order of magnitude larger than the vertical ones. The resulting $RMSE$ is 0.5238 slightly worse than the flat-surface case.

6.5.2 The effect of medium heterogeneities

From now on we model the displacement field generated by the same fracture described in section 6.5.1, taking into account both the topography and the stratification of the geological profile of the area (Figure 66 and Table 16). It's clear that we had to face the problem of realizing a geological profile that is variable when considering different GPS stations, analogously to what discussed when we decribed the process of topography inclusion. Because of that, the resolution of the profile is not high, but we decided to include all the layers reported in the geological maps available for the Val Belluna. It is worth noting that the layers showed in Figure 66 extend horizontally until the end of the domain, where they encounter the vertical boundaries. Since the horizontal domain is 1000 km long, we could not effectively represent in a figure the entire horizontal stratification. From Figure 66 we see that the upper part of the backthrust fault, which we consider as a possible source of deformation, extends from the surface down to a depth of -300 m, so that the width is about 1 km as in the flat-surface case. It is worth noting that the choice of a bottom depth of -300 m is arbitrary: in order to constrain it additional hydro-geological data would be necessary, but they are not available in this study area. In section 6.6.1 we will discuss this problem in more detail.

For the horizontal displacement patterns (Figure 68b), the results obtained when considering stratification are in good agreement both with the case where stratification is not included (Figure 67) and the simplest case without topography (Figure 63); to be more precise according to the $RMSE$ criterium the agreement slightly decreases ($RMSE = 0.6033$). When considering vertical displacements, we observe that the layered domain is the case that better reproduces the ICA displacement pattern; furthermore, the Von Mises stress values increases.

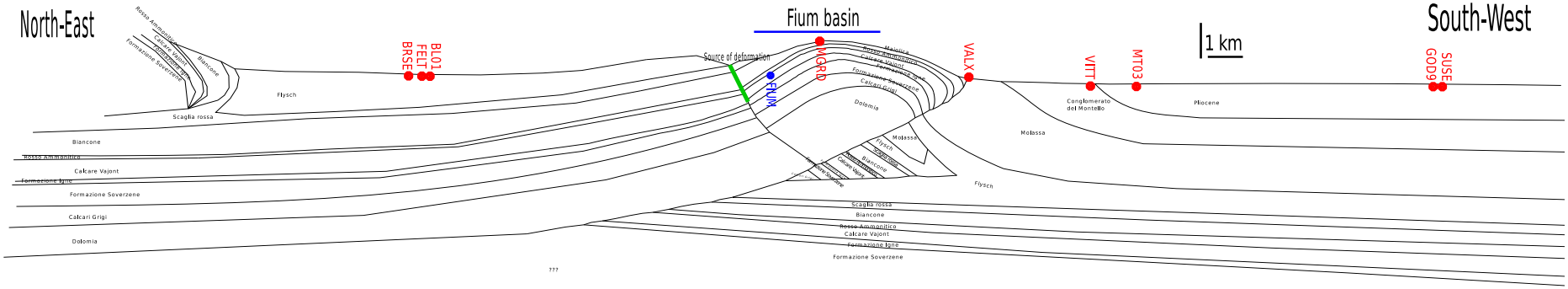

Figure 66: Profile used in COMSOL, built starting from the geological and topographic information of Figure 51. Red dots: position along the profile of the GPS stations. Green line: reference source of deformation.

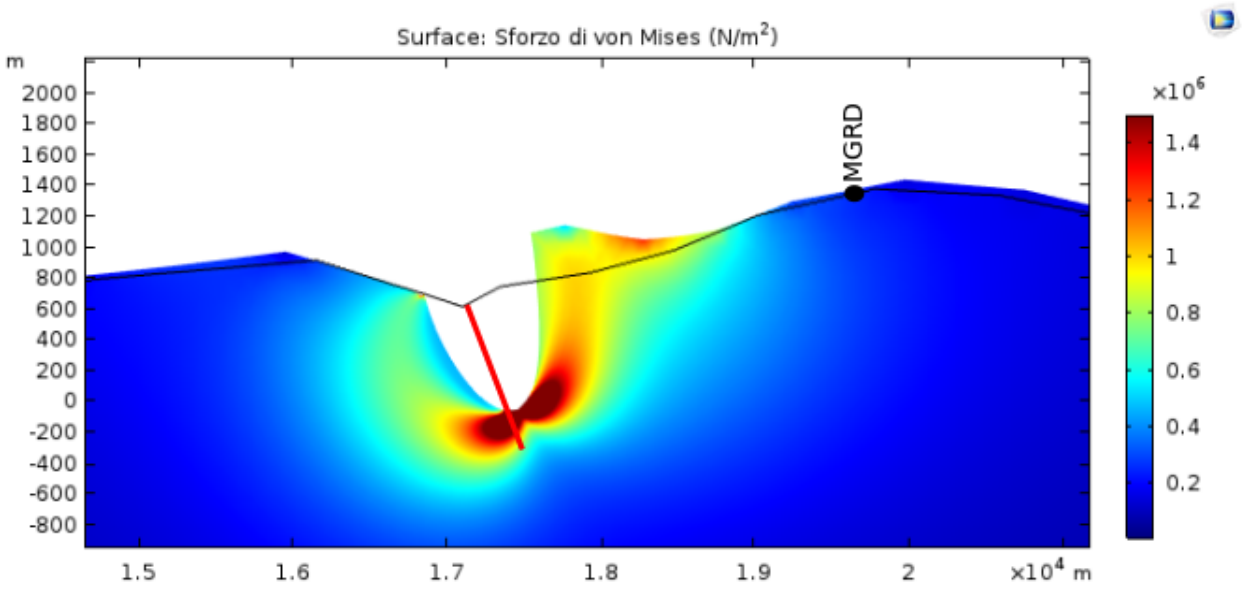

(a)

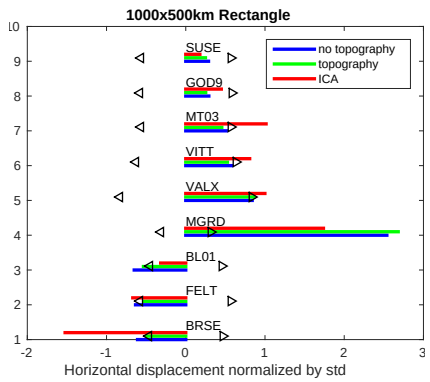

(b)

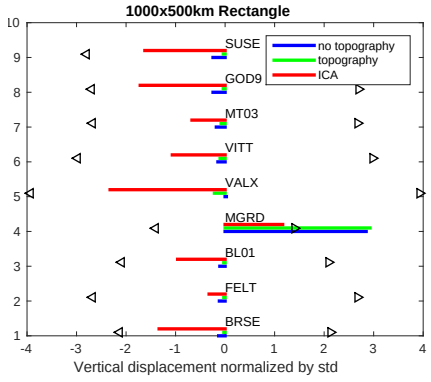

(c)

Figure 67: (a) Same as Figure 63 with a domain bounded upperly by a realistic topography (black line). (b and c) the black arrows indicate the noise level, normalized dividing by the standard deviation of the displacements reconstructed by IC2. The standard deviation of horizontal displacements is 6.8 mm for the COMSOL model and 4.1 mm for ICA; while for the vertical displacements it is 1.6 mm for COMSOL and 2.3 mm for ICA.

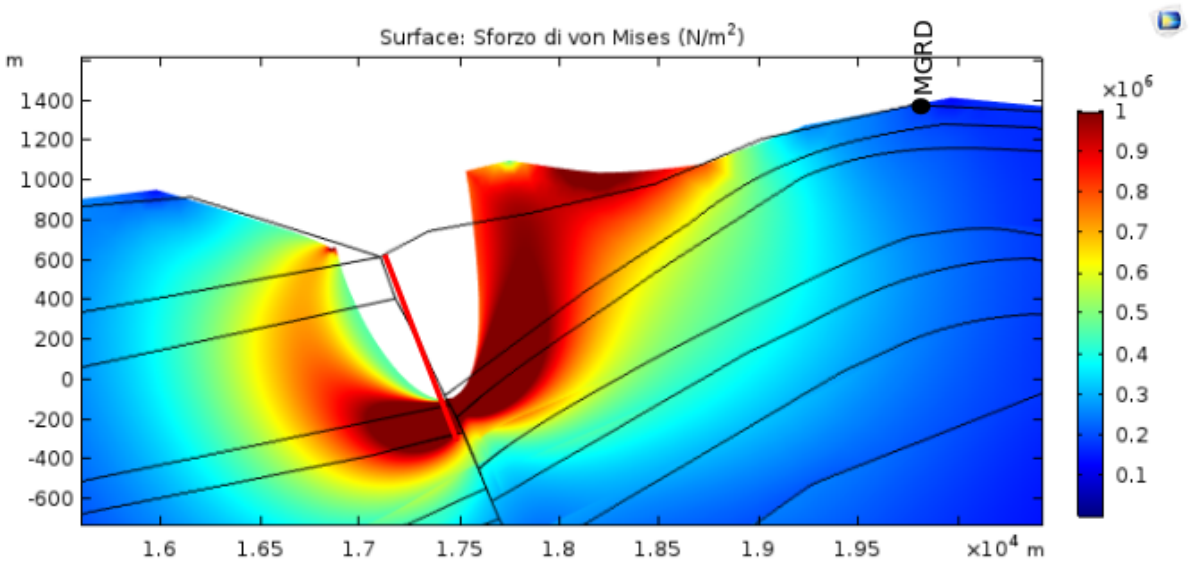

(a)

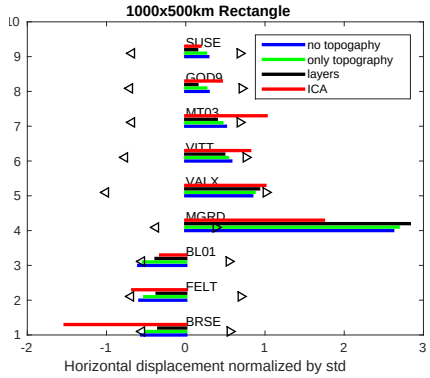

(b)

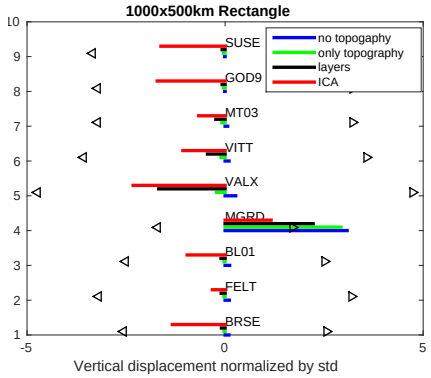

(c)

Figure 68: Same as Figure 67 with a different domain accounting for topography and elastic heterogeneities as in Figure 66. The standard deviation of COMSOL displacements is 7.3 mm for the horizontal components and 2.1 mm for the vertical.

Rock type	Young's modulus [GPa]	Poisson's ratio
Maiolica	59	0.26
Calcare del Vajont	70	0.35
Rosso Ammonitico	62	0.33
Formazione di Igne	64	0.3
Formazione di Soverzene	69	0.3
Flysh	26	0.2
Scaglia Rossa	38	0.3
Dolomite	95	0.32
Conglomerato Montello	26	0.2
Molassa	26	0.2
Calcari Grigi	71	0.25
Pliocene sediments	15	0.35

Table 16: Rock parameters used in COMSOL, taken from Barla *et al.*, 2007; Superchi, 2012; Bragato *et al.*, 2012; Fasiol, 2010; Anselmi *et al.*, 2011.

In this case, we could not use the physics-controlled mesh with extremely fine resolution, as in 6.5.1, because the resolution of the mesh was too low where the fracture intersects the surface that divide two different layers. Then, we used a user-controlled mesh, selecting the same parameters that characterize the extremely fine mesh (Table 15) except for the *minimum element size*, that we selected equal to 0.01 m.

Tilt computations Even if we do not have data at disposal for the MCCV anticline, in this paragraph, we compare the tilting expected at the stations in the half-space case and in the case with topography and layering (Figure 70).

The tilt of a station is computed by evaluating the displacement of two points at the same altitude of the station, with horizontal positions that are +10 m and -10 m with respect to the stations. In particular, if we call dy' the distance in the vertical component of the two stations and dx' the horizontal one after the application of the source of deformation, the tilt angle b is computed as (Figure 69):

$$b = tan^{-1}\left(\frac{dy'}{dx'}\right) \tag{110}$$

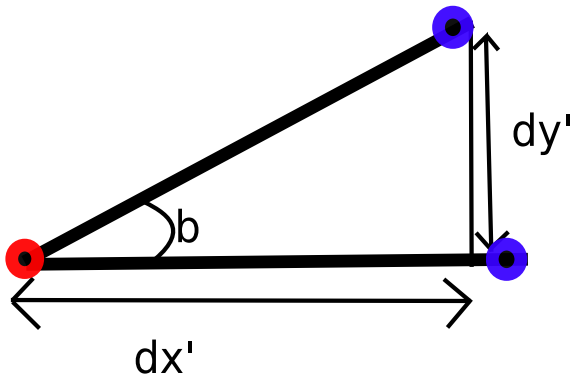

Figure 69: Schematic view of the tilting. The red dot represent the point located -10 m with respect the GPS station (kept fixed for simplicity), the blue one is located +10 m and moves upward.

When we compare the tilt patterns of the three cases (Figure 70), we observe that not considering the topography and layering causes smaller tilting in terms of absolute values, especially in MGRD and VALX. In VALX we observe the largest differences among the models: not including the topography causes a change of sign of the tilting; in addition including the layering causes a much larger tilt than the case of homogeneous domain.

For the layered domain case we computed how tilt varies assuming both different dip angles, keeping fixed the fracture bottom depth (-300 m) and the intersection point with the free surface, and variable fracture bottom depths once set the dip angle at 69° (Figure 71).

We observe that the tilt, when normalized by standard deviation, is not very sensitive to the variation of the depth or dip. When looking at absolute values of displacement and tilting, great differences emerge due to increasing values of the fracture width, both caused by increasing values of the bottom depth and decreasing values of the dip. A larger width causes larger displacements, as we already noticed at the end of section 6.4. This is because the wider a fracture is, the larger the depths it reaches and the displacements caused by it are.

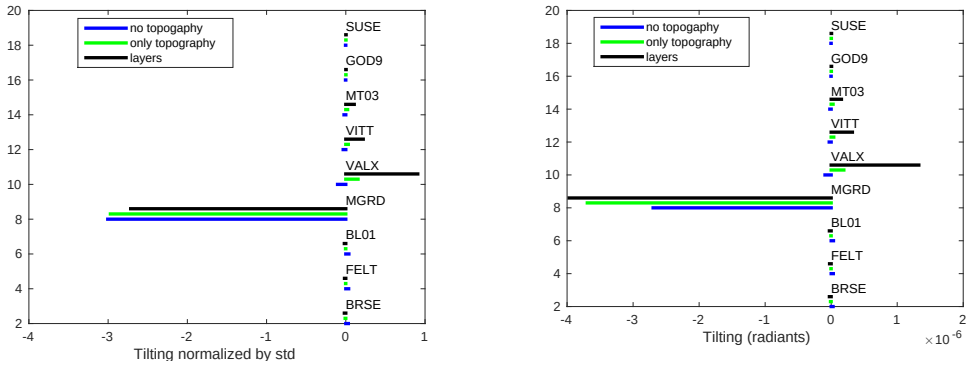

(a) Tilting normalized by std

(b) Tilting (radiants)

Figure 70: Values of tilting normalized by std (a) and absolute (b) considering the same sources of deformation of Figure 68.

6.5.3 Deep fracture

In the previous sections, we have always considered a fracture that reaches the free surface; anyway, there are no evidences that this is the most realistic way to represent the source of deformation. Then, in this subsection we study the displacement field generated by a fracture that does not reach the free surface. This fracture is assumed as 1000 m wide, its bottom depth is - 400 m and it has a dip angle of 69° (Figure 72a). The domain extension (1000 km × 500 km) and initial opening (0.1 m) is the same of the fractures previously discussed. In addition, the mesh used is the same of section 6.5.2.

We observe (Figure 72b,c) that the pattern of the horizontal displacement is essentially the same of what obtained by using a fracture that reaches the free surface, in fact $RMSE = 0.5983$.

The standard deviation of the horizontal and vertical displacements is 2.5 mm and 0.8 mm, respectively about half the correspondent values related to IC2. This means that a buried tensile crack severely underestimate the absolute values of observed displacements.

6.6 Comparison between COMSOL models

We proposed a fracture as the source of deformation responsible for the displacements reconstructed by IC2. Other several potential sources considered embedded within the layered domain (described in 6.5.2) are discussed in Appendix C, where we demonstrated that they are not suitable to reproduce the observations.

In particular, we found that a fracture opening reproduces the displacement pattern better than the loading that the water may exert on the layers interfaces which behave as acquicludes (Figure C.6). In Appendix C we also point out that sources of deformation different from a fracture generate vertical displacements much larger than the horizontal ones, contrarily to what expected.

We used the $RMSE$ criterion to numerically evaluate which source of deformation better reproduces the ICA results. According to it, an oblique fracture following the inclination of the backthrust, reaching the flat free surface in a homogeneous domain, is the one to use (Table C.1). The addition of the topography and the layering cause a small increase of the $RMSE$, indicating that the addition of complexities is unuseful for a better modeling. The reason may be the great simplification made on the geographic and geologic features of the area, represented by using a

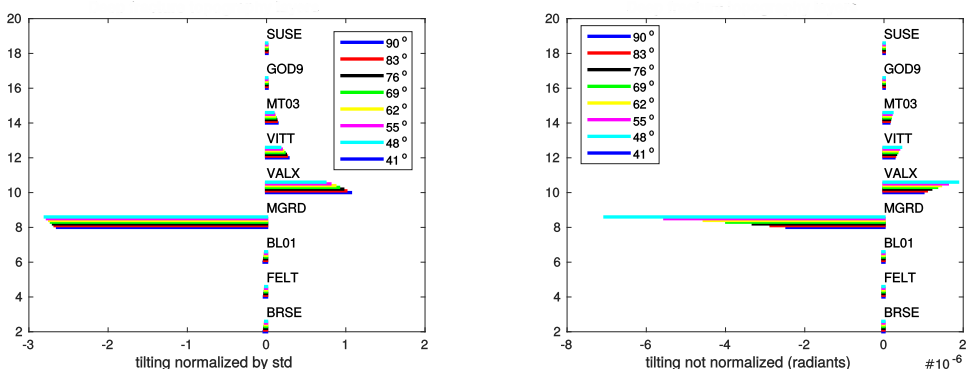

(a) Tilting normalized by std

(b) Tilting (radiants)

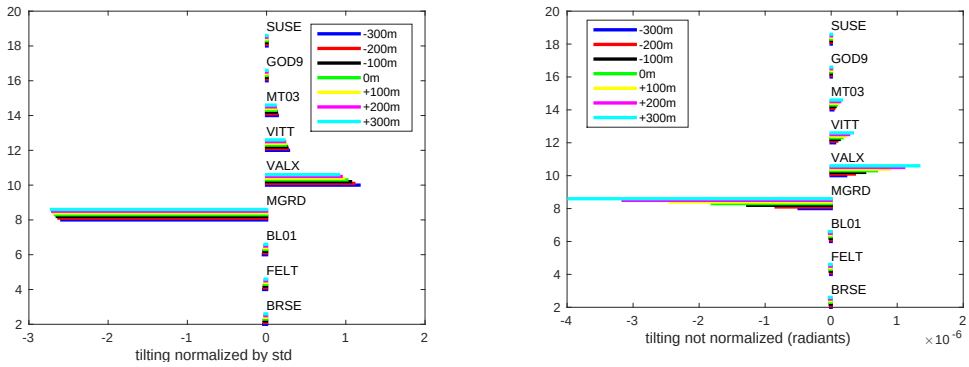

(c) Tilting normalized by std

(d) Tilting (radiants)

Figure 71: Values of tilting normalized by std (a) and absolute (b) considering variable dip angles; and variables bottom depths (c), (d) assuming 69° as dip angle.

2-D model instead of a 3-D. As a consequence, the introduction of the layering and the topography resulted to be not significant. The only modeling improvement obtained by using topography and layering is the reproduction of the vertical displacement pattern, but it is not as important as the horizontal one, since in the IC2 results it is indistinguishable from noise in most of the stations (Figure 68).

We also observed that the displacement pattern generated by a fracture that does not reach the free surface is essentially the same of the one reaching it (Figure 72b,c). Anyway, the absolute horizontal displacements modeled by the deep fracture are about three times smaller than the ones generated by the fracture reaching the surface, even if the width of the two fractures is the same (see caption of Figure 72). Moreover, we expect that analogous displacements can be obtained by considering fractures with larger along-dip-width and smaller pressures on fracture walls, highlighting a cross-talk (trade-off) between fracture along-dip-width and applied stress. As we will see in section 6.6.1, this is the case of a deep fracture, while for a fracture reaching the surface the pressure change is better constrained than the fracture width (Figure 75), in agreement with Serpelloni *et al.* (2018).

6.6.1 Constraining fracture width and overpressure

In this subsection we make some test to identify which is the overpressure and the fracture width that minimize the absolute RMSE

$$RMSE_{abs} = \sqrt{\frac{\sum_{i=1}^{N} (u_i - U_i)^2}{N}} \tag{111}$$

In particular, we considered fractures embedded in the layered domain of Figure 66 and the case of a deep fracture as in section 6.5.3, keeping the top position and fracture dip as fixed and varying its bottom position. Then, we considered a fracture reaching the free surface but not completely pressurized: we considered the case of the water level reaching +300 m and +600 m,

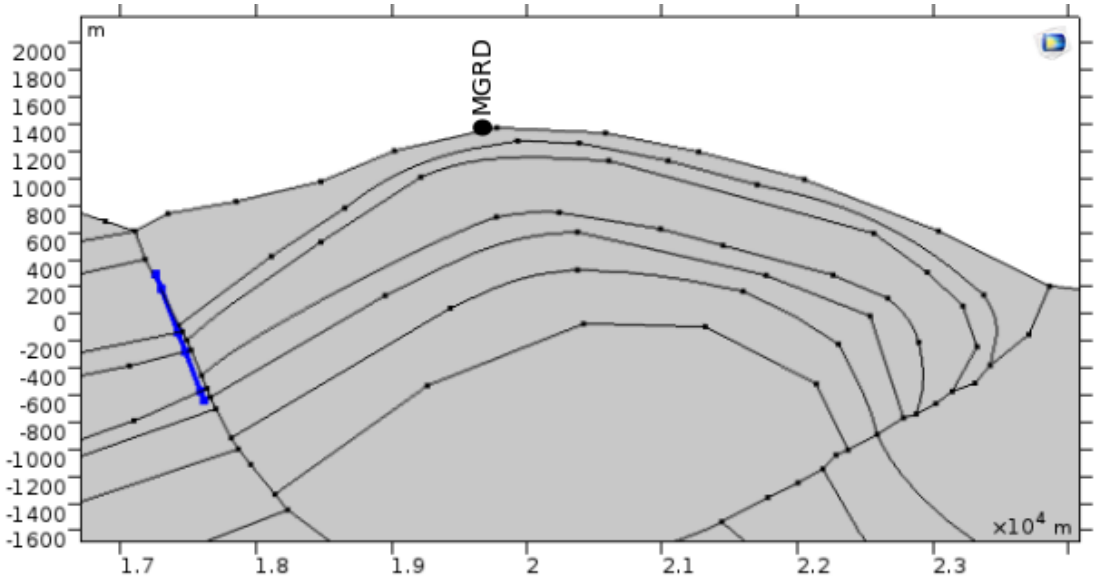

(a)

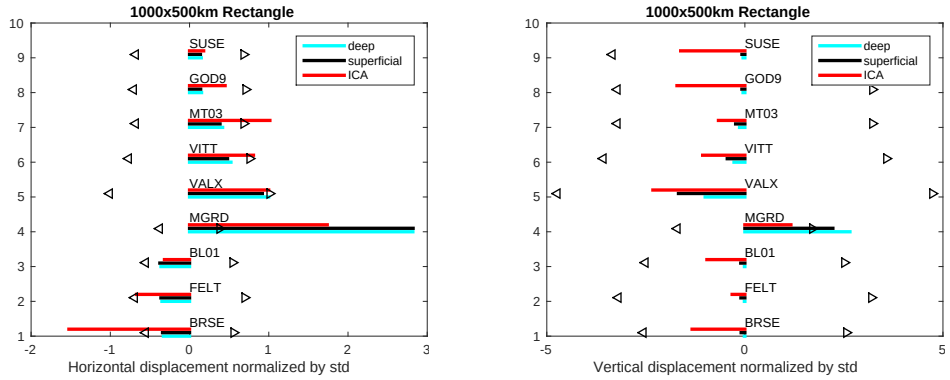

(b) (c)

Figure 72: Comparison between displacements obtained in the layered domain assuming both a deep fracture, as represented in (a, blue line) and a shallow fracture with the same width (Figure 68a). (b,c) displacements normalized by standard deviation, *red*: reconstructed by IC2 (standard deviation 4.1 mm and 2.3 mm for horizontal and vertical components, respectively); *cyan*: in the case of the deep fracture (standard deviation 2.5 mm and 0.8 mm for horizontal and vertical components, respectively), *black* in the case of shallow fracture (standard deviation 7.3 mm and 1.6 mm for horizontal and vertical components, respectively).

Source of deformation	*RMSE* horizontal	*RMSE* vertical	Pressure applied (MPa)
Oblique fracture flat surface	2.2934	0.3925	1
Oblique fracture only topography	2.7381	0.4698	1
Oblique fracture topography and layers	2.6768	0.3402	1
Oblique deep fracture	0.9516	0.3692	1

Table 17: RMSE between horizontal displacement modeled by using different sources of deformation and IC2. When we do not consider stratification, the std is computed by considering Maiolica in the entire region.

just below the free surface (Figure 75).

Up to now, for simplicity we have always considered the fracture as uniformly pressurized, even if the pressure on fracture walls is assumed to be caused by water level variations. If we call $ROOT$ the part of the fracture initially filled with water and ΔH the water level rise inside the fracture, from Pascal's principle it follows that in the ROOT part of the fracture the overpressure is uniform and equal to $\Delta H \times g \times \rho$, where ρ is water density and g the gravity acceleration. On the other hand, in the ΔH portion of the fracture the overpressure is not constant, but it linearly decreases with height, becoming zero at the top of the column of water (Figure C.3) (longuevergne *et al.*, 2009).

In Figure 74 we show the displacement patterns in case of the source of deformation represented in Figure 68 (a) for a water level variation of about 200 m, then generating an overpressure of 2 MPa. Considering the pressure as constant in the entire portion $\Delta H + ROOT$ of the fracture (blue lines), we observe that the displacement pattern does not change with respect to the case where the pressure decreases in the ΔH portion (black lines). Anyway, as the values of the standard deviations indicate, considering all the portion of the fracture as pressurized causes an overestimation of the displacements. It follows that it is possible to use the approximation of a uniformly-pressurized fracture when studying displacement patterns; anyway, this may generate bias when trying to constrain absolute values like fracture width and overpressure. Then, in the following discussion, we will consider the pressure variation inside the fracture as constant only in its $ROOT$ part and linearly decreasing in the region where ΔH occurs.

In the deep fracture case (Figure 75a), the minimum values of $RMSE_{abs}$ are obtained when considering an overpressure of 2 MPa and a fracture bottom depth (Z_{bottom}) of -500 m. In order to obtain such pressure variations, the water level variations in the fracture (ΔH) should be about 200 m, which is a lot, even in karst systems (Milanovic, 2005). Furthermore, the modeled bottom depth of the fracture is more than 500 m below the mean sea level altitude. Combining both these results, this source of deformations seems to be unlikely.

When considering fractures reaching the surface, when the maximum level reached by the water (Z_{top}) is 300 m it is hard to constrain at the same time fracture bottom position and water level rise. Excluding the case of 300 m of water level rise (Milanovic, 2005) as before and looking at the $RMSE_{abs}$ values, we observe that it is minimized for level rise of 100/200 m and a fracture bottom position of -300/-200 m (Figure 75b). These values are more reasonable than the deep fracture case, but still uncommon.

Since there are no evidence in this area of aquifers reaching depths that are hundreds of meters below the sea level surface and the maximum water level variation in karst system is 300 m (Milanovic, 2005), we believe that the model representing the most-likely configuration is a fracture where the water level inside it gets close to the free surface. In this case, even though the bottom depth is not well constrained when investigating the 0/-300 m range, the water level rise that minimize the $RMSE_{abs}$ is always about 100 m (Figure 75c). Unluckily, in this area hydrological observations that could help constraining the fracture width or water level fluctuations, like borehole measurements, are not available. Then, it becomes impossible to make further inferences: we can only say what is more likely from observations in other areas, but it is not possible exclude any of the configurations described in this subsection.

6.7 Coulomb failure stress variation on active faults

Can the pressure changes within the fractured fault rock cause significant stress changes at seismogenic depths? In the Introduction of this thesis we discussed the importance of recognizing non-tectonic deformation and their impact on the seismic cycle. Here we study the stress variation on the Bassano-Valdobbiadene thrust fault, which lies in the proximity of the source of deformation we identified. This fault is included in the Database of Individual Seismogenic Sources (http://diss.rm.ingv.it/diss/), but its features are still debated. It follows that it is important to understand which are the depth and the intensity of stress variations on the fault plane. Then, we compute the Coulomb failure stress change ($\Delta\sigma_c$) on the plane of this fault. It is defined as

$$\Delta\sigma_c = \Delta\tau_r - \mu\,(\Delta\sigma_n - \Delta p) \tag{112}$$

where $\Delta\tau_r$ is the change in the shear stress on the plane in the expected slip direction on the target fault, $\Delta\sigma_n$ is the change on normal stress (compression is positive), μ is the coefficient of friction and Δp is the change in pore fluid pressure (Harris and Simpson, 1992).

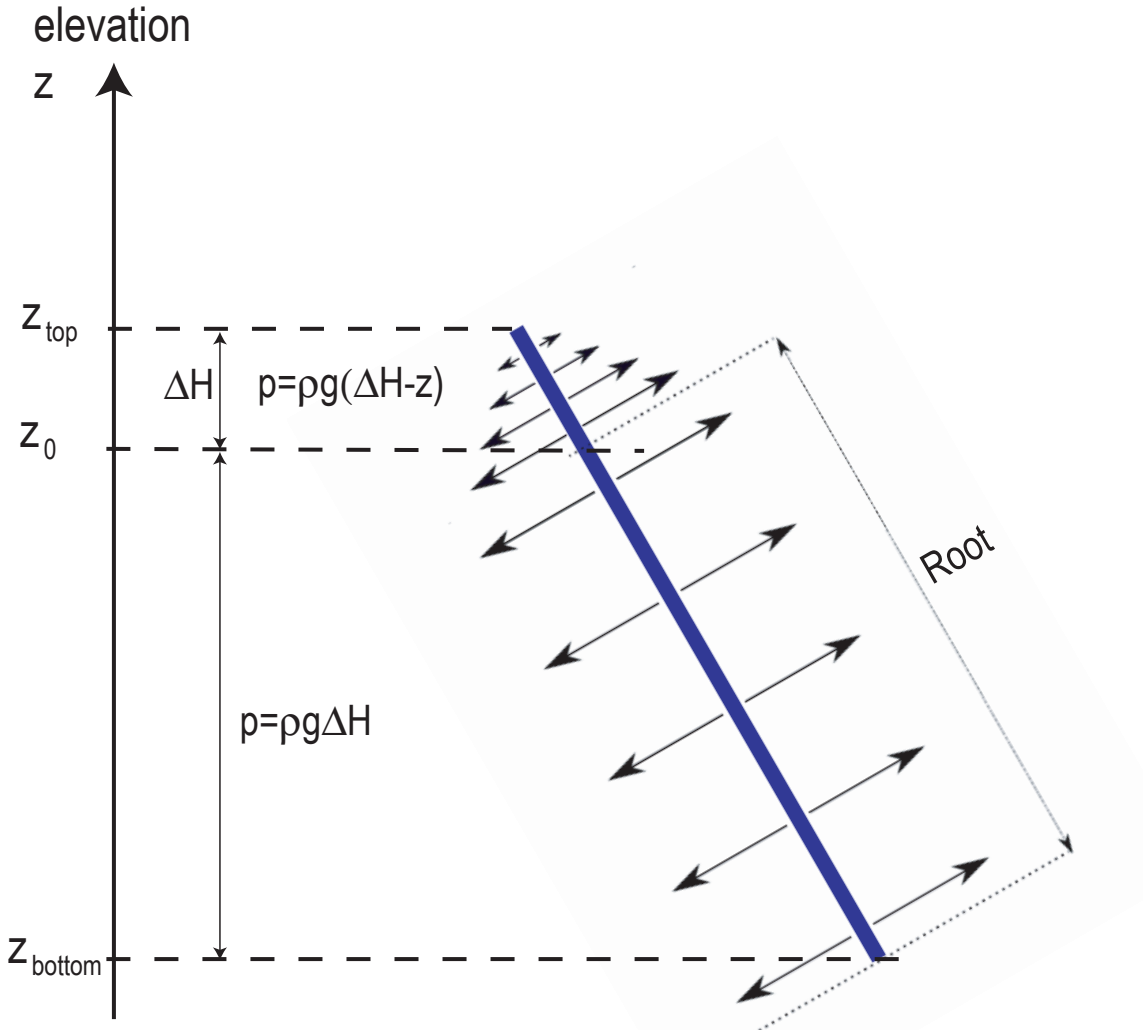

Figure 73: Schematic representation of the pressure exerted by the water on fracture walls when water level increases from $ROOT$ to $ROOT+\Delta H$. ρ represents water density, while g is the gravity acceleration. Z_{bottom} represents the position of the bottom of the fracture, Z_{top} the maximum elevation of the water column, while Z_0 the water level before a recharge event.

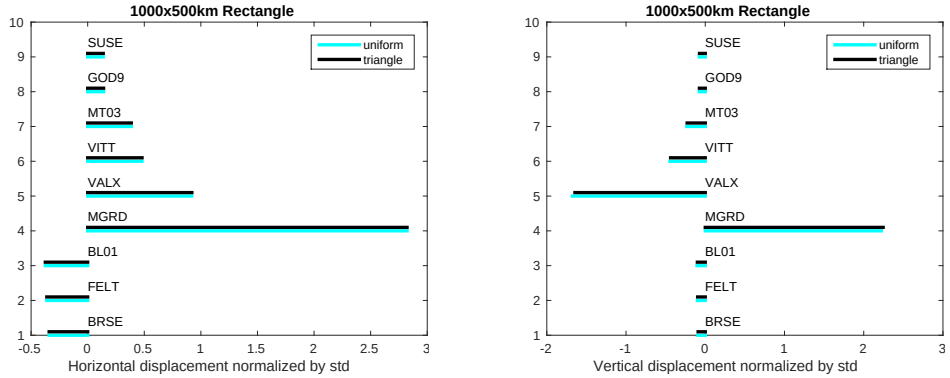

(a) (b)

Figure 74: Comparison between horizontal (a) and vertical (b) displacement patterns in the case of a 2MPa overpressure uniformly applied to fracture walls as in Figure 68 (blue) and an overpressure linearly decreasing in its ΔH portion as represented in Figure dafare The standard deviation of the displacements are 14 mm and 12 mm for the uniform and linearly-decreasing cases in the horizontal component, while they are 3.2 mm and 2.8 mm respectively for the vertical one.

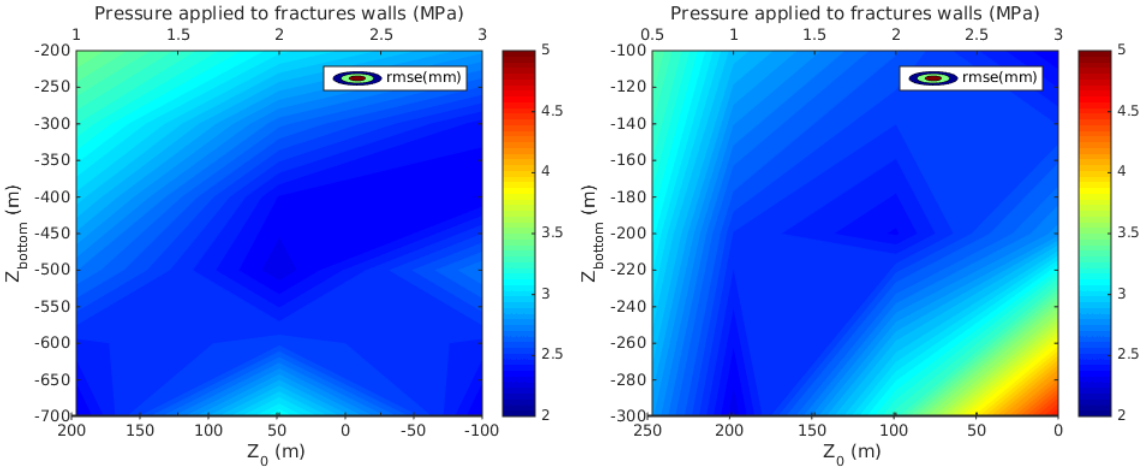

(a) Deep fracture, $Z_{top} = 300$ m. (b) Fracture reaching the surface, $Z_{top} = 300$ m.

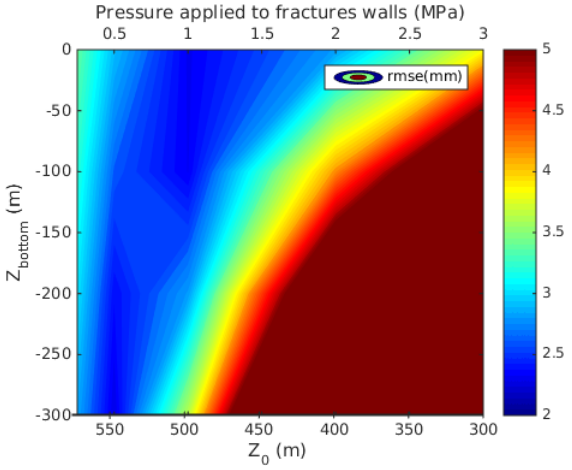

(c) Fracture reaching the surface, $Z_{top} = 600$ m.

Figure 75: $RMSE_{abs}$ values for the three cases considered in section 6.6.1.

COMSOL provides the three components of the stress tensor (S_{xx}, S_{yy}, S_{xy}) in a x, y reference frame, where y is vertical positive with elevation and x horizontal, positive toward south - west. It is possible to compute the variations on the normal and shear stress component of S in a plane parallel to the fault plane by performing a rotation of the reference frame:

$$\Delta\sigma_n = S_{xx}cos^2(\theta) + S_{yy}sin^2(\theta) + 2S_{xy}sin(\theta)cos(\theta) \tag{113}$$

$$\Delta\tau_r = (S_{yy} - S_{xx})\, sin(\theta)cos(\theta) + S_{xy}\left(cos^2(\theta) - sin^2(\theta)\right) \tag{114}$$

Since the dip angle of the Bassano-Valdobbiadene thrust fault is assumed to be 30°, then $\theta = 60°$. We assumed $\Delta p = 0$, so that there is no fluid in the thrust fault. Furthermore, according to Cattin *et al.* (2009), laboratory experiments typically find values for μ of around 0.6 to 0.85 for most rock materials, then here we use a mean value 0.7.

In Figure 76 we present color maps of the Coulomb failure stress change in the case of layered domain both considering positive and negative pressure variations (±1 MPa as in section 6.4) on the walls of the fracture (highlighted in red) we chose as source of deformation. On the fault plane, for the case of water level increase inside the fracture (positive stress applied on fracture walls), the maximum values of $\Delta\sigma_c$ are of the order of 10^4Pa at a depth of about 2500 m below sea level, while the minima are close to the free surface (Figure 76a). It is interesting to note that values of 0.1 bar are present also at $\sim$ -3 km, even though as the depth increases the stress variations tend to zero. When considering water level decreases (Figure 76b), the stress variation pattern is the same, with the sign reversed.

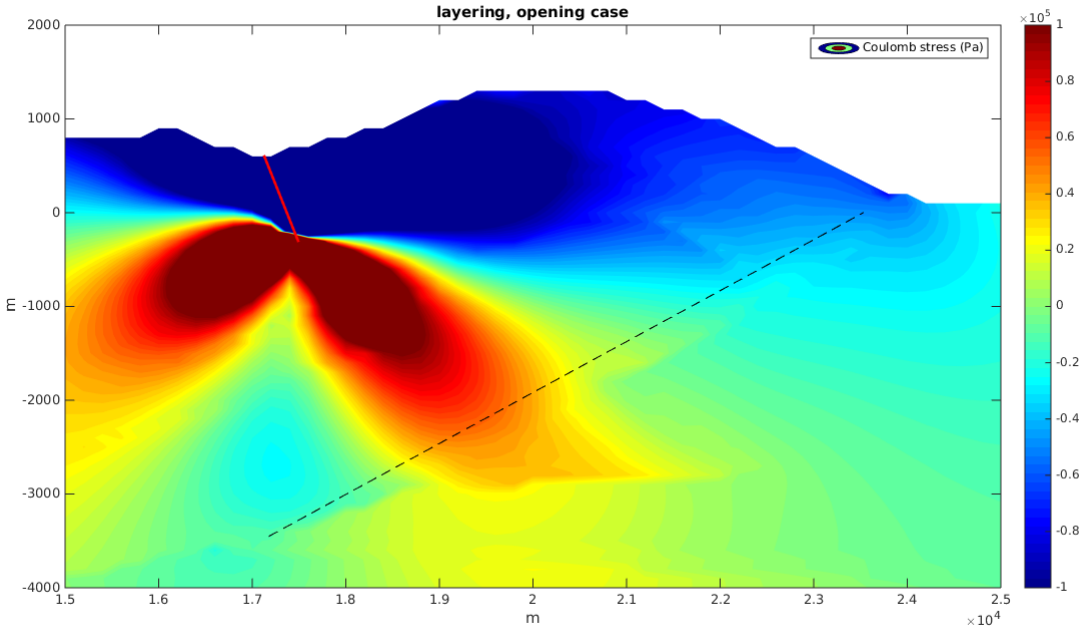

(a) Opening phase

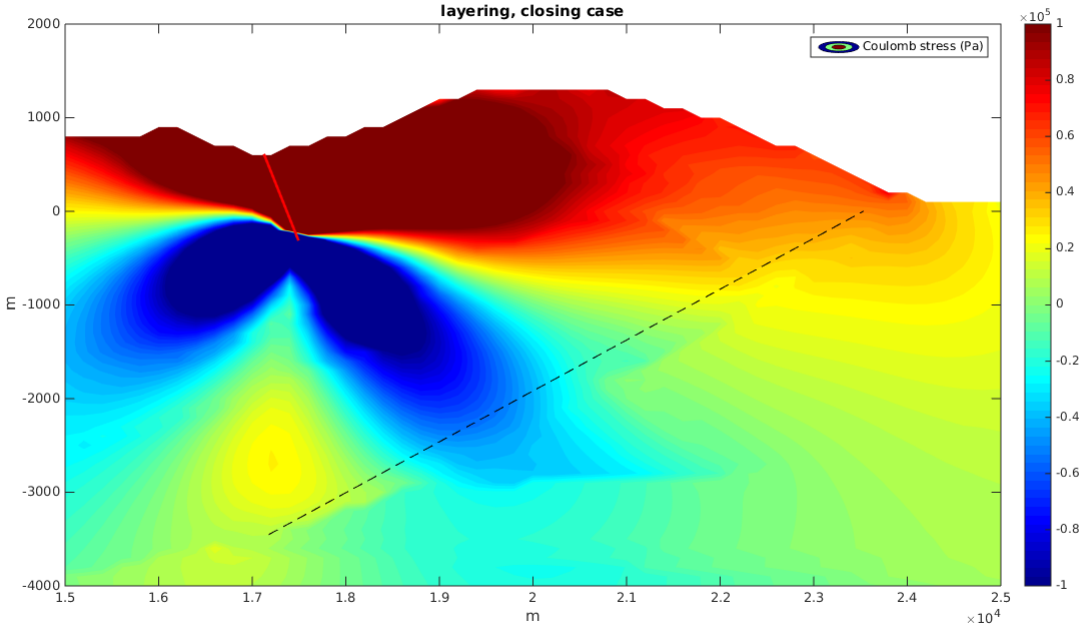

(b) Closing phase

Figure 76: Contour map of the Coulomb stress change evaluated on planes parallel to the Bassano-Valdobbiadene thrust falut (black dashed line) and generated by the chosen source of deformation (red line), assuming an increase (a)/decrease (b) of pressure on its walls of 1MPa.

Appendix C Alternative sources of deformation

In this appendix we discuss other possible sources of deformation for the displacements reconstructed by IC2. We will essentially test the effect of water pressure in different portions of the profile represented in Figure 66 and analyze the displacement pattern.

We will also consider how large the vertical displacements are compared with the horizontal ones. If we obtain large vertical displacements, the model fails to reproduce IC2 displacements, which show a low signal to noise ratio for the vertical component unlike the horizontal one. Then, each configuration that causes the vertical displacement to be larger than the horizontal should be excluded from the range of the possible sources of deformation. Even when comparing the effects of different sources, we consider displacements normalized to the standard deviation of the displacement distribution in all the stations. In this way we mainly compare the displacement pattern generated by the source of deformation.

A possible source of deformation is a vertical fracture, similar to what described by Serpelloni *et al.*, 2018, i.e. a sub-vertical synfolding radial fracture originated in the hinge zone of the Monte Grappa Anticline. We compared the resulting displacement pattern (Figure C.1b and C.1c) with the one obtained by COMSOL considering a fracture orientated along the backthrust (Figure 68a).

We observe that there are not very large differences among these displacement patterns. Nonetheless, the worst choice for the source of deformation seems to be the vertical fracture ($RMSE = 0.7629$), which underestimates the horizontal displacements in all the stations except MGRD, where the displacement is more significantly overestimated than in the reference case.

We also made the hypothesis that the water could flow through the Maiolica, Rosso Ammonitico and Calcare del Vajont, reaching the Formazione di Igne, much more impermeable than the overlying layers. In addition, we considered the backthrust fault as aquiclude. The relation between faults and water is not univocal: on one side the region next to a fault can be more fracturated than the sourrounding rocks; on the other side, some authors like Steven Phillips (*https://www.livescience.com/39625-aquifers.html*) stated that a fault can block the groundwater movement. Following this last hypothesis, we imagine that the water can reach the depth of the interface between Calcare del Vajont and Formazione di Igne, where it is stopped because of the impermeable layer. Assuming that this process is prevalent in the north-western part of the profile (different assumptions will be discussed later), the water flows toward the backthrust because of the inclination of the layers. Then the water reaches the backthrust, but it does not pass through it, so that it accumulates within the region whose borders are highlighted in Figure C.2a. In this case, the region where the water can be stored is wider than a fracture, then it is unlikely that the water can reach the surface and so the applied pressure. Furthermore, we assumed the same uniform pressure both on the backthrust and on the Calcare del Vajont-Formazione di Igne interface.

The displacement pattern generated by this source of deformation is in strong contrast with the results of IC2 ($RMSE = 1.8011$), in particular we observe from Figure C.2b that VALX is the only station where the sign of the displacement is the same both for IC2 and COMSOL. Then, this source of deformation must be excluded.

We decided to investigate if a plausible source of defomation is generated by the water accumulation in the south-eastern part of the profile above the Rosso Ammonitico layer. Here, a significative amount of water may be stored because the thrust fault could prevent the water from flowing toward south. At the same time, the Rosso Ammonitico formation, more impermeable than Maiolica, could obstruct the downward and northern flow of the water.

We specify that the tectonics of this area is characterized by the convergence of the Adriatic and the Eurasian plates, that generated a thrust front, characterized by thrust and backthrust faults and anticline folds that result in mountain sectors, like the one we are now discussing. As a consequence, because of the collision between the two plates, the layers that are next to the thrust front happen to be subvertical.

We also want to point out that in the previous case (Figure C.2a) we made the hypothesis that the water crosses the Rosso Ammonitico layer, reaching the Calcare del Vajont, while now (Figure C.4a) we consider it as an acquiclude. The Rosso Ammonitico is actually more impermeable than Maiolica, but it is very thin and might be fracturated somewhere. Furthermore, some studies (Lucio D'Alberto personal comunication) revealed that the Fium spring, located in the north-western part of the anticline (Figure 66), drains water that flows through the Calcare del Vajont formation. Then, for the north-western sector of the anticline we consider the Rosso Ammonitico

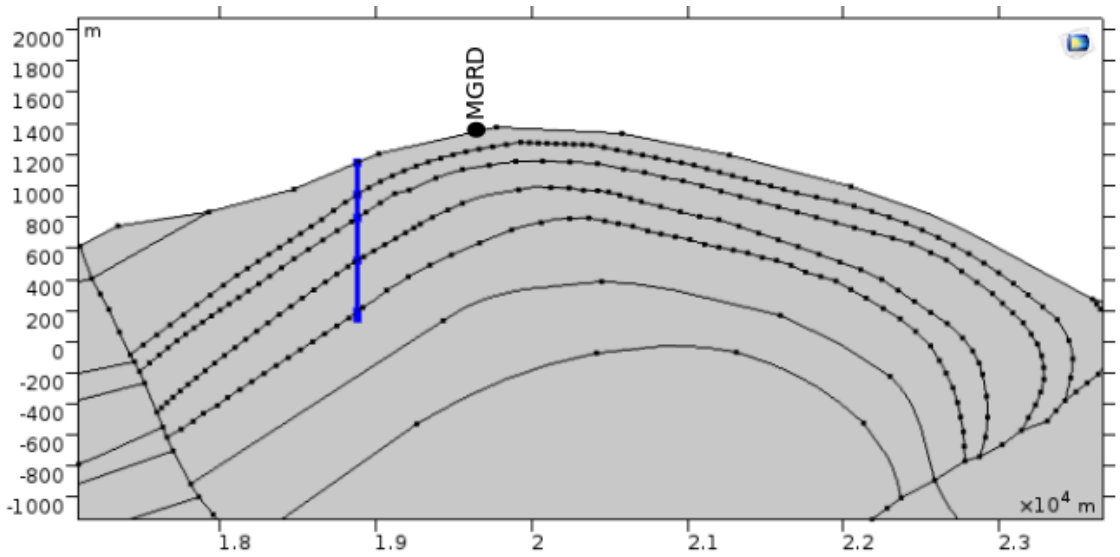

(a)

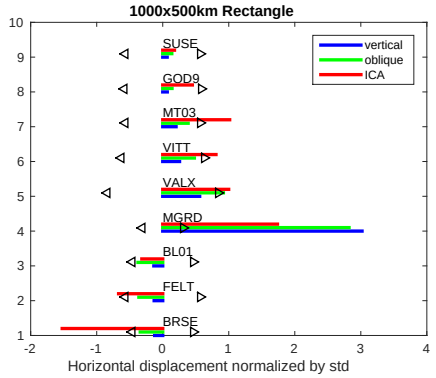

(b)

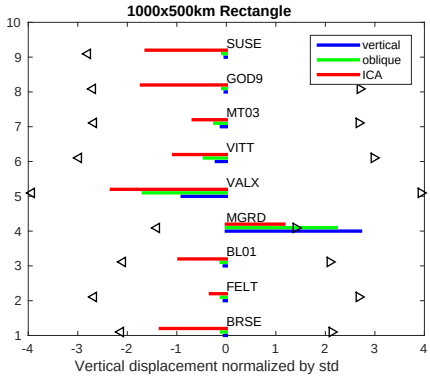

(c)

Figure C.1: (b,c) *red*: reconstructed by IC2; *blue*: modeled by COMSOL using a source of deformation as in Figure C.1a, where the blue line marks the boundariy where we apply pressure. *green*: modeled by COMSOL using a fracture orientated along the backthrust as in Figure 68a. Horizontal displacement is positive when it is toward S-E; vertical displacement is positive when upward.

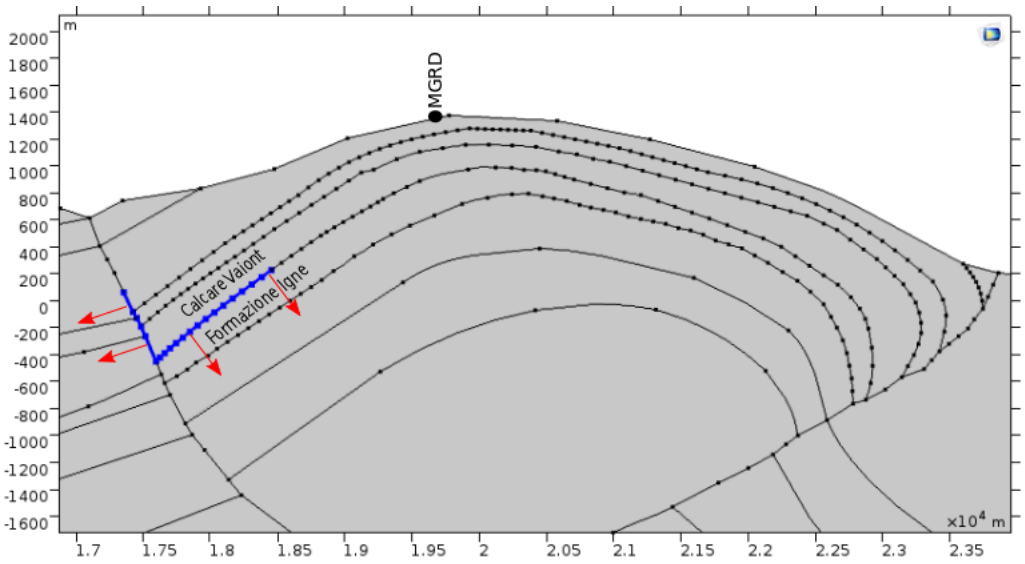

(a)

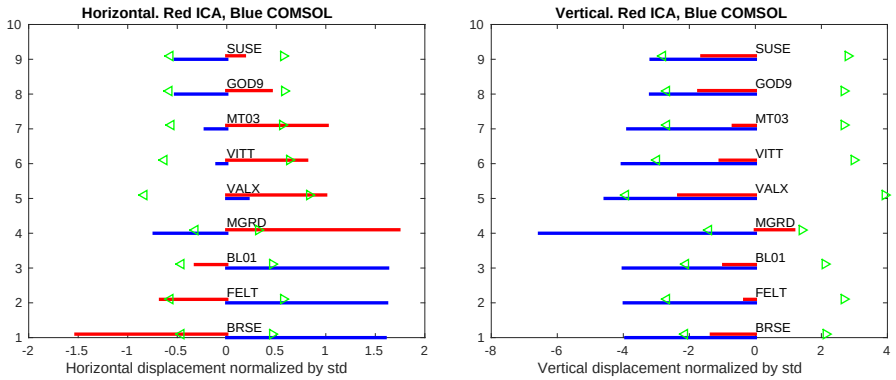

(b) (c)

Figure C.2: Same as Figure C.1 for a different deformation source. Red arrows indicate how pressure is applied on rock layer interfaces (blue), which represents the source of deformation.

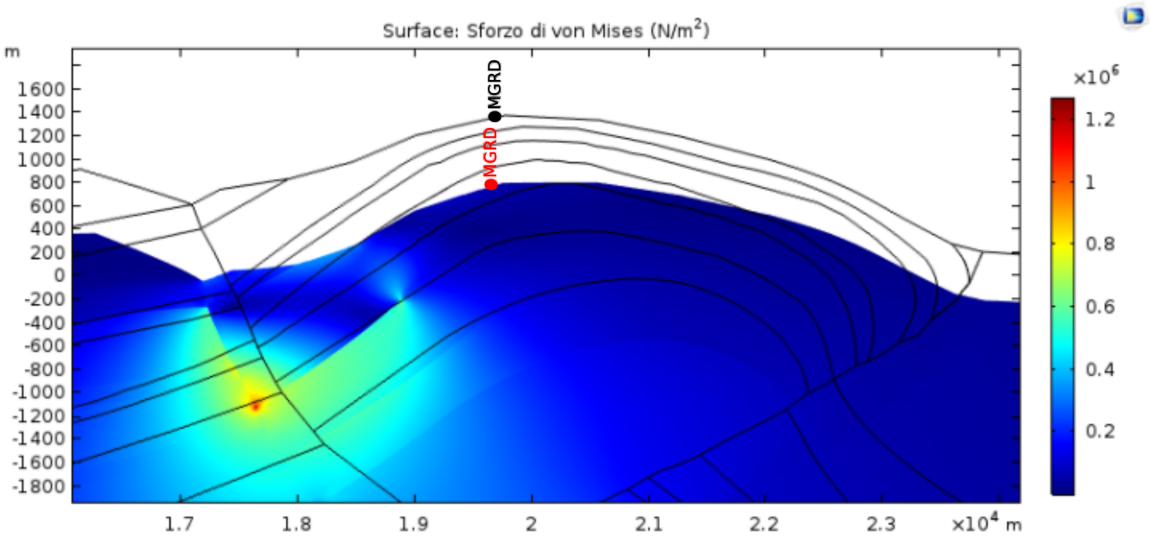

Figure C.3: Displacement pattern and Von Mises stress (Pa) generated by the source of deformation represented in Figure C.2a. The amplitude of the displacements are multiplied by a scale factor of 10^4 for a better visualization. The black lines (and the MGRD position denoted in black) represent the undeformed configuration, while the position of MGRD in red represents its position in the deformed configuration.

as fracturated, so that the water can easily reach the Calcare del Vajont. In the south-eastern part of the anticline we have less reliable data about the behavior of water when encountering the Rosso Ammonitico, then we decided to consider it as acquiclude. If we admitted that the water could pass the Rosso Ammonitico also in this case, the source of deformation would be still similar to Figure C.4a in shape, with the difference that it would reach a larger depth.

The results obtained disagree with the IC2 reconstruction ($RMSE = 1.2682$), in fact MGRD and VALX are the only stations where the horizontal displacements reconstructed by COMSOL and IC2 are someway in agreement (Figure C.4b).

We then study the effect of the two sources of deformation just described, represented in Figure C.2a and C.4a, acting together at the same time. We consider the same value of pressure acting to each portion of the profile that constitutes the source of deformation (highlighted in blue in Figure C.5a).

We observe that even considering the two sources of deformation at the same time, there is basically no agreement between the pattern of displacement reconstructed by IC2 and modeled by COMSOL ($RMSE = 1.6904$). Furthermore, it is interesting to compare the absolute values of the horizontal and vertical displacements. If we consider only the source shown in Figure C.2a, the resulting vertical displacements are more than one order of magnitude larger than the horizontal ones, except for BL01, FELT and BRSE, where the vertical component is about 5 times larger than the horizontal one. When we consider the other two sources of deformation shown in Figures C.4a and C.5a, the ratio between vertical and horizontal displacements remains around 10 for most of the stations; furthermore, in none stations the horizontal displacements are larger than the vertical. In light of what we have shown up to this point, the three sources of deformation described do not fit at all to what we are looking for.

Finally, we made the hypothesis that the water exerts a load on the interface between Calcare del Vajont and Formazione di Igne along all the profile, from the backthrust to the thrust, as in Figure C.6a.

We observe that the sign of the horizontal displacement (Figure C.6b) is opposite with respect to the IC2 results, except for MGRD ($RMSE = 1.7429$). In addition, for each station, the vertical displacements are larger than the horizontal; consequently this source of deformation is not plausible.

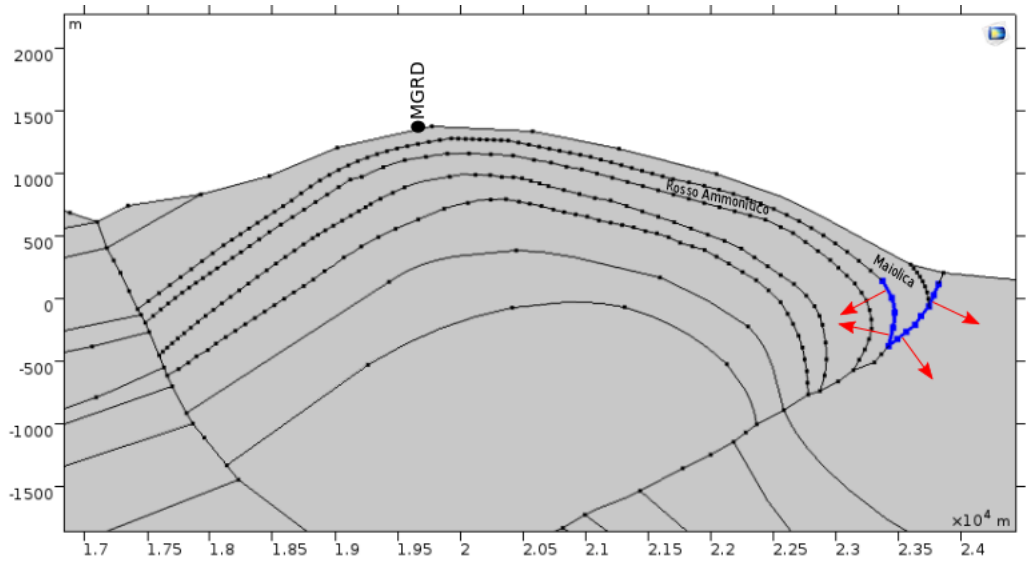

(a)

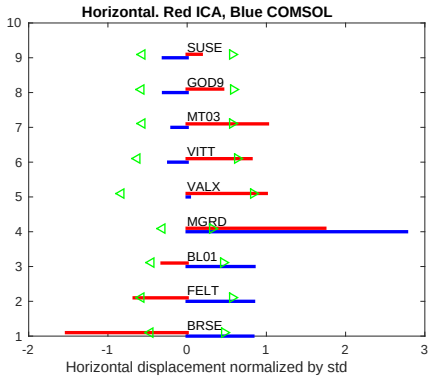

(b)

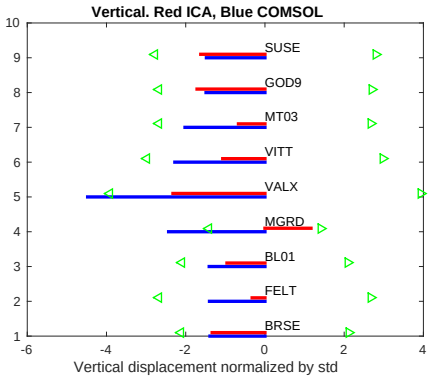

(c)

Figure C.4: Same as Figure C.1 for a different deformation source. Red arrows indicate how pressure is applied on rock layer interfaces (blue), which represents the source of deformation.

Source of deformation	*RMSE*
Oblique fracture flat surface	0.4907
Oblique fracture only topography	0.5238
Oblique fracture topography and layers	0.6033
Oblique deep fracture	0.5983
Vertical fracture anticlyine	0.7629
Loading left side	1.8011
Loading right side	1.2682
Loading left and right side	1.6904
Loading entire interface	1.74287

Table C.1: RMSE between horizontal displacement modeled by using different sources of deformation and IC2. When we do not consider stratification, the std is computed by considering Maiolica in the entire region.

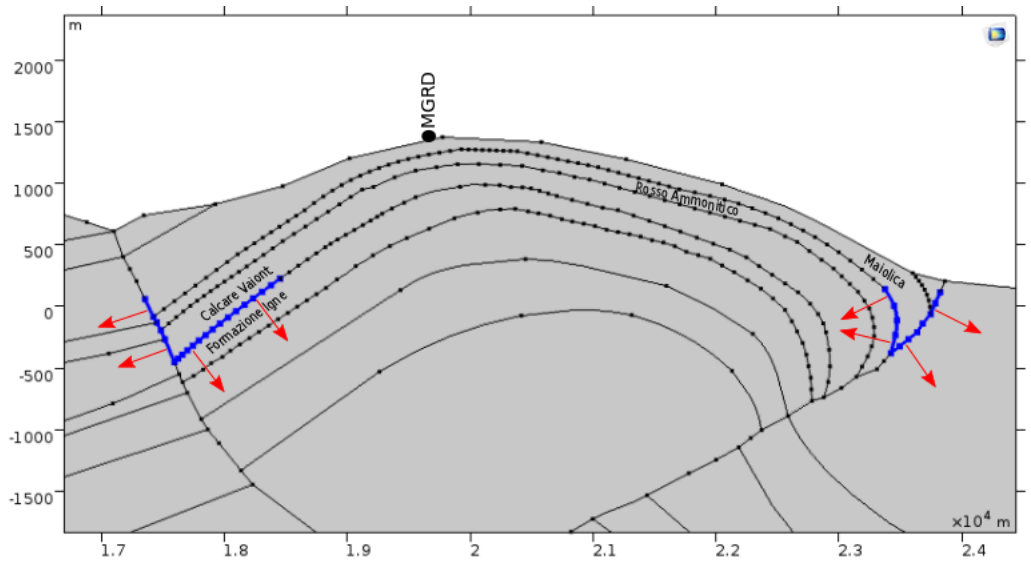

(a)

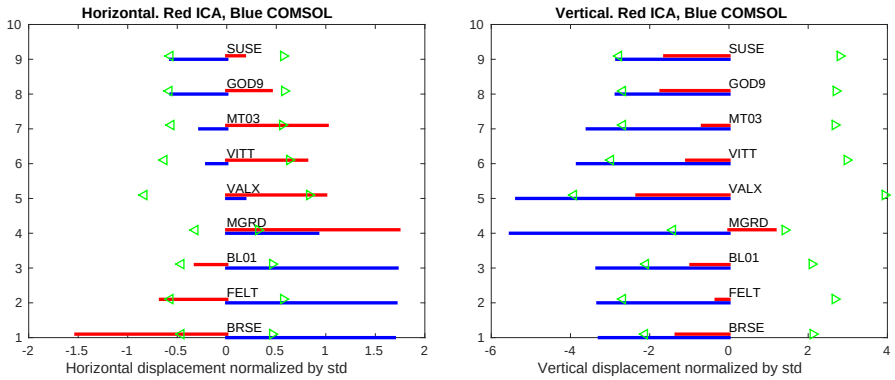

(b) (c)

Figure C.5: Same as Figure C.1 for a different deformation source. Red arrows indicate how pressure is applied on rock layer interfaces (blue), which represents the source of deformation.

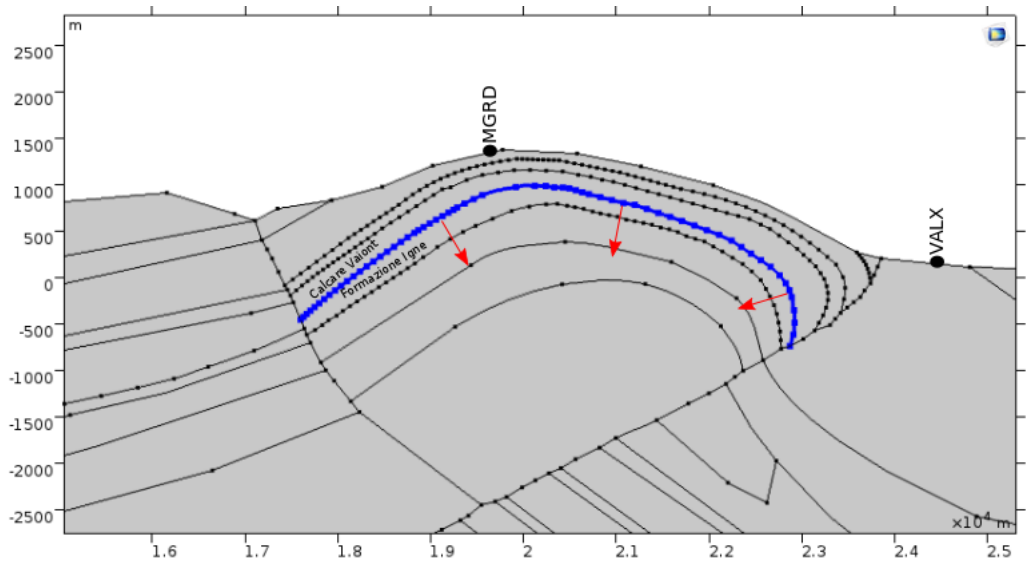

(a)

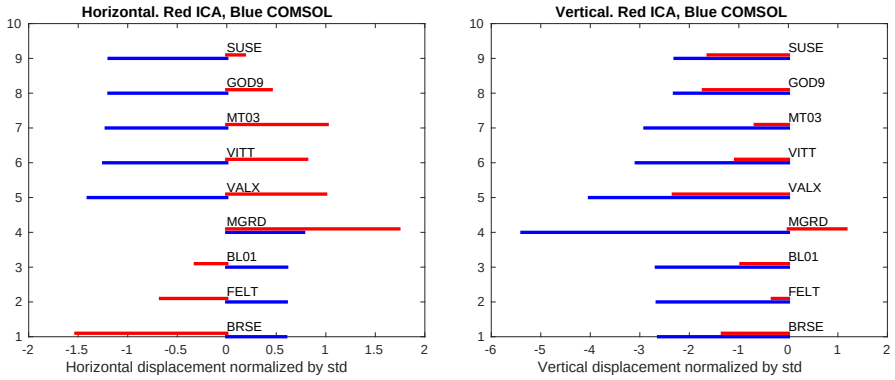

(b)

(c)

Figure C.6: Same as Figure C.1 for a different deformation source. Red arrows indicate how pressure is applied on rock layer interfaces (blue), which represents the source of deformation.

7 Discussion

Earth surface displacements are largely affected by superficial hydrological seasonal processes, which significantly impact GPS time series (e.g., Dong *et al.*, 2002; Herring *et al.*, 2016; Tregoning *et al.*, 2009). Then, consistently the application of a VbICA analysis to GPS time series made in this thesis for the Eastern Southern Alps (ESA) and northern Dinarides clearly show the presence of common mode annual signals in ground displacements, IC1 and IC3. In the last decades, superficial hydrological signals have been recorded and modeled by several research projects using different approaches. In section 4.2.1 we described models that are mainly based on surface measurements of meteorological variables, like GLDAS (Rondell, 2004) and ERA-Interim (Berrisford *et al.*, 2009; Dee *et al.*, 2011), and a model that is based on satellite measurements of gravity variations computed by the GRACE mission. Even though GRACE is widely used to compute displacements caused by water storage variations, in this thesis we compared the displacements reconstructed by IC1 and IC3 with GLDAS and ERA-interim products, since the spatial dimension of the area under analysis is very small compared to the resolution of GRACE data (Tregoning *et al.*, 2009).

Finding correlations with both models, our interpretation for IC1 and IC3 is that they both represent displacement caused by hydrological loading variation involving processes at the surface of the Earth and within the first few meters of depth (soil, see Table 2). In particular, IC1 reproduces the vertical displacements caused by it while IC3 the horizontal ones. The reason why two ICs are associated with the same source of deformation is that the annual temporal evolution of the horizontal and vertical displacements is characterized by a phase shift. It follows that, according to vbICA analysis, they are statistically independent (Gelb and Vander Velde, 1968) and then reconstructed in two separate ICs.

We found the highest correlations in the vertical component, which also shows the highest amplitudes, while in the horizontal components the correlations decrease, especially in the east one, where we found a slight anti-correlation (0.5). In fact, while it has been well established by Farrell (1972) that assuming a spherical and layered model is the correct way to model both horizontal and vertical components simultaneously, Chanard *et al.* (2018), modeling GRACE observations, showed that the fit to the phase and amplitude of both horizontal and vertical data can be improved by estimating a degree-1 deformation field rather than using the degree-1 coefficients from Swenson et *al.* (2008). Furthermore, regional misfits may also arise from lateral variations of the Earth's elastic parameters, although to a lesser extent than proposed by Chanard *et al.* (2014) once degree-1 contribution has been adjusted. In addition, the amplitude of the horizontal displacements is small and there are other systematic errors in GPS time series that can contribute to the annual signals, as reported in 3.2.2 (Dong *et al.*, 2002). These contributions usually marginally affect the observed displacements, but in the case of the east component of the displacement, they may have a relevance similar to the hydrological loading in generating the observed signal.

In this thesis we focused on the second IC (IC2), and on the Venetian sector of the ESA fold-and-thrust belt, across the Mount Cesen- Col Visentin (MCCV) anticline (area 2) because here active thrusting is accommodating large part of the Aria-Alps convergence, arising seismic potential issues if constrained by GPS tectonic rates, and the GPS network is denser. Since the tectonic displacements are parallel to the ones reconstructed by IC2 (see Figure 5 in Serpelloni *et al.*, 2016), it becomes crucial to recognize the physical phenomenon generating this kind of deformation and separate it from GPS time series in order to avoid misinterpretations, for example with transient signals of tectonic origins, and improve the knowledge of the seismic potential of the area, which is still poor. In order to assess that IC2 is a hydrological-induced signal we compared its temporal dependence (V2) with time series of cumulated precipitation over different time windows. We found a correlation with cumulative precipitation curves computed by using three different gridded datasets, which are the one obtained from the Tropical Rainfall Measuring Mission (TRMM), E-Obs and the Alpine Precipitation Grid Dataset from the Federal Office of Meteorology and Climatology MeteoSwiss, independently from the number of days used to calculate the cumulative precipitation and the different origin of precipitation data. If TRMM is based on satellite data, E-Obs or MeteoSwiss consider in-situ measurements. These results point toward a common hydrological forcing for the observed time-variable deformation signal in the study area, confirming the results of other authors who used different approaches and data, like the pendulums of Grotta Gigante and tiltmeters in the Cansiglio Plateau (Tenze *et al.*, 2012; Grillo *et al.*, 2018; Braitenberg *et al.*, 2006; Braitenberg *et al.*, 2001; Braitenberg and Zadro, 2006; Braitenberg, 1999). The orientation of the

horizontal strain axes associated with IC2 (Figure 17) suggests that this hydrological forcing acts on existing rock fractures and the signal is amplified in karst terrains. At a local scale, water infiltration and associated pressure change were proposed to explain tilt and surface deformation signals in fractured outcrops (e.g., Devoti *et al.*, 2015; Jacob *et al.*, 2010; Longuevergne *et al.*, 2009; Schuite *et al.*, 2015). In this work we made the hypothesis that these processes happen at larger scale, like the one that characterize the analysis made on area 2. It is worth noting that other authors found correlation between precipitation and deformation in karst regions (Devoti *et al.*, 2015, Silverii *et al.*, 2016, Jacob *et al.*, 2010, Gilli *et al.*, 2010), which have been interpreted as caused by water level variations in fractures, even if none of them considered the cumulative precipitation as defined in this thesis. The only authors who considered the number of cumulative days of precipitation were Fiorillo and Doglioni (2010), analyzing the link between spring discharge and precipitation in the Southern Apennines. They found good correlations between spring discharge and rainfall, which is maximized when considering about 200-300 days of cumulative precipitation, and interpret it as pressure pulse on phreatic conduits caused by the water when it reaches the saturated zone. Silverii *et al.* (2016) have then demonstrated that this process can lead to deformation signals. It is interesting to note that in this thesis the number of days which maximize the correlation between cumulative precipitation and V2 is equal to 240-300 days (section 5.1), about the same values found by Fiorillo and Doglioni (2010). Important water level changes (of the order of tens of meters) are common in karst environments (Milanovic, 2005, 2014), where narrow fractures can drain water from large areas, focusing the effects of pressure changes within thin, sub-vertical structures located in the transmission zone (see Figure 5). Water level rise and subsequent draining could therefore account for the observed alternating phases of extension and contraction across fractures. The time windows that maximize the correlation between V2 and cumulated precipitation curves (Figure 25B) might relate to the time needed to saturate and then drain these structures and depends on the different rates at which groundwater can flow in a karstic environment. Recession coefficients (section 2.3.2) indicate that the time scale of the diffusion time of the water within a karst aquifer is generally about 160-250 days, which is consistent with our results. Opening/recharge phases reflect faster water flows associated with positive linear trends of dilatational strain (e.g., T1 in Figure 24C), while the closing/discharge phases relates to slower and nonlinear negative trends (e.g., part of T2 in Figure 24C). This different behavior resembles that of typical unit hydrographs of karst spring hydrographs (Milanovic, 1981). This could be explained by different dominant flow regimes characterizing the hydraulic responses during the recharge and discharge phases, as also proposed by Devoti *et al.* (2015) and Grillo *et al.*, (2018) for the Cansiglio Plateau.

Starting from the assumption that deformation is caused by water level variations in fractures, we made the hypothesis that these are directly linked to the amount of water stored in the subsurface. We computed watershed water storage variations by means of hydrological models whose parameters are calibrated reproducing river flows data, starting from input data of precipitation, potential evapotranspiration and temperature only. Because of the poor knowledge and the complexity of the hydrological features of the basins we considered, we did not try to reproduce exactly all the physical processes governing water flows inside them and we used lumped parameter models (Yang *et al.*, 2004). In fact, this kind of models is based on a rough simplification of the various physical processes that take place in hydrological systems (e.g. evapotranspiration, generation of water flow, etc.). As a consequence, they are not built to simulate explicitly internal processes (Longuevergne *et al.*, 2009). GR5J (Perrin *et al.*, 2003) is the model that allows us to best describe the hydrological basin among all the other tested models. Once calibrated the model by using precipitation and temperature data obtained from either gridded dataset or in-situ measurements (section 5.3.2), we found that the rivers flow is better reproduced using in-situ precipitation measurements than gridded data, probably because through pluviometers measurements the estimation of the precipitation is more accurate. The Nash-Sutcliffe efficiency criterion (Nash and Sutcliffe, 1970), widely used in hydrology, confirms that the better the basin is modeled, the larger the correlation between the hydrological and geodetic signal is (section 5.3.3). The temporal evolution of IC2 better correlates with water storage variations than cumulated precipitation: this demonstrates that considering only the cumulated precipitation history, we were roughly estimating the total water storage variations.

The response time of a system indicates how long the memory of the previous input conditions is kept after a change of them. In order to interpret the time interval that gives rise to the maximum correlation between V2 and cumulated precipitation, in chapter 5 we evaluated the response time of GR5J as a function of model parameters, both numerically and analytically. For best parameters

values to reproduce discharge in area 2 (optimal parameters) the response time of emptying is about 300 days, which is comparable with the cumulation time of the precipitation that makes it well correlated with V2. We found that the response time basically increases with the parameter x_1 defining the dimension of the production store; anyway, since we are using an empirical model, it is not possible to link it to any physical parameter. Using GR5J with optimal parameters we evaluated also the so-called residence time, defined as the ratio between the reservoir average storage and the average rate of input/output and characterizing the timing of aquifer responses to change in recharge (Dingman, 1994). We found that it is about 260 days, a value that also resembles the number of days of cumulated precipitation that maximize the correlation with IC2. It is worth noting that since response and residence time are comparable, they both describe the same physical property of an hydrological basin, even if they are computed differently, answering the question "how fast does an aquifer react to input variations?". The response time is a parameter that allows to best fit the temporal evolution of the recharge/emptying of an aquifer through an exponential function, then should be evaluated during abrupt changes of input conditions. On the other hand, the residence time only depends on mean values of input/output and storage expressing a characteristic time of the hydrological basin on the basis of a steady state mass balance.

To model the temporal dependence of a variable, such as surface displacement due to the hydrological sub-surface load, a poroelastic model with suitable values of permeability and description of the source of pore pressure diffusion should be used. However elastostatic models can provide end members helpful to constrain such hydromechanical models (Schuite *et al.*, 2017). In the last part of this thesis we use an elastostatic model to interpret the displacement variation reconstructed by IC2 during the time-interval where the V2 variation is the largest, so that the strain rate is maximized (see Figure 24). The spatial extent of the deformation associated with IC2 suggests that this is likely the cumulated result of several distinct sources within the fractured karst system. The contribution of each distinct deformation source is practically impossible to estimate because of the numerous parameters involved, including fractures number, density, dimension, position, orientation, and opening/closing values. However, we can approximate their overall behavior as the one due to a single, equivalent tensile fracture (e.g., Jade and Sitharam, 2003; Sitharam *et al.*, 2001), to gain a first-order estimation of the pressure changes required to explain the observed horizontal displacement patterns. A similar approach has been used by Silverii *et al.* (2016) to model displacements associated with karst aquifers in the southern Apennines with elastic dislocation. Also Devoti *et al.* (2015) used a dislocation model to reproduce hydrological effects on displacement and tilt in the Cansiglio Plateau. It is worth to notice that unlike Silverii et *al.* (2016) and Devoti *et al.*, (2015), here we estimate directly the pressure change by comparison with data obtaining a value of 1 MPa equivalent to a water level rise of 100 m. Water level variations of this order of magnitude have been recorded by Bonacci and Roje-Bonacci (2000), in the Dinarc karst.

In particular, modeling has been performed using both a boundary elements for a crack in a homogeneous halfspace (LibHalfspace, Ferrari *et al.*, 2016) and the finite-element-based software COMSOL, which allowed us to consider the geological and topographical heterogeneities of the area. Then, it was possible to identify the source of deformation that is compatible with these features and best reproduces the IC2 displacements, finding that it is a fracture corresponding to the upper part of the backthrust of the Bassano-Valdobbiadene thrust. Nonetheless, we cannot directly discern the vertical boundaries of the fracture, which eventually must be estimated taking into account independent data (e.g. geological constraints), but only its horizontal position along the profile. Instead we can quantify about 1 MPa overpressure applied to the fracture walls to generate the observed displacements, at least in the case where the fracture is assumed to open at the surface and the maximum water level is allowed to get very shallow, even if also in this case the fracture width (Figure 75) remains unknown, in agreement with Serpelloni *et al.* (2018). If the maximum level of water inside the fracture is deeper a trade-off between overpressure and fracture width appears. Finally, if the fracture is buried, it is hard to constrain either the width or the overpressure owing to the scarce sensitivity of surface displacements to these parameters. Accordingly, the most-likely source of deformation is a fracture that reaches the surface and can be filled up to an elevation of +600 m, for which we assumed a 1 km extension along dip. The inclusion of topography and rock heterogeneities does not lead to improvement of the agreement between the model and the horizontal displacements reconstructed by VbICA, since the inclusion of these features only slightly affect the displacement patterns. Anyway, when considering vertical displacements, even though they are below the noise level, the inclusion of both topography and

layering results to a better modeling (Figure 68). This can be observed in particular at the stations VITT, MGRD and VALX. Moreover, the model including only topography is worse than the one including also rock heterogeneities (Table 17) in agreement with Trasatti *et al.* (2011).

There is still a big question to answer: how does the precipitation water reach the source of deformation, causing level variations that generate deformation? According to Singhal and Gupta (1999), the rock fracturation degree and spacing depends on the thickness of the layers; in particular, the spacing of the fractures perpendicular to the layers is proportional to the layers thickness. It is worth noting that the upper formations (Maiolica and Rosso Ammonitico) of the MCCV anticline have a thin (1-20 cm) or medium (20 - <100 cm) stratification, while below them the Calcare del Vajont formation has a thickness of 10 - 15 m. This provides estimates of fractures spacing of some meter and decimeters in the Calcare del Vajont and upper layers, respectively. In addition, the presence of clayey interstates cause that the fractures do not cross more than one layer, so they can not be connected directly in the vertical direction. We then make the hypothesis that Maiolica and Rosso Ammonitico generate an "epikarst", particularly developed at the top of the anticline where tensile stress are the largest ones (Feng and Gu, 2017), which is not connected with the underlying deep karst. As in Figure 7, following the inclination of the layers toward north and the stratification, the epikarst may drive the water toward the backthrust and in its surrounding, which convey the water in the deep karst system because of the presence of larger vertical fractures in the Calcare del Vajont layer that are filled from above. Finally, water level changes inside these fractures may generate the pressure variations causing the observed displacements.

This interpretation is also useful in order to constrain the initial opening of the fracture chosen as the source of deformation. We assume (Figure 7) that the mean distance between the top of the anticline and the backthrust is about 3 km and that the water in between the top of the anticline and the backthust flows toward and then inside the fracture generating deformation. Since the water storage variations according to the GR5J model are up to 300 mm per unit area and the water level variations inside the fracture about 100 m, we can compute the initial opening of the fracture (d) by using the following formula of mass conservation:

$$d = \frac{300\,mm \times 3\,km}{100\,m} = 9\,m \tag{1}$$

This value is for sure too large to be realistic, since there are not evidence of a structure of this kind in the MCCV anticline. Anyway, it is worth noting that this result has been obtained considering that all the water stored in between the top of the anticline and the backthrust reaches the fracture. It is possible that the water follows different paths from the anticline to the Piave river, and only a small percentage of it transits inside the fracture generating deformation. Furthermore, the fracture we have chosen as the source of deformation is a representation of an area that is more fracturated than its surroundings, not a real open fracture. Then, it is possible that this highly fracturated zone in correspondence of the upper part of the backthrust fault has an extent of some meters (Faulkner *et al.*, 2010) and a porosity of 0.1 (Zempolich, 1997). The extension of the fracture area in a direction almost orthogonal to the backthrust can be estimated using equation 1 too, including porosity at the dominator and obtaining 90 m, which is consistent with the observations in Faulkner *et al.* (2010).

It has been shown that in several regions, like karst systems of the Italian Apennines (D'Agostino *et al.*, 2018) and the Mt. Hochstaufen alpine region (Hainzl *et al.*, 2005), the groundwater variations modulate seismicity rates and eventually trigger large earthquakes. This has also been observed at larger scale, like in the Himalayas, where seismicity rates, based on the declustered catalogue of (Bollinger *et al.*, 2007), depends on water storage variations induced by the monsoon season (Bettinelli *et al.*, 2008). In the study area geodetic data (e.g., Barba *et al.*, 2013) suggest that the Bassano-Valdobbiadene thrust is active and elastically locked, pointing toward a significant seismic potential of this fault (Castaldini and Panizza, 1991; Galadini *et al.*, 2001; Barba *et al.*, 2013). We studied the Coulomb stress change induced on this fault during the two main phases of the transient of hydrological origin here identified. Owing to the shallow vertical extension of the related source of deformation, a tensile fracture with 1 km width, we found that the Coulomb stress changes are confined within a depth of -3 km. During the opening phase of the fracture the Coulomb stress change on the Bassano-Valdobbiadene thrust surface is negative up to a depth of about -500 m, while in between -500 m and -2500 m it is positive with maximum values of the order of 0.1 bar at about -2500 m, while during the closing phase, we observed the same pattern, with the sign reversed. In Apennines D'Agostino *et al.* (2018) provide estimation of the Coulomb

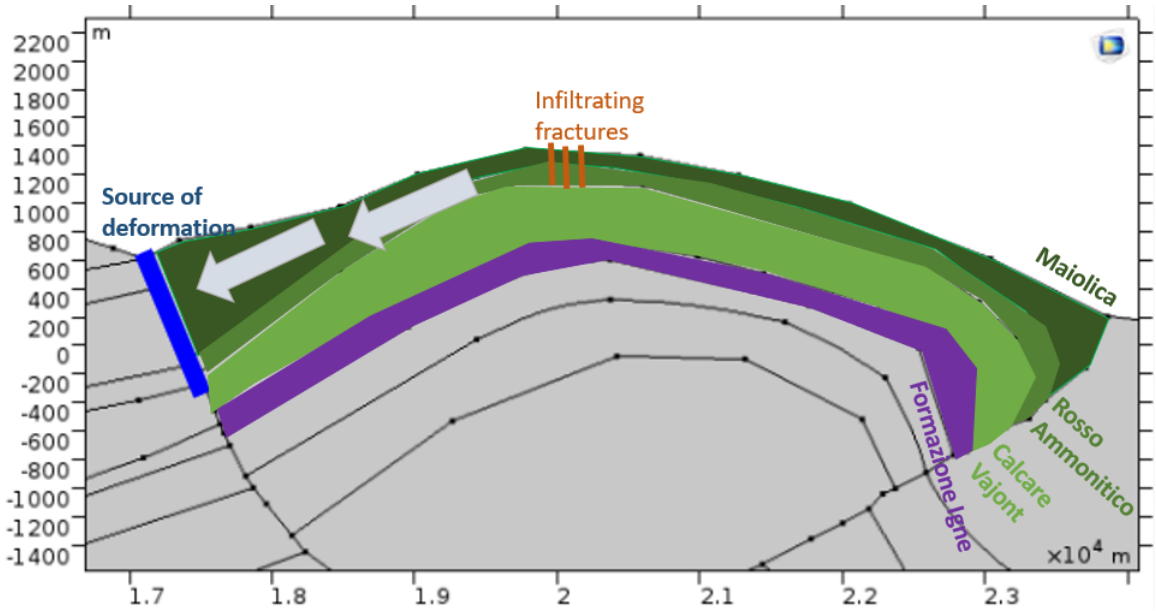

Figure 7: Hypothesis of the water recharge of the fracture (in blue) chosen as source of deformation. Grey arrows: water flow direction. Green layers: permeable. Purple layer: impermeable. Red lines: fracture on the top of the mountain chain, causing the water infiltration.

stress change, considering a 9 km depth, as large as 4-5 and 10-15 kPa for hydrological processes at seasonal and multiannual time scales, respectively. This seems consistent with our results, even though we considered a more shallow portion of Earth's crust. Considering larger scales, Bettinelli *et al.* (2008) estimated that water storage variations in the Ganges basin cause Coulomb stress variations at 10-15 km depth of 2-4 kPa.

8 Conclusions

In this thesis, we applied a blind source separation method to displacement time series obtained from the analysis of continuous GPS stations located in South-Eastern Alps and Northern Dinarides, with the goal of identifying and interpreting the physical processes that cause non-tectonic deformation in this area.

The results of this analysis show that, once the tectonic trend has been removed, it is possible to detect and separate two signals, which are caused by hydrological processes having different spatial and temporal signature. One is an annual signal that is evenly present in all GPS time series (common mode signal); the other one is a transient signal mainly present in the horizontal component, which have a non-periodic temporal evolution and mostly affects three regions corresponding to karst systems.

Changes of surface hydrological loads are responsible for the observed seasonal common mode displacements, which are significantly larger in the vertical component than in the horizontal one, showing the whole region under analysis moving up and down with an annual period. On the contrary, we found evidence of local-scale horizontal deformation with amplitudes and orientations controlled by structural and geological features in karst terrains. In particular, in three different karstic areas of the study region we observed stations moving in the opposite directions and reversing the sense of movement in time, implying a succession of extensional/compressional strains with variable amplitudes through time, acting normal to rock fractures. Initially, the evolution of ground displacements and dilatational strains associated with this signal were compared with cumulated precipitation curves obtained by summing, for each day, the precipitation occurred during a certain number of days before, with the number of days maximizing the correlation, varying between 150-220 and 240-300 days, if potential evapotranspiration correction is considered or not, respectively. We made the hypothesis that the cumulative precipitation curves were an indicator of water level variations in karst fractures of the three areas where the amplitude of the horizontal signal is the largest, highlighting a correlation between water storage variations in karst systems and ground deformation.

Water storage variations in a hydrological basin can be computed once known actual evapotranspiration, precipitation and river flow draining the basin. It follows that considering only precipitation and potential evapotranspiration provides a partial description of water storage variations. A more precise characterization of hydrological basins has been achieved through the application of rainfall-runoff hydrological models, which provide as output water storage variations of hydrological basins once given as input potential evapotranspiration, precipitation and temperature. Having found high correlations between the temporal evolution of the transient deformation signal and the water storage modeled by rainfall-runoff models, we could confirm the hypothesis that the transient deformation is linked to hydrologic processes. We also showed that using in-situ measurements of precipitation and temperature, instead of global datasets having a much lower spatial resolution, allows rainfall-runoff models better reproducing river flow data; furthermore, correlation between the geodetic and hydrologic signal increases when using in-situ data as well. Nonetheless, we recall that the acquisition and the interpolation of local data is much more time-consuming than analyzing gridded datasets, furthermore in-situ measurements are not available everywhere. It follows that using gridded dataset is preferable when performing quick preliminary analysis; anyway, when looking for the best available set of input data, it is better to use in-situ measurements that are more accurate than gridded ones.

In order to find how water storage variation causes the compressional/dilatational strain signal we initially considered a dislocation and a crack model in a homogeneous elastic half-space. This preliminary result suggests that the displacement pattern is consistent with deformation caused by water level variations of tens of meters in a fracture having a width of about 1 km. Then, we developed a two dimensional numerical model, based on the finite-element method, that includes the geological features of the area. In particular, we built the model starting from a geological profile that cross the Monte Cesen - Col Visentin mountain chain and tested different sources of deformation that are compatible with the geology of this area. We found that it is possible to link the source of deformation with a pre-existing fault and identify the hydrogeological processes that lead to the observed transient deformation, quantifying the involved forces. We tested 2-D models having different degrees of complexity: from a homogeneous domain with a flat free surface, to one where both topography and rock stratification is included. We proved that the modeled displacements are not very sensitive for the degree of sophistication of the model; nonetheless, the

initial inclusion of the layering and topography was necessary to test sources of deformation that differs from a fracture, like the loading on the interface between rocks of different permeability.

The identification and characterization, both in space and time, of transient deformation signals, such as the ones associated with water storage variations and groundwater flow, is crucial in interpreting active tectonic processes. The importance is twofold; first because a proper modeling of non-seasonal transient deformation can improve the accuracy of long-term tectonic rates from geodetic data, second because transient processes, mainly of tectonic origin, can perturb crustal stress at seismogenic depths, with effects on the background seismicity rate or on the seismic cycle. We found relevant Coulomb stress change induced by hydrological loading of our reference source of deformation on an active fault (Bassano-Valdobbiadene thrust) located nearby, down to a depth of 3 km. Since the earthquakes catalogs available for this region are not very precise, we cannot go on finding correlations between seismicity rates and water storage variations. Nonetheless, we believe that is important to hint a possible application of the results of this thesis.

References

Abbott, M.B., Bathrust, J.C., Cunge, J.A., O'Connell, P.E. and Rasmussen, J.; 1986: *An introduction to Europeen hydrological system-systeme hydrologique Europeen (SHE) Part 2. Structure of a physically based distributed modeling system.* Journal of Hydrology, 87, 61-77

Aliabadi, M.H. and Wrobel, L.C.; 2002: *The Boundary Element Method.* John Wiley & Sons. New York

Altamimi, Z., Collilieux, X. and Metivier, L.; 2011: *ITRF2008: An improved solution of the international terrestrial reference frame.* Journal of Geodesy, 85(8), 457473. https://doi.org/10.1007/s00190-011-0444-4

Amos, C. B., Audet, P., Hammond, W. C., Burgmann, R., Johanson, I. A. and Blewitt, G.; 2014: *Uplift and seismicity driven by groundwater depletion in central California.* Nature, 509(7501), 483486. https://doi.org/10.1038/nature13275

Anselmi, M., Govoni, A., DeGori, P. and Chiarabba, C.; (2011): *Seismicity and velocity structures along the southAlpine thrust front of the Venetian Alps (NEItaly)*, Tectonophysics, 513, 3748, doi:10.1016/j.tecto.2011.09.023

Argus, D. F., Fu, Y. and Landerer, F. W.; 2014: *Seasonal variation in total waterstorage in California inferred from GPS observations of vertical land motion.* Geophysical Research Letters, 41, 19711980. https://doi.org/10.1002/2014GL059570

Bakalowicz, M.; 1995: *La zone d'infiltration des aquiferes karstiques. Methodes d'etude. Structure et fonctionnement.* Hydrogeologie 4, 3-21

Bailey, S.; 2012: *Principal Component Analysis with Noisy and/or Missing Data.* Publications of the Astronomical Society of the Pacific, 124(919):10151023

Barba, S., Finocchio, D., Sikdar, E. and Burrato, P.; 2013: *Modelling the interseismic deformation of a thrust system: seismogenic potential of the Southern Alps.* Terra Nova.

Barla, G., Barla, M., Chiappone, A. and Rabagliati, U.; 2007: *Analisi di Stabilit della Miniera a Cielo Aperto di Alpetto - Cesana Brianza (Lecco)*, Rock Slope Stability Analysis of the Surface Mine of Alpetto - Cesana Brianza (Lecco), in Italian. 111-126

Benedetti, L., Tapponnier, P., King, G., Meyer, B. and Manighetti, I.; 2000: *Growth folding and active thrusting in the Montello region, Veneto, northern Italy.* J. Geophys. Res. 105, 739766

Berrisford, P., Dee, D., Fielding, K., Fuentes, M., Kallberg, P., Kobayashi, S. and Uppala, S.; 2009. *The ERA-Interim archive*, ERA Rep. Ser. (Vol. 1). Reading, UK: Eur. Cent. for Medium Range Forecasts

Bettinelli, P., Avouac, J.-P., Flouzat, M., Bollinger, L., Ramillien, G., Rajaure, S. and Sapkota, S.; 2008: *Seasonal variations of seismicity and geodetic strain in the Himalaya induced by surface hydrology.* Earth and Planetary Science Letters, 266(34), 332344. https://doi.org/10.1016/j.epsl.2007.11.021

Beven, K. J. and Kirkby, M. J.; 1979: *A physically based variable contributing area model of basin hydrology*, Hydrol. Sci. Bull., 24(1), 4369

Blewitt, G., andLavallee, D.; 2002: *Effect of annual signals on geodetic velocity.* Journal of Geophysical Research, 107(B7), 2145. https://doi.org/10.1029/2001JB000570

Boehm, J., Werl, B. and Schuh, H.;2006: *Troposphere mapping functions for GPS and very long baseline interferometry from European Centre for Medium-Range Weather Forecasts operational analysis data.* Journal of Geophysical Research, 111, B02406. https://doi.org/10.1029/2005JB003629

Bollinger, L., Perrier, F., Avouac, J. P., Sapkota, S., Gautam, U., and Tiwari, D. R.; 2007: *Seasonal modulation of seismicity in the Himalaya of Nepal.* Geophysical Research Letters, 34, L08304. https://doi.org/10.1029/2006GL029192

Bonacci, O. and Roje-Bonacci, T.; 2000: *Interpretation of groundwater level monitoring results in karst aquifers: examples from the Dinaric karst*, HYDROL PROC, 14(14), 2000, pp. 2423-2438 Bonacci, O; Matesa.

Borsa, A. A., Agnew, D. C. and Cayan, D. R.; 2014: *Ongoing drought-induced uplift in the western United States.* Science, 345(6204), 15871590. https://doi.org/10.1126/science.1260279

Boscolo, C., D'Alberto, L. and Mion, F.; 2007: *Atlante delle sorgenti del Veneto*

Boy, J.-P., Longuevergne, L., Boudin, F., Jacob, T., Lyard, F., Llubes, M., Florsch, N. and Esnoult, M .F.; 2009: *Modelling atmospheric and induced non-tidal oceanic loading contributions to surface gravity and tilt measurements*, J. Geodyn.,48, 182188, doi:10.1016/j.jog.2009.09.022

Bragato, P., Peruzza, L., Bernardi, P., Bertoni, M., Bressan, G., Bragato, P., Comelli, P., Del Negro, E., Di Bartolomeo, P., Garbin, M., Gentili, S., Klin, P., Palmieri, F., Peruzza, L., Pesaresi, D., Petronio, L., Plasencia L., Milton P., Ponton, C., Priolo, E., Dur, G.; 2012: *Regione Veneto - Gestione della rete di controllo sismico, studio della sismicit regionale e ricerca sismologica a fini di protezione civile Anno 2011*

Braitenberg, C.; 1999: *Estimating the hydrologic induced signal in geodetic measurements with predicitive filtering methods.* Geophys. Res. Letters, 26, 775-778

Braitenberg, C., Nagy, I., Negusini, M., Romagnoli, C., Zadro, M., Zerbini, S.; 2001: *Geodetic measurements at the northern border of the Adria plate.* Journal of Geodynamics, Vol.32, N. 1/2, 267-286

Braitenberg, C., Romeo, G., Taccetti, Q. and Nagy, I.; 2006: *The very broad-band long-base tiltmeters of Grotta Gigante (Trieste, Italy): secular term tilting and the great Sumatra-Andaman Islands earthquake of December 26, 2004.* J. of Geodynamics, 41, 164-174

Braitenberg, C. and Zadro, M.; 2001: *Time series modeling of the hydrologic signal in geodetic measurements.* Journal of the Geodetic Society of Japan, 47, No.1, 95-100, (PDF file 293 KB)

Burrato, P., Poli, M.E., Vannoli, P., Zanferrari, A., Basili, R. and Galadini, F.; 2008: *Sources of Mw 5+ earthquakes in northeastern Italy and western Slovenia: an updated view based on geological and seismological evidence.* Tectonophysics 453, 157176. http://dx.doi.org/10.1016/j.tecto.2007.07.009

Cardoso, J.F.; 1999; *High-order contrasts for Independent Component Analysis.* Neural Computation, 11:157192, 1999

Castaldini, D. and Panizza, M.; 1991: *Inventario delle faglie attive tra i fiumi Po e Piave e il Lago di Como (Italia settentrionale)*, Il Quaternario, 4, 333410

Castellarin, A. and Cantelli, L.; 2000: *Neo-Alpine evolution of the Southern Eastern Alps.* J. Geodyn. 30, 251274. http://dx.doi.org/10.1016/s0264-3707(99)00036-8

Cattin, R., Chamot-Rooke, N., Pubellier, M., Rabaute, A., Delescluse, M. et al.; 2009: *Stress change and effective friction coefficient along the Sumatra-Andaman-Sagaing fault system after the 26 December 2004 (M-w=9.2) and the 28 March 2005 (M-w=8.7) earthquakes.* Geochemistry, Geophysics, Geosystems, AGU and the Geochemical Society, 2009, 10 (3), pp.Q03011

Cavallo, C., Dal Molin, L., De Waele, J., Mietto, P., Piccini, L., Preziosi, E., et al.; 2003: *Il censimento delle sorgenti carsiche dItalia, Atti del XIX Congresso Nazionale di Speleologia* (Vol. 2, pp. 2934). Bologna, 2731 Agosto, 2003

Cervelli, P., Murray, M. H., Segall, P., Aoki, Y. and Kato, T.; 2001: *Estimating source parameters from deformation data, with an application to the March 1997 earthquake swarm off the Izu Peninsula, Japan.* Journal of Geophysical Research, 106(B6), 11,21711,237. https://doi.org/10.1029/2000JB900399

Chan, K. L., Lee, T. W. and Sejnowski, T. J.; 2003: *Variational Bayesian learning of ICA with missing data.* Neural Computation, 15(8), 19912011. https://doi.org/10.1162/08997660360675116

Chanard, K., Avouac, J. P., Ramillien, G. and Genrich, J.; 2014: *Modeling deformation induced by seasonal variations of continental water in the Himalaya region: Sensitivity to Earth elastic structure.* Journal of Geophysical Research: Solid Earth, 119, 50975113. https://doi.org/10.1002/2013JB010451

Chanard, K., Fleitout, L., Calais, E., Rebischung, P. and Avouac, J. P.; 2018: *Toward a global horizontal and vertical elastic load deformation model derived from GRACE and GNSS station position time series.* Journal of Geophysical Research: Solid Earth, 128. https://doi.org/10.1002/2017JB015245

Cheloni, D., D'Agostino, N., D'Anastasio, E., Selvaggi, G.; 2012: *Reassessment of the source of the 1976 Friuli, NE Italy, earthquake sequence from the joint inversion of high-precision levelling and triangulation data.* Geophys. J. Int. 190, 12791294. http://dx.doi.org/10.1111/j.1365-246X.2012.05561.x

Cheloni, D., D'Agostino, N., and Selvaggi, G.; 2014: *Interseismic coupling, seismic potential, and earthquake recurrence on the southern front of the Eastern Alps (NE Italy).* Journal of Geophysical Research: Solid Earth, 119, 44484468. https://doi.org/10.1002/2014JB010954

Chen Z., Auler A.S., Bakalowicz M., Drew D., Griger F., Hartmann J., Jiang G., Moosdorf N., Richts A., Stevanovic Z., Veni G. and Goldscheider N.;2017: *The world karst aquifer mapping project: concept, mapping procedure and map of Europe.* Hydrogeol J 25:771785

Chen, F., Mitchell, K., Schaake, J., Xue, H.L., Koren, V., Duan, Q.Y., Ek, M. and Betts, A.; 1996: *Modeling of landsurface evaporation by four schemes and comparison with FIFE observations*,

J. Geophys. Res., 101 (D3), 72517268

Chen, J. L., Rodell M., Wilson C. R. and Famiglietti J. S.; 2005: *Low degree spherical harmonic influences on Gravity Recovery and Climate Experiment (GRACE) water storage estimates*, Geophys. Res. Lett., 32, L14405, doi:10.1029/2005GL022964

Choudrey, R. A. and Roberts, S. J.; 2003: *Variational mixture of Bayesian independent component analyzers.* Neural Computation, 15(1),213252. https://doi.org/10.1162/089976603321043766

Choudrey, R. A.; 2002: *Variational Methods for Bayesian Independent Component Analysis.* Pattern analysis and machine learning - robotics research group, University of Oxford

Comon, P.; 1994: *Independent component analysis, A new concept?* Signal Processing, 36:287314.

Costa, V., Doglioni, C., Grandesso, P., Masetti, D., Pellegrini, G.B., Tracanella, E.; 1992: *Carta Geologica d'Italia scala 1:50000 e note illustrative del Foglio 063 Belluno.* Servizio Geologico dItalia, Roma 1996

D'Agostino, N., Silverii, F., Amoroso, O., Convertito, V., Fiorillo, F., Ventafridda, G., and Zollo, A.; 2018: *Crustal deformation and seismicity modulated by groundwater recharge of karst aquifers.* Geophysical Research Letters, 45, 12,25312,262. https://doi.org/10.1029/2018GL079794

Danesi, S., Pondrelli, S., Salimbeni, S., Cavaliere, A., Serpelloni, E., Danecek, P., et al.; 2015: *Active deformation and seismicity in the Southern Alps (Italy): The Montello hill as a case study.* Tectonophysics, 653, 95108. https://doi.org/10.1016/j.tecto.2015.03.028

Davis, J. L., Wernicke, B. P. and Tamisiea, M. E.; 2012: *On seasonal signals in geodetic time series.* Journal of Geophysical Research, 117, B01403. https://doi.org/10.1029/2011JB008690

Decker, K. and Peresson, H.; 1996: *Tertiary kinematics in the Alpine-Carpathian-Pannonian system: Links between thrusting, transform faulting and crustal extension.* In G. Wessely & W. Liebl (Eds.), Oil and gas in alpidic thrust belts and basins of central and eastern Europe, EAGE Spec. Publ (Vol. 5, pp. 6977). London: The Geological Society

Dee, D., Uppala, S., Simmons, A., Berrisford, P., Poli, P., Kobayashi, S., et al.; 2011: *The ERA-Interim reanalysis: Configuration and performance of the data assimilation system.* Quarterly Journal of the Royal Meteorological Society, 137(656), 553597. https://doi.org/10.1002/qj.828

Devoti, R., D'Agostino, N., Serpelloni, E., Pietrantonio, G., Riguzzi, F., Avallone, A., et al.; 2017): *A combined velocity field of the Mediterranean region.* Annals of Geophysics, 60(2), S0215. https://doi.org/10.4401/ag-7059

Devoti, R., Falcucci, E., Gori, S., Poli, M. E., Zanferrari, A., Braitenberg, C., et al.; 2016: *Karstic slope breathing: Morpho-structural influence and hazard implications.* Geophysical Research Abstracts, 18, EGU2016EGU15231

Devoti, R., Zuliani, D., Braitenberg, C., Fabris, P. and Grillo, B.; 2015: *Hydrologically induced slope deformations detected by GPS and clinometric surveys in the Cansiglio Plateau, Southern Alps.* Earth and Planetary Science Letters, 419, 134142. https://doi.org/10.1016/j.epsl.2015.03.023

Di Napoli Alliata, E., Protodecima, F. and Pellegrini,G.B.; 1970: *Studio geologico, stratigrafico e micropa leontologico dei dintorni di Belluno.* Mem. Soc. Geol. It., v.9, pp.1-28,Roma

Dieterich, J.; 1979: *Modelling of rock friction: 1. Experimental results and constitutive equations.* J. Geophys. Res. 84, 21612168

Dingman, S. L.; 1994: *Physical Hydrology.* Macmillan Publishing Company

DISS Working Group; 2018: *Database of Individual Seismogenic Sources (DISS), Version 3.2.1: A compilation of potential sources for earthquakes larger than M 5.5 in Italy and surrounding areas.* http://diss.rm.ingv.it/diss/, Istituto Nazionale di Geofisica e Vulcanologia; DOI:10.6092/INGV.IT-DISS3.2.1

Doglioni, C.; 1987: *Tectonics of the dolomites (Southern Alps, Northern Italy).* J. Struct. Geol. 9, 181193

Dong, D., Fang, P., Bock, Y., Cheng, M. and Miyazaki, S.; 2002: *Anatomy of apparent seasonal variations from GPS-derived site position time series.* Journal of Geophysical Research, 107(B4), 2075. https://doi.org /10.1029/2001JB000573

Dong, D., Fang, P., Bock, Y., Webb, F., Prawirodirdjo, L., Kedar, S. and Jamason, P.; 2006: *Spatiotemporal filtering using principal component analysis and Karhunen-Loeve expansion approaches for regional GPS network analysis.* Journal of Geophysical Research, 111, B03405. https://doi.org/10.1029/2005JB003806

Dong, D., Herring, T. and King, R.; 1998: *Estimating regional deformation from a combination of space and terrestrial geodetic data.* Journal of Geodesy, 72(4), 200214. https://doi.org /10.1007/s001900050161

Dyke C.; 1995: *How sensitive is natural fracture permeability at depth to variation in effective stress?*, In Myer, L.R, Tsang, C.-F., Cook, N.G.W, and Goodman, R.E.(Editors), Proceedings Fractured and Jointed Rock Masses Conference, Balkema, Rotterdam, 81-88

Dziewonski, A. M. and Anderson, D. L.; 1981: *Preliminary reference Earth model.* Physics of the Earth and Planetary Interiors, 25(4), 297356. https://doi.org/10.1016/0031-9201(81)90046-7

Edijatno, Nascimento, N.O., Yang, X., Makhlouf, Z. and Michel, C.; 1999: *GR3J: a daily watershed model with three free parameters.* Hydrological Sciences Jurnal 44 (2), 263 277

Fang, H., Beaudoing, H.K., Rodell, M., Teng, W.L. and Vollmer, B.E.; 2009: *Global Land Data Assimilation System (GLDAS) products, services and application from NASA Hydrology Data and Information Services Center (HDISC)*, ASPRS 2009 Annual Conference, Baltimore, MD, 813 March 2009

Fantoni, R., Barbieri, C., Catellani, D., Castellarin, D., Di Giulio, A. and Pessina, C.; 2001: *The record of south-Alpine events in the Venetian foreland and foredeep.* Mitt. Geol. Palaontol. Innsbruck 25, 7981

Farrell, W. E.; 1972: *Deformation of the Earth by surface loads.* Reviews of Geophysics, 10(3), 761. https://doi.org/10.1029/RG010i003p00761

Fasiol, G.; 2010: *AUTOSTRADA A PEDAGGIO PEDEMONTANA VENETA*, technical report

Faulkner, D. R., Jackson, C. A. L., Lunn, R. J., Schlische, R. W., Shipton, Z. K., Wibberley, C. A. J. and Withjack, M. O.; 2010: *A review of recent developments concerning the structure, mechanics and fluid flow properties of fault zones*, J. Struct. Geol.,32 ,15571575, doi:10.1016/j.jsg.2010.06.009

Feng, J. and Gu, K.; 2017: *Geomechanical Modeling of Stress and Fracture Distribution during Contractional Fault-Related Folding.* Journal of Geoscience and Environment Protection, 5, 61-93. doi: 10.4236/gep.2017.511006

Ferrari, C., Bonafede, M. and Belardinelli, M. E.; 2016: *LibHalfSpace: A C++ object-oriented library to study deformation and stress in elastic half-spaces.* Computers & Geosciences, 96, 136146. https://doi.org/10.1016/j.cageo.2016.08.011

Fileccia, A.; 2006: *Delineation of spring head protection zones (Tegorzo and Fium springs).* Comunicazione Workshop progetto Interreg IIIB CADSES Kater II, 8 giugno 2006, Vas (BL), Regione del Veneto

Fiorillo, F. and A. Doglioni, A.; 2010: *The relation between karst spring discharge and rainfall by cross-correlation analysis (Campania, southern Italy)*, Hydrogeology Journal , 18 (8), 1881-1895, doi:s10040-010-0666-1

Fleury, P., Plagnes, V. and Bakalowicz, M.; 2007: *Modelling of the functioning of karst aquifers with a reservoir model: Application to Fontaine de Vaucluse (South of France).* Journal of Hydrology, 345(12), 3849. https://doi.org/10.1016/j.jhydrol.2007.07.014

Forkasiewicz, J. and Paloc, H.; 1967: *Le rgime de tarissement de la Foux de la Vis, etude prliminaire.* In Hydrology of fractured rocks proccedings of the Dubrovnik Symposium, October 1965 (Vol. 1, pp. 213226)

Fu, Y., Argus, D. F., Freymueller, J. T. and Heflin, M. B.; 2013: *Horizontal motion in elastic response to seasonal loading of rain water in the Amazon Basin and monsoon water in Southeast Asia observed by GPS and inferred from GRACE.* Geophysical Research Letters, 40, 60486053. https://doi.org/10.1002/2013GL058093

Galadini, F., Meletti, C. and Vittori, E.; 2001: *Major active faults in Italy: available surficial data*, Geol. en Mijn. (Netherlands Journal of Geosciences), 80, 273296.

Galadini, F., Galli, P., Molin, D. and Ciurletti, G.; 2001: *Searching for the seismogenic source of the 1117 earthquake in northern Italy: a multidisciplinary approach.* In: Glade, T., Albini, P., Frances, F. (Eds.), The Use of Historical Data in Natural Hazards Assessment. Kluwer Academic publishers, Dordrecht, the Netherlands, pp. 327

Galadini, F., Poli, M.E. and Zanferrari, A.; 2005: *Seismogenic sources potentially responsible for earthquakes with $M \geq 6$ in the eastern Southern Alps (Thiene-Udine sector, NE Italy).* Geophys. J. Int. 161, 739762. http://dx.doi.org/10.1111/j.1365-.2005.02571.x

Gayathri, K.D., Ganasri, B.P. and Dwarakish, G.S; 2015: *A Review on Hydrological Model.* Aquatic Procedia 4 (2015) 1001 1007. doi: 10.1016/j.aqpro.2015.02.126

Gegout, P., Boy, J.-P., Hinderer, J. and Ferhat, G.;2010: *Modeling and observation of loading contribution to time-variable GPS sites positions.* International Association of Geodesy Symposia, 135(8), 651659. https://doi.org/10.1007/978-3-642-10634-7_86

Gelb, A., and Vander Velde W. E.; 1968: *Multiple-Input Describing Functions and Nonlinear System Design.* McGraw Hill.

Gentler, S.; 1986: *Morphologie et comportement hydromdcanique d'une fracture naturelle dans un granite sous contrainte normate. Etude expgrimentale et theorique.* PhD thesis, Universite d'Orlrans, France

Gilli, E., Boudin, F., Longuevergne, L., Florsch, N., Walch, J.-J., Gomez, A., et al.; 2010: *Neotectonics and current hydrologically-induced karst deformation. Case study of the Plateau de Calern (Alpes-Maritimes, France).* Geodinamica Acta, 23(13), 4964. https://doi.org/10.3166/ga.23.49-64

Goddard Earth Sciences Data and Information Services Center; 2016: *TRMM (TMPA) precipitation L3 1 day 0.25 degree 0.25 degree V7, Goddard Earth Sciences Data and Information Services Center (GES DISC).* Retrieved from https://disc.gsfc.nasa.gov/datacollection/TRMM_3B42_Daily_7.html, Accessed (March 2017)

Grillo, B., Braitenberg, C., Devoti, R., and Nagy, I.; 2011: *The study of karstic aquifers by geodetic measurements in Bus de la Genziana station- Cansiglio plateau (Northeastern Italy).* Acta Carsologica, 40(1), 161173. https://doi.org/10.3986/ac.v40i1.35

Grillo, B., Braitenberg, C., Nagy, I., Devoti, R., Zuliani, D., and Fabris, P.; 2018: *Cansiglio Karst Plateau: 10 years of geodetichydrological observations in Seismically Active Northeast Italy.* Pure and Applied Geophysics. https://doi.org/10.1007/s00024-018-1860-7.

Gualandi, A.; 2015: *Spatial and temporal characterisation of ground deformation recorded by geodetic techniques.* Phd thesis. Universit di Bologna, Italy

Gualandi, A., Avouac, J. P., Galetzka, J., Genrich, J. F., Blewitt, G., Adhikari, L. B., et al.; 2016: *Pre- and post-seismic deformation related to the 2015, Mw 7.8 Gorkha earthquake, Nepal.* Tectonophysics, 714-715, 90106. https://doi.org /10.1016/j.tecto.2016.06.014

Gualandi, A., Nichele, C., Serpelloni, E., Chiaraluce, L., Anderlini, L., Latorre, D., et al.; 2017: *Aseismic deformation associated with an earthquake swarm in the northern Apennines (Italy).* Geophysical Research Letters, 44, 77067714. https://doi.org /10.1002/2017GL073687

Gualandi, A., Perfettini, H., Radiguet, M., Cotte, N. and Kostoglodov, V.; 2017: *GPS deformation related to the Mw 7.3, 2014, Papanoa earthquake(Mexico) reveals the aseismic behavior of the Guerrero seismic gap.* Geophysical Research Letters, 44, 60396047. https://doi.org/10.1002/2017GL072913

Gualandi, A., Serpelloni, E. and Belardinelli, M. E.; 2016: *Blind source separation problem in GPS time series.* Journal of Geodesy, 90(4), 323341. https://doi.org /10.1007/s00190-015-0875-4

Guglielmi, Y., Cappa, F. and Binet, S.; 2005: *Coupling between hydrogeology and deformation of mountainous rock slopes: Insights from La Clapire area (Southern Alps, France).* Comptes Rendus Geoscience, 337(13), 11541163. https://doi.org/ 10.1016/j.crte.2005.04.016

Hainzl, S., Kraft, T., Wassermann, J., Igel, H. and Schmedes, E.; 2006: *Evidence for rainfall-triggered earthquake activity.* Geophysical Research Letters, 33, L19303. https://doi.org/10.1029/2006GL027642

Harris, R. A. and Simpson R. W.; 1992: *Changes in static stress on southern California faults after the 1992 Landers earthquake*, Nature, 360, 313-318

Hartmann, A., Goldscheider, N., Wagener, T., Lange, J. and Weiler, M.; 2014: *Karst water resources in a changing world: Review of hydrological modeling approaches*, Rev. Geophys., 52, 218242, doi:10.1002/2013RG000443

Haylock, M. R., Hofstra, N., Klein Tank, A. M. G., Klok, E. J., Jones, P. D. and New, M.; 2008: *A European daily high-resolution gridded data set of surface temperature and precipitation for 19502006.* Journal of Geophysical Research, 113, D20119. https://doi.org/10.1029/2008JD010201

Herring, T. A., King, R. W., Floyd, M. A. and McClusky, S. C.; 2015: *Introduction to GAMIT/GLOBK, Release 10.6.* Retrieved from http://www-gpsg.mit.edu/ simon/gtgk/Intro_GG.pdf

Herring, T.A., Melbourne, T.I., Murray,M.H., Floyd, M.A., Szeliga, W.M., King R. W., Phillips, D.A., Puskas,C.M., Santillan,M. and Wang, L.; 2016: *Plate Boundary Observatory and Related Networks: GPS Data Analysis Methods and Geodetic Products*, Rev. of Geophys., 54, doi:10.1002/2016RG000529

Hirose, H., Hirahara, K., Kimata, F., Fujii, N. and Miyazaki, S.; 1999: *A slow thrust slip event following the two 1996 Hyuganada earthquakes beneath the Bungo Channel, Southwest Japan*, Geophys. Res. Lett. ,26 (21), 32373240

Hyvarinen, A. and Oja, E.;1997: *A fast fixed-point algorithm for Independent Component Analysis.* Neural Computation, 9(7):14831492

Ismail-Zadeh, A., and Tackley, P. J.; 2010: *Computational Methods for Geodynamics*, Cambridge University Press, Cambridge

Jacob, T., Chery, J., Boudin, F. and Bayer, R.; 2010: *Monitoring deformation from hydrologic processes in a karst aquifer using long-baseline tiltmeters.* Water Resources Research, 46, W09542. https://doi.org/10.1029/2009WR008082

Jade, S. and Sitharam, T.; 2003: *Characterization of strength and deformation of jointed rock mass based on statistical analysis.* International Journal of Geomechanics, 3(1), 4354

James, L.D.; 1972: *Hydrologic modelling, parameter estimation and watershed characteristics.* J. Hydrol. 17, 383-397

Jensen, M.E., Burman, R.D. and Allen, R.G.; 1990: *Evapotranspiration and water requirements*, ASCE Manual 70, New York, USA 1990. 332 pp

Johnson, C. W., Fu, Y. and Burgmann, R.; 2017: *Seasonal water storage, stress modulation, and California seismicity.* Science 356, 11611164

Jiang, Y., Wdowinski, S., Dixon, T. H., Hackl, M., Protti, M. and Gonzalez, V.; 2012. *Slow slip events in Costa Rica detected by continuous GPS observations, 20022011. Geochemistry*, Geophysics, Geosystems, 13, Q04006. https://doi.org/10.1029/2012GC004058

Jones, P. and Harris, I.; 2013: *CRU TS3.21: Climatic Research Unit (CRU) Time-Series (TS) Version 3.21 of High Resolution Gridded Data of Month-by-month Variation in Climate (Jan. 1901 - Dec. 2012).* NCAS British Atmospheric Data Centre

Koren, V., Schaake, J., Mitchell, K., Duan, Q.Y., Chen, F. and Baker, J.M.; 1999: *A parameterization of snowpack and frozen ground intended for NCEP weather and climate models*, J.Geophys.Res., 104, 19 56919 585

Kositsky, A.P. and Avouac J.P.; 2010: *Inverting geodetic time series with a principal component analysis-based inversion method.* Journal of Geophysical Research, 115(B03401). doi:10.1029/2009JB006535

Kullback, S. and Leibler, R.A.; 1951: *On information and sufficiency.* Annals of Mathematical Statistics, 22(1):7986, 1951. doi:10.1214aoms/1177729694

Kusche, J. and E. J. O. Schrama; 2005: *Surface mass redistribution inversion from global GPS deformation and Gravity Recovery and Climate Experiment (GRACE) gravity data*, J. Geophys. Res.,110,B09409, doi:10.1029/2004JB003556

Lagler, K., Schindelegger, M., Bohm, J., Krasna, H. and Nilsson, T.; 2013: GPT2: Empirical slant delay model for radio space geodetic techniques. Geophysical Research Letters, 40, 10691073. https://doi.org/10.1002/grl.50288

Lancia, M., Saroli, M. and Petitta, M.; 2018: *A Double Scale Methodology to Investigate Flow in Karst Fractured Media via Numerical Analysis*: The Cassino Plain Case Study (Central Apennine, Italy), Geofluids, vol. 2018, Article ID 2937105, 12 pages. https://doi.org/10.1155/2018/2937105

Laubscher, H.P.; 1996: *Shallow and deep rotation in the Miocene alps.* Tectonics 15 (5), 10221035

Laubscher, H.P.; 1989: *The tectonics of the southern Alps and the AustroAlpine nappes: a comparison.* In: Coward, M.P., Dietrich, D. & Park, R.G. (eds.), Alpine Tectonics, Geological Society Special Publication, 45: 1-29; Oxford (Blackwell)

Lin, L. I.-K.; 1989; *A concordance correlation coefficient to evaluate reproducibility.* Biometrics, 45(1), 255268. https://doi.org/10.2307/ 2532051

Lin, L. I.-K.; 2000: *Correction: A note on the concordance correlation coefficient.* Biometrics, 56(1), 324325

Lindstrom, G., Johansson, B., Persson, M., Gardelin, M., Bergstrom, S.; 1997: *Development and test of the distributed HBV-96 hydrological model.* Journal of Hydrology 201, 272 288

Longuevergne, L., Florsch, N., Boudin, F., Oudin, L. and Camerlynck, C.: 2009; *Tilt and strain deformation induced by hydrologically active natural fractures: Application to the tiltmeters installed in Sainte-Croix-aux-Mines observatory (France).* Geophysical Journal International, 178(2), 667677. https://doi.org/10.1111/j.1365-246X.2009.04197.x

Lyard, F., Lefevre, F., Letellier, T. and Francis, O.; 2006: *Modelling the global ocean tides: Modern insights from FES2004.* Ocean Dynamics, 56(5-6), 394415. https://doi.org/10.1007/s10236-006-0086-x

MacKay, D.J.C.; 1995: *Probable networks and plausible predictions - a review of practical Bayesian methods for supervised neural networks*, Network: Computation in Neural Systems, vol. 6, pp. 469505, 1995

Maillet, E.; 1905: *Essais D'hydraulique Souterraine Et Fluviale*, Librairie Sci. (p. 218). Paris: A. Hermann

Mangin, A.; 1975: *Contribution a letude hydrodynamique des aquiferes karstiques.* Annales de Speleologie, 26, 283-339

Mao, A., Harrison, C. and Dixon, T.; 1999: *Noise in GPS coordinate time series*, J. Geophys. Res.,104, 2797-2816, 1999

Massironi, M., Zampieri, D. and Caporali, A.; 2006: *Miocene to present major fault linkages through the Adriatic indenter and the AustroalpinePenninic collisional wedge (Alps of NE Italy).* In: Moratti, G., Chalouan, A. (Eds.), Active Tectonics of the Western Mediterranean Region and North Africa Vol. 262. Geological Society, London, pp. 245258 In: Special Publications

McGuinness, J.L. and Bordne, E.F.; 1972: *A comparison of lysimeter-derived potential evapotranspiration with computed values.* Technical Bulletin 1452, Agricultural Research Service, US Department of Agriculture, Washington, DC

Mekik, C. and Can, O.; 2010: *An Investigation on Multipath Errors in Real Time Kinematic GPS Method*, Sci. Res. Essays, 5(16): 2186-2200

Melbourne, T. I., Webb, F. H., Stock, J. M. and Reigber, C.; 2002: *Rapid postseismic transients in subduction zones from continuous GPS*, J. Geophys. Res.107 2241

Mietto, P. and Sauro, U.; 2000: *Grotte del Veneto. Paesaggi Carsici e Grotte del Veneto* (p. 480). Vago di Lavagno: Editrice La Grafica

Milanovic, P.; 1981: *Karst hydrogeology* (p. 434). Littleton, Colo: Water Resources Publication

Milanovic, P.; 2005: *Water resources engineering in karst.* Choice Reviews Online, 42(5), 42-2822. https://doi.org/10.5860/choice.42-2822

Milanovic, P.; 2014: *Hydraulic properties of karst groundwater and its impacts on large structures.* In J. Mudry, F. Zwahlen, C. Bertrand, & J. W. LaMoreaux (Eds.), H2Karst Research in Limestone Hydrogeology (pp. 1948). Cham: Springer International Publishing. https://doi.org/10.1007/978-3-319-06139-9_2

Ming, F., Yang, Y., Zeng, A., Zhao, B.; 2017: *Spatiotemporal filtering for regional GPS network in China using independent component analysis*, J. Geodyn., 91 (4), 419 440. https://doi.org/10.1007 s00190-016-0973-y

Mitchell, K.E., Lohmann, D., Houser, P.R., Wood, E.F., Schaake, J.C., Robock, A., Cosgrove, B.A., Sheffield, J., Duan, Q., Luo, L., Higgins, R.W., Pinker, R.T., Tarpley, J.D., Lettenmaier, D.P., Marshall, C.H., Entin, J.K., Pan, M., Shi, W., Koren, V., Meng, J., Ramsay, B.H. and Bailey, A.A.; 2004: *The multiinstitution North American Land Data Assimilation System (NLDAS): Utilizing multiple GCIP products and partners in a continental distributed hydrological modeling system*, J . Geophys. Res. , 109, D07S90, doi:10.1029/2003JD003823

Monteith, J. L.; 1965: *Evaporation and environment*, Sym. Soc. Exp. Biol., 19, 205234

Moore, D.S., McCabe, G.P., Duckworth, W.M. and Sclove, S.L.; 2003: *The Practice of Business Statistics: Using Data for Decisions*, 2nd edn, Freeman , WH New York, 859 pp

Moreau, F. and Dauteuil, O.; 2013: *Geodetic tools for hydrogeological surveys: 3D-displacements above a fractured aquifer from GPS time series.* Engineering Geology, 152(1), 19

Nash, J. E. and Sutcliffe, J. V.; 1970: *River flow forecasting through conceptual models part I A discussion of principles.* Journal of Hydrology. 10 (3): 282290. doi:10.1016/0022-1694(70)90255-6.

Okada, Y.; 1985: *Surface deformation to shear and tensile faults in a halfspace.* Bulletin of the Seismological Society of America, 75, 11351154

Oudin, L., Andrassian, V., Perrin, C. and Anctil, F.; 2004: Locating the sources of low-pass behavior within rainfall-runoff models, Water Resour. Res., 40, W11101

Oudin, L., Michel, C. and Anctil, F.; 2005: *Which potential evapotranspiration input for a lumped rainfall-runoff model ? Part 2-Towards asimple and efficient potential evapotranspiration model for rainfall-runoff modelling*, Journal of Hydrology, 303(1-4), 290306

Perrin, C., Michel, C. and Andreassian, V.; 2003: *Improvement of a parsimonious model for stream flow simulation*, Journal of Hydrology, 279(1-4), 275289

Petrie, E. J., King, M. A., Moore, P. and Lavallee, D. A.; 2010: *Higher-order ionospheric effects on the GPS reference frame and velocities.* Journal of Geophysical Research, 115, B03417. https://doi.org/10.1029/2009JB006677

Placer, L.; 1999b: *Contribution to the macrotectonic subdivision of the border region between Southern Alps and External Dinarides.* Geologija 41, 223255, Ljubljana

Placer, L.; 1999: *Structural meaning of the Sava folds.* Geologija 41, 191221

Placer, L. and Car, J.; 1998: *Structure of Mt. Blegos between the Inner and Outer Dinarides.* Geologija 40, 305323

Pizzaia (2006) personal communication

Poli, M.E., Peruzza, L., Rebez, A., Renner, G., Slejko, D. and Zanferrari, A.; 2002: *New seismotectonic evidence from analysis of the 19761977 and 19771999 seismicity in Friuli (NE Italy).* Boll. Geofis. Teor. Appl. 43 (12), 5378

Prey, S.; 1978: *Rekonstruktionsversuch der alpidischen Entwicklung der Ostalpen.* Mitt. osterr. geol. Ges., 69: 1-25

Rahnama, M. and Gloaguen, R.; 2014a: *TecLines: A MATLAB-based toolbox for tectonic lineament analysis from satellite images and DEMs, Part 1: Line segment detection and extraction.* Remote Sensing, 6(7), 59385958. https://doi.org/10.3390/rs6075938

Rahnama, M. and Gloaguen, R.; (2014b): *TecLines: A MATLAB-based toolbox for tectonic lineament analysis from satellite images and DEMs, Part 2: Line segments linking and merging.* Remote Sensing, 6(11), 11,46811,493. https://doi.org/10.3390/rs61111468

Ramsay, J. G. and Huber, M. I.; 1983: *The Techniques of Modern Structural Geology.* Volume 1: Strain. Analysis (307 pp.). London: Academic Press

Rodell, M., Houser, P. R., Jambor, U., Gottschalck, J., Mitchell, K., Meng, C., et al.; 2004: *The Global Land Data Assimilation System.* Bulletin of the American Meteorological Society, 85, 381394. https://doi.org/10.1175/BAMS-85-3-381

Roeloffs, E. A.; 2006: *Evidence for aseismic deformation rate changes prior to earthquakes* Annu. Rev. Earth Planet. Sci. 34 591 627

Sausse, J.; 2002: *Hydromechanical properties and alteration of natural fracture surfaces in the Soultz granite (Bas-Rhin, France).*Tectonophysics, 348, 169-185

Sauter, M.; 1992: *Quantification and forecasting of regional groundwater flow and transport in a karst aquifer (Gallusquelle, Malm, SW. Germany).* Tubinger Geowissenschaftliche Arbeiten C13, Tubingen

Shepherd, A., et al.; 2012: *A reconciled estimate of ice sheet mass balance*, Science, 338(6111), 11831189

Schmid, S.M., Aebli, H.R., Heller, F.and Zingg, A.; 1989: *The role of the Periadriatic line in the tectonic evolution of the Alps.* In: Coward, M.P., Dietrich, D. & Park, R.G. (eds.), Alpine Tectonics, Geological Society Special Publication,45: 1-29; Oxford (Blackwell)

Schmid, R., Rothacher, M., Thaller, D. and Steigenberger, P.; 2005: *Absolute phase center corrections of satellite and receiver antennas.* GPS Solutions, 9(4), 283293. https://doi.org/10.1007/s10291-005-0134-x

Schmid, R., Steigenberger, P., Gendt, G., Ge, M. and Rothacher, M.; 2007: *Generation of a consistent absolute phase-center correction model for GPS receiver and satellite antennas.* Journal of Geodesy, 81(12), 781798. https://doi.org/10.1007/s00190-007-0148-y

Schmidt, S., Geyer, T., Guttman, J., Marei, A., Ries, F. and Sauter, M.; 2014: *Characterisation and modelling of conduit restricted karst aquifersExample of the Auja spring, Jordan Valley.* Journal of Hydrology, 511, 750763. https://doi.org/10.1016/j.jhydrol.2014.02.019

Schonenberg, R. and Neugebauer, J.; 1997: *Einfuhrung in die Geologie Europas* (7^{th} edition): 385 p.; Rombach (Freiburg)

Schuite, J., Longuevergne, L., Bour, O., Boudin, F., Durand, S. and Lavenant, N.; 2015: *Inferring field-scale properties of a fractured aquifer from ground surface deformation during a well test.* Geophysical Research Letters, 42, 10,69610,703. https://doi.org/10.1002/2015GL066387

Schuite, J., Longuevergne, L., Bour, O., Burbey, T. J., Boudin, F., Lavenant, N. and Davy, P.; (2017): *Understanding the hydromechanical behavior of a fault zone from transient surface tilt and fluid pressure observations at hourly time scales.* Water Resources Research, 53, 10,558-10,582. https://doi.org/10.1002/2017WR020588

Schwartz, S. Y. and Rokosky, J. M.; 2007: *Slow slip events and seismic tremor at circum-Pacific subduction zones*, Rev. Geophys. 45

Serpelloni, E., Casula, G., Galvani, A., Anzidei, M. and Baldi, P.; 2006: *Data analysis of permanent GPS networks in Italy and surrounding regions: Application of a distributed processing approach.* Annales Geophysique, 49, 897928. https://doi.org/10.4401/ag-4410

Serpelloni, E., Faccenna, C., Spada, G., Dong, D. and Williams, S. D. P.; 2013: *Vertical GPS ground motion rates in the Euro-Mediterranean region: New evidence of velocity gradients at different spatial scales along the Nubia-Eurasia plate boundary.* Journal of Geophysical Research: Solid Earth, 118, 60036024. https://doi.org/10.1002/2013JB010102

Serpelloni, E., Pintori, F., Gualandi, A., Scoccimarro, E., Anderlini, L., Belardinelli, M. E. and Todesco, M.; 2018: *Hydrologically induced karst deformation: Insights from GPS measurements*

in the Adria-Eurasia plate boundary zone, Journal of Geophysical Research: Solid Earth, vol. 123

Serpelloni, E., Vannucci, G., Anderlini, L. and Bennett, R. A.; 2016: *Kinematics, seismotectonics and seismic potential of the eastern sector of the European Alps from GPS and seismic deformation data*. Tectonophysics, 688, 157181. https://doi.org/10.1016/j.tecto.2016.09.026

Singhal, B. B. S. and Gupta, R. P.; 1999: *Fractures and discontinuities*. Springer, Dordrecht

Silverii, F.; 2016: *Study of the transient deformation of Central and Southern Apennines from GPS observations*. Phd thesis. Universit di Bologna, Italy

Silverii, F., D'Agostino, N. and Metois, M.; 2016: *Transient deformation of karst aquifers due to seasonal and multiyear groundwater variations observed by GPS in southern Apennines (Italy)*. Journal of Geophysical Research: Solid Earth, 121, 83158337. https://doi.org/10.1002/2016JB013361

Sitharam, T. G., Sridevi, J. and Shimizu, N.; 2001: *Practical equivalent continuum characterization of jointed rock masses*. International Journal of Rock Mechanics and Mining Sciences, 38(3), 437448. https://doi.org/10.1016/S1365-1609(01)00010-7

Sneddom, I.; 1946: *The distribution of the stress in the neighbourhood of a crack in an elastic solid*. Proceedings of the Royal Society of London. Series A, Mathematical and Physical Sciences. 187(1009):229 60

Sneddon, I. and Elliot, H.; 1946: *The opening of a Griffith crack under internal pressure*. Quarterly of Applied Mathematics. 4(3):262 7

Srebro, N. and Jaakkola, T.; 2003: *Weighted low-rank approximations*. Twentieth International Conference on Machine Learning. http://ttic.uchicago.edu/nati/Publications/SrebroJaakkolaICML03.pdf

Superchi, L.; 2012: *The Vajont rockslide: new techniques and traditional methods to re-evaluate the catastrophic event*. PhD Thesis

Swenson, S., Chambers, D. and Wahr, J.; 2008: *Estimating geocenter variations from a combination of GRACE and ocean model output*. Journal of Geophysical Research, 113, B08410. https://doi.org/10.1029/2007JB005338

Tenze, D., Braitenberg, C. and Nagy, I.; 2012: *Karst deformations due to environmental factors: evidences from the horizontal pendulums of Grotta Gigante, Italy.* Bollettino di Geofisica Teorica ed Applicata, 53, 331-345, doi:10.4430/bgta0049.

Topper, R., K. L. Spray, W. H. Bellis, J.L. Hamilton, and P. E. Barkmann; 2003: *Ground Water Atlas of Colorado*. Special Publications, SP-53. Denver, CO: Colorado Geological Survey, Division of Minerals and Geology, Department of Natural Resources

Trasatti, E., Kyriakopoulos, C. and Chini, M.; 2011: *Finite element inversion of DInSAR data from the Mw 6.3 L'Aquila earthquake, 2009 (Italy)*, Geophys. Res. Lett., 38, L08306, doi:10.1029/2011GL046714.

Tregoning, P., Watson, C., Ramillien, G., McQueen, H., Zhang, J.; 2009: *Detecting hydrologic deformation using GRACE and GPS*. Geophys Res Lett 36:L15401. doi:10.1029/2009GL038718

Tregoning, P. and van Dam, T.; 2005: *Atmospheric pressure loading corrections applied to GPS data at the observation level*. Geophysical Research Letters, 32, L22310. https://doi.org/10.1029/2005GL024104

van Dam, T. M., Blewitt, G. and Heflin, M. B.; 1994: *Atmospheric pressure loading effects on global positioning system coordinate determinations*. Journal of Geophysical Research, 99(B12), 23,93923,950. https://doi.org/10.1029/94JB02122

Villagra, M., Bacchi, O., Tuon, R. L. and Reichardt, K.; 1995: *Difficulties of estimating evapotranspiration from the water-balance equation*. Agricultural and Forest Meteorology, 72(34), 317325. https://doi.org/10.1016/0168-1923(94)02168-J

Wdowinski, S., Bock, Y., Zhang, J., Fang, P. and Genrich, J.; 1997: S*outhern California Permanent GPS Geodetic Array: spatial filtering of daily positions for estimating coseismic and postseismic displacements induced by the 1992 Landers earthquake*, J. geophys. Res.,102,18 05718 070

Westergaard, H.M.W.; 1939: *Bearing Pressures and Cracks*. Journal of Applied Mechanics, 6, A49-A53.

Williams, P.W.; 1983: *The role of the subcutaneous zone in karst hydrology*. Journal of Hydrology,61 , 4567

Williams P.W.; 2008: *The role of the epikarst in karst and cave hydrogeology: a review*. International Journal of Speleology, 37 (1), 1-10. Bologna (Italy). ISSN 0392-6672

Williams, S. D. P.; 2003: *The effect of coloured noise on the uncertainties of rates estimated from geodetic time series*, J. Geod., 76 , 483494, doi:10.1007/s00190-002-0283-4

Williams, S. D. P. and Penna, N. T.; 2011: *Non-tidal ocean loading effects on geodetic GPS heights*. Geophys Res Lett 38: L09314. doi: 10.1029/2011GL046940

Yang, D., Koike, T., Tanizawa, H.; 2004: *Application of a distributed hydrological model and weather radar observations for flood management in the upper Tone River of Japan.* Hydrol. Process. 18, 31193132

Zeller, S. S. and Pollard, D. D.; 1992: *Boundary conditions for rock fracture analysis using the boundary element method*, J. Geophys. Res., 97(B2), 19911997, doi:10.1029/91JB02254.

Zempolich, W. G. and Hardie, L. A.; 1997: *Geometry of Dolomite Bodies Within Deep-Water Resedimented Oolite of the Middle Jurassic Vajont Limestone, Venetian Alps, Italy: Analogs for Hydrocarbon Reservoirs Created Through Fault-Related Burial Dolomitization.* In J.A. Kupecz, J.Gluyas, and S. Bloch, eds., Reservoir quality prediction in sandstones and carbonates. AAPG Memoir 69, p. 127-162